Numerical analysis of metallographic preparation effect on the hardness of titanium alloy

Slokar Benić, Ljerka; Ivec, Ivan; Šimić, Klara; Jandrlić, Ivan

Conference presentation / Izlaganje na skupu

Permanent link / Trajna poveznica: https://urn.nsk.hr/urn:nbn:hr:115:885670

Rights / Prava: In copyright / Zaštićeno autorskim pravom.

Download date / Datum preuzimanja: **2025-03-19**

SVEUČILIŠTE U ZAGREBU METALURŠKI FAKULTET
UNIVERSITY OF ZAGREB FACULTY OF METALLURGY
SISAK

Repository / Repozitorij:

Repository of Faculty of Metallurgy University of Zagreb - Repository of Faculty of Metallurgy University of Zagreb

DIGITALNI AKADEMSKI ARHIVI I REPOZITORIJI

XIX INTERNATIONAL SCIENTIFIC CONGRESS

WINTER SESSION

09 - 12.03.2022, BOROVETS, BULGARIA

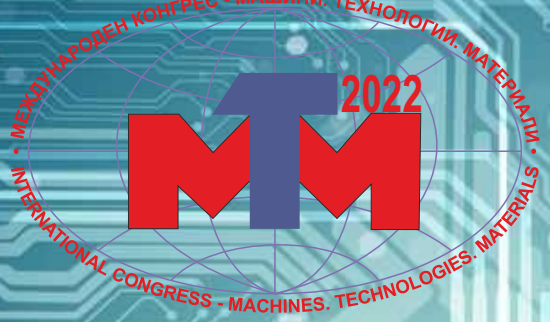

MACHINES. TECHNOLOGIES. MATERIALS 2022

PROCEEDINGS

VOLUME I
MACHINES
MATERIALS

ISSN 2535-0021 (PRINT)
ISSN 2535-003X (ONLINE)

SCIENTIFIC-TECHNICAL UNION OF MECHANICAL ENGINEERING - INDUSTRY 4.0
BULGARIA

XIX INTERNATIONAL SCIENTIFIC CONGRESS

MACHINES. TECHNOLOGIES. MATERIALS

09-12.03.2022, BOROVETS, BULGARIA

PROCEEDINGS

YEAR V, ISSUE 1 (21), BOROVETS, BULGARIA 2022

VOLUME I

MACHINES. MATERIALS.

ISSN 2535-0021 (PRINT)
ISSN 2535-003X (ONLINE)

PUBLISHER:

SCIENTIFIC TECHNICAL UNION OF MECHANICAL ENGINEERING INDUSTRY-4.0

108, Rakovski Str., 1000 Sofia, Bulgaria
tel. (+359 2) 987 72 90,
tel./fax (+359 2) 986 22 40**,**
office@mtmcongress.com
www.mtmcongress.com

INTERNATIONAL EDITORIAL BOARD

Chairman: Prof. DHC Georgi Popov

Vice Chairman: Prof. D.Sc. Tsanka Dikova

Members:

Acad. Ivan Vedyakov	RU	Prof. Mihail Aurel Titu	RO
Acad. Yurij Kuznetsov	UA	Prof. Mladen Velev	BG
Prof. Aleksander Mihaylov	UA	Prof. Mohamed El Mansori	FR
Prof. Anatoliy Kostin	RU	Prof. Movlazade Vagif Zahid	AZ
Prof. Adel Mahmud	IQ	Prof. Nikolay Dyulgerov	BG
Prof. Ahmet Ertas	TR	Prof. Oana Dodun	RO
Prof. Andrzej Golabczak	PL	Prof. Olga Krivtsova	KZ
Prof. Boncho Bonev	BG	Prof. Peter Kostal	SK
Prof. Gennady Bagluk	UA	Prof. Raul Turmanidze	GE
Prof. Detlef Redlich	DE	Prof. Renato Goulart	BR
Prof. Dipten Misra	IN	Prof. Roumen Petrov	BE
Prof. Dmitry Kaputkin	RU	Prof. Sasho Guergov	BG
Prof. Dmitry Dmitriev	UA	Prof. Seiji Katayama	JP
Prof. Eugene Eremin	RU	Prof. Sergej Dobatkin	RU
Prof. Ernest Nazarian	AM	Prof. Sergej Nikulin	RU
Prof. Juan Alberto Montano	MX	Prof. Stefan Dimov	UK
Prof. Esam Husein	KW	Prof. Svetan Ratchev	UK
Prof. Ilir Doci	KO	Prof. Svetlana Gubenko	UA
Prof. Ivo Malakov	BG	Prof. Sveto Cvetkovski	NM
Prof. Katia Vutova	BG	Prof. Tale Geramitchioski	NM
Prof. Krasimir Marchev	USA	Prof. Vadim Kovtun	BY
Prof. Leon Kukielka	PL	Prof. William Singhose	USA
Prof. Lyudmila Ryabicheva	UA	Prof. Yasar Pancar	TR
Prof. Milan Vukcevic	ME	Prof. Wu Kaiming	CN

C O N T E N T S

MACHINES

MATERIALS

Development of an environmentally friendly commercial kitchen cooker using hydrogen as fuel

Zafer Kahraman[1], Murat Hacı[1], Erdinç Baştuğ[1], Hakan Serhad Soyhan[2,3]
[1]Öztiryakiler Madeni Eşya San. Ve Tic. A.Ş, R&D Technology Center
34500 Büyükçekmece, İstanbul, Turkey
[2]Sakarya University, Fire and Combustion Research Centre, Esentepe Campus, Sakarya, Turkey
[3] Team-San Ltd. Sti., Esentepe Campus, Sakarya University, 54050, Sakarya, Turkey
zkahraman@oztiryakiler.com.tr

Abstract: *Commercial kitchen cookers are widely used in various capacities and fuels (natural gas, LPG, etc.). Depending on the decrease in fossil resources and the increase in energy needs, several researches in alternative fuels have been accelerated. Especially in recent years, R&D studies and investments in renewable and environmentally friendly energy sources (solar, wind, biomass etc.) have increased. In line with the EU's Renewable Energy Directive (Directive 2018/2001/EU), it is aimed to use at least 32% renewable energy sources by 2030. Significant R&D gains have been achieved with the cooperation of industry-university in order to use hydrogen as clean energy as an environmentally friendly alternative energy source for commercial kitchens. In this work, we developed an environmentally friendly commercial kitchen cooker prototype using hydrogen with a uniquely designed burner has been achieved. Results show that using hydrogen in commercial kitchens is promising if hydrogen safety is locally possible.*

Keywords*: COMMERCIAL KITCHEN COOKER, HYDROGEN TECHNOLOGY, BURNER DESIGN*

1. Introduction

Concerns about global warming and the environment have been increasing in recent years, along with the use of fossil fuels (natural gas, coal, etc.). For this reason, studies on the dissemination of renewable energy sources (solar, wind, biomass, etc.) are increasing [1, 2]. In this respect, hydrogen has gained importance in studies to use it as an alternative fuel in various fields [3-8].

Various model cookers are indispensable for cooking in commercial kitchens (restaurants, factories, shopping malls, etc.). The use of various gas fuels (natural gas and LPG, etc.) instead of electricity in commercial kitchen cookers is preferred by many enterprises for economic reasons. However, alternative renewable fuel researches are increasing in line with the risk of fossil fuels in terms of the environment. In addition to the use of hydrogen alone, studies have been carried out on the combustion performance with natural gas [9, 10], methane [11-13], ammonia [14] etc.

The envisaged situation for various application areas of hydrogen in the energy system in the future is given in Fig. 1 [15].

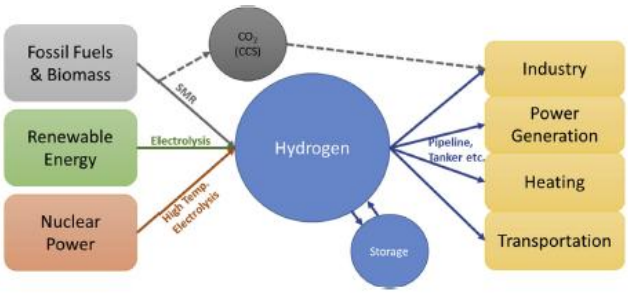

Fig. 1 *Various application areas of hydrogen in the energy system in the future [15].*

There is no study for hydrogen as an alternative fuel in commercial kitchen cookers. However, various studies have been conducted on hydrogen in households and portable type cookers/stoves. Various studies in this field are summarized below;

The hydrogen cooking process obtained from a proton exchange membrane electrolyzer (PEM) with solar energy using photovoltaic panels was carried out by Topriska and her team. They stated that the hydrogen production mechanism established in the simulation studies was sufficient for cooking small amounts of food [16].

Rivera and his team compared conventional fuels (LPG, charcoal, firewood) with hydrogen obtained by electrolysis in cooking in developing countries. Compared with conventional fuels, hydrogen has a significant impact on fossil fuel consumption, climate change, ozone depletion, etc. emphasized its superiority over other fuels in terms of properties. However, they stated that more research should be done on hydrogen for developing countries [17].

The hydrogen operation of the design-specific glass-ceramic cooking unit was evaluated by Fumey and the scientific study group. Performance test applications of the developed system were carried out under the DIN EN 30-2-1: 2005-08 standard. According to this standard, high-efficiency values of up to 80% have been achieved. The cooking unit is made in the dimensions of 400x290x94 mm. The active area of the combustion system was also 2x176 cm^2 [18].

The combustion unit for working with hydrogen is formed from a highly porous (>90%) SiC foam ceramic structure. The porous SiC foam ceramic structure provides advantages due to its high-temperature stability and good thermal shock resistance. SiC foam has been used with different pore sizes. The schematic representation of the combustion system is given in Fig. 2 [18].

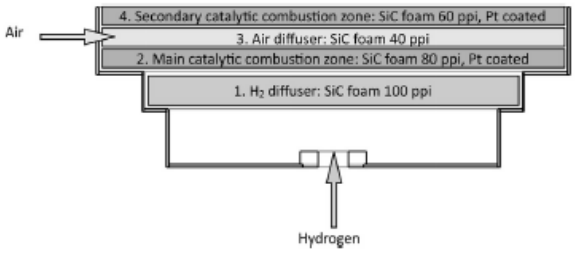

Fig. 2 *Schematic representation of the SiC foam ceramic containing hydrogen combustion unit. [18].*

Singh and his research group have evaluated the hydrogen economy. A comparison of the energy values of various fuels is shown in Fig. 3 [19].

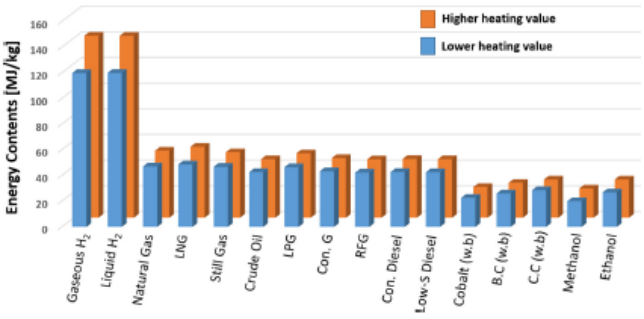

Fig. 3 *Energy heating values of various fuels. [19].*

Depending on the development of the conditions related to the acquisition, storage, and safety of hydrogen, its usage areas as the clean fuel of the future will increase. It is expected that the importance of hydrogen as an alternative fuel will increase in the coming years due to the environmental problems caused by fossil fuels.

2. Methodology

First of all, the original design of the hydrogen burner was developed for the burner used in commercial kitchens. The innovative hydrogen burner is made of stainless steel (AISI 304) material.

Combustion analysis was performed by parametric study for different pressures and burner hole diameters. It has been determined at which burner hole diameter and pressures the maximum value of 650ºC is reached, which is determined according to safe use, depending on the material properties for the under-pan temperature. As a result of the trials, the operating range of the system was determined.

In addition, with the visible results obtained from the analyzes, how the flames are shaped, the chemical conditions of the fuel and air in the system, and at the time of combustion were obtained. The temperatures formed under the cooker and in flames are presented visually.

The technical drawing of the burner using hydrogen as fuel in a commercial cooker is given in Fig. 4.

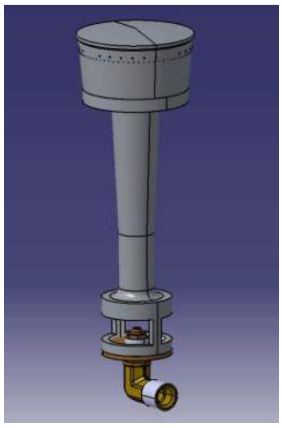

Fig. 4 *The technical drawing of the burner using hydrogen as fuel in a commercial cooker.*

A view of the innovative commercial kitchen cooker prototype (top view) is given in Fig. 5.

Fig. 5 *View of the innovative commercial kitchen cooker prototype (top view – surface with H_2 logo).*

It has also been painted green to make the innovative prototype appear environmentally friendly. View of the innovative commercial kitchen cooker prototype using hydrogen as fuel is given in Fig. 6.

Fig. 6 *View of the innovative commercial kitchen cooker prototype using hydrogen as fuel.*

3. Experimental procedure

The hydrogen used in the test phase was obtained from the hydrogen gas cylinder. High purity hydrogen (99.999%) is used in the innovative commercial kitchen cooker prototype with a unique design. During the test phase, special connection equipment (flowmeter, regulator, etc.) was used between the hydrogen gas cylinder and the innovative commercial kitchen cooker prototype.

The sensitivity of the burner, which was developed with a unique design in a commercial kitchen cooker that uses hydrogen as an alternative fuel, to different hydrogen pressures was evaluated according to various operating conditions.

Pot bottom temperature simulations according to burner hole diameters from 0.25 mm to 0.4 mm (respectively hole diameters 0.25, 0.3, 0.35 and 0.40 mm) for 8 mbar fuel pressure, are shown in Fig. 7.

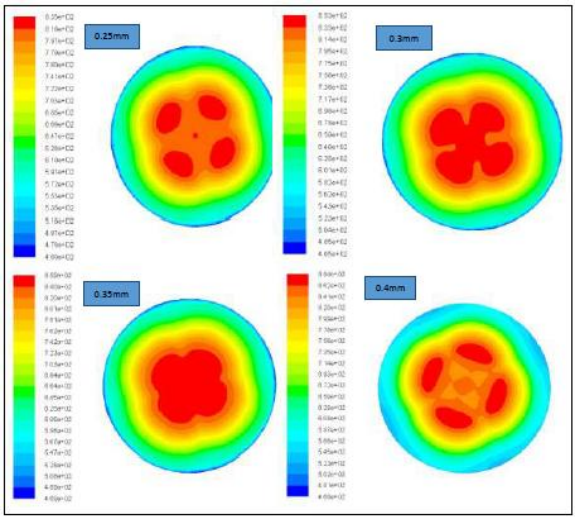

Fig. 7 *Pot bottom temperature for 8 mbar fuel pressure.*

Efficiency measurement tests of high purity hydrogen were carried out according to EN 203-2-3 standard (Gas heated catering equipment - Part 2-3: Specific requirements - Boiling pans).

4. Conclusions

With R&D studies, an innovative prototype was obtained with the original burner that uses hydrogen as fuel in the eco-friendly cooker for commercial kitchens. The gains achieved through R&D activities are given below.

Simulation studies were carried out according to 16 situations according to different hydrogen fuel pressures (8, 14, 20, and 32 mbar) and different burner hole diameters (0.25, 0.3, 0.35 and 0.4 mm). In the evaluations made with simulation analysis, it was determined that combustion with hydrogen was at 8 mbar fuel pressure and 0.3 mm burner hole diameter.

It has been determined that all values are close to each other in the evaluations made according to different burner hole diameters at the lowest value of the fuel pressure (8 mbar).

It has been observed that the temperature values increase in direct proportion to the increasing fuel pressure values.

As a result of the test and evaluation studies, the innovative burner, which works in harmony with hydrogen, in the prototype of the commercial kitchen cooker was achieved. Thus, it has been achieved to reduce the innovative product's CO and NOx emission values in an environmentally friendly manner. It has been shown that hydrogen can be used efficiently in commercial kitchen appliances as an alternative fuel.

Acknowledgment

This study was prepared within the scope of TÜBİTAK-TEYDEB 1501 coded Industrial Research Technology Development and Innovation Projects Support Program project numbered 3120882. We would like to thank TÜBİTAK-TEYDEB Transport, Defense, Energy and Textile Technologies Group (USETEG) for their contribution to the project.

5. References

1. Schenone, C., Delponte, I., Energy Policy, **156**, 112475, (2021)
2. Vivek, C. M., Ramkumar, P., Srividhya, P. K., Sivasubramanian, M., Materials Today: Proceedings, **46**, 8204-8208, (2021)
3. Endo, N., Goshome, K., Tetsuhiko, M., Segawa, Y., Shimoda, E., Nozu, T., Int. Journal of Hydrogen Energy, **46**, 262-271, (2021)
4. Yamamoto, H., Fujioka, H., Okano, K., Renewable Energy, **178**, 1165-1173, (2021)
5. Capurso, T., Stefanizzi, M., Torresi, M., Camporeale, S. M., Energy Conversion and Management, **251**, 114898, (2022)
6. Momirlan, M., Veziroglu, T.N., International Journal of Hydrogen Energy, **30**, 795 – 802, (2005)
7. Yue, M., Lambert, H., Pahon, E., Roche, R., Jemei, S., Hissel, D., Renewable and Sustainable Energy Reviews, **146**, 111180, (2021)
8. Chapman, A., Itaoka, K., Farabi-Asl, H., Fujii, Y., Nakahara, M., Int. Journal of Hydrogen Energy, **45**, 3883- 3898, (2020)
9. Vries, H., Mokhov,A. V., Levinsky, H. B., Applied Energy, **208**, 1007–1019, (2017)
10. Zhao, Y., McDonell, V., Samuelsen, S., Int. Journal of Hydrogen Energy, **44**, 12239-12253, (2019)
11. Escobedo E. G., Cubero, A., Ochoa, J. S., Fueyo, N., Int. Journal of Hydrogen Energy, **44**, 27123- 27140, (2019)
12. Burbano, H. J., Amell, A. A., Garcia, J. M., Int. Journal of Hydrogen Energy, **33**, 3410- 3415, (2008)
13. Choi, J., Rajasegar, R., Lee, W., Lee, T., Yoo, J., Int. Journal of Hydrogen Energy, **46**, 23906-23915, (2021)
14. Hussein, N. A., Medina, A. V., Alsaegh, A. S., Energy Procedia, **158**, 2305–2310, (2019)
15. Chapman, A., Itaoka, K., Hirose, K., Davidson, F. T., Nagasawa, K., Lloyd, A. C., Webber, M. E., Kurban, Z., Managi, S., Tamaki, T., Lewis, M. C., Hebner, R. E., Fujii, Y., Int. Journal of Hydrogen Energy, **44**, 6371-6382, (2019)
16. Topriska, E., Kolokotroni, M., Dehouche, Z., Wilson, E., Renewable Energy, **83**, 717-728, (2015)
17. Rivera, X. C. S., Topriska, E., Kolokotroni, M., Azapagic, A., Journal of Cleaner Production, **196**, 863-879, (2018)
18. Fumey, B., Stoller, S., Fricker, R., Weber, R., V. Dorer, V., Vogt, U.F., Int. Journal of Hydrogen Energy, **41**, 7494-7499, (2016)
19. Singh, R., Singh, M., Gautam, S., Materials Today: Proceedings, **46**, 5420–5427, (2021)

On the study of some characteristics ensuring loading capacity of rack drives

Emilia Abadjieva
Institute of Mechanics - Bulgarian Academy of Science, Sofia, Bulgaria
abadjieva@gmail.com

Abstract: *This research deals with the study of some kinematic characteristics, which can be used to ensure the loading capacity of the rack drives, including its hydrodynamic component. A brief analysis of the spatial rack drives in terms of their load capacity is realized. When mutually enveloping tooth surfaces are synthesized, it is possible to appear singular contact points appear on the active tooth surfaces. Two kinds of singular points exist, depending on the normal vector to the meshed tooth surfaces in their common points: singular points of first-order (called ordinary nodes), and singular points of second-order. Singular points of first order should be registered and eliminated from the mesh region since increased specific friction, worsen lubrication, and heat transfer are present, which result in a decreased loading capacity of the gear set A special accent is placed on the registration and elimination of singular points on the tooth surfaces of the synthesized rack drives. Analytical expressions are written defining total transference velocity and its normal component to an instantaneous contact line at an arbitrary contact point.*

Keywords*: RACK DRIVES, SINGULAR POINTS, HYDRODYNAMIC LOADING CAPACITY,*

1. Introduction

The choice of a rational form of spatial gearing (as a basic element of any mechanical transmission) is an essential problem, the optimal solution of which is related to the following requirements:

- satisfying the preliminary given loading capacity with minimal energy consumption for operation;
- ensuring optimal accuracy of the realization/implementation of the law of motions transformation;
- application of the most effective technological approaches in the technical realization of the mechanical system.

The object of the current study is spatial rack mechanisms, in which the rotating link has helical surfaces with a constant axial pitch. The theoretical synthesis of the studied mechanisms is subordinated to the second principle of T. Olivier [1].

When comparing the different types of rack drives in terms of their loading capacity, it is necessary to take into account the technological approaches to their practical realization. Here it is necessary to mention that to fully reach the given loading capacity (power transmitted through the transmission) it is necessary to realize the planned tooth contact with optimal accuracy. This is achieved by ensuring optimality between the working (theoretical) and instrumental (technological) conjugation of the tooth surfaces of the movable links. This requires searching for technical approaches for the exact elaboration of the tooth surfaces of both the worm and the gear rack. This is achieved when the manufacturing technology is ensured the appropriate finishing operations that accompany the generation of the tooth surfaces of the movable links. Technologically-based and effective approaches of the mentioned type can be provided when the rotating movable link is an involute worm or a worm with a circular profile of the teeth. These approaches create conditions for the final processing of the active tooth surfaces of the movable links after heat treatment by grinding. This ensures increased hardness, smoothness, and durability of the working tooth surfaces of the tooth links, which is a premise for increasing their contact strength and hydrodynamic loading capacity. Increasing the load capacity of the rack drives and in particular, its hydrodynamic loading capacity is achieved by choosing the appropriate geometry of the conjugated tooth surfaces. This is achieved by satisfying the quality of gearing within the mesh region by registering and eliminating the occurrence of the singular contact points in the mesh region of the synthesized gear set; selection of appropriate placement of the contact lines between the tooth surfaces of the movable links in relation to the transference velocities of the links in the different contact points, which are part of them, etc.

The focus of the study is put on some kinematic characteristics, which can be used to ensure the loading capacity of the rack drives, including its hydrodynamic component.

2. Study of the Singularity of Tooth Surfaces Materials

The researches, related to the singularity of the conjugated active tooth surfaces of the hyperboloid gear mechanisms, are dedicated studies of many scientists including A. Georgiev ((independently [2] and in co-authorship with V. Goldfarb [3]), V. Ganshin [4], I. Dusev and V. Vasilev [5], F. Litvin [1, 6], S. Lagutin [7, 8], K. Minkov [9], V. Abadjiev [10], W. Nelson [11] and others. The author of the current study in co-authorship with other researchers has devoted several of her publications on this topic, related to the study of spatial gears of the Wildhaber type [12] and Planoid gears [13-15].

Here is presented a study (see Fig. 1) of the conditions, under which in the process of meshing of the kinematic conjugated surfaces Σ_1 and Σ_2 of the spatial rack drives, the contact points "degenerate" into *nodes (singular) points*. This research is based on the theoretical approach offered by F. Litvin [1, 6]. According to it the nodes in the most common case are those common points between Σ_1 and Σ_2, for which the condition *their relative velocity on one of the contacting surfaces* ($i = 1,\ 2$), written in the fixed coordinate system:

$$\overline{\rho}_i = \overline{\rho}_i(u_i, \vartheta_i, \Phi_i), \tag{1}$$

to be equal to zero is fulfilled, i.e., :

$$\overline{V}_{r,i} = \frac{\partial \overline{\rho}_i}{\partial u_i}.\frac{du_i}{dt} + \frac{\partial \overline{\rho}_i}{\partial \vartheta_i}.\frac{d\vartheta_i}{dt} = \overline{0}. \tag{2}$$

The expression (2) is correct because it refers to the relative velocity of a point on a particular contact line corresponding to $\Phi_i = const.$ For the studied case, both mutually enveloping surfaces are presented by the meshing parameter of the rotating link, i.e. $\Phi_1 = \varphi_1$, $\Phi_2 = j_{21}\varphi_1$, $j_{21} = const$. Depending on the behavior of the normal vector $\overline{n}_i$ in the common contact point of the conjugated surfaces Σ_1 and Σ_2, there are two types of singular points:

- *singular points of the first-order* ***(****ordinary contact nodes****)****,* for which it is fulfilled $\overline{n}_i \neq \overline{0}$ and hence, $\dot{\overline{n}}_{r,i} = \overline{0}$ ($\dot{\overline{n}}_{r,i}$ is the relative velocity at the tip of the normal vector $\overline{n}_i$);

- *singular points of second-order* ***(****undercutting points****)****,* for which it is fulfilled $\overline{n}_i = \overline{0}$.

Further, the character of the two types of singular points are going to be explained in the context of kinematically conjugated tooth surfaces, the synthesis of which is realized in accordance t the second principle of T. Olivier. It will be searched for vector and analytical dependences, which define the conditions for their appearance on the mesh region, respectively on the meshed tooth surfaces of the synthesized gear mechanism, as well as possible approaches for their elimination in the process of the synthesis.

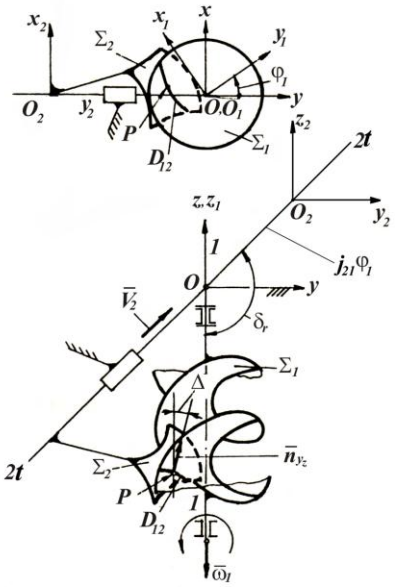

Fig. 1. *Geometric-kinematic scheme of spatial motions transformation of type rotation into translation*

For the contact points in the fixed coordinate system, as points from the mesh region it can be written:

$$\dot{\bar{\rho}}_1 = \dot{\bar{\rho}}_2 = \dot{\bar{V}}, \tag{3}$$

respectively

$$\bar{V}_1 + \bar{V}_{1r} = \bar{V}_2 + \bar{V}_{2r} = \bar{V}, \tag{4}$$

where $\dot{\bar{\rho}}_i$ is an absolute velocity vector of the contact point that belongs to the surface Σ_i; $\bar{V}_i$ - transference velocity of the contact point; $\bar{V}_{ir}$ - relative velocity vector belonging to Σ_i; $\bar{V}$ - velocity of the contact point as a point of the mesh region.

In addition to the vector equalities (3) and (4) for the contact points of the mutually enveloping surfaces Σ_1 and Σ_2 the basic equation of meshing is valid, which in this case is presented in the form:

$$\bar{n}_i \bar{V}_{12} = f_i(u_i, \vartheta_i, \varphi_1) = 0. \tag{5}$$

The equation of meshing (5) is fulfilled for every value of the meshing parameter, which determines the ability to differentiate it, i.e:

$$\frac{\partial f_i}{\partial u_i}.\frac{du_i}{dt} + \frac{\partial f_i}{\partial \vartheta_i}.\frac{d\vartheta_i}{dt} + \frac{\partial f_i}{\partial \varphi_1}.\frac{d\varphi_1}{dt} = 0. \tag{6}$$

The equalities (3), (4), (5), and (6) are fulfilled for every contact point of the conjugated tooth surfaces Σ_1 and Σ_2 of the studied rack drives.

Registration and elimination of the ordinary nodes on the mesh region. It is possible to exist undesired ordinary nodes (singular points of first-order) on the conjugated tooth surfaces of spatial gear mechanisms. They are points of contact or intersection of the contact lines. Their existence in the mesh region should be registered and eliminated from the mesh region since increased specific friction, worsen lubrication, and heat transfer are present, which result in a decreased hydrodynamic loading capacity in the synthesized transmission.

Let's consider the case when on the meshed tooth surfaces Σ_1 and Σ_2 of the spatial rack drive, there is a singularity of first-order. Equation (6) is written in the form:

$$\dot{\bar{n}}_i \bar{V}_{12} + \bar{n}_i \dot{\bar{V}}_{12} = 0, \tag{7}$$

where

$$\begin{aligned} &\bar{V}_{12} = \bar{V}_1 - \bar{V}_2, \\ &\dot{\bar{V}}_{12} = \dot{\bar{V}}_1 - \dot{\bar{V}}_2 = \dot{\bar{\omega}}_1 \times \bar{\rho}_1 + \bar{\omega}_1 \times \dot{\bar{\rho}}_1 - \dot{\bar{V}}_2. \end{aligned} \tag{8}$$

When the contact points are ordinary nodes, the condition $\dot{\bar{n}}_i \neq \bar{0}$ is fulfilled. Besides $\dot{\bar{\omega}}_1 = \bar{0}$ ($\omega_1 = const$) and $\dot{\bar{V}}_2 = \bar{0}$ ($V_2 = const.$) and from (7) and (8) it is obtained:

$$\dot{\bar{n}}_i \bar{V}_{12} + \bar{n}_i (\bar{\omega}_1 \times \dot{\bar{\rho}}_1) = 0. \tag{9}$$

a) Spatial rack drives are synthesized in accordance with the second principle of T. Olivier and the instrumental surfaces (preliminary defined) are the active tooth surfaces Σ_1 of the rotating link, i.e. $\bar{V}_{1r} = \bar{0}$, $\bar{n}_i \equiv \bar{n}_1 \neq \bar{0}$ and $\dot{\bar{n}}_{1r} = \bar{0}$.

Then (9) is of the type

$$\dot{\bar{n}}_1 \bar{V}_{12} + \bar{n}_1 (\bar{\omega}_1 \times \dot{\bar{\rho}}_1) = 0. \tag{10}$$

Since $\dot{\bar{n}}_1 = (\bar{\omega}_1 \times \bar{n}_1)$, $\dot{\bar{\rho}}_1 = \bar{V}_1$, then from (10) the following equality is obtained

$$(\bar{\omega}_1 \times \bar{n}_1)\bar{V}_2 = 0. \tag{11}$$

b) Spatial rack drives are synthesized in accordance with the second principle of T. Olivier and the instrumental surfaces (preliminary defined) are the surfaces Σ_2 of the gear rack, i.e. $\bar{V}_{2r} = \bar{0}$, $\bar{n}_i \equiv \bar{n}_2 \neq \bar{0}$ and $\dot{\bar{n}}_{2r} = \bar{0}$.

Then, analogously to the above cases, it can be written

$$\dot{\bar{n}}_2 = (\bar{\omega}_2 \times \bar{n}_2) = \bar{0}, \quad \dot{\bar{\rho}}_2 = \bar{V}_2. \tag{12}$$

In this case from (9) and (12) it is obtained

$$\bar{n}_2 (\bar{\omega}_1 \times \bar{V}_2) = 0. \tag{13}$$

The equalities (11) and (13) are equivalent since at the common contact point of the conjugated surfaces Σ_1 and Σ_2 of the spatial rack drive, the following condition is fulfilled:

$$\bar{n}_i . \bar{\omega}_1 . \bar{V}_2 = 0, \quad (i = 1, \ 2). \tag{14}$$

From (14) follows, that in order to exclude the singular points of first-order from the mesh region of the rack drive, in the process of its synthesis, the following inequality is a sufficient condition:

$$\bar{n}_i . \bar{\omega}_1 . \bar{V}_2 \neq 0, \quad (i = 1, \ 2). \tag{15}$$

According to the task, illustrated in Fig. 1 and Fig 2, it is obvious that inequality (15) is equivalent to

$$\bar{n}_{i,x} \neq \bar{0} \qquad (16)$$

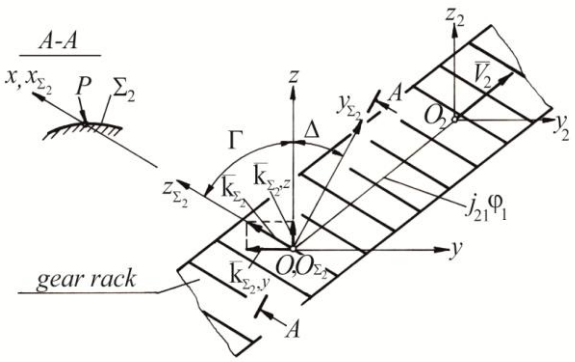

Fig. 2. *Orientation of the coordinate system* $S_2(O_2, x_2, y_2, z_2)$ *of the cylindrical surface* Σ_2

Let us accept, that the spatial rack drive is synthesized in accordance with the conditions described in (a). Let us write the equation of meshing

$$\tan\Delta = \frac{n_{1,y}}{n_{1,z}} = \frac{p + j_{21}\cos\delta_r}{j_{21}\sin\delta_r} = const. \quad [16]$$ for the case of the existence of ordinary nodes in the mesh region, i.e. when the condition is fulfilled:

$$\bar{n}_{1,x} \neq \bar{0}. \qquad (17)$$

For this case, the equation of meshing is of the type

$$(x + j_{21}\sin\delta_r)\tan\Delta - j_{21}\cos\delta_r \neq 0. \qquad (18)$$

After simple transformations based on (18) it can be written a sufficient condition under which the singularity of the first order is missing in the region of mesh:

$$p \neq -x\tan\Delta. \qquad (19)$$

Besides

$$\tan\Delta = \frac{p - j_{21}\cos\Sigma_r}{j_{21}\sin\Sigma_r} = \frac{p - p_{z_0}}{j_{21}\sin\Sigma_r}. \qquad (20)$$

From (20) it can be seen that if the condition is fulfilled

$$p = p_{z_0}, \qquad (21)$$

i. e. if the helical parameter of the helical gear with the helical teeth is equal to the parameter of the relative helices of the sliding velocity vector field, then $\tan\Delta = 0$ and condition (19) is always fulfilled.

Registration and elimination of the undercutting points from the action surface. The singular points of second order should be eliminated from the action surface/region of mesh since they are undercutting points in instrumental meshing or points of interference in the case of work gearing of the conjugated tooth surfaces of the synthesized gear transmissions. The process of undercutting of the surfaces $\Sigma_2^{(j)}$ ($j = 1,\ 2$), when their generation is realized in accordance with the second principle of T. Olivier, concludes that the transition surface formed by the tip of the cutting edge of the instrumental surface Σ_J takes part of the active surface $\Sigma_2^{(j)}$. In this case, the transition and the active tooth surface $\Sigma_2^{(j)}$ have no tangent contact, and they intersect in the undercutting points.

Undercutting, as a rule, leads to weakening of the tooth and deterioration of the bending gear strength. The curvature of the tooth in the vicinity of the undercutting points assumes values unfavorable for the contact strength of the generated teeth.

The study of the appearance of singular points of second-order on the action surface/mesh region of the spatial rack drive is realized for the case in which the generating tooth surfaces are the surfaces Σ_1 of the rotating link. For this case, the result of avoidance of undercutting points on Σ_2 is an absence of undercutting. According to the accepted methodology [1] and taking into account the vector equality (4), if the generated tooth surface Σ_2 is composed only of non-singular points, i.e. for all points from Σ_2, that belongs to the action surface, the following equality is valid:

$$\dot{\bar{\rho}}_2 = \bar{V}_2 + \bar{V}_{2r} = \bar{V}. \qquad (22)$$

It is known, [1, 6], that the absolute velocity $\bar{V}$ of an arbitrary point from the action surface/mesh region, lies in the tangential surface to it, i.e. the following form of the equation of meshing is true:

$$\bar{n}_{AS}\bar{V} = \bar{n}_{AS}\bar{V}_2 + \bar{n}_{AS}\bar{V}_{2r} = 0, \qquad (23)$$

where $\bar{n}_{AS}$ is a normal vector to the action surface/mesh region in its arbitrary point.

Since the mesh region is composed only of non-singular points for which it is fulfilled

$$\bar{n}_{AS} \neq \bar{0},\ \ \bar{V}_{2r} \neq \bar{0}, \qquad (24)$$

Then from (23), it follows that the sufficient condition that there are no undercutting points on the action surface/mesh region is:

$$\bar{n}_{AS}.\bar{V}_2 \neq \bar{0}. \qquad (25)$$

From [16] and Fig. 2, the action surface/region of mesh is a cylindrical surface with a generatrix -a line parallel to the axis Oz and the directed line – a contact line for an arbitrary $\varphi_1 = const.$ The normal vector $\bar{n}_{AS}$ in every point that belongs to generatrix, is the same.

Let us consider a cross-section of the action surface/region of mesh with a plane perpendicular to the axis Oz. The normal line to the curve of the cross-section coincides with $\bar{n}_{AS}$. Let, the action surface be presented through the contact points, that belongs to the rotating link $i = 1$:

$$\begin{aligned} &\bar{\rho}_1 = \bar{\rho}_1(u_1, \vartheta_1, \varphi_1) = \bar{\rho}(u, \vartheta, \varphi_1), \\ &\bar{n}_1\bar{V}_{12} = f_1(u_1, \vartheta_1, \varphi_1) = f(u, \vartheta, \varphi_1) = 0, \end{aligned} \qquad (26)$$

where $u_1 \equiv u,\ \ \vartheta_1 \equiv \vartheta$ are curvilinear coordinates of Σ_1.

The curve of the cross-section of the action surface is found by the projection of an arbitrary contact line (corresponding to an arbitrary $\varphi_1 = const$.) on the plane Oxy ($z = 0$). Without disturbing the community of arguments, let this in the contact line corresponds to the $\varphi_1 = 0$.

Then the system (26) is written of the type:

$$\bar{\rho} = \bar{\rho}(u, \vartheta, 0), \quad f(u, \vartheta, 0) = 0, \tag{27}$$

and the analytical type of the action surface obtains:

$$\begin{aligned} &x = x(u, \vartheta), \quad y = y(u, \vartheta), \\ &z = w, \quad w \in (-\infty, +\infty), \quad f(u, \vartheta, 0) = 0. \end{aligned} \tag{28}$$

As can be seen from (28), the equation of meshing is an implicit function. From the theorem for functions given implicitly [17], when $\partial f / \partial \vartheta \neq 0$ there is a derivative,

$$\frac{d\vartheta}{du} = -\frac{\partial f / \partial u}{\partial f / \partial \vartheta}, \tag{29}$$

as well a function

$$\vartheta = \vartheta(u). \tag{30}$$

Then action surface can be written as:

$$\bar{\rho} = \bar{\rho}(u, w), \quad w \in (-\infty, +\infty), \tag{31}$$

or

$$\begin{aligned} &x = x[u, \vartheta(u)], \quad y = y[u, \vartheta(u)], \\ &z = w, \quad w \in (-\infty, +\infty). \end{aligned} \tag{32}$$

Using (32) for the normal vector of the action surface it can be written:

$$\bar{n}_{AS} = \frac{\partial \bar{\rho}}{\partial u} \times \frac{\partial \bar{\rho}}{\partial w}, \tag{33}$$

$$\begin{aligned} n_{AS,x} &= \begin{vmatrix} \frac{\partial y}{\partial u} & \frac{\partial y}{\partial w} \\ \frac{\partial z}{\partial u} & \frac{\partial z}{\partial w} \end{vmatrix} = \frac{\partial y}{\partial u} + \frac{\partial y}{\partial \vartheta} \frac{d\vartheta}{du}, \\ n_{AS,y} &= \begin{vmatrix} \frac{\partial z}{\partial u} & \frac{\partial z}{\partial w} \\ \frac{\partial x}{\partial u} & \frac{\partial x}{\partial w} \end{vmatrix} = -\left(\frac{\partial x}{\partial u} + \frac{\partial x}{\partial \vartheta} \frac{d\vartheta}{du} \right), \\ n_{AS,z} &= \begin{vmatrix} \frac{\partial x}{\partial u} & \frac{\partial x}{\partial w} \\ \frac{\partial y}{\partial u} & \frac{\partial y}{\partial w} \end{vmatrix} = 0. \end{aligned} \tag{34}$$

After substitution of (2.94) into (2.100):

$$\begin{aligned} n_{AS,x} &= \frac{\partial y}{\partial u} - \frac{\partial y}{\partial \vartheta} \frac{\partial f / \partial u}{\partial f / \partial \vartheta} = \\ &= \frac{1}{\partial f / \partial \vartheta} \left(\frac{\partial y}{\partial u} \frac{\partial f}{\partial \vartheta} - \frac{\partial y}{\partial \vartheta} \frac{\partial f}{\partial u} \right), \\ n_{AS,y} &= -\left(\frac{\partial x}{\partial u} + \frac{\partial x}{\partial \vartheta} \frac{\partial f / \partial u}{\partial f / \partial \vartheta} \right) = \\ &= -\frac{1}{\partial f / \partial \vartheta} \left(\frac{\partial x}{\partial u} \frac{\partial f}{\partial \vartheta} - \frac{\partial x}{\partial \vartheta} \frac{\partial f}{\partial u} \right), \\ n_{AS,z} &= 0. \end{aligned} \tag{35}$$

Then, substituting (29) and (35), in (25), it is established the following dependence:

$$n_{AS,y} j_{21} \sin \delta_r \neq 0, \tag{36}$$

i.e. when $\sin \delta_r \neq 0$ the conditions for the absence of undercutting points on the action surface of the spatial rack set are

$$\frac{\partial x}{\partial u} . \frac{\partial f}{\partial \vartheta} \neq \frac{\partial x}{\partial \vartheta} . \frac{\partial f}{\partial u}, \quad f(u, \vartheta, 0) = 0. \tag{37}$$

3. Total Transference Velocity

Contact-hydrodynamic theory of lubrication is a branch of Fluid Mechanics and explains the phenomena arising from fluid friction between moving solid surfaces [18]. This theory takes into account both the hydrodynamic and heating processes occurring in the lubricating fluid and the elastic deformations of firm surfaces. The mentioned phenomena are present in all types of gear mechanisms [1, 10, 19]. For this type of mechanical system, it is necessary to transfer forces from one friction surface to another by using an oil film located between them. The lubricating fluid adheres to the friction surfaces and during their relative motion, a hydrodynamic pressure arises in it, the equivalent of which - the hydrodynamic lift force, balances the external load applied to the gears. In turn, the hydrodynamic pressure acting on the conjugated tooth surfaces causes their elastic deformation at the points of contact. This affects the backlash between the meshed tooth surfaces and therefore the size and type of the hydrodynamic pressure distribution. The brief comment made here shows that the solution of the contact hydrodynamic problem is a problem of extreme complexity, which according to the information available to the author is still not enough studied. Clarification of one or another side of it is related to the prevention of such damages on the active tooth surfaces of the treated mechanical systems such as pitting, scuffing, accelerated wear, etc.

This study does not offer a solution to the hydrodynamic and contact task for spatial rack mechanisms. It is subject to the analytical definition of the magnitude of the total transference velocity and its normal component to the instantaneous contact line at an arbitrary contact point. This component of the total transference velocity is placed on the tangent plane between the conjugated tooth surfaces at an arbitrary contact point. The magnitude V_Σ total transference velocity $\bar{V}_\Sigma$ is determined in accordance with the given symbols in Fig. 3, i.e.:

$$\bar{V}_\Sigma = \bar{V}_1 + \bar{V}_2 = \bar{\omega}_1 \times \bar{\rho}_1 + \bar{V}_2, \tag{38}$$

It is written the (38) in the fixed coordinate system $S(O, x, y, z)$, and the following is obtained:

$$\bar{V}_\Sigma = -y\bar{i} + (x - j_{21} \sin \Sigma_r)\bar{j} - j_{21} \cos \Sigma_r . \bar{k}. \tag{39}$$

Then for the magnitude of $\bar{V}_\Sigma$ it can be written:

$$\begin{aligned} V_\Sigma &= \sqrt{V_{\Sigma,x}^2 + V_{\Sigma,y}^2 + V_{\Sigma,z}^2} = \\ &= \sqrt{x^2 + y^2 + j_{21}^2 - 2 j_{21} \sin \Sigma_r . x}. \end{aligned} \tag{40}$$

The normal component of $\bar{V}_{\Sigma,n_1}$ to the instantaneous contact line at an arbitrary contact point is determined by using the symbols shown in Fig. 3, through the scalar triple product:

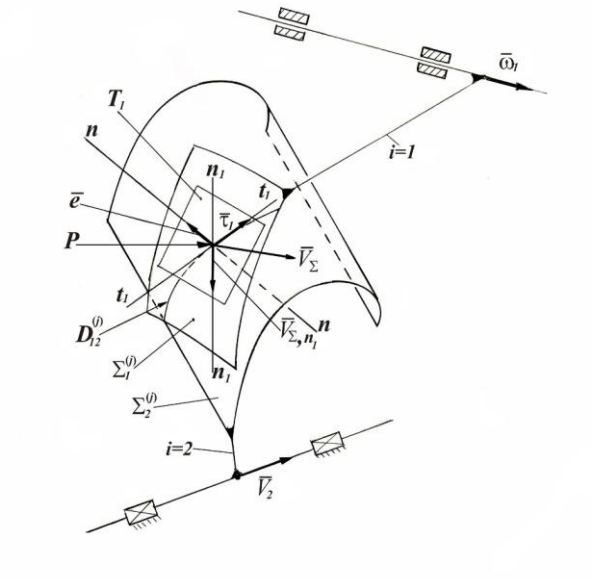

Fig. 3. *Geometric-kinematic scheme of the process of the motions transformation of type rotation into translation and vice versa:* $\Sigma_i^{(j)}$ *– geometric elements of kinematic joint (*$\Sigma_1^{(j)}:\Sigma_2^{(j)}$*);* $\bar{\omega}_1$ *- an angular velocity vector of the link* $i=1$*;* $\bar{V}_2$ *- translation velocity vector of the* $i=2$*;* $D_{12}^{(j)}$ *- instantaneous contact line;* P *- instantaneous contact point;* T_1 *- a tangent plane to the* $\Sigma_1^{(j)}$ *and* $\Sigma_2^{(j)}$ *in point* P*;* t_1-t_1 *and* n_1-n_1 *- tangent line and normal line to the* $D_{12}^{(j)}$ *at point* P

$$V_{\Sigma,n_1}=\left[\bar{\tau}_1 \quad \bar{e}_1 \quad \bar{V}_\Sigma\right], \tag{41}$$

where $\bar{\tau}_1$ - is the normed tangent vector to the contact line D_{12} in an arbitrary contact point P; $\bar{e}_1$ - unit vector to Σ_1 at point P.

From (41) is obvious that $\bar{V}_{\Sigma,n_1}$ depends on the geometry and kinematic of the studied transmissions. Increasing this kinematic characteristic leads to an improvement in the hydrodynamic loading capacity of the transmission.

4. Conclusion

This work deals with the research of some kinematic characteristics that can be used to ensure the loading capacity of the rack drives, including its hydrodynamic component. Here, an analysis of the spatial rack drives in terms of their loading capacity is done. A special accent is put on the study of the singularity of the tooth surfaces of the rack drive, and the condition for registration and elimination of the ordinary nodes and undercutting points from the mesh region of the synthesized rack drive are written. Analytical expression, defining the total transference velocity and its normal component to an instantaneous contact line at an arbitrary contact point therewith. The defined relations are important for the improvement of the hydrodynamic loading capacity of the transmission.

5. Acknowledgment

The author gratefully acknowledges the funding by project BG05M2OP001-1.002 “Center of Competence MIRACLe – Mechatronics, Innovation, Robotics, Automation and Clean Technologies”, financed by the Operational Programme “Science and Education for Smart Growth” and co-financed by the European Union through the European Structural and Investment funds.

6. References

1. F. Litvin, *Theory of Gearing*. Publishing house Nauka, Moscow, 584, (1968), (in Russian).
2. A. Georgiev. *Elements of Geometric Theory and Some Questions of Design and Manufacture of Hypoid - Worm Gears*. Sc. D. Thesis, IMI, Izhevsk, 258, (1965).
3. A. Georgiev, V. Goldfarb. On Node Lines of Mesh in Orthogonal Spiroid Gears with Convex-Concave Threads Profile of the Cylindrical Worm. Problems of Research, Design, and Manufacture of Gears. A summary of reports for the V zonal conference, 114-119, (1974).
4. V, Ganshin. *Analytical and Experimental Study of Spiroid Transmission with an Involute Worm*. Sc. D. Thesis, Ministry of Heavy Power and Transport Engineering, Moscow, 161, (1970).
5. I. Dusev, V. Vasiliev. Analytical Theory of Spatial Gearing and its Application to the Study of Hypoid Gears. Novocherkaskiy Polytechnic Institute, 147, (1968).
6. Litvin, F. *Theory of Gearing*. NASA Reference Publication 1212, AVSCOM Technical Report 88-C-035, US Government Printing Office, Washington, 1989, 470, (1989).
7. S. Lagutin. Once Again on the Problems of Singularities and Undercutting of Teeth. Proc. of the Int. Conf. “Theory and Practice of Gears”, Izhevsk, 193-199, (1998).
8. S. Lagutin. Spatial Gearing and ASynthesis of Worm Gears with a Localized Contact, Proc. of the Int. Conf. “Theory and Practice of Gears”, Izhevsk, 185-192, (1998).
9. K. Minkov, Mechanical and Mathematical Modeling of Hyperbolic Gears. Sc. D. Thesis, Sofia, 330, (1986), (in Bulgarian).
10. V. Abadjiev, V. Gearing Theory and Technical Applications of Hyperboloid Drives, Sc. D. Thesis, Institute of Mechanics, Bulgarian Academy of Sciences, Sofia, 309, (2007),(in Bulgarian)
11. W. Nelson, Spiroid Gearing Part 1 - Basic Design Practices. J. Machine Design, 136-144, (1961).
12. V. Abadjiev, D. Petrova, E. Abadjieva. Mathematical Modelling for Synthesis and Design of Non-Orthogonal Wormgears with a Straight-Line Tooth Contact, III European Conference on Computational Mechanics Solids, Structures and Coupled Problems in Engineering, Portugal, (2006), (Published on CD).
13. V. Abadjiev, E, Abadjieva. Two Approaches for Elimination of the Ordinary Nodes from the Planoid Meshing. Scientific Papers of the Jubilee Scientific Conference 2006 of the Rousse University, International Scientific Conference AMTECH 44(2), Rousse University, 674-678, (2005).
14. E. Abadjieva, V. Abadjiev V. On the Synthesis of Hypoid Gears with Linear Contact. Part 1 – Geometric Synthesis Practices in the Pitch Contact Point. 10th Jubilee National Congress on Theor. and Appl. Mech., 1, 1-6, (2005).
15. E. Abadjieva, V. Abadjiev V. On the Synthesis of Hypoid Gears with Linear Contact. Part 2 – Geometric Synthesis of the Planoid Gearing. 10th Jubilee National Congress on Theor. and Appl.Mech., 1, 7-11, (2005).
16. E. Abadjieva, *Mathematical Models of the Kinematic Processes in Spatial Rack Mechanisms and Their Application*, Ph. D Thesis, Institute of Mechanics, Sofia, 165, (2010), (in Bulgarian)
17. G. Korn, T. Korn, Mathematical Guide for Scientists and Engineers. Definitions, Theorems, Formulas. Nauka Publishing House, Moscow, 831, (1973).
18. I. Krivenko, S. Chervenkova. To the Calculation of the Total Length of the Contact Lines of the Worm Gears. Proc. of Higher Educational Institutions. Mashinostroenie. Scientific and Technical Journal, 10, 42-46, (1978).
19. V. Abadjiev, K. Minkov. On the Geometry of the Helical Surfaces of Spiroid Gears. Theor. and Appl. Mech., Publishing House at BAN, 2, 17-27,(1981).

Exergy analysis of a complex four-cylinder steam turbine

PhD. Mrzljak Vedran[1], Prof. PhD. Prpić-Oršić Jasna[1], PhD. Senčić Tomislav[1], PhD. Jelić Maro[2]
[1]Faculty of Engineering, University of Rijeka, Vukovarska 58, 51000 Rijeka, Croatia
[2]Maritime Department, University of Dubrovnik, Ćira Carića 4, 20000 Dubrovnik, Croatia
E-mail: vedran.mrzljak@riteh.hr, jasna.prpic-orsic@riteh.hr, tomislav.sencic@riteh.hr, maro.jelic@unidu.hr

Abstract: *This paper presents an exergy analysis of a complex four-cylinder steam turbine, which operate in a coal-fired power plant. Analyzed steam turbine consists of high pressure single flow cylinder (HPC), intermediate pressure dual flow cylinder (IPC) and two low pressure dual flow cylinders (LPC1 and LPC2). The highest part of cumulative mechanical power (787.87 MW) is developed in IPC (389.85 MW) and HPC (254.67 MW), while both low pressure cylinders develop a small part of cumulative mechanical power (70.29 MW in LPC1 and 73.06 MW in LPC2). Cylinder exergy destruction (cylinder exergy power loss) continuously increases as the steam expands through the turbine. The lowest exergy destruction has HPC (13.07 MW), followed by the IPC (20.95 MW), while the highest exergy destructions are noted in low pressure cylinders (24.37 MW in LPC1 and 27.17 MW in LPC2). Cylinder exergy efficiency continuously decreases as the steam expands through the turbine. The highest exergy efficiency has HPC (95.12%), followed by the IPC (94.90%) and LPC1 (74.25%), while the lowest exergy efficiency of all cylinders is obtained in LPC2 (72.89%). Exergy efficiencies of LPC1 and LPC2 are much lower in comparison to other low pressure dual flow cylinders from comparable steam power plants. The whole observed steam turbine has exergy efficiency equal to 90.20%.*

KEYWORDS: EXERGY ANALYSIS, COMPLEX STEAM TURBINE, TURBINE CYLINDERS, DESTRUCTION, EFFICIENCY

1. Introduction

Steam turbines can nowadays be found in a variety of power plants [1-3]. In the most of the cases, the dominant function of steam turbines is electrical generators driving [4, 5]. However, steam turbine can also be used for marine propulsion as a single component [6, 7] or as a part of the complex marine propulsion systems where is integrated with other propulsion elements [8, 9]. Also, steam turbine can be a constituent component of various power systems in many facilities or industries with a several different functions [10].

The most complex steam turbines can be found in conventional land-based steam power plants. Such plants can be composed of several blocks, where inside each block steam turbine is usually composed of many cylinders connected to the same shaft [11]. Each steam turbine can be considered as a complex one if it is composed of two or more cylinders [12]. More complexity into any analysis brings dual flow symmetrical or non-symmetrical cylinders in which steam expands through both cylinder parts [13].

In this paper is analyzed, from an exergy viewpoint, a complex four-cylinder steam turbine, which operates in a coal-fired power plant. Analyzed steam turbine consists of high pressure single flow cylinder, intermediate pressure dual flow symmetrical cylinder and two low pressure dual flow symmetrical cylinders connected to the same shaft. Analysis will be a baseline for further optimization because it will detect cylinders which improvement will bring the most benefits in the whole turbine operation.

2. Description of the four-cylinder steam turbine

Analyzed steam turbine, along with all of its connections to other systems and with operating points required for the exergy analysis, is presented in Fig. 1. Superheated steam from the steam generator [14] is firstly delivered to High Pressure Cylinder (HPC). HPC is a single flow cylinder and it has one steam extraction for steam delivery to high pressure feed water heating system. After expansion in HPC (operating point 3), one small part of the steam is delivered again to high pressure feed water heating system (operating point 4). The remaining steam mass flow rate is returned to reheater (mounted inside the steam generator) which is used for increasing of steam temperature before its expansion in Intermediate Pressure Cylinder (IPC). IPC is a symmetrical dual flow cylinder which means that steam after reheater (operating point 6) enters into the cylinder and expands through both of its parts (IPC-L and IPC-R). One half of the steam mass flow rate expands through IPC-L (left part of the IPC), while the other half of the steam mass flow rate expands through IPC-R (right part of the IPC). Both IPC parts have three steam extractions for steam delivering to high pressure feed water heating system, deaerator, to Main Feed water Pump Turbine [15] and to low pressure feed water heating system. In each extraction of both IPC parts is extracted the same steam mass flow rate at the same pressure and temperature, what confirms that this cylinder is symmetrical, Fig. 1. After steam expansion through both IPC parts (operating point 10), steam is delivered to both low pressure cylinders (LPC1 and LPC2). One small part of the steam mass flow rate send from IPC to both LPC's is taken and delivered to low pressure feed water heating system (operating point 15). Rectangles below or above each cylinder are mixing chambers to which is delivered two or more steam mass flow rates (or from which are taken steam mass flow rates in at least two directions). Remaining steam mass flow rate from IPC (operating point 16) is equally divided to both low pressure cylinders. As IPC, both low pressure cylinders (LPC1 and LPC2) are dual flow symmetrical cylinders, therefore each LPC cylinder consist of two symmetrical parts (left and right). All steam extractions of both LPC cylinders are used for steam delivery to low pressure feed water heating system. However, it should be highlighted that steam temperature and pressure in LPC1 extractions (operating point 19) is not the same as in LPC2 extractions (operating point 22). Therefore, LPC1 and LPC2 will develop different mechanical power and will have different efficiencies and losses, what will be confirmed in this analysis. Remaining steam mass flow rates, after expansion through both parts of each LPC are delivered to steam condenser [16].

All four cylinders of the observed steam turbine are connected to the same shaft, as presented in Fig. 1, which drives an Electrical Generator (EG). Due to the limited space, exergy analysis in this paper will be performed for the whole cylinders, not also for its parts. However, it should be highlighted that cumulative developed mechanical power and cumulative exergy destruction (cumulative exergy power loss) of IPC, LPC1 and LPC2 are equally divided on both parts of each cylinder (left and right). Exergy efficiency of IPC, LPC1 and LPC2 will be the same if it is calculated for each part of each cylinder, or for the whole cylinder.

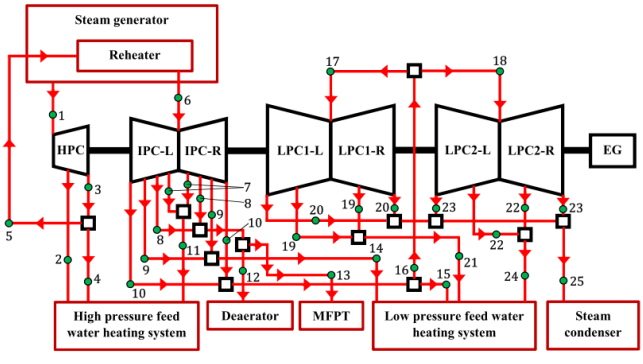

Fig. 1. *Analyzed complex four-cylinder steam turbine along with operating points required for the exergy analysis*

The analyzed steam turbine is a complex one with four cylinders where three of four cylinders are symmetrical dual flow cylinders. Along with necessary knowledge of steam pressure and temperature in each operating point from Fig. 1, special attention should be paid on the proper calculation of steam mass flow rates through all cylinders and in each extraction. Therefore, the mass flow rate balances related to all required operating points in this analysis are presented in Table 1 where $\dot{m}$ is the steam mass flow rate in (kg/s), while the operating point numeration is related to Fig. 1. Also, it should be mentioned that additional losses related to the whole turbine and each cylinder are in this analysis neglected [17-19].

Table 1. *Steam mass flow rate balances for the analyzed turbine*

Mass flow rate balance	Eq.
$\dot{m}_1 = \dot{m}_2 + \dot{m}_3.$	(1)
$\dot{m}_5 = \dot{m}_3 - \dot{m}_4.$	(2)
$\dot{m}_6 = 2 \cdot \dot{m}_7 + 2 \cdot \dot{m}_8 + 2 \cdot \dot{m}_9 + 2 \cdot \dot{m}_{10}.$	(3)
$\dot{m}_{11} = 2 \cdot \dot{m}_7.$	(4)
$\dot{m}_{12} + \dot{m}_{13} = 2 \cdot \dot{m}_8.$	(5)
$\dot{m}_{14} = 2 \cdot \dot{m}_9.$	(6)
$\dot{m}_{15} + \dot{m}_{16} = 2 \cdot \dot{m}_{10}.$	(7)
$\dot{m}_{17} + \dot{m}_{18} = \dot{m}_{16}.$	(8)
$\dot{m}_{17} = 2 \cdot \dot{m}_{19} + 2 \cdot \dot{m}_{20}.$	(9)
$\dot{m}_{21} = 2 \cdot \dot{m}_{19}.$	(10)
$\dot{m}_{18} = 2 \cdot \dot{m}_{22} + 2 \cdot \dot{m}_{23}.$	(11)
$\dot{m}_{24} = 2 \cdot \dot{m}_{22}.$	(12)
$\dot{m}_{25} = 2 \cdot \dot{m}_{20} + 2 \cdot \dot{m}_{23}.$	(13)

3. Exergy analysis equations

3.1. Overall exergy analysis balances and equations

The basis of exergy analysis is the second law of thermodynamics [20, 21]. Second law of thermodynamics takes into consideration the ambient state in which any component or the entire system operates. The base exergy balance equation, valid for any component or the entire system, according to [22] can be defined as:

$$\dot{Q}_{\mathrm{EX}} + P_{\mathrm{input}} + \sum \dot{E}x_{\mathrm{input}} = P_{\mathrm{output}} + \sum \dot{E}x_{\mathrm{output}} + \dot{E}x_{\mathrm{D}}. \quad (14)$$

In the base exergy balance equation above, P is mechanical power in (kW) and $\dot{E}x_{\mathrm{D}}$ is exergy destruction (exergy power loss) in (kW). $\dot{Q}_{\mathrm{EX}}$ is the exergy transfer by heat at the temperature T in (kW), defined according to literature [23] as:

$$\dot{Q}_{\mathrm{EX}} = \sum (1 - \frac{T_0}{T}) \cdot \dot{Q}. \quad (15)$$

In Eq. (15), T is temperature in (K), $\dot{Q}$ is the energy transfer by heat in (kW) and 0 is the index related to the ambient state. The last undefined element from the base exergy balance equation is $\dot{E}x$ - a total exergy power of fluid flow in (kW), which definition is [24]:

$$\dot{E}x = \dot{m} \cdot \varepsilon, \quad (16)$$

where ε is fluid specific exergy in (kJ/kg), calculated as [25]:

$$\varepsilon = (h - h_0) - T_0 \cdot (s - s_0). \quad (17)$$

In Eq. (17), h is fluid specific enthalpy in (kJ/kg) and s is fluid specific entropy in (kJ/kg·K). During standard operation of any component or the entire system, fluid mass flow rate leakage did not occur, therefore the valid mass flow rate balance is [26]:

$$\sum \dot{m}_{\mathrm{input}} = \sum \dot{m}_{\mathrm{output}}. \quad (18)$$

The general definition of any component or the entire system exergy efficiency is [27]:

$$\eta x = \frac{\text{cumulative exergy output}}{\text{cumulative exergy input}}, \quad (19)$$

however, it should be highlighted that proper exergy efficiency definition varies according to operating characteristics and type of the analyzed component or the entire system.

Presented balance and equations will be used in exergy analysis of the whole observed steam turbine and each cylinder.

3.2. Equations for the exergy analysis of the whole observed steam turbine and each cylinder

Equations for the exergy analysis of the whole observed steam turbine and each of its cylinders are defined by using operating point markings from Fig. 1 and mass flow rate balances from Table 1. All the equations are defined according to recommendations from the literature [28, 29]:

High Pressure Cylinder (HPC)

- Developed mechanical power:

$$P_{\mathrm{HPC}} = \dot{m}_1 \cdot (h_1 - h_2) + \dot{m}_3 \cdot (h_2 - h_3). \quad (20)$$

- Exergy destruction:

$$\dot{E}x_{\mathrm{D,HPC}} = \dot{E}x_1 - \dot{E}x_2 - \dot{E}x_3 - P_{\mathrm{HPC}}. \quad (21)$$

- Exergy efficiency:

$$\eta x_{\mathrm{HPC}} = \frac{P_{\mathrm{HPC}}}{\dot{E}x_{\mathrm{D,HPC}} + P_{\mathrm{HP\,C}}}. \quad (22)$$

Intermediate Pressure Cylinder (IPC)

- Developed mechanical power:

$$P_{\mathrm{IPC}} = 2 \cdot P_{\mathrm{IPC-L}} = 2 \cdot P_{\mathrm{IPC-R}}. \quad (23)$$

$$P_{\mathrm{IPC-L}} = P_{\mathrm{IPC-R}} = \frac{\dot{m}_6}{2} \cdot (h_6 - h_7) + \left(\frac{\dot{m}_6}{2} - \dot{m}_7\right) \cdot (h_7 - h_8) + \left(\frac{\dot{m}_6}{2} - \dot{m}_7 - \dot{m}_8\right) \cdot (h_8 - h_9) + \left(\frac{\dot{m}_6}{2} - \dot{m}_7 - \dot{m}_8 - \dot{m}_9\right) \cdot (h_9 - h_{10}). \quad (24)$$

- Exergy destruction:

$$\dot{E}x_{\mathrm{D,IPC}} = 2 \cdot \dot{E}x_{\mathrm{D,IPC-L}} = 2 \cdot \dot{E}x_{\mathrm{D,IPC-R}}. \quad (25)$$

$$\dot{E}x_{\mathrm{D,IPC-L}} = \dot{E}x_{\mathrm{D,IPC-R}} = \frac{\dot{E}x_6}{2} - \dot{E}x_7 - \dot{E}x_8 - \dot{E}x_9 - \dot{E}x_{10} - P_{\mathrm{IPC-L}}. \quad (26)$$

- Exergy efficiency:

$$\eta x_{\mathrm{IPC}} = \frac{P_{\mathrm{IPC}}}{\dot{E}x_{\mathrm{D,IPC}} + P_{\mathrm{IPC}}}. \quad (27)$$

Low Pressure Cylinder 1 (LPC1)

- Developed mechanical power:

$$P_{\mathrm{LPC\,1}} = 2 \cdot P_{\mathrm{LPC\,1-L}} = 2 \cdot P_{\mathrm{LPC\,1-R}}. \quad (28)$$

$$P_{\mathrm{LPC\,1-L}} = P_{\mathrm{LPC\,1-R}} = \frac{\dot{m}_{17}}{2} \cdot (h_{17} - h_{19}) + \left(\frac{\dot{m}_{17}}{2} - \dot{m}_{19}\right) \cdot (h_{19} - h_{20}). \quad (29)$$

- Exergy destruction:

$$\dot{E}x_{\mathrm{D,LPC\,1}} = 2 \cdot \dot{E}x_{\mathrm{D,LPC\,1-L}} = 2 \cdot \dot{E}x_{\mathrm{D,LPC\,1-R}}. \quad (30)$$

$$\dot{E}x_{\mathrm{D,LPC\,1-L}} = \dot{E}x_{\mathrm{D,LPC\,1-R}} = \frac{\dot{E}x_{17}}{2} - \dot{E}x_{19} - \dot{E}x_{20} - P_{\mathrm{LPC\,1-L}}. \quad (31)$$

- Exergy efficiency:

$$\eta x_{\mathrm{LPC\,1}} = \frac{P_{\mathrm{LPC\,1}}}{\dot{E}x_{\mathrm{D,LPC\,1}} + P_{\mathrm{LPC\,1}}}. \quad (32)$$

Low Pressure Cylinder 2 (LPC2)

- Developed mechanical power:

$$P_{\mathrm{LPC\,2}} = 2 \cdot P_{\mathrm{LPC\,2-L}} = 2 \cdot P_{\mathrm{LPC\,2-R}}. \quad (33)$$

$$P_{\mathrm{LPC\,2-L}} = P_{\mathrm{LPC\,2-R}} = \frac{\dot{m}_{18}}{2} \cdot (h_{18} - h_{22}) + \left(\frac{\dot{m}_{18}}{2} - \dot{m}_{22}\right) \cdot (h_{22} - h_{23}). \quad (34)$$

- Exergy destruction:

$$\dot{E}x_{\mathrm{D,LPC\,2}} = 2 \cdot \dot{E}x_{\mathrm{D,LPC\,2-L}} = 2 \cdot \dot{E}x_{\mathrm{D,LPC\,2-R}}. \quad (35)$$

$$\dot{E}x_{\mathrm{D,LPC\,2-L}} = \dot{E}x_{\mathrm{D,LPC\,2-R}} = \frac{\dot{E}x_{18}}{2} - \dot{E}x_{22} - \dot{E}x_{23} - P_{\mathrm{LPC\,2-L}}. \quad (36)$$

- Exergy efficiency:

$$\eta x_{\mathrm{LPC\,2}} = \frac{P_{\mathrm{LPC\,2}}}{\dot{E}x_{\mathrm{D,LPC\,2}} + P_{\mathrm{LPC\,2}}}. \quad (37)$$

Whole Turbine (WT)

- Developed mechanical power:

$$P_{\mathrm{WT}} = P_{\mathrm{HPC}} + P_{\mathrm{IPC}} + P_{\mathrm{LPC\,1}} + P_{\mathrm{LPC\,2}}. \quad (38)$$

- Exergy destruction:

$$\dot{E}x_{\mathrm{D,WT}} = \dot{E}x_{\mathrm{D,HPC}} + \dot{E}x_{\mathrm{D,IPC}} + \dot{E}x_{\mathrm{D,LPC\,1}} + \dot{E}x_{\mathrm{D,LPC\,2}}. \quad (39)$$

- Exergy efficiency:

$$\eta x_{\mathrm{WT}} = \frac{P_{\mathrm{WT}}}{\dot{E}x_{\mathrm{D,WT}} + P_{\mathrm{WT}}}. \quad (40)$$

4. Steam operating parameters for the exergy analysis

Steam operating parameters required for the exergy analysis of the observed steam turbine and each of its cylinders are steam temperature, steam pressure and the steam mass flow rate in each operating point from Fig. 1. These operating parameters are found in the literature [30]. Steam specific enthalpy, steam specific entropy and steam quality in each operating point of Fig. 1 are calculated from known steam temperature and steam pressure by using NIST REFPROP 9.0 software [31]. The base ambient state required for the calculation of steam specific exergy is defined through the ambient pressure of 1 bar and the ambient temperature of 25 °C.

5. Exergy analysis results and discussion

While observing all cylinders, it can be seen that in IPC is developed the highest mechanical power (389.85 MW), with a note that half of developed mechanical power in IPC is developed in left cylinder part (IPC-L), while the other half is developed in right cylinder part (IPC-R). The lowest mechanical power of all cylinders is developed in LPC1 (70.29 MW) – again, half of that mechanical power is developed in LPC1-L and the other half in LPC1-R, Fig. 2.

Further observation of developed mechanical power related to all cylinders shows that HPC develop a notable mechanical power (254.67 MW), regardless of the fact that HPC is the only single flow cylinder from the observed steam turbine. Also, from Fig. 2 can be clearly seen that both low pressure cylinders develop significantly lower mechanical power in comparison to HPC and IPC. LPC2 develop slightly higher mechanical power in comparison to LPC1 (73.06 MW in comparison to 70.29 MW). The whole observed steam turbine develop mechanical power equal to 787.87 MW, Fig. 2.

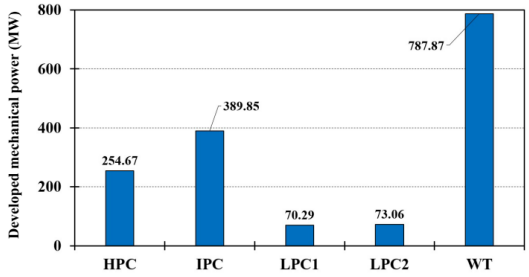

Fig. 2. *Developed mechanical power of the whole observed steam turbine and each cylinder*

Exergy destructions (exergy power losses) of each cylinder and the whole observed steam turbine are presented in Fig. 3.

Observation of all cylinders shows that cylinder exergy destruction continuously increases as the steam expands through the turbine. Therefore, the lowest exergy destruction is calculated in HPC (13.07 MW), followed by the IPC (20.95 MW), while the highest exergy destructions are calculated for low pressure cylinders (24.37 MW for LPC1 and 27.17 MW for LPC2). The whole observed steam turbine has exergy destruction equal to 85.56 MW, Fig. 3, which is obtained as a sum of exergy destructions in all cylinders, Eq. (39).

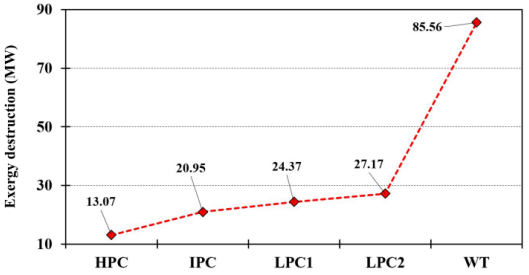

Fig. 3. *Exergy destruction of the whole observed steam turbine and each cylinder*

Exergy efficiencies of each turbine cylinder and the whole observed steam turbine are presented in Fig. 4.

Comparison of all turbine cylinders shows that cylinder exergy efficiency continuously decreases as the steam expands through the turbine. Therefore, the highest exergy efficiency has HPC (95.12%), followed by the IPC (94.90%) and LPC1 (74.25%), while the lowest exergy efficiency of all cylinders is calculated in LPC2 (72.89%).

The whole observed steam turbine has exergy efficiency equal to 90.20%. The exergy efficiency of the whole observed steam turbine is much closer to exergy efficiencies of HPC and IPC (which are dominant mechanical power producers) than to exergy efficiencies of LPC1 and LPC2 (which are not dominant mechanical power producers), Fig. 4.

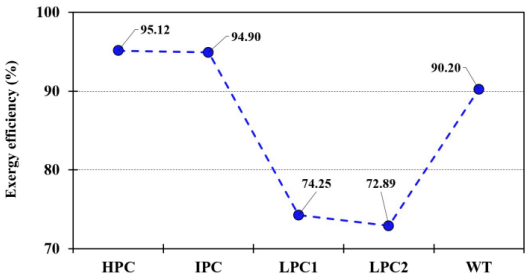

Fig. 4. *The exergy efficiency of the whole observed steam turbine and each cylinder*

From the observations above it can be concluded that LPC1 and LPC2 have higher exergy destructions and much lower exergy efficiencies in comparison to other cylinders from the observed turbine. Also, exergy efficiencies of LPC1 and LPC2 are much

lower in comparison to other low pressure dual flow cylinders from comparable steam power plants [32].

6. Conclusions

In this paper is performed an exergy analysis of a complex four-cylinder steam turbine, which operate in a coal-fired power plant. Exergy analysis takes into consideration exergy parameters of each cylinder and the whole observed steam turbine. The most important conclusions from the analysis are:

- When observing all turbine cylinders, the highest part of cumulative mechanical power is developed in IPC (389.85 MW), followed by HPC (254.67 MW), while both low pressure cylinders develop a small part of cumulative mechanical power (70.29 MW in LPC1 and 73.06 MW in LPC2). A cumulative mechanical power developed in the whole observed steam turbine is 787.87 MW.
- Cylinder exergy destruction (cylinder exergy power loss) continuously increases as the steam expands through the turbine. The lowest exergy destruction is calculated in HPC (13.07 MW), followed by the IPC (20.95 MW), while the highest exergy destructions are calculated for low pressure cylinders (24.37 MW for LPC1 and 27.17 MW for LPC2). The whole observed steam turbine has exergy destruction equal to 85.56 MW.
- Cylinder exergy efficiency continuously decreases as the steam expands through the turbine. The highest exergy efficiency has HPC (95.12%), followed by the IPC (94.90%) and LPC1 (74.25%), while the lowest exergy efficiency of all cylinders is obtained in LPC2 (72.89%). The whole observed steam turbine has exergy efficiency equal to 90.20%.
- Low pressure cylinders from the observed steam turbine (LPC1 and LPC2) have higher exergy destructions and much lower exergy efficiencies in comparison to the other cylinders. Therefore, future research and possible improvement of the analyzed steam turbine should be based firstly on both low pressure cylinders.

7. Acknowledgment

This research has been supported by the Croatian Science Foundation under the project IP-2018-01-3739, CEEPUS network CIII-HR-0108, European Regional Development Fund under the grant KK.01.1.1.01.0009 (DATACROSS), project CEKOM under the grant KK.01.2.2.03.0004, CEI project "COVIDAi" (305.6019-20), University of Rijeka scientific grants: uniri-tehnic-18-275-1447, uniri-tehnic-18-18-1146 and uniri-tehnic-18-14.

8. References

[1] Zhao, Z., Su, S., Si, N., Hu, S., Wang, Y., Xu, J., ... & Xiang, J. (2017). Exergy analysis of the turbine system in a 1000 MW double reheat ultra-supercritical power plant. Energy, 119, 540-548. (doi:10.1016/j.energy.2016.12.072)

[2] Burin, E. K., Vogel, T., Multhaupt, S., Thelen, A., Oeljeklaus, G., Gorner, K., & Bazzo, E. (2016). Thermodynamic and economic evaluation of a solar aided sugarcane bagasse cogeneration power plant. Energy, 117, 416-428. (doi:10.1016/j.energy.2016.06.071)

[3] Lorencin, I., Anđelić, N., Mrzljak, V., & Car, Z. (2019). Genetic Algorithm Approach to Design of Multi-Layer Perceptron for Combined Cycle Power Plant Electrical Power Output Estimation. Energies, 12(22), 4352. (doi:10.3390/en12224352)

[4] Kumar, V., Pandya, B., & Matawala, V. (2019). Thermodynamic studies and parametric effects on exergetic performance of a steam power plant. International Journal of Ambient Energy, 40(1), 1-11. (doi:10.1080/01430750.2017.1354326)

[5] Mrzljak, V., Senčić, T., & Žarković, B. (2018). Turbogenerator steam turbine variation in developed power: Analysis of exergy efficiency and exergy destruction change. Modelling and Simulation in Engineering, 2018. (doi:10.1155/2018/2945325)

[6] Koroglu, T., & Sogut, O. S. (2018). Conventional and advanced exergy analyses of a marine steam power plant. Energy, 163, 392-403. (doi:10.1016/j.energy.2018.08.119)

[7] Mrzljak, V., & Poljak, I. (2019). Energy Analysis of Main Propulsion Steam Turbine from Conventional LNG Carrier at Three Different Loads. NAŠE MORE: znanstveno-stručni časopis za more i pomorstvo, 66(1), 10-18. (doi:10.17818/NM/2019/1.2)

[8] Behrendt, C., & Stoyanov, R. (2018). Operational Characteristic of Selected Marine Turbounits Powered by Steam from Auxiliary Oil-Fired Boilers. New Trends in Production Engineering, 1(1), 495-501. (doi:10.2478/ntpe-2018-0061)

[9] Fernández, I. A., Gómez, M. R., Gómez, J. R., & Insua, Á. B. (2017). Review of propulsion systems on LNG carriers. Renewable and Sustainable Energy Reviews, 67, 1395-1411. (doi:10.1016/j.rser.2016.09.095)

[10] Hafdhi, F., Khir, T., Yahyia, A. B., & Brahim, A. B. (2015). Energetic and exergetic analysis of a steam turbine power plant in an existing phosphoric acid factory. Energy Conversion and Man., 106, 1230-1241. (doi:10.1016/j.enconman.2015.10.044)

[11] Tanuma, T. (Ed.). (2017). Advances in Steam Turbines for Modern Power Plants. Woodhead Publishing.

[12] Mrzljak, V., Poljak, I., & Prpić-Oršić, J. (2019). Exergy analysis of the main propulsion steam turbine from marine propulsion plant. Brodogradnja: Teorija i praksa brodogradnje i pomorske tehnike, 70(1), 59-77. (doi:10.21278/brod70105)

[13] Adibhatla, S., & Kaushik, S. C. (2014). Energy and exergy analysis of a super critical thermal power plant at various load conditions under constant and pure sliding pressure operation. Applied thermal engineering, 73(1), 51-65. (doi:10.1016/j.applthermaleng.2014.07.030)

[14] Mrzljak, V., Poljak, I., & Medica-Viola, V. (2017). Dual fuel consumption and efficiency of marine steam generators for the propulsion of LNG carrier. Applied Thermal Engineering, 119, 331-346. (doi:10.1016/j.applthermaleng.2017.03.078)

[15] Mrzljak, V., Prpić-Oršić, J., & Poljak, I. (2018). Energy Power Losses and Efficiency of Low Power Steam Turbine for the Main Feed Water Pump Drive in the Marine Steam Propulsion System. Pomorski zbornik, 54(1), 37-51. (doi:10.18048/2018.54.03)

[16] Škopac, L., Medica-Viola, V., & Mrzljak, V. (2020). Selection Maps of Explicit Colebrook Approximations according to Calculation Time and Precision. Heat Transfer Engineering, 1-15. (doi:10.1080/01457632.2020.1744248)

[17] Mrzljak, V., Kudláček, J., Begić-Hajdarević, Đ., & Musulin, J. (2020). The Leakage of Steam Mass Flow Rate through the Gland Seals–Influence on Turbine Produced Power. Pomorski zbornik, 58(1), 39-56. (doi:10.18048/2020.58.03.)

[18] Cangioli, F., Chatterton, S., Pennacchi, P., Nettis, L., & Ciuchicchi, L. (2018). Thermo-elasto bulk-flow model for labyrinth seals in steam turbines. Tribology international, 119, 359-371. (doi:10.1016/j.triboint.2017.11.016)

[19] Medica-Viola, V., Mrzljak, V., Anđelić, N., & Jelić, M. (2020). Analysis of Low-Power Steam Turbine With One Extraction for Marine Applications. NAŠE MORE: znanstveni časopis za more i pomorstvo, 67(2), 87-95. (doi:10.17818/NM/2020/2.1)

[20] Szargut, J. (2005). Exergy method: technical and ecological applications (Vol. 18). WIT press.

[21] Kanoğlu, M., Çengel, Y. A. & Dincer, I. (2012). Efficiency Evaluation of Energy Systems. Springer Briefs in Energy. (doi:10.1007/978-1-4614-2242-6)

[22] Mrzljak, V., Poljak, I., Prpić-Oršić, J., & Jelić, M. (2020). Exergy analysis of marine waste heat recovery CO2 closed-cycle gas turbine system. Pomorstvo, 34(2), 309-322. (doi:10.31217/p.34.2.12)

[23] Aljundi, I. H. (2009). Energy and exergy analysis of a steam power plant in Jordan. Applied thermal engineering, 29(2-3), 324-328. (doi:10.1016/j.applthermaleng.2008.02.029)

[24] Mrzljak, V., Anđelić, N., Lorencin, I., & Sandi Baressi Šegota, S. (2021). The influence of various optimization algorithms on nuclear power plant steam turbine exergy efficiency and destruction. Pomorstvo, 35(1), 69-86. (doi:10.31217/p.35.1.8)

[25] Tan, H., Shan, S., Nie, Y., & Zhao, Q. (2018). A new boil-off gas re-liquefaction system for LNG carriers based on dual mixed refrigerant cycle. Cryogenics, 92, 84-92. (doi:10.1016/j.cryogenics.2018.04.009)

[26] Medica-Viola, V., Baressi Šegota, S., Mrzljak, V., & Štifanić, D. (2020). Comparison of conventional and heat balance based energy analyses of steam turbine. Pomorstvo, 34(1), 74-85. (doi:10.31217/p.34.1.9)
[27] Baldi, F., Ahlgren, F., Nguyen, T. V., Thern, M., & Andersson, K. (2018). Energy and exergy analysis of a cruise ship. Energies, 11(10), 2508. (doi:10.3390/en11102508)
[28] Erdem, H. H., Akkaya, A. V., Cetin, B., Dagdas, A., Sevilgen, S. H., Sahin, B., ... & Atas, S. (2009). Comparative energetic and exergetic performance analyses for coal-fired thermal power plants in Turkey. International Journal of Thermal Sciences, 48(11), 2179-2186. (doi:10.1016/j.ijthermalsci.2009.03.007)
[29] Mrzljak, V., Poljak, I., & Mrakovčić, T. (2017). Energy and exergy analysis of the turbo-generators and steam turbine for the main feed water pump drive on LNG carrier. Energy conversion and management, 140, 307-323. (doi:10.1016/j.enconman.2017.03.007)
[30] Suresh, M.V.J.J., Reddy, K.S., & Kumar Kolar, A. (2011). ANN-GA based optimization of a high ash coal-fired supercritical power plant. Applied Energy, 88, 4867–4873. (doi:10.1016/j.apenergy.2011.06.029)
[31] Lemmon, E. W., Huber, M. L., & McLinden, M. O. (2010). NIST Standard Reference Database 23, Reference Fluid Thermodynamic and Transport Properties (REFPROP), version 9.0.
[32] Ahmadi, G. R., & Toghraie, D. (2016). Energy and exergy analysis of Montazeri steam power plant in Iran. Renewable and Sustainable Energy Reviews, 56, 454-463. (doi:10.1016/j.rser.2015.11.074)

Research of combustion engine oil quality over exploitation period

Mažeika Darius[1], Balnys Rytis[1], Kandrotaitė Janutienė Rasa[1]
Faculty of Mechanical Engineering and Design – Kaunas University of Technology, Lithuania[1]
E-mail: darius.mazeika@ktu.lt, raskand@ktu.lt

Abstract. *Different types of oil are used widely in all over the world. It is used for lowering friction force at the contact zones, e. g., bearings, gears and other areas where at least one element is moving in relation to another one. Several types of oils find place in automotive industry: mineral, semi-synthetic and synthetic. Over the time oil characteristics were improved by enriching with different additives. Special additives can reduce friction forces, present better wash of abrasion products, extend oil life, etc.*

This article deals with the research of degradation of oil lubrication quality in vehicle combustion engine over the exploitation period. Quantity of contaminating particles in oil sample was determined by optical microscopy. Oil film strength test was performed with oil samples used after various exploitation periods.

Keywords: OIL QUALITY, INTERNAL COMBUSTION ENGINE, EXPLOITATION PERIOD, OIL FILTER, CONTAMINATION PARTICLES.

1. Introduction

Automotive industry contains companies and activities involved in the manufacture of motor vehicles, including components such as engines and bodies. This industry produces transport means, that are very popular and used in all over the world. Every mechanical assembly of transport mean in order to operate smoothly, it is necessary to use lubricating liquids for lowering friction forces and increasing its lifetime. The lifetime of lubricating liquids can be increased by using additional elements: zinc dialkyl dithiophosphates, titanium, graphite, molybdenum disulfide, tungsten disulfide, polytetrafluoroethylene or chlorine [1]. Recently, lubricating liquids are of very high quality, that allows to use it for longer exploitation time. However, during exploitation time engines or gearboxes of cars, vans or trucks, fail. Inside of these mechanisms most of car services have founded motor oil of high viscosity and polluted with abrasive particles. Over the exploiting time these particles can mix with motor oil and pollute oil filter. Polluted oil filter decreases oil flow for journal bearings and increase combustion engine wear.

The problem is a common internal combustion engine damage due to insufficient, inefficient engine lubrication. Modern car manufacturers recommend oil change via intervals from 8000 km up to 60000 km. Change interval depends on the car's lubrication system design and on the filtration system. For example, Ford manufacturers recommend their car oil change every 20000 km up to 50000 km depending on the vehicle model and type of internal combustion engine. Oil and oil filters also must meet the requirements for longer distances and engine working hours. However, different car manufacturer has different specifications, for example, Nissan recommends oil change from 8000 km up to 30000 km intervals [2].

While car operates over time, the oil physical and chemical properties change, the oil loses its active ingredients, which gives additives. Aging oil usually increases its viscosity and a variety of contaminants and oil oxidation occurs due to temperature changes. Oil durability also depends on the engine design, oil tanks – sump size and the amount of oil poured into the engine lubrication system, the oil pump performance, air, oil and fuel filtration system design. So, without changing the oil on time, pollution significantly increases and the effectiveness of the active substances diminishes. If the oil is not changed in time, further consequences may occur – the rapid growth of contamination of engine parts, as well as increased mechanical and corrosive abrasion, oil filter clogging, lubricating channel blockage and other destructive processes [3].

Oil can be tested in a variety of methods, starting with contamination determination and finishing with chemical composition of used oil. Carrying out such research and in order to identify problems, it is necessary to gather information and adhere to certain set goals. In order to study the oil for some reason and to get more accurate data and results, it is necessary to determine which mode the car will be running, what oil type and filters will be used, how many kilometers or operating hours will be performed [4]. As billions of money are spent every year on replacing or repairing faulty units due to poor or insufficient lubrication, it is appropriate to carry out studies that may help to reduce the problem. Table 1 shows the most common oil tests performed [4].

Table 1. *Usually performed oil quality tests* [4]

Category	Research object	Methods of analysis
Wear	Quantity size and distribution of contamination particles	Microscopy
	Particles shape	Ferrography
	Metal particles	Spectroscopy of a rotating disk electrode (RDE)
Pollution	Sand and mud	Microscopy
	Unburnt fuel	Fuel Sniffer Spectro, Gas chromatography (GC)
	Water	Infrared (IR)*, Karl Fischer Titration (KF)
	Water coolant, antifreeze	Infrared (IR)
	Soot	Infrared, soot meter
	Other liquids	
Fatigue	Oxidation, nitration, sulphitization	Infrared (IR)
	Viscosity	Viscosity testers
	Acid numbers or base numbers	Titration

3. Research methodology

An optical microscope Nikon was used for studies to see solid particles inside the used oil. An objective Nikon TU Plan Fluor 20x / 0.45 A was chosen, and Nikon DS-Ri2 with a 16x megapixel camera was used to obtain images. NIS-Elements D software was used to process the images.

The Timken test is a test that meets international standards and is a test method that meets American standards (ASTM No. D 2782) [5]. A special experimental stand is used for this test (Fig. 1).

The Timken machine has an electric motor (4) that rotates the shaft (5) at 800 rpm. At the beginning of the test, the sample (2) is placed in the lever, then the oil bath (3) is filled with the oil to be analyzed and the apparatus is started. After the apparatus has been tampered with, the selected weight (2.5 kg) is placed on the lever (1) for a few seconds and the sample is further abraded for the selected time. The tests usually give a constant load and a constant wear time. After the tests, the samples are removed from the lever and further examined by other methods.

After all samples have been tested by Timken test, they are carefully analyzed visually. Filter samples were taken in three stages. The first stage, when the car travels about 25,000 kilometers, the second stage, when the maximum permissible mileage is achieved, e.g. 50,000 kilometers, and the third stage, when the car travels the maximum permissible mileage, but the filter is used only

half the range, e.g. after about 25,000 kilometers only the oil filter was replaced.

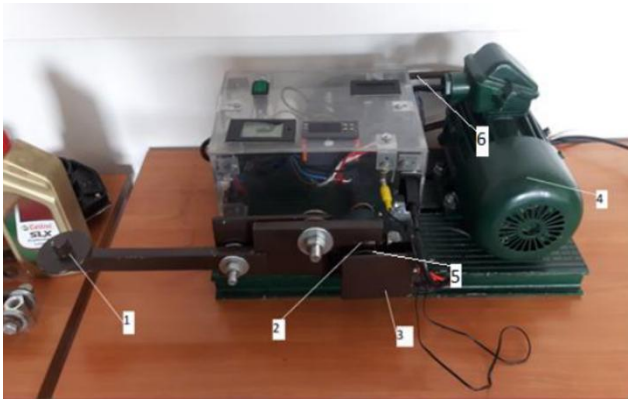

Fig. 1. *The Timken test experimental setup: 1 – lever with the load, 2 – sample, 3 – oil bath, 4 – electric motor, 5 – shaft*

4. Research progress

Oil samples from five different cars were collected for the study. When the car arrived for service maintenance, 40 ml of used oil was taken as a sample, which was safely placed in a sealed tube (Fig. 2). Some literature sources [6, 7] mention that the oil filter often becomes dirty faster than the oil change time comes and the oil does not longer flow through the safety valve, causing contamination increase rapidly and can cause significant damage of the engine or its components. Therefore, it was decided to collect the oil samples at a halfway of the oil change interval (~ 25000 km), without changing the oil itself, to change only the oil filter, take a sample of used oil and the used filter, and repeat this procedure after 50000 km.

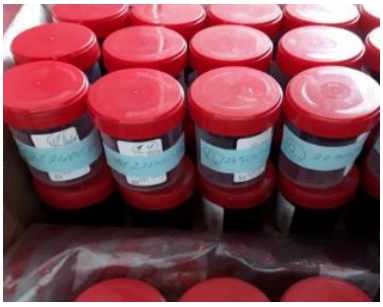

Fig. 2. *Tubes with samples of used oil*

For testing and operation of the cars, original Ford oil was used, which meets the requirements set by the car engine manufacturer. The oil specification is given in Table 2.

Table 2. *Specifications of engine oil used*

Oil name	Oil type	Oil specification
Ford FORMULA F	SAE 5W-30	ACEA A5/B5 WSS-M2C913-C WSS-M2C913-B WSS-M2C913-A

This oil is suitable for most Ford cars. It is a high quality fully synthetic oil. It reduces friction of engine parts and fuel consumption, features excellent motor protection and wash quality. It ensures optimal engine start at low temperatures and reduces CO_2 emissions [8].

Timken samples (Steel grade 1010, Ø12 mm) were prepared according standard requirements [5] and used during the investigation. After placing the Timken sample on the test bench (Fig. 1), the oil bath was filled with oil. The apparatus started before any load had been applied, the load was applied to the load lever when the stand was launched and the Timken sample was further abraded for the selected time. Figure 3 shows a Timken sample when tested for 7 minutes in a new, unused oil.

Fig. 3. *Timken sample after 7 minutes of abrasion*

For further tests, the abrasion time and load of the first Timken sample were set up. Accurate collecting of the results requires the same load and abrasion time that should be maintained for all Timken samples and different oil samples.

At the beginning of the tests, the Timken sample was first tested in a clean, unused oil, the wear was measured, for the purpose to have comparable results with the ones obtained for the used oil samples.

After every test, a different oil sample was changed, the oil bath was washed with a special oil and grease-washing liquid to remove unwanted impurities, as abrasion of the sample could accumulate its abrasive particles in the oil, which later could deteriorate the lubricating properties of the oil.

Fig. 4 shows scar diameter of Timken sample obtained after the test of abrasion in used oil for three different situations – I, II and III. Here is the description of the mentioned situations:

I – car mileage was about 50000 km, oil filter exploitation duration was the same;

II – car mileage was about 50000 km, oil filter was changed after each 25000 km (twice);

III – car mileage was about 25000 km, oil filter exploitation duration was the same.

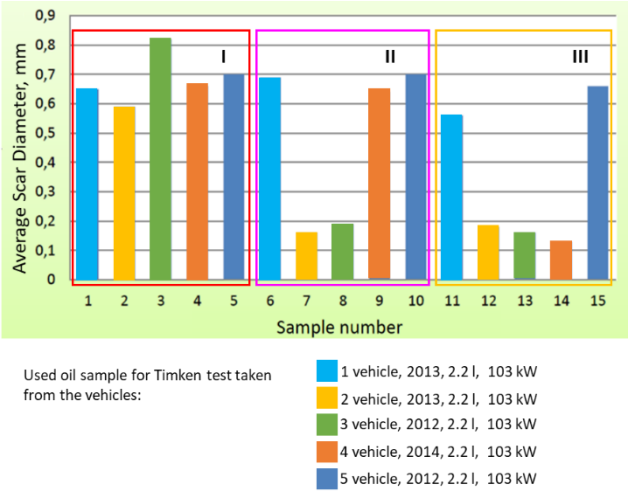

Fig. 4. *Measurement of average scar diameter of Timken sample after abrasion test in oil*

Determination of hard particles in oil

After all the oil samples have been collected, they were further examined under a microscope to determine how the oil contamination has changed with the number of kilometers traveled. When examining oil samples under a microscope, the focus was on hard particles and their content in the oil. After microscopic analysis of all samples, the results were compared to check for a change in oil contamination after changing the oil filter in the middle of the oil change interval.

The nature of the objects found under the microscope was assessed on the basis of similar studies already carried out, which described in detail the characteristics of every object. The scientists describe how the shape, color, surface structure and dimensions of an object can be used to partially determine what kind of material is in, as well as to decide, based on the surface profile, what kind of wear can prevail [9, 10]. Figure 5 shows the oil containing undesirable particles. Figure 6 shows the surface of an abrasion particle, showing abrasion marks, i.e., longitudinal scratches, from which it can be inferred that this particle may be a rupture of the cylinder walls or from where the slip tinnitus predominates [9, 10].

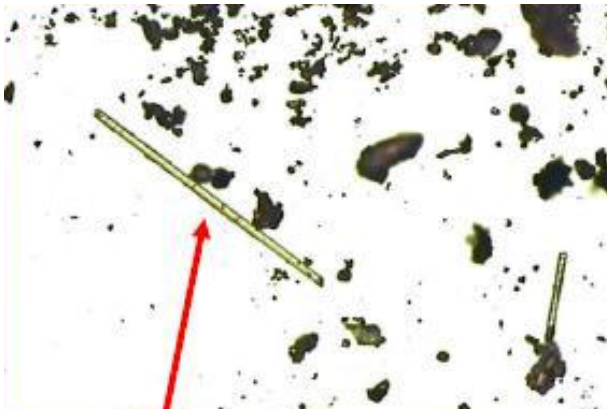

Fig. 5. *Microscopic photo of used engine oil (200x)* [9]

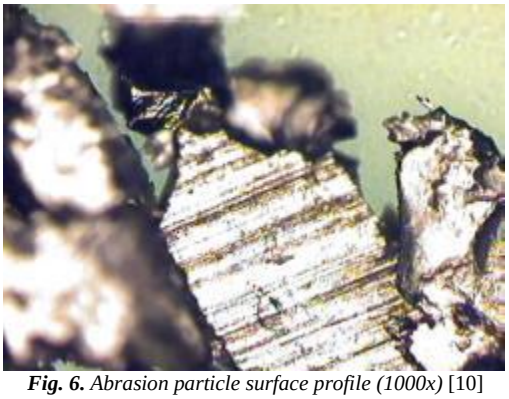

Fig. 6. *Abrasion particle surface profile (1000x)* [10]

The Fig. 7 and 8 show optical microscopic images oil samples taken from the first car. Particles larger than 10µm were measured and marked on the images, while other, smaller visible particles were marked with arrows during microscopic image analysis and examination of the detected particles.

Examination of the microscopic images and the particles seen in them revealed that, in terms of dimensions, the largest particles were observed in the oil samples which were taken from cars that had worked approximately 50,000 km. The dimensions of the largest particles detected in the first sample (Fig. 7) were 49 µm and 45 µm. According to the dimensions and shape of these hard particles, based on the literature sources [10, 11], it can be stated that it could be a metal chips, which may be caused friction of parts. The particles of such size do not pass through the filter material, e.g. they are trapped by the oil filter, therefore, it can be argued that the oil filter did not filter the oil at fully, i.e., part of the oil flowed through the filter and other one flowed through the safety valve and the filter had already started to clog. Further examination of the first five samples showed that in terms of the amount of particles in the oil, most of them are visible in the third sample. Theoretically, it is normal for this oil to have the highest levels of contaminants, as this oil has been in operation for 51500 km.

Examination of oil samples 6-10 of car exploited approximately 50,000 km, but replaced the oil filter at the 25000 km, showed a difference compared to the first five samples. Slightly fewer hard particles were observed in these oil samples, and the largest particle detected was only 20µm, which was several times larger than the particles detected in the first samples.

In samples with a mileage of up to 25000 km (11-15), the observed particles are only up to 10µm, compared to the first ten oil samples, these hard particles are less visible. The most noticeable feature is a soot, as well as small particles whose shape and dimensions are difficult to detect by optical microscopy.

Fig. 9 presents the number of found particles larger than 5 µm per 0,36 mm^2 test oil smear area.

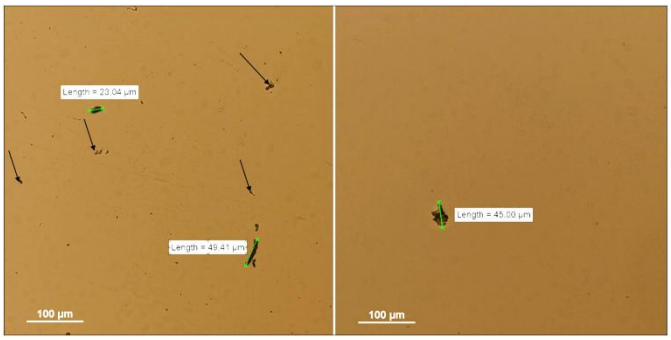

Fig. 7. *Sample No. 1 after mileage of 49000 km*

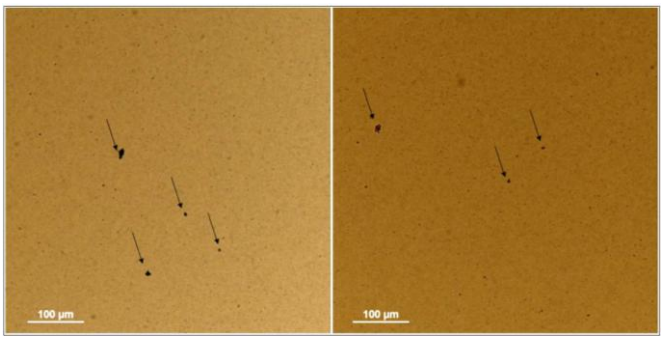

Fig. 8. *Sample No. 11 after mileage of 20000 km*

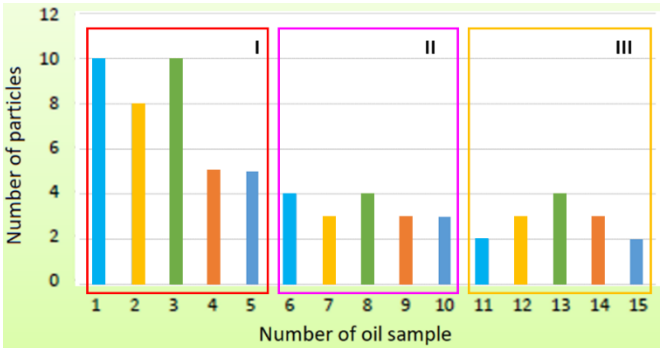

Fig. 9. *Number of particles per 0.36 mm^2 area. Designation with colors is the same like in Fig. 4*

5. Discussion

As technology advances but oil resources dwindle, oil and car manufacturers are increasingly striving to increase oil quality while increasing the oil change interval. It is no secret that a significant proportion of modern cars have a range of 50000 km or more. However, faults caused by insufficient lubrication are not uncommon. The question arises as to whether the oil with which the car has traveled 40000 to 50000 km can be fit for use and do not damage the engine components. We know that when operating a car in different operating modes, the oil is affected unequally, if the car is used at high loads more often, then the oil is subjected to a higher load, so it loses its lubrication properties faster. Perhaps when operating the vehicle in more severe conditions, the interval should

be shortened or measures taken to reduce oil contamination, such as changing the filters between the change intervals.

After analyzing all the oil samples in terms of mileage, the biggest contamination and biggest hard particles were found in the first five samples, where the oil life was 50000 kilometers and more. In this case, the oil was heavily contaminated, the oil filter inefficiently filtered the oil, engine components with more contaminated oil wear faster, and as a result, the contamination increased much faster than with clean oil.

After analysis, it was determined that the cleanest oil was the one that had been operating for about 25000 km, in this oil, no hard particles were observed that could pose a significant threat to the internal combustion engine assemblies. There could be stated that the oil filter and the whole filtration system filtered the oil sufficiently, the filter was not clogged and worked effectively.

After performing the experiment and changing the oil filter, in the middle of the oil change interval, after microscopic analysis, it could be seen that the particle content and dimensions were much lower than in the oil samples that served the full range. Changing the oil filter after half-termed exploitation was effective and expedient.

6. Conclusions

1. In the course of the investigation, oil samples were collected from five different cars with identical engines, and the engine oil used and the oil filters were the same in all cars. For more accurate data, cars with similar operating conditions were selected. The nature of oil contamination was determined by microscopic analysis of oil samples based on literature sources. The shape and visual appearance of the objects visible in the oil determine the nature of the particle, e.g. whether it is a metal particle, dross, dust, or something like that.

2. The oil samples contaminated mostly were determined during microscopic analysis: 1 (49000 km.), 2 (47500 km.), 3 (51500 km.), 4 (48650 km.). The biggest hard particles were observed analyzing these samples. A comparison of all the oil samples collected showed that the least contaminated samples were those with a mileage of up to 25000 km and the most contaminated were those with a mileage of about 50000 km.

3. During the oil sampling, an experiment was performed – as the aforementioned car oil change interval was 50000 km. After performing this experiment and comparing the results with the results of all the oil samples, it was observed that the oil contamination is significantly reduced when just the oil filter was changed between the oil change intervals.

4. A visual analysis of the used oil filters was performed, during which was determined that the most contaminated filter is No. 3 (51500 km.). It showed many metal wear particles and other foreign objects.

6. The Timken test revealed that the quality of the sample No. 3 (51500 km.) oil was the worst, as with this oil the Timken sample wear out the most - 0.82 mm. Abrasions were also found to be lower when tested with oil in which only the oil filter was changed. Thus, the study showed that the quality of the oil, its lubrication properties could be improved and the contamination could be reduced when only the oil filter has been changed between oil change intervals.

7. References

1. Experimental Aircraft Info. Available in: https://www.experimentalaircraft.info/articles/engine-lubrication-6.php

2. 2016 Service and Maintenance Guide. Available in: https://owners.nissanusa.com/content/techpub/common/2016/2016-nissan-service-maintenance-guide.pdf

3. Jučas P. Exploitation Materials. Kaunas, 2007, 61-67 p.

4. Oil Analysis Handbook. Predictive Equipment Maintenance. Third Edition. Available in: https://info.spectrosci.com/oil-analysis-handbook-download

5. ASTM D2782-20 Standard Test Method for Measurement of Extreme-Pressure Properties of Lubricating Fluids (Timken Method).

6. OPTIMIZING OIL CHANGE INTERVALS. Available in: https://www.macallister.com/parts-service/service-solutions/machine-fluid-analysis/optimizing-oil-change-intervals/

7. Ewa Rostek, Maciej Babiak. The experimental analysis of engine oil degradation utilizing selected thermoanalytical methods. 13th International Scientific Conference on Sustainable, Modern and Safe Transport (TRANSCOM 2019), High Tatras, Novy Smokovec – Grand Hotel Bellevue, Slovak Republic, May 29-31, 2019. Transportation Research Procedia 40 (2019) 82–89.

8. Original Ford Motor Oil. Available in: https://www.ford.co.uk/owner/service-and-maintenance/service-promotions/castrol-products

9. Used Engine Oil Analysis. User Interpretation Guide 16-17p., elaborated by the CIMAC Working Group 'Marine Lubricants' in May.

10. Used Lube Oil Analysis and Analytical Ferrography. Available in: https://www.academia.edu/40653688/Used_Lube_Oil_Analysis_and_Analytical_Ferrography

11. R.K.Upadhyay. Microscopic technique to determine various wear modes of used engine oil. Journal of Microscopy and Ultrastructure Volume 1, Issue 3, December 2013, 11-114.

Влияние на плътността при 3д принтирани материали върху коефициента на реституция.

Influence of density in 3d printed materials on the restitution coefficient.

Stanislav Gyoshev*, Blagoy Sokolov

stanislav.gyoshev@iict.bas.bg

Институт по информационни и комуникационни технологии-Българска академия на науките, София 1113, ул. акад. Георги Бончев, бл.2.

Abstract: *The coefficient of restitution in the case of impact of two different materials (plate and sphere) is necessary in order to be able to determine the extent to which the impact is elastic or plastic. For 3D printing materials, which have recently become very popular, this ratio is not known, so it needs to be determined. The gravitational method with the determination of the rebound height is used for the experiments. The material used for the research is TPU, with different filling coefficient during its printing: 20%, 50%, 70% and 100%, respectively different density of the material, the aim is to check and determine the dependence of the restitution coefficient on the different density of the material. The sphere for carrying out the experiments is made of steel.*

Key words: *coefficient of restitution, impact, elastic impact, plastic impact, 3D printed materials, 3D printing*

1. *Въведение.*

Този коефициент определя съотношението между параметрите на удрящите се тела преди и след удара. Ако с означим скоростите на тела с маса преди удара, а с скоростите им след удар (фиг.1), от условието за запазване количеството на движение се получава $e = \frac{u_2 - u_1}{v_1 - v_2}$

(1)

За случая на удар на тяло в неподвижна преграда (1) има вида

$$e = \frac{u}{v}, \qquad (2)$$

където е скоростта преди удар, а скоростта след удар на движещото се тяло.

При падане на тяло от височина върху неподвижна плоча, то отскача на височина и

$$e = \sqrt{\frac{h}{H}} \qquad (3)$$

Коефициентът има стойности . При удар на еластични тела , а при идеално-пластични тела

Коефициентът на реституция е мярка за това колко кинетична енергия остава след сблъсъка на две тела. Стойността му варира от 0 до 1. Ако е от по-горната страна (т.е. близо до 1), това предполага, че по време на сблъсъка се губи много малко кинетична енергия; от друга страна, ако стойността е ниска, това показва, че голямо количество кинетична енергия се преобразува в топлина или се абсорбира по друг начин чрез деформация.

В случай на идеално еластичен сблъсък, който не се случва в реални условия, коефициентът на реституция би бил точно 1. Следователно, тялото след удара ще се върне на същата височина от която е паднало.

Това може да се случи опитно, изчислението му става по формулата [3], където е-коефициент на реституция, h- височина на първия отскок след удара на тяло 2, Н- начална височина на падане на материала 2. (фиг.1)

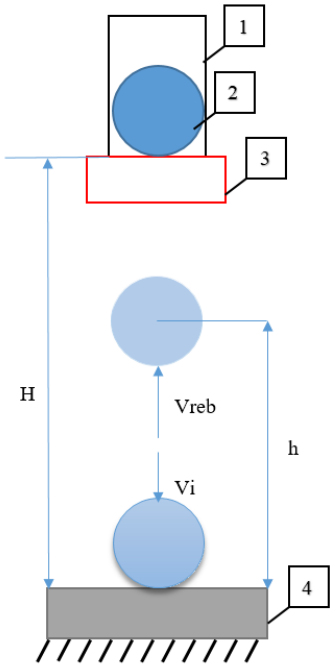

Фиг.1 *Схема на опитната постановка*

2. *Материали за провеждане на експериментите*

Размерите на плочата от TPU са 60х60 мм с дебелина 10мм, плътностите на различните коефициенти на запълване 20, 50, 70 и 100% са показани в таблица 1. Стоманената сфера е с диаметър 9 мм.

Таблица 1. Размери и плътност на плочата при различен коефициент на запълване при принтиране.

материал плоча	L mm	D mm	H mm	обем mm3	маса gr	плътност gr/cm3
TPU 20%	60	60	10	36000	13,4	0,372
TPU 50%	60	60	10	36000	24,2	0,672
TPU 70%	60	60	10	36000	32,3	0,897
TPU 100%	60	60	10	36000	40,9	1,136

3. *Експериментални данни*

В таблица 1 са показани резултатите от експериментите със сфера от стомана и диаметър 9мм и 3д принтиран TPU материал с плътност 20-50-70-100 %.

Таблица 2. Коефициент на реституция при метална сфера с 3д принтиран TPU материал с различна плътност.

основа/сфера	№ експеримент	начална височина mm	височина на отскока mm	е-коефициент реституция
TPU 20/Steel	1	539	182,16	0,581343
	2	539	174,35	0,568744
	3	539	171,9	0,564734
	средна стойност	539	176,1367	0,57165
TPU 50/Steel	1	539	114,7	0,461304
	2	539	113,96	0,459814
	3	539	129,52	0,490201
	средна стойност	539	119,3933	0,470647
TPU 70/Steel	1	539	195,61	0,602422
	2	539	198,1	0,606245
	3	539	199,77	0,608795
	средна стойност	539	197,8267	0,605826
TPU 100/Steel	1	539	146,34	0,521059
	2	539	157,67	0,540854
	3	539	160,76	0,546128
	средна стойност	539	154,9233	0,536122

От графика на фиг.2 се вижда че плътността на плочата нараства почти линейно, спрямо коефициентът на запълване при принтирането на 3д принтер. Трябва да се вземе предвид, че например при коефициент на запълване при принтиране 20% останалите 80% са въздух, затова и нарастването на кривата не е изцяло линейно.

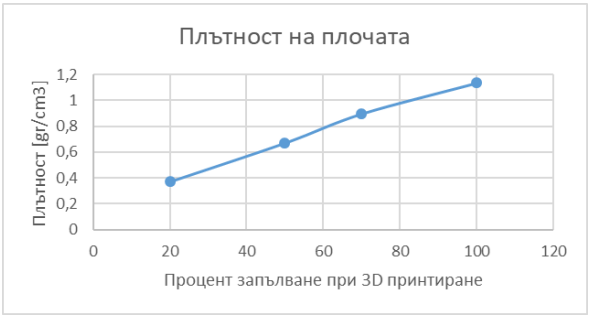

Фиг.2 *Плътност на плочата при различен коефициент на запълване при 3д принтирането и.*

На графиката (фиг.3) се вижда че плътността на плочата почти не влияе на коефициента на реституция, ще бъдат направени по-задълбочени изследвания, в които ще се тества какво влияние има повърхностната структура и твърдост на детайла.

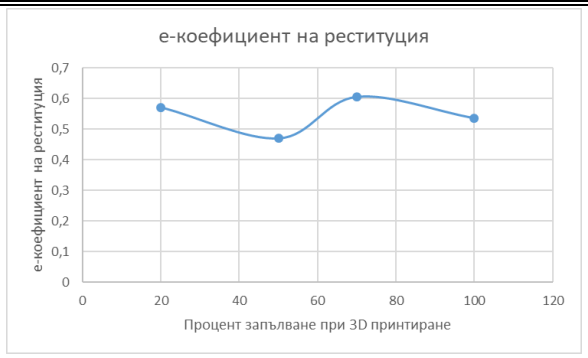

Фиг.3 *Изменение на коефициента на реституция.*

Получените резултати ще бъдат симулирани, с цел проверка и настройка на симулацията за бъдещи проучвания. След проверка на коефициента на реституция, процеса на движение и взаимодействие между смилащата среда и смилащата среда ще бъдат изследвани в 2D лабораторна мелница, показана на фиг. 4. Мелницата е проектирана по начин, който позволява за наблюдение на процеса на капаци на коритото (1), бърза смяна на барабана (2), който съдържа смилащата среда и ще бъде заменен с по-тънък барабан; 1,1kW двигател (3) с безстепенно регулиране на скоростта; възможност за захващане на барабана само от едната страна (при барабани, изработени по адитивна технология) чрез лагер (4); интелигентно управление (5) включително опции: за настройка на скоростта (rpm), запис на консумацията на енергия в реално време (мониторинг на енергийната ефективност), измерване на постигнатата скорост с лазерен тахометър. По време на лабораторния експеримент ще бъде определена критичната скорост на мелницата при запълване от 20% от мелницата. Ъгълът на разделяне (ъгъл на рамото) и ъгълът на падане (ъгъл на пръста), RPM на лабораторната мелница ще бъдат записани. Получените данни ще бъдат сравнени със симулация, като се използват същите параметри.

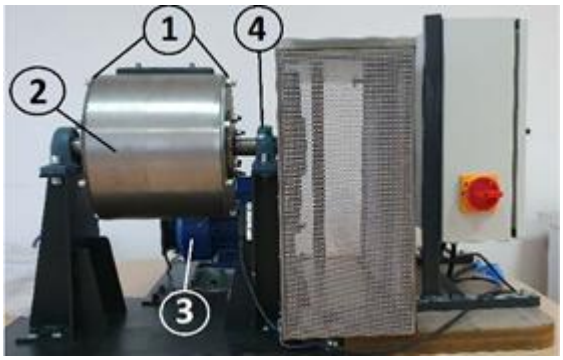

Фиг.4 *Лабораторна мелница*

4. *Заключение*

Определен е коефициентът на реституция между стоманена сфера и плоча от TPU 3D принтиран материал с различна плътност, която се постига с различен коефициент на запълване при 3D принтирането. Както се вижда от резултатите, плътността нараства почти линейно, но не и коефициентът на реституция. За момента не се вижда зависимост между обемната плътност на детайла и коефициентът на реституция. Необходимо е да се направят още изследвания, където ще бъде измерена повърхностната твърдост на плочите при различно ниво на запълване при 3D принтиране, за да може да се провери дали там ще има връзка с промяната на коефициента на реституция.

Благодарности

Това изследване е извършено като част от проект № КР-06-N47/5 „Изследване и оптимизиране на взаимодействието между смилащи тела и среда с иновативна форма", финансиран от Фонд Научни Изследвания.

Литература

1. P.Bodurov, T.Penchev, Industrial Rocket Engine and its Application for Propelling of Forging Hammers, J. of Mater. Processing Technology, 2005, 161, 504-508.

2. Т.Пенчев, П.Бодуров, Уредба за изследване удара на падащо тяло върху масивна плоча, Заявка за патент №110729/10.08.2010.

3. Beljaev, J. V. Forces and energy distribution at impact processing of materials. – Vestnik mashinostroenija, 1974, 4, 70 - 73. (In Russian).

4. Hunter, S. C. Energy absorbed by elastic waves during impact. – *J. Mech. Phys. Solids*, 1957, 8, pp. 162-171.

5.Gyoshev S., Stoimenov N., Paneva M.. Determination of the friction coefficient of 3D printed materials - Part II - Sliding friction. 10th International Conference on Mechanical Technologies and Structural Materials (MTSM 2021), 43-46.

Productivity of specialized gripper-dispenser

Продуктивност на специализиран хващач-диспенсър

Petko Stoev, Nayden Cheivarov *, Nikolay Stoimenov
Institute of Information and Communication Technologies at the Bulgarian Academy of Sciences,
Acad G. Bonchev str., Block 2, 1113 Sofia, Bulgaria
*nchivarov@gmail.com

Abstract: Grinding processes are one of the largest consumers of energy. Accurate dosing with grinding bodies in the mills contributes to the proper study of the grinding process. Specialized gripper-dispenser for dosing a laboratory mill is designed, modeled and 3D printed. Productivity studies have been performed on different sizes and shapes of grinding. The results of the experiments are presented, as well as a comparative analysis of the different grinding bodies used in a laboratory ball mill.

Key words*: Milling bodies, 3D printing, milling processes, Enrichment process, anthropomorphic robot, gripper-dispenser*

1. Въведение

Процесите на смилане са едни от най-големите консуматори на енергия. Сведения сочат, че 20% от общата земна енергия се използва за смилане и раздробяване на различни материали. Процесът се използва в имитационната индустрия, фармацията, производството на различни видове керамика и др. Изследването на такива процеси е предизвикателство дори за съвременния свят. Процесът на смилане в повечето случаи използва смилателни тела. Те могат да варира по размер, форма, материал, тонаж. Размерът варира от фактори като материал за смилане, размер на мелницата, желана продукция (едрина на смилания материал). Най-използваната и разпространена форма за смилане в топковите мелници (фиг. 1) са сферите (фиг. 2). Зареждането на мелницата с подходящи смилателни тела може да допринесе за по-добри резултати от крайната продукция, като намалено време за смилане, подобри разпределение на частиците, енергийна ефективност на процеса, намаляване на оборотите на мелницата [1-3].

Настоящият доклад представя изследвания, свързани с продуктивността, базирани на роботизирана система за дозиране на лабораторна мелница за обогатяване на руда.

Фиг. 1 *Топкова мелница*

Фиг. 2 *Мелещи тела*

2. Система за дозиране

Съвременните мелници трябва да бъдат с висока производителност, повишена производствена (експлоатационна) надеждност и с минимален разход на енергия. Основен фактор за повишена производителност е времето за смилане и работните обороти [4]. Едрината на изходния продукт, разходът на енергия и разходът на мелещи тела зависи от редица фактори, някои от тях включват и точно дозиране както с материал за смилане, така и с мелещи тела.

За точното, навременно и контролирано дозиране на лабораторна мелница, проучваща движението и взаимодействието на обогатителните процеси при руди е разработена система, съставена от специално проектиран за целта диспенсър, прикрепен към антропоморфен робот.

Антропоморфен робот:

За целите на изследванията е избран 6-осен антропоморфен робот с 6 степени на свобода Niryo One. Формално може да бъде разделен на 7 части. Размерите на основните части изграждащи конструкцията са както следва: Основа - 103 mm, рамо – 80 mm, първи лост – 210mm, втори лост – 180mm, показан на фиг. 3.

Роботът е с максимален достиг от 440 mm. Фиксира се към определената работна повърхност чрез 4 вендузи и гумени крачета. Максималният ъгъл на завъртане за всяка от осите е както следва: J1: от -175 ° до 175 °, J2: от -90 ° до 36,7 °, J3: от -80 ° до 90 °, J4: от -175 ° до 175 °, J5: от -100 ° до 110 °, J6: от -147,5 ° до 147,5.

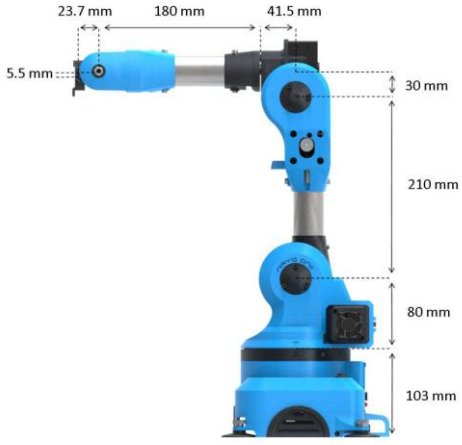

Фиг. 3 *Антропоморфен робот Niryo One*

Управлението и задвижването на робота се извършва от командния панел в управляващото приложение Niryo One

Studio. При пристъпване към управлението на робота трябва предварително да бъде извършено калибриране. Софтуера, управляващ робота се състои от 3 различни раздела. За цели се ползва раздела „Arm command“ [5]. В него може да се избира от между два подраздела - „стави“ или „поза“. Преместването на всяко съединение, независимо едно от друго се осъществява от подраздела „стави“. Подразделът „поза“ позволява да се премести TCP (Point Center Point, или просто казано: краят на рамото) с декартови координати, относителни спрямо началните (x, y: средата на основата на робота, z: земята). Позицията на TCP, както и неговата ориентация можете да се промени.

Специализиран хващач-диспенсър:

Контрола на потока от мелещи тела, които постъпват в лабораторната мелница, тяхното преброяване и точното дозиране се извършва от конструираният специализиран хващач-диспенсър.

Устройството се състои от 3 главни компонента, към които биват поместени допълнителните части за неговото функциониране. Реализираният прототип е осъществен посредством адитивна технология. Основни детайли на общата конструкция са следните - бункерно тяло, револверна шайба, разпределително тяло (фиг. 4- 1), 2), 3)). Общите размери на сглобката са 108x145x197,5mm (ширина x дължина x височина).

Бункерното тяло представлява цилиндър с диаметър 70 mm и височина 95 mm, като към горната част има допълнително скосение, за улеснено загребване на смилателнителните тела. В задната част е проектирано място за захващането на сглобката към антропоморфния робот посредством резбово съединение. В предната част са разположени две малки плоскости, към които се закрепва стопера (фиг. 4 - 4)), фиксиращ револверната шайба. В дъното на цилиндъра е направен отвор със скосение към него, което да гарантира насочването на мелещите тела, които да преминат през револверната шайба към разпределителното тяло. В бункерното тяло е позиционирана бъркалка. Необходимостта и се обуславя от възможността мелещите тела да се самонаместят и заклинят така, спирайки потока от преминаващи през отвора в дъното на бункера мелещи тела тип сфера [6].

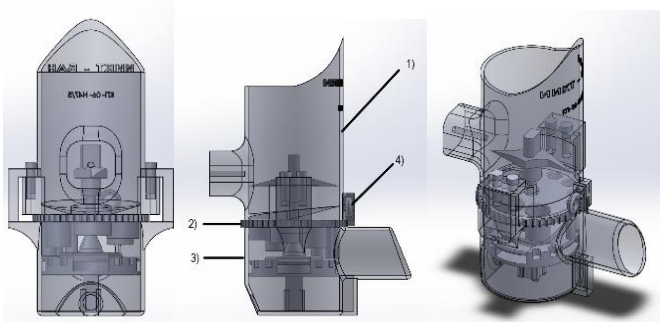

Фиг. 4 *Изгледи на проектирания хващач-диспенсър*

В револверната шайба са проектирани отвори с различни диаметри, съответстващи на диаметрите на различните мелещи тела [7]. Поставя се между бункерното и разпределително тела, като се ротира при смяна на работните отворите. Страничната част на шайбата е назъбена с малки каналчета, които се ползват за по-лесно и удобно завъртане при пренастройка с друг работен размер (фиг. 5). В каналчетата влиза стопера, като по този начин законтря и фиксира положението на шайбата. Към всеки един от отворите в револверната шайба е продължена тръбна конструкция с диаметър, съответстващ на диаметъра на конкретния отвор, като във вертикала всяка от тях е с различна дължина. Целта на тръбните конструкции е да ориентират и подредят мелещите тела, които минават през тях, като така да се осигурява освобождаването по хоризонтала на само едно мелещо тяло при попадане на мелещото тяло в разпределителната перка.

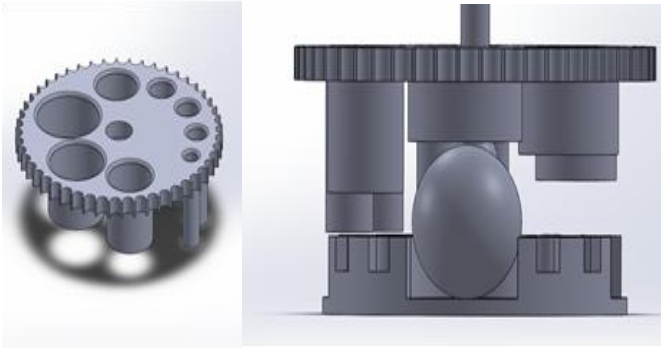

Фиг. 5 *Револверна шайба и принципа и на действие*

Разпределителното и бункерно тела са свързани посредством п-образна структура (фиг. 6 -1)). Размерите на разпределителното тяло са: диаметър 70 mm и височина 62,5 mm. В предната му част е проектиран отвор с улей (фиг. 6 – 2) с дължина 50 mm с вътрешен диаметър 32mm, през който излизат мелещите тела и се насипват в лабораторната мелницата. Преброителен фотосензор е поместен в гнездо под улея, който през прорез отчита преминалото тяло [8]. В центъра на основата на цилиндричното тяло са екструдирани 4 г-образни профила (фиг. 6 – 3)), които да фиксират електромотора, задвижващ разпределителните перки, придвижващи мелещите тела към улея.

Разпределителните перки биват 2 разновидности [9] спрямо размерите на мелещите тела, с които работят. И двете перки имат следните еднакви размери: външният диаметър – 64 mm, височината – 25,5 mm. Дълбочината на гнездата за пренос на тела е 9,2 mm, дебелината на дъното на всяко гнездо – 2,5 mm и размерите на правоъгълният вал – 6 x 4 mm, предаващ въртеливо движение от електромотора към бъркалката на бункера. Прикрепването към електромотора се осъществява посредством фланци. За да работи с най-малките мелещи тела, към едната разпределителна перка се прикрепя капак (фиг. 7).

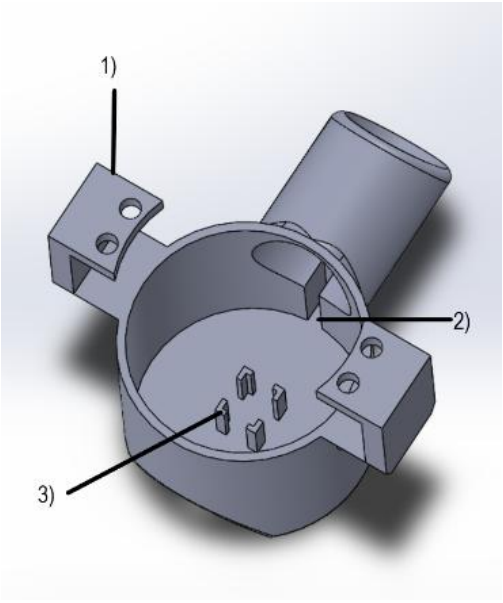

Фиг.6 *Разпределително тяло*

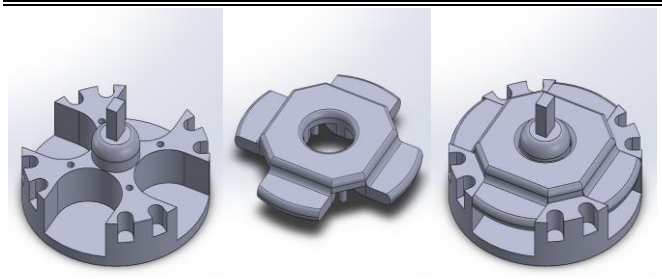

а) б) в)

Фиг. 7 *Компоненти – Перка а), капак б), сглобка за работа най-малките мелещи тела в)*

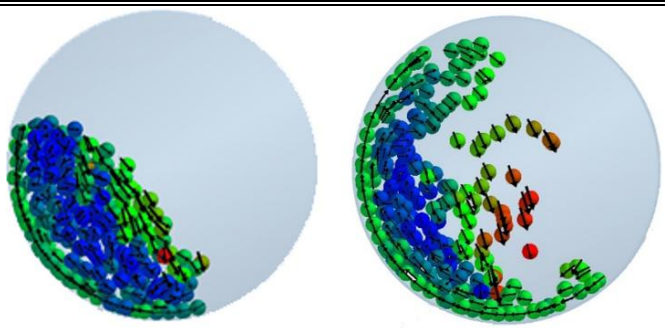

Фиг. 8 *Режими на работа: а) Каскаден режими на работа; б) Катарактен режим на работа.*

3. Метод на действие на разработената система

Антропоморфният робот с прикрепения прибор загребва мелещи сферични тела с настроеният от оператор работен размер и така запълва бункерното тяло. Електромотора, който движи разпределителната перка задвижва и бъркалката в бункера. В бункерното тяло под въздействие на бъркалката, мелещите тела преминават през отвора в дъното. От отвора на бункера през револверната шайба телата преминават и влизат в тръбната конструкция, явяваща се продължение на работния отвор. По този начин мелещите тела се ориентират вертикално. Подредени в този ред преминават през тръбната конструкция. В края на тръбната конструкция биват освободени хоризонтално и попадат в свободно гнездо на разпределителната перка, която въртейки се загребва тялото. Перката завърта тялото до изходния улей, където под въздействие на сили излиза от гнездото и влиза в улея. При попадане в улея, придвижвайки се в него, мелещо тяло бива отчетено от фотосензора, който добавя + 1 брой в софтуерния брояч. Мелещото тяло излиза от улея и попада в мелницата.

4. Теоритична обосновка, тестове и резултати

Осъществяването на ефективен обогатителен процес изисква изходния продукт да претърпи технологична преработка за осредняване на минералния и химичния състав на продукта. Преработката се осъществява в различни видове мелници, както и при различни режими на работа, показани на фиг. 8. Смилането на различни материали представлява важен индустриален процес, при който материала се натрошава и смила до определен предварително желан размер чрез взаимодействие между материал, мелещи тела и мелеща среда.

Продуктивността при тези процеси зависи до голяма степен от мелещите тела. В предходни изследвания бяха проведени тестове със сферични мелещи тела вариращи в размери. В настоящият доклад се изследва времева зависимост за преминаването на 10 мелещи тела с форма на сферичен тетраедър през отвора на проектирания диспенсър. На базата на изследване е установено, че при един и същи обем и маса, повърхността при сферичният тетраедър спрямо сфера е по-голяма [10]. Членове от ИИКТ-БАН имат защитен патент на сфероидалет тетраедър, който може да бъде използван при топкови мелници [12, 13].

Трябва да се отбележи, че използваният тетраедър е от 3D принтиран материал PLA (фиг.9), който има различен коефициент на триене. Сфероидалния тетраедър се плъзга по повърхността на диспенсър-хващач, коефициента на триене в този случай е 0,351 [14]. Поради геометричните форми, коефициента на триене при металните сфери, контактуващи с материал PLA е коефициент на триене при търкаляне, който опитно е определен на 0,053.

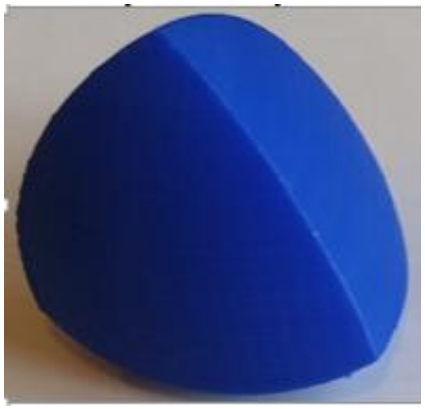

Фиг.9 *Мелещо тяло с форма на сферичен тетраедър, принтирано от 3D принтер с PLA материал*

При имплементиране им в процеса на обогатяване на руда под формата на друг вид мелещи тела следва да доведе до повишена продуктивност. Важно е да се отбележи, че при еднакви маса и обем, радиусите на сферата и на сферичният тетраедър са различни. Обемът на сферичен тетраедър се изчислява по формулата: $V = ((8/3)\pi - (27/4)\cos^{-1}(1/3)+(\sqrt{2}/4))\,r^3$ [10].

След получаване на новите данни за времевите зависимости на сферичните тетраедри е направен сравнителен анализ спрямо досега използваните сферични мелещи тела в диспенсъра. За всяка от трите размера групи от по 10 мелещи сфери са направени по три отделни измервания. За провеждане на експеримента са използвани хронометър и камера за запис на процеса. Намерената връзка е показана в таблица 1. В таблица 2 са отчетени получените стойностите от предходно изследване със сферични мелещи тела.

Таблица 1. *Времена тетраедър.*

D, [mm]	t_1, s	t_2, s	t_3, s	$T_{ср.}$, s
10.5mm	2,1	2	2,3	2,13
17mm	2,8	2,8	2,6	2,73
21mm	3,1	3	2,8	2,96

Таблица 2. *Времена сфери.*

D, [mm]	t_1, s	t_2, s	t_3, s	$T_{ср.}$, s
9mm	1.8	2	2	1,93
16mm	2,4	2,5	2,5	2,46
20mm	2,9	2,8	2,8	2,83

5.Заключение

На база на получените резултати от проведеното изследване може да отбележим следното:

Разликата при една и съща маса и обем на сферичните мелещи тела и тези с формата на сферичен тетраедър е в площта, която е в полза на вторите. По-голямата контактуваща площ между отделните тела повишава продуктивността като намалява същевременно по този начин броя на телата изискуеми в мелница за раздробяването до определен размер. При изследване на времевата зависимост за преминаване на 10 мелещи тела през изходния улей на проектирания специализиран диспенсър се виждат сходни резултати. Като заключение може да се каже , че ползването на тук представена разработената система за зареждането на мелница за рудни обогатителни процеси заедно с имплементирането на мелещите тела с формата на сферичен тетраедър довеждат до повишаване на продуктивността при тези процеси.

Благодарности

Това изследване е извършено като част от проект № КР-06-N47/5 „Изследване и оптимизиране на взаимодействието между смилащи тела и среда с иновативна форма”, финансиран от Фонд Научни Изследвания.

Литература

1. Tsvetkov H. (1988), Enrichment machines (In Bulgarian), Publ. House„Technique“, Sofia.
2. Stoimenov N., Karastoyanov D., Klochkov L., Study of the Factors Increasing the Quality and Productivity of Drum, Rod and Ball mills, 2nd Int. Conf. on Environment, Chemical Engineering & Materials, ECEM '18, Publishing house AIP (American Institute of Physics), Vol. 2022, Issue 1, ISBN: 978-0-7354-1740-3, pp. 020024-1-020024-6, 2018
3. Ruzic J., Stoimenov N., (2016) Advanced copper matrix composites, Monography in English, „Prof. Marin Drinov“ Publishing House of Bulgarian Academy of Sciences, ISBN 978-954-322-859-1
4. Жълтов А. (1980), Машини за строителни материали“ ДИ „Техника“, София.

https://niryo.com/docs/niryo-one/user-manual/complete-user-manual/

5. https://www.cmiindustries.it/en/chemical/filling-cup-chemical/filling-machine-rotative-chemical/ (последно посетен март 2021)
6. https://www.zen.biz/videos.php (последно посетен март 2021)
7. https://www.accutekpackaging.com/filling-machines/tablet-counters/accucounter (последно посетен март 2021)
8. https://www.spee-dee.com/rotary-fillers/ (последно посетен март 2021)

Bodurov P., Genchev V., New and More Effective Grinding Bodies for Drum Mills Alternative of the Spherical Grinding Bodies, Journal of Multidisciplinary Engineering Science and Technology (JMEST) ISSN: 3159-0040, Vol. 2 Issue 9, pp. 2516-2520, 2015

https://www.math.unl.edu/~bharbourne1/ST/sphericaltetrahedron.html

Бодуров П., Пенчев Т., Мелещо тяло, действащ патент на Р. България, Рег.№ 66576 / 31.05.2017

Бодуров П., Пенчев Т., Мелещо тяло, действащ патент на Р. България, Рег.№ 66577 / 31.05.2017

9. Gyoshev S., Stoimenov N., Paneva M., Determination of the friction coefficient of 3D printed materials - Part II - Sliding friction, 10th International Conference on Mechanical Technologies and Structural Materials (MTSM 2021), Split, Croatia, September 23-24, 2021, Croatian Society for Mechanical Technologies, Croatia, ISSN: 1847-7917, pp. 43-46

Анализ опыта создания роботов на базе магнитных транспортных устройств

Analysis of the experience of creating robots based
On magnetic transport devices

Prof., Dr.Sc.(Eng.) Koryagin S.I., Assoc. Prof., Dr.Sc.(Eng.) Sharkov O.V., Prof., Dr.Sc.(Eng.) Velikanov N.L.
Immanuel Kant Baltic Federal University – Russia, Kaliningrad
E-mail: skoryagin@kantiana.ru, osharkov@kantiana.ru, nvelikanov@kantiana.ru

Abstract: *The results of the development of mobile robotic devices were evaluated. The devices are designed to perform work in places with complex volumetric surfaces, in a polluted environment. One of the main requirements is the ability to move freely independently on the surface and stay on it. Magnetic transport devices are the most promising for metal structures. Devices with various modes of movement, permanent and alternating magnets are considered. The most promising designs for full automation of surface treatment processes and the use of robotics have been selected.*

KEYWORDS*: MAGNETIC TRANSPORT DEVICE, FERROMAGNETIC SURFACE, ROBOT*

1. Введение

Экономическая эффективность различных инженерных систем во многом определяется отношением времени их эксплуатации к общему жизненному циклу, который складывается из времени эксплуатации и времени простоя. Причем основную часть простоя занимают периоды технического обслуживания и ремонта.

В связи с этим актуальной является задача повышения уровня механизации и автоматизации в целях сокращения сроков проведения мероприятий в системе технического обслуживания и ремонта инженерных систем.

Составным звеном механизации этих работ является использование транспортных устройств для доставки к рабочим элементам технологического оборудования. Например, в судоремонте они применяются для перемещения по поверхности бортовой обшивки оборудования для очистки, окраски, сварки и приборов для её освидетельствования.

Среди инженерных систем можно выделить объекты, в состав которых входят конструктивные элементы, представляющие собой ферромагнитные поверхности.

Перспективным направлением в этой области является использование для перемещения инструментов дистанционно управляемых магнитных транспортных устройств, которые перемещаются непосредственно по рабочей поверхности и удерживаются на ней за счет действия магнитных сил.

Работы по созданию и внедрению в различные отрасли промышленности магнитных транспортных устройств, перемещающихся по произвольно ориентированным в пространстве ферромагнитным поверхностям, и несущих на себе различное технологическое и диагностическое оборудование, ведутся довольно широко и во многих странах [1–2].

Агрегаты и технологическое оборудование таких транспортных устройств получают питание с помощью гибких шлангов и кабелей, а управление ими осуществляется операторами дистанционно с выносных пультов.

Предыстория развития наземных транспортных средств наложила свой отпечаток на конструкции магнитных транспортных устройств, перемещающихся по поверхностям, плоскости расположения которых значительно отклоняются от горизонтали.

2. Классификации магнитных транспортных устройств

Магнитные транспортные устройства в зависимости от типа магнитного элемента, обеспечивающего нагрузку от ведущих колес на опорную поверхность, можно классифицировать на устройства с постоянными магнитами, электромагнитами, комбинированными магнитами.

Транспортные устройства с постоянными магнитами не требуют дополнительного расхода энергии на создание сил, обеспечивающих прижим устройства к ферромагнитной поверхности. Кроме того, постоянные магниты не выделяют тепла, поэтому не требуют охлаждения.

Однако применение постоянных магнитов имеет определенные ограничения. Так. постоянные магниты весьма чувствительны к величине зазора между магнитом и ферромагнитной поверхностью, так как при увеличении этого зазора сила притяжения резко падает. Применение же магнитов из редкоземельных материалов встречает затруднения из-за ограниченного их выпуска и высокой стоимости.

С помощью электромагнитов можно создать практически любые силы притяжения, однако протекающий через них ток вызывает выделение тепла. Поэтому электромагниты, имеющие небольшую массу при относительно большой развиваемой силе притяжения, требуют не только электроснабжения, но и систем охлаждения.

Транспортные устройства с комбинированными электромагнитами имеют в своей конструкции как электромагниты, обеспечивающие надежное их удержание на ферромагнитной поверхности, так и постоянные магниты, которые позволяют удерживаться транспортному устройству на ферромагнитной поверхности в случае исчезновения питания на электромагнитах.

В зависимости от принципа движения магнитные транспортные устройства можно классифицировать на устройства: колесного типа; гусеничного типа; шагающего типа и комбинированного типа.

Транспортные устройства колесного типа можно подразделить на транспортные устройства с поворотным двигателем и с раздельным приводом ведущих колес.

Ферромагнитные поверхности могут иметь самые различные формы и площади. Поэтому к поворотливости (маневренности) транспортного устройства предъявляются повышенные требования. Критерием поворотливости является минимальный радиус поворота, который характеризует площадь, необходимую для маневрирования и разворота транспортного устройства.

Поворот с помощью управляемых колес (с помощью поворотного двигателя) является наиболее распространенным способом для колесных устройств любых назначений.

Однако при этом способе трудно обеспечить малый радиус разворота. Кроме того, установка дополнительного двигателя для поворота приводит к увеличению массы транспортного устройства, которая в силу специфики работы на произвольно ориентированной поверхности ограничена.

Принудительное изменение соотношения частот вращения колес (гусениц) разных бортов для поворота транспортных устройств с неповоротными колесами дает возможность существенно уменьшить минимальный радиус поворота по сравнению с радиусом поворота экипажей с управляемыми колесами.

Поскольку пет ограничения на величину и направление частоты вращения тяговых двигателей левого и правого бортов

транспортного устройства, возможен разворот с минимальным радиусом поворота, близким к нулю.

В то же время транспортные устройства с избыточной поворачиваемостью при прочих разных условиях более чувствительны в управлении и требуют от оператора большей точности в работе. В этом отношении особое место занимает вопрос автоматизации процесса движения транспортного устройства.

В общем случае транспортные устройства колесного типа легче и маневреннее, чем транспортные устройства гусеничного и шагающего типов.

В то же время грузоподъемность транспортных устройств гусеничного и шагающего типов выше, чем у транспортных устройств колесного типа, так как магнитные элементы, установленные на гусеничных и шагающих транспортных устройствах для обеспечения их удержания на произвольно ориентированной поверхности, непосредственно соприкасаются с последней или находятся относительно нее на небольшом зазоре, определяемом толщиной немагнитной ленты гусеницы и толщиной слоя краски, окалины и др.

При выборе транспортного устройства того или иного типа необходимо учитывать:

1. характер проводимой работы, т.е. назначение транспортного устройства (например, перевозка оборудования для очистки, где возможны вибрация, удары; перевозка оборудования для окраски, что сказывается на размещении его на платформе транспортного устройства; перевозка диагностических датчиков и др.);

2. характер перевозимого груза (габариты, масса, комплектность, характер соприкосновения с поверхностью, необходимость частых остановок и маневрирования);

3. состояние поверхности передвижения (ее площадь, кривизна, высота неровностей, толщина обшивки, толщина немагнитного покрытия, влажность, замасленность, наличие обрастаний и др.);

4. состояние внешней среды (воздух, вода, агрессивность, температура и др.).

Например, для проведения окраски крупно- тоннажного корпуса судна для большей производительности лучше применить транспортное устройство колесного типа, имеющее высокую скорость, маневренность, легкость в управлении.

В то же время при проведении работ по очистке подводной поверхности корпуса судна, имеющего значительные наросты и отложения, предпочтение следует отдать транспортному устройству гусеничного типа, которое имеет высокий коэффициент сцепления с обрабатываемой поверхностью благодаря большой площади соприкосновения гусениц с последней.

Там, где имеется возможность использовать внешний привод для перемещения транспортного устройства, его следует применять, так как проходимость транспортного устройства по «скользким» поверхностям возрастает и отпадает необходимость в принятии дополнительных мер по их страховке от падения в случае обесточивания электромагнитов.

3. Обзор конструкций магнитных транспортных устройств

Гусеничные магнитные транспортные устройства по своей конструкции схожи с конструкцией гусеничного трактора. Отличительной особенностью является сама гусеница, которая снабжается постоянными магнитами или электромагнитами.

Приводы гусениц выполняются независимыми, что позволяет обеспечить как прямолинейное движение вперед или назад (в режиме равных частот вращения приводных двигателей левой и правой гусениц), так и разворот в ту или другую сторону (в режиме разных или противоположных частот вращения).

На рис. 1 представлен робот для очистки подводной части корпуса судна (Китай), созданный на базе магнитного транспортного устройства гусеничного типа [1].

В данной конструкции используется комбинация постоянного магнита и электромагнита

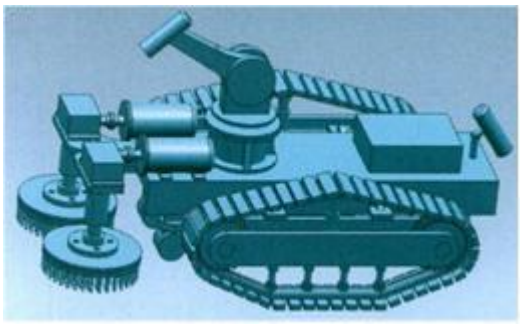

Рис. 1. *Робот для подводной очистки корпуса судна [1].*

На рис. 2 представлена конструкция работа-контролера NanoMag (США) на базе магнитного гусеничного мобильного устройства [2].

Рис. 2. *Гусеничный робот-контроллер NanoMag [2].*

Данный робот предназначен для использования в агрессивных средах в целях контроля коррозии. В нем используются магниты из редкоземельных металлов, что позволяет ему перемещаться горизонтально, вертикально и вверх дном.

На рис. 3 показан работ Tripillar (Швейцария) представляющий собой магнитное гусеничное транспортное устройство [3–4].

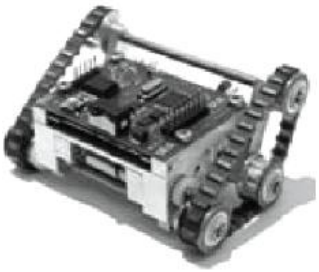

Рис. 3. *Гусеничный робот-контроллер Tripillar [4].*

Он создавался для технического обслуживания внутренних поверхностей угольных котлов. Транспортное устройство имеет магниты как на гусеничной ленте, так и на корпусе.

Колесные магнитные транспортные устройства имеют наибольшее распространение.

Их можно разделить на устройства, в которых магниты конструктивно встроены в колеса и с магнитами, расположенными вне колесной базы.

На рис. 3 представлено робот M2000 (США) [3, 5], размещенный на платформе магнитного транспортного устройства на колесной базе с магнитами, расположенными вне колес.

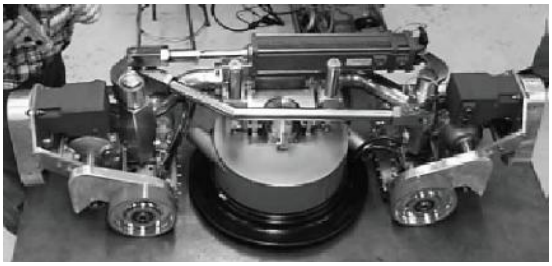

Рис. 4. *Робот М2000 на базе магнитного транспортного устройства с колесной базой [5].*

Он имеет четыре колеса, размещенные на шарнирно-сочлененной раме, и оснащен дифференциалом и электромотором. Робот оборудован двумя постоянными магнитами, установленными на нижней части мостов.

На рис. 5 представлено робот Турболаз (Россия) [3, 6], размещенный на базе магнитного транспортного устройства на колесной базе, к которой магниты встроены в колеса.

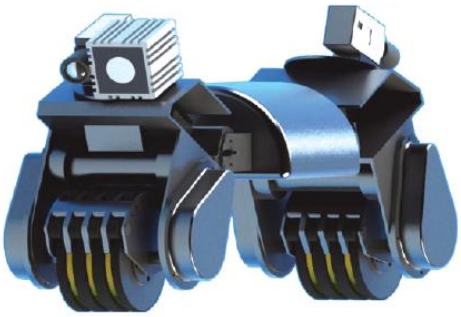

Рис. 5. *Робот Турболаз на базе магнитного транспортного устройства с колесной базой [6].*

Робот предназначено для неразрушающего контроля генератора ветровой турбины при установленном роторе.

На рис. 6 представлен робот для внутритрубной диагностики А2072 (Россия) [7].

Колесная база выполнена в виде магнитных колес-редукторов. Усилие отрыва от ферромагнитной поверхности 60 кг, что позволяет роботу, зависать в потолочном положении.

Рис. 6. *Робот* А2072 *на базе магнитного транспортного устройства с колесной базой [7].*

Магнитные транспортные устройства могут иметь внешний привод, который одновременно обеспечивает страховку транспортного устройства.

Необходимость применения внешнего привода обусловлена сложностью перемещения магнитного транспортного устройства со встроенным приводом по скользкой поверхности, так как коэффициент сцепления ведущих колес с поверхностью при этом очень низок и транспортное устройство буксует на месте.

Шагающие магнитные транспортные устройства обычно имеют от двух до шести ног.

На рис. 7 показан робот Winspecbot (Германия-Швеция) [3, 8], созданный на базе шагающего магнитного транспортного устройства.

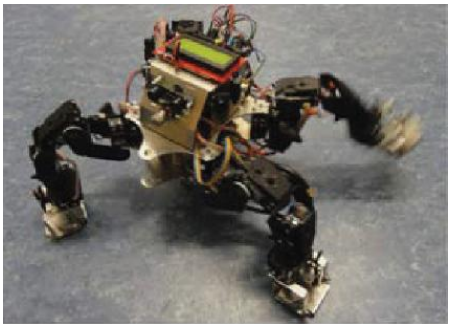

Рис. 7. *Робот Winspecbot на базе шагающего магнитного транспортного устройства [8].*

Он предназначен для инспекции стальных трубопроводов. При шагании робот с помощью сервопривода увеличивает расстояние между магнитом и поверхностью перемещения, тем самым достигается уменьшение удерживающей силы.

4. Выводы

Передвижные мобильные магнитные транспортные устройства широко применяются в различных отраслях техники. Они подразделяются на гусеничные, колесные и шагающие с постоянными магнитами или электромагнитами. Наиболее часто такие устройства используются в труднодоступных для измерения местах.

Использование магнитных транспортных устройств в качестве базы для размещения роботов, предназначенных для технического обслуживания, диагностики и ремонта инженерных конструкций имеет широкие перспективы, и их применение в мировой практике постоянно расширяется.

5. Литература

[1] Zeng C., Cai Z.X. The study of hull cleaning remote-control machine. Robot Technique and Application. 2012. V. 29(1). P. 14–17.

[2] Eddyfi Technologis. Products. NanoMag. URL: https://www.eddyfi.com/en/product/nanomag.

[3] Сырых Н.В., Чащухин В.Г. Роботы вертикального перемещения с контактными устройствами на основе постоянных магнитов: конструкции и принципы управления контактными устройствами. Известия РАН. Теория и системы управления. 2019. №5. С. 163-173.

[4] Xu Z., Ma P. A Wall-climbing robot for labelling scale of oil tank's volume. Robotica. 2002 V.20. No2. P. 209–212.

[5] Ross B., Bares J., Fromme C. A Semi-autonomous robot for stripping paint from large vessels. International journal of robotics research. 2003. V. 22. No 7–8. P. 617–626.

[6] Мунасыпов Р.А., Шахмаметьев Т.Р., Москвичев С.С. Телеуправляемая робототехническая система внутритрубной диагностики. Робототехника и техническая кибернетика. 2014. №3. С. 73–77.

[6] Российские роботы для неразрушающего контроля: какие они бывают? URL: www. https://habr.com/ru/post/566000/

[8] Kamagaluh B., Kumar J.S., Virk G.S. Design of a multi-terrain climbing robot for petrochemical applications. Proceedings of the 15th International conference on climbing and walking robots and the support technologies for mobile machines CLAWAR-2012. Baltimore: World Scientific Publishing, 2012. P. 639–646.

[9] Zhu J., Sun D., Tso S.-K. Development of a tracked climbing robot. Journal of intelligent and robotic systems. 2002. V.35. P. 427–443.

Modeling of dynamic processes when a cone shaped electric hoist motor is established to work

Моделиране на динамични процеси при установена работа на конусен телферен електродвигател

Assoc. Prof. PhD. Toni Uzunov
University of Ruse "Angel Kanchev", Ruse, Bulgaria
tuzunov@uni-ruse.bg

Abstract: *An axial movement of the shaft appears when a cone shaped electric hoist motor is established to work, the reason for this movement is end play and the crossing of the shaft's axis and the bearing holes provoked by the diversions of the shape and the position of the surfaces and the tolerance of the sizes of the electrical motor's details. The present work reviews mechanic-mathematical models of an axial motion of the rotor -movable friction cone system when the motor is established to work. The models are used to be explained the conditions when the system can be separated from the axial support, which provoke micro impacts appearing.*
Keywords*: CONE-SHAPED ELECTRIC HOIST MOTOR, DYNAMIC PROCESSES, MODELLING*

1. Увод

Характерна особеност при установена работа на телферен електродвигател с конусен ротор 11 (фиг. 1) и статор 10 е наличието на постоянно действаща аксиална електромагнитна сила, насочена към върха на конуса на ротора [1, 2, 3]. Тази сила преодолява силата на пружината 5, като притиска прехода на вала 6 към опорната шайба 4 и се предава до корпуса 12 на двигателя чрез аксиален лагер 3, външна гривна на радиален лагер 2, регулиращ винт 1, преден щит 13 и винтове 14.

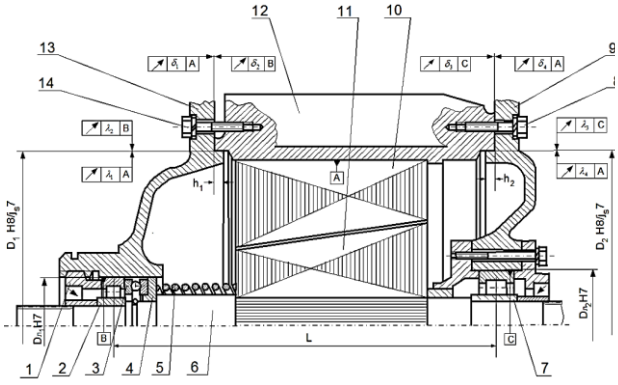

Фиг. 1 *Телферен електродвигател с конусен ротор и статор*

В резултат от кръстосване на осите на вала и лагерните гнезда и челно биене, предизвикани от отклонения на формата и разположението на повърхнините и от допуските на размерите на детайлите на електродвигателя, може да бъде предизвикано осово движение на вала в процес на установена работа на телферния електродвигател [4]. Това осово движение може да предизвика износване на шлицовото съединение между вала на електродвигателя и главината на съединителя в процес на установена работа на двигателя, което не винаги може да бъде възстановено [5, 6, 7, 8]. Затова се налага да се установят кинематичните характеристики на това движение и параметрите, които ги определят.

Примерно разположение на вала и опорната шайба, при установена работа на електродвигателя, при наличие на челно биене на прехода на вала и кръстосване на осите на лагерните отвори е показана на фиг. 2.

Показаното пълно челно биене – разстоянието между точките 1 и 2' - може да бъде получено, както от челно биене δ спрямо оста на въртене на вала, така и от неуспоредност на повърхнините *B* и *C* на опорната шайба, а също и в комбинация от двете.

Валът и опорната шайба се въртят с еднаква ъглова скорост ω, но спрямо различни оси и при завъртането им на 180^0, т.1, като точка от вала се премества в положение т.1', а т.2 в положение т.2', а като точка от шайбата т.1 се премества в т.1".

Тъй като валът е в непрекъснат контакт с опорната шайба под въздействието аксиалната електромагнитна сила F_A, при въртенето си ще извършва принудени трептения в осово направление с амплитуда *h* и период *T*, равен на отношението

(1) $$T = \frac{2\pi}{\omega}, \text{s},$$

където ω е ъгловата скорост на електродвигателя при установена работа, s^{-1}.

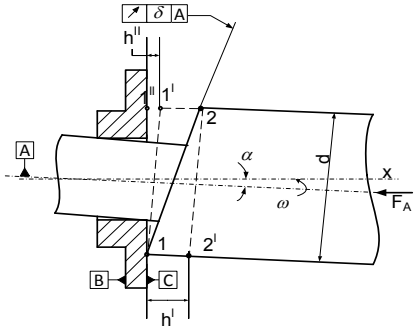

Фиг. 2 *Схема на вала и опорната шайба*

Амплитудата h на трептенето може да се определи от израза

(2) $$2h = min\{h', h''\},$$

където h^l е максималното преместване на вала по оста *x*, предизвикано от кръстосване на двете оси на въртене на ъгъл α и наличието на челно биене δ на прехода на вала спрямо оста му на въртене и може да се изрази със зависимостта

(3) $$h' = 2\delta cos\alpha,$$

h'' - максималното преместване на вала по оста *x*, ограничавано от ъгъла на кръстосване α и от диаметъра на вала *d* (фиг.1) и се определя по израза

(4) $$h'' = d \sin\alpha.$$

За изследване на кинематичните и динамичните процеси при установена работа на телферния конусен двигател е необходимо да се определи закона на движение на системата ротор-подвижен спирачен конус в осово направление.

2. Изложение

2.1. Формулиране на параметрите, определящи амплитудата на принудените осови трептения

Кръстосване между оста на вала (фиг.1) и оста на лагерния възел възниква вследствие радиална несъосност и относително завъртане на лагерните гнезда оформени в предния 13 и задния 9 щитове на двигателя и относително голямата радиална хлабина ($40 \div 75\mu m$) в използваните ролкови лагери 2 и 7.

Максималната радиална несъосност, която може да се получи между двете лагерни гнезда, вследствие максималните стойности на радиалните биенета, съгласно фиг. 1 е

(5) $$\lambda_{max} = \sum_{i=1}^{4} \lambda_i, m,$$

където $\lambda_1+\lambda_2$ е максималното радиално биене, което може да се получи при монтиране на предния щит към корпуса на двигателя 12, по диаметъра D_1, *m*; λ_1 - граничното отклонение на радиалното биене на повърхнината на сглобяване от корпуса на двигателя с диаметър D_1 (фиг. 1), спрямо оста на отвора *A, m*; λ_2 - граничното отклонение на радиалното биене на повърхнината на сглобяване на предния щит с диаметър D_1, спрямо оста на отвора *B, m*; $\lambda_3+\lambda_4$ - максималното радиално биене, което може да се получи при закрепване на задния щит към корпуса на двигателя по диаметъра D_2, *m*; λ_3 - граничното отклонение на радиалното биене на повърхнината на сглобяване на задния щит с диаметър D_2, спрямо оста на отвора *C* (фиг. 1), m; λ_4 - граничното отклонение на радиалното биене на повърхнината на сглобяване от корпуса на двигателя с диаметър D_2, спрямо оста на отвора *A, m*;

Максималното относително завъртане между отворите на двете лагерни гнезда може да се определи по зависимостта

(6) $$\theta = \theta_1 + \theta_2,$$

където θ_1 и θ_2 са максимално възможните завъртания на отворите на лагерните гнезда съответно в предния и задния щитове на двигателя, спрямо оста на вала, която се приема за база.

Ъгълът на завъртане θ_1 е $\theta_1 = min\{\theta_1^{'}, \theta_1^{''}\}$, като $\theta_1^{'}$се определя от условието за възможно завъртане на лагерното гнездо в предния щит (повърхнината *B* на фиг.1), предизвикано от наличието на максимално челно биене δ_1 и δ_2 на корпуса на двигателя и на предния щит

(7) $$\theta_1^{'} = arctg\left(\frac{2(\delta 1+ \delta 2)}{D_1}\right),$$

където δ_1 и δ_2 са максималните стойности на граничните отклонения на челното биене съответно на корпуса на двигателя спрямо оста на отвора *A* (фиг. 1) и на предния щит спрямо оста на отвора *B, m*; D_1 – диаметърът на центроване на капака към корпуса (фиг. 1), *m*.

Завъртането $\theta_1^{''}$ на лагерното гнездо се ограничава от максималната хлабина J_{1max} на реализираната сглобка по диаметъра D_1 на предния щит с корпуса на двигателя и съгласно фиг. 1 се определя по израза

(8) $$\theta_1^{''} = arctg\left(\frac{J_{1max}}{h_1}\right),$$

където $J_{1max} = ES_1 - ei_1$ е определена, като разлика между горното ES_1 и долното ei_1 гранични отклонения на реализираната сглобка по диаметъра D_1, съответно на отвора на корпуса и на повърхнината на предния щит, *m*; h_1 - височината на стъпалото (фиг. 1) на предния капак, *m*.

Ъгълът на завъртане θ_2 се определя по аналогичен начин, като $\theta_2 = min\{\theta_2^{'}, \theta_2^{''}\}$, където $\theta_2^{'}$и $\theta_2^{''}$ се определят съответно по зависимостите

(9) $$\theta_2^{'} = arctg\left(\frac{2(\delta_3+ \delta_4)}{D_2}\right)$$

където δ_3 и δ_4 са максималните стойности на граничните отклонения на челното биене съответно на задния щит спрямо оста на отвора *C* (фиг. 1) и на корпуса на двигателя спрямо оста на отвора *A, m*;

(10) $$\theta_2^{''} = arctg\left(\frac{J_{2max}}{h_2}\right),$$

където $J_{2max} = ES_2 - ei_2$ е определена като разлика между горното ES_2 и долното ei_2 гранично отклонение на реализираната сглобка по диаметъра D_2, съответно на отвора на корпуса и на повърхнината на задния щит, *m*; h_2 - височината на стъпалото (фиг. 1) на задния капак, *m*.

Максимално възможното кръстосване на осите на лагерните отвори е

(11) $$\alpha = min\{\alpha_1, \alpha_2\},$$

където α_1 е максималното кръстосване вследствие радиалната несъосност λ_{max}, и относителното завъртане θ и се определя по израза

(12) $$\alpha_1 = arctg\left(\frac{\lambda_{max}}{L}\right)+\theta,$$

където L е разстоянието между радиалните лагери в осово направление, *m*; α_2 - максималното кръстосване, което може да настъпи вследствие завъртане на радиалните лагери в лагерните отвори и се определя със зависимостта

(13) $$\alpha_2 = \alpha_2^{'} + \alpha_2^{''},$$

където $\alpha_2^{'}$ е максималният ъгъл на завъртане, зависещ от радиалната хлабина между вътрешните гривни и ролките, °; $\alpha_2^{''}$ - максималният ъгъл на завъртане, породен от максималните хлабини $J_{л1max}$ и $J_{л2max}$ на реализираните сглобки, на лагерите и отворите, °.

Максималните ъгли на завъртане $\alpha_2^{'}$ и $\alpha_2^{''}$ се определят съответно по формулите

(14) $$\alpha_2^{'} = arctg\left(\frac{J_{p1max}}{B_{p1}} + \frac{J_{p2max}}{B_{p2}}\right);$$

(15) $$\alpha_2^{''} = arctg\left(\frac{J_{л1max}}{B_{л1}} + \frac{J_{л2max}}{B_{л2}}\right),$$

където J_{p_1max} и J_{p_2max} са максималните хлабини между вътрешната гривна и ролките съответно на предния и задния радиални лагери, m; B_{p_1} и B_{p_2}- дължината на ролките съответно на предния и задния радиални лагери, m; $J_{л_1max} = ES_{л_1} - ei_{л_1}$- определена като разлика между горното $ES_{л_1}$ и долното $ei_{л_1}$ гранично отклонение на реализираната сглобка по диаметъра $D_{л_1}$ (фиг.1), съответно на отвора на предния щит и външния диаметър на лагера, *m*; $J_{л_2max} = ES_{л_2} - ei_{л_2}$- определена като разлика между горното $ES_{л_2}$ и долното $ei_{л_2}$ гранично отклонение на реализираната сглобка по диаметъра $D_{л_2}$ (фиг. 1), съответно на отвора на задния щит и външния диаметър на лагера, *m*; $B_{л_1}$ и $B_{л_2}$- широчината на външните гривни, съответно на предния и задния радиални лагери, m;

Като резултат от осовото преместване на вала при установена работа, ще се създава хармонично кинематично смущение от вида

(16) $$\zeta = h\sin pt,$$

където h е амплитудата на кинематичното смущение, определена по (2), m; p - кръговата честота, която е равна на ъгловата скорост ω на вала на двигателя, s^{-1}.

След направените разсъждения до тук могат да се направят следните изводи:

- Определени са причините за наличието на осово движение на системата вал - ротор - подвижен спирачен конус при установена работа на двигателя.
- При установена работа на двигателя възниква осово движение, на вала, което се оказва съществен фактор и може да е основна причина за износване на шлицовото съединение между вала на електродвигателя и главината на съединителя.
- Намерена е максималната стойност на осовото преместване, предизвикано от граничните отклонения на формата и разположението на повърхнините и от допуските на размерите на детайлите на електродвигателя (2).
- Осовото преместване ще създава хармонично кинематично смущение от вида (16).
- Необходимо е да се изследва влиянието на параметрите, определящи характеристиките на осовото движение на системата вал-ротор-подвижен спирачен конус с цел намиране на границите на изменение на амплитудата *h*.

2.2. Определяне закона на движение в осово направление на системата ротор-подвижен спирачен конус.

Разглежда се тяло с маса *m* равна на сумата от масите на ротора, подвижния спирачен конус и свързващия ги вал, извършващо принудени трептения в хоризонтално направление под въздействие на хармонично кинематично смущение от вида (16).

Челото на прехода на вала, който при установена работа на двигателя се притиска до опорната шайба (фиг. 1 и фиг. 2) е изобразено с ролка, свързана твърдо с тялото, която се търкаля по криволинейна повърхнина, имитираща кинематичното смущение (фиг. 3).

Криволинейната повърхнина се премества вертикално с постоянна скорост *v* и осигурява движение на ролката по оста *x* по закона

(17) $x = h\sin pt.$

Приемаме, че ролката и криволинейната повърхнина са идеално твърди тела, като движението на ролката по повърхнината е без триене и на динамичния модел действат следните сили:

F_{A3} - аксиалната електромагнитна сила, *N*;

$F_{ПР}$ - силата на затварящата пружина при установена работа на двигателя, *N;*

$c.x$ - промяната на пружинната сила вследствие изменение на деформацията ѝ от кинематичното смущение, *N*;

F_R - реакцията между тялото и аксиалната опора, *N*;

F_{TP} - силата на триене в осово направление в радиалните опори, *N*.

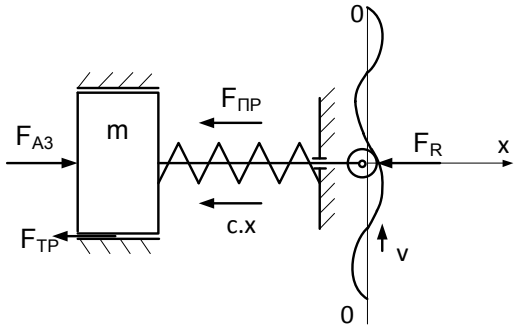

Фиг. 3 *Динамичен модел на системата при установена работа на двигателя.*

От четвъртия закон на Нютон за независимостта на действието на силите , $m\ddot{x} = \sum F_i$ уравнението на движението на модела може да се запише

(18) $m\ddot{x} = F_A - F_{\text{ПР}} - cx - F_R \mp F_{TP},$

където $m\ddot{x}$ е инерционната сила, предизвикана от кинематичното смущение, *N*, като знаците "-" и "+" са съответно при $\dot{x} > 0$ и $\dot{x} < 0$.

Тъй като е известен закона на движение на тялото по оста x (17), след двойното му диференциране и заместване в (18) се получава

(19) $mp^2 h\sin pt = F_A - F_{\text{ПР}} - F_R \mp F_{TP} - ch\sin pt,$

откъдето може да се определи реакцията F_R за общия случай на движение

(20) $F_R = F_A - F_{\text{ПР}} \mp F_{TP} - (c + mp^2)h\sin pt,$

като знакът "-" пред силата F_{TP} е при $t = \left[\frac{\pi(3+2k)}{2p}, \frac{\pi(1+2k)}{2p}\right]$, а знакът "+" – при $t = \left[\frac{\pi(1+2k)}{2p}, \frac{\pi(3+2k)}{2p}\right]$, където *k = 0, 2, 4, 6, 8 ...*

Ако в даден момент от време реакцията се окаже по-малка от нула ($F_R < 0$), това означава, че изчезва контактът между тялото и опората. За целта е необходимо да се изследва уравнение (20) при какви стойности на параметрите дясната му част може да стане отрицателна. Тъй като за всеки тип двигател само параметъра h е променлив от (20) следва, че тялото ще се отделя от опората ако е изпълнено условието

(21) $h > \frac{F_A - F_{\text{ПР}} \mp F_{TP}}{(c + mp^2)\sin pt}.$

За да бъде $h > 0$, тъй като числителят на дясната част на (21) е положително число, решението трябва да бъде при $t = \left[0 + \frac{k\pi}{p} \div \frac{\pi(1+k)}{p}\right]$, а от друга страна, тъй като се търсят минимални значения на *h*, за да бъде силата F_{TP} със знак "-" е необходимо $t = \left[\frac{\pi(3+2k)}{2p}, \frac{\pi(1+2k)}{2p}\right]$, откъдето следва че решението на неравенството ще се търси при $t = \left[0 + \frac{k\pi}{p}, \frac{\pi(1+2k)}{2p}\right]$.

Минималните стойности за амплитудата h се получават в моментите $t = \frac{\pi}{2p}, \frac{5\pi}{2p}, \frac{9\pi}{2p}, \frac{13\pi}{2p}, \frac{17\pi}{2p} \ldots$, за които синусът има положителни максимуми.

Ако за амплитудата h на осовото преместване определено по зависимост (2) е изпълнено условието (21), това означава че контактът между системата и аксиалната опора се прекъсва, но вследствие на действащите сили системата отново се притиска към аксиалната опора. По такъв начин между челото на прехода на вала и аксиалната опора възникват микроудари с период T, определен от (1), които ще натоварват с по-големи осови сили елементите, предаващи тези сили до корпуса на двигателя.

В случаите когато не е изпълнено условие (21), контактът между системата и аксиалната опора няма да се прекъсва, но принудените хармонични трептения в хоризонтално направление, които се предават до неподвижно закрепения корпус, ще предизвикат вибрации и шум.

От зависимост (21) се вижда, че минималната амплитуда h на осовото движение на системата, е обратно пропорционална на квадрата на кръговата честота *p*, т.е. при електродвигатели с по-големи ъглови скорости, опасността от възникване на микроудари нараства значително.

3. Заключение

1. Получени са механо-математически модели на движението на системата ротор-подвижен спирачен конус в осово направление при установена работа на двигателя.
2. Намерени са условията, при които системата може да се отдели от аксиалната опора, с което ще се предизвика поява на микроудари.
3. Наличието на трептения в осово направление, е предпоставка за предизвикване на вибрации и шум при установена работа на електродвигателя.
4. Осовото движение, в процеса на установена работа на двигателя, може да предизвика изтриване на шлицовото съединение между вала на електродвигателя и главината на съединителя.

4. Литература

1. Uzunov T., I. Todorov. Theoretical investigation of the dynamic loading of a lifting mechanism. In: AIP Conference Proceedings Transport, Ecology - Sustainable Development EKO Varna 2021, pp. 020025-1–020025-6.

2. Uzunov T. Experimental determination of dynamic characteristics of electric wire rope hoist. Acta technica corviniensis – Bulletin of engineering, University Politehnica Timisoara, Tome III, Fascicule 1, Romania, 2010, pp. 113-116.

3. Uzunov T. Investigation of the axial movement of the rotor when switching on a conical hoist electric motor. In: IX International Scientific Conference Technics. Technologies. Education. Safety, Borovets, Bulgaria, 2021, vol. 1, pp. 11-13.

4. Узунов Т. Динамични процеси на телферни електродвигатели с конусен ротор - монография. Русе, Дема прес, 2020, стр. 130, ISBN: 978-619-7546-12-5

5. Nikolov M. Restorative vibro-welded coatings in shielding gases and their mixtures - scientific monograph, Academic Publishing House, University of Ruse, 2019, p 144, ISBN: 978 954 712 756 2.

6. Nikolov M., I. Todorov, M. Zach, P. Máchal, J. Mareček. A research about wear-resistance of applied layers obtained by gas metal arc overlaying process with increased wire electrode vibrating frequency. In: Acta Universitatis Agriculturae et Silviculturae Mendelianae Brunensis. Mendel University of Agriculture and Forestry Brno, 2015, pp. 101-105.

7. Todorov I., M. Nikolov. A research about coefficient and moment of friction during interaction of deposited layers obtained through increased wire electrode vibrating frequency. In: Machines technologies Materials, No 8, 2014, pp. 44-46.

8. Kangalov P., M. Nikolov. Research about wear process of reconditioning coatings for shafts and bearings of agriculture machinery. In: Agricultural Machinery, vol. 1/7, 2020, pp. 4-7.

Worm gearboxes laser alignment influence on temperature and vibration level of the bearings.

Dmitry Litvinov[1]., Andris Priževaitis[2]
Riga Technical University, Liepaja Study and Science Centre – Liepaja[1,2] , Latvia
E-mail: dmitrijs.litvinovs@rtu.lv[1], andris.prizevaitis@rtu.lv[2]

Abstract: *Condition monitoring of production equipment is an important task in any industrial production. This article describes the features of laser alignment of worm gearboxes and its effect on the temperature and vibration level of rolling bearings. The necessity of periodic temperature and vibration signal measurements and analysis of bearing's condition for timely forecasting of equipment condition and planning of repairs, is also justified.*
KEYWORDS: *VIBRATION, TEMPERATURE, ENVELOPE SPECTRUM, DIRECT SPECTRUM, SIGNAL ANALYSIS, WORM GEARBOX.*

1. Introduction

Modern industry development produces the promoted requirements to reduction gearboxes reliability. Laser alignment of worm gearboxes is a very important event in the installation of equipment. In the absence of alignment, the reliability of operation and the durability of the equipment is sharply reduced. The quality of alignment affects the temperature, vibration level and the condition of such critical parts of worm gearboxes as bearings, gears (worm wheels and worms), as well as the condition of bearing places. To establish the relationship between the accuracy of laser alignment and the values of temperature and vibration, it is necessary to conduct an experiment, analyze the data obtained and draw conclusions.

2. Establishing the relationship between laser alignment quality, temperature and vibration

2.1. Laser shaft alignment methods

The worm gearbox unit's shaft alignment methods are differing nothing from the majority of rotor equipment shaft alignment methods. At an alignment the followings methods are used [1, 2, 3, 4, 7, 9, 11].

- By a caliper or probes is measuring of radial and butt-end gaps on couplings. (see Fig.1, a)
- By equipment with the sentinel type indicators:
  - A rim and face method, (see Fig.1, b);
  - Reversed indicators method, (see Fig.1, c);
- By the scopes.
- By devices with the contactless sensors of shaft pulsations.
- By laser devices. Laser sensor's location, accordingly, on the S-machine and M-machine. Where S – immobile (stationary), and M – movable machines. (see Fig.1, d).

For the shaft alignment of all rotor equipment, including worm gearbox, it is most correct to apply a laser method. This method abbreviates time of alignment, not only considerably, but also allows to conduct alignment with maximal exactness (to 0,001 mm) [7].

Now in the world exists a great number of companies which produce equipment for laser shaft alignment. Principle of the laser shaft alignment system operation is simple enough. Any laser alignment systems consist of two sensors: S (stationary) and M (moving), which in same queue are set on stationary (S) and mobile (M) machines.

As sensors used the PSD (Position Sensitive Device) sensor. It is an analog component, with theoretically unlimited resolution. When the laser beam hits the PSD, an electric current flow through the point hit

by the beam. The electric currents at the two electrodes are proportional to the position of the beam. This makes it possible to determine the position of the beam center. The resolution possible is, quite literally, one in a million [7].

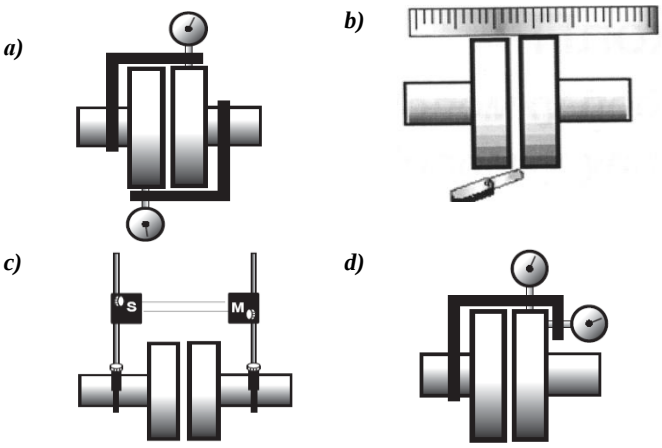

Fig 1. *Shaft alignment methods [7]*

Mainly, the laser shaft alignment systems use a visible red laser beam as a measurement reference. The laser beam is directed to the PSD detector. Then the measurement programs in the computer calculate the values from the PSD and present the result according to which program is used [7].

2.2. Experimental stand

For the relationship between the accuracy of laser alignment and the values of temperature and vibration the experiment was conducted. For the experiment the special experimental stand was used Fig.2, which consists of electromotor Pos.1, worm gearbox Nr.1 Pos.2, worm gearbox Nr.2 Pos.3, brake mechanism for loading creation Pos.4, v-belt transmission Pos.5. For the v-belt transmission alignment, the laser alignment system Pos.6 is used [10, 14]. Shaft laser alignment system also were used.

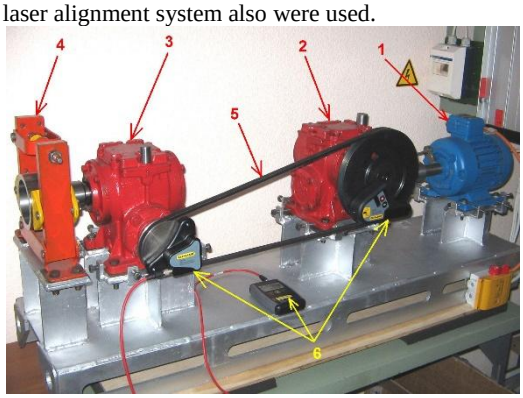

Fig.2. *Experimental stand: 1 – electromotor, 2 - worm gearbox Nr.1, 3 - worm gearbox Nr.2, 4 - brake mechanism, 5 - v-belt transmission, 6 – laser alignment system [10]*

3. Laser shaft alignment of worm gearboxes

In an order to provide reliable and long work a worm gearbox (see Fig. 3), it is necessary to provide the precision laser shaft alignment

of the gearbox and electromotor. The laser alignment procedure directly affects the temperature of the working units of the gearbox, the level of vibration, as well as the overall performance of the gearbox. To verify this and determine the important values of the alignment parameters, an experiment was carried out, which is described below. As a system for laser alignment, SKF TKSA 41 [17] and Damalini D525 [7] systems were used.

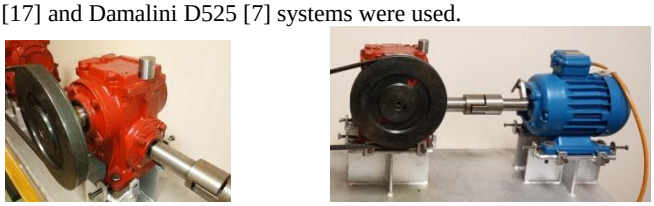

Fig. 3. *Worm gearbox unit*

On the figure 4 the laser shaft alignment conducting algorithm is presented [7].

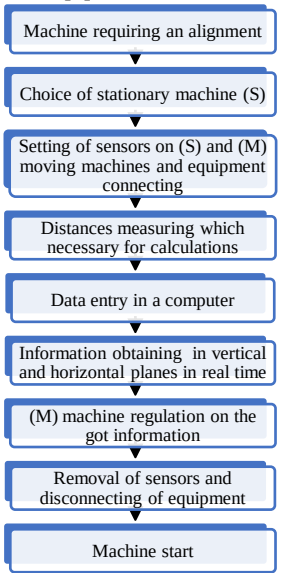

Fig. 4. *Laser shaft alignment conducting algorithm [7]*

4. Worm gearbox's bearings vibration

Vibration of worm gearbox is the important information about the unit's working condition. At general vibration level measuring it is possible only roughly to judge about the unit condition. In an order to expose a concrete defect, it is necessary to measure a direct spectrum and envelope spectrum of vibration and conduct the analysis of informative frequencies of gearbox's parts. Mainly, at rotation machinery vibrodiagnostics informative frequencies of bearings are analyzed.

Rolling bearing's work in worm gearbox composition and at presence faults in it can influence on a vibration and modulating it processes with the following's fundamental frequencies [6]:

- Rotation frequency of movable ring in relation to immobile: f_{rot} ;
- Rotation frequency of separator in relation to an outer ring:

(1) $$f_r = \frac{1}{2} \cdot f_{rot} \cdot \left(1 - \frac{d_{sr}}{d_r} \cdot \cos(\alpha)\right);$$

Where: d_{sr} - solid of revolution diameter;

$d_r \approx \frac{1}{2}(d_{out} - d_{in})$ - Diameter of separator;

d_{out} - Diameter of outer ring;

d_{in} - Diameter of inner ring;

α - contact angle of bodies and rolling paths;

- Rolling frequency of solid of revolution on an outer ring:

(2) $$f_{out} = \frac{1}{2} \cdot f_{rot}\left(1 - \frac{d_{sr}}{d_r} \cdot \cos(\alpha)\right) \cdot z = f_r \cdot z;$$

Where: z - solid of revolution number;

- Rolling frequency of solid of revolution on an inner ring:

(3) $$f_{in} = \frac{1}{2} \cdot f_{rot}\left(1 + \frac{d_{sr}}{d_r} \cdot \cos(\alpha)\right) \cdot z = (f_{rot} - f_r) \cdot z;$$

- Rolling frequency of solid of revolution in relation to the surface of rings:

(4) $$f_{sr} = \frac{1}{2} \cdot f_{rot} \cdot \frac{d_r}{d_{sr}}\left(1 - \frac{d_{sr}^2}{d_r^2} \cdot \cos^2(\alpha)\right)$$

Expressions (Eq.1, Eq.2, Eq.3, and Eq.4) are evaluating only basic harmonics frequencies in the vibration spectrums and envelope of its high-frequency components at the different types of defects [6, 9].

4. Vibration measurement of the worm gearbox

Measurement and analysis of the vibration signal of the worm gearbox was carried out using the СД-21 vibration analysis system [16], which consists of the main unit connected to the vibration transducer (see Figure 1, item 1).

During vibration measurement of the worm gearboxes, has been used route, consisting of the following components [12, 13]:

1. Direct spectrum AS1 dB(A): - $F_l = 800Hz$; the number of lines in the spectrum - 400; the number of averages - 10.

2. Envelope spectrum ES1 dB(A): limit frequency - $F_l = 400Hz$; bandpass filter - $F_a = 10kHz$; the number of lines in the spectrum – 400; the number of averages - 12.

3. Overall level of vibration OVLV dB(A): Detector - RMS; bandpass filter - $F_a = 10 - 25kHz$; the number of samples - 6.

4. Time signal TS (m/s^2): the sampling frequency - 1024 Hz; bandpass filter - $F_a = 8kHz$; the number of samples - 4000.

5. Vibration level – Vibration Velocity (mm/s) (see Table 1).

In the system of vibration diagnostics that was used in this study, there is the software for automatic diagnostics. But if in doubt, you can examine the spectra, the time signal of vibration and the vibration level manually.

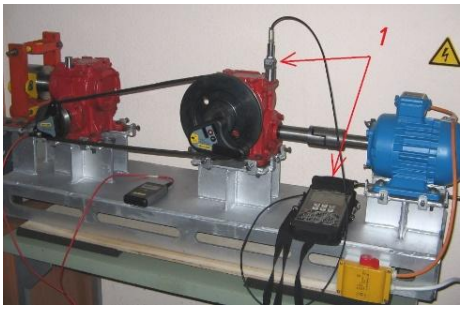

Fig.5. *Experimental stand with vibration analyzer: 1 – vibration analysis system СД-21 [16]*

6. Worm gearbox's temperature control

Temperature control of worm gearboxes must be done regularly according to a predetermined schedule. Control must be carried out remotely by using thermal imagers (see Fig. 6, pos.1) or with contact by temperature sensors installed permanently (see Fig. 7, a). Temperature control, both non-contact and contact methods, is carried out at points: No. 1, No. 2, No. 3 and No. 4 (see Fig. 7, b). An image with measuring results (see Fig. 6, pos.2).

Fig.6. *Temperature measurement remotely: 1 – thermal imager FLIR TG297 [15], 2 – an image with measuring results.*

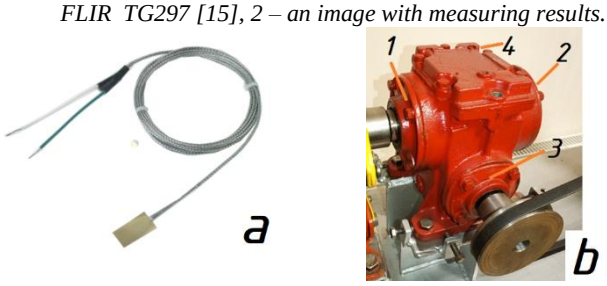

Fig.7. *Temperature measurement by contact: a – Leaf/Shim thermocouple sensor TGLEA [18], b – worm gearbox (1; 2; 3; 4 – temperature control poins)*

The average temperature of the worm gearbox Nr. 1 (see Fig. 2) was taken as the temperature value for Table 1.

7. Conducting the experiment and analyzing the results

The experiment matter consists in the following. Before start of the experiment, the worm gearbox was horizontally and vertically aligned and the horizontal and vertical values are set as in the Table 1.

During the experiment the stand was turned on, and an electromotor is rotating with frequency 50 Hz (3000 rpm) and works so 10 minutes. During all experiment the worm gearbox Nr.1 (see Fig.2, pos.2) temperature and vibration control is fulfilled, and the results was summarized in a Table 1. Totally were conducted 10 experiments.

When planning the experiment, a central compositional plan and a third-order model were used. In this study, a rotatable design was used in which the response variance is constant at all points equidistant from the center of the design [5].

Temperature and vibration level were used as dependent variables (response) (results are summarized in Figures 9 and 10, respectively). As factors influencing the response were: the offset and angular deviation values in the horizontal and vertical planes [5]. Processing of experimental data was carried out using STATISTICA 10 software, which produced by StatSoft.

Table 1*:Experimental data.*

Vertical offset value (mm)	**Vertical angular deviation value** (mm)	**Horizontal offset value** (mm)	**Horizontal angular deviation value** (mm)	**Temperature** (t° C)	**Vibration level** (mm/s)
0.01	0.02	0.02	-0.01	20.8	0.4
0.03	-0.01	0.01	0.02	20.9	0.5
0.01	0.03	0.01	0.01	21.2	0.7
0.01	0.03	0.02	-0.01	21.5	0.9
-0.01	0.01	0.03	-0.01	21.6	1
0.02	0.01	-0.01	0.03	21.8	1.4
0.02	0.01	0.02	0.02	22.5	1.8
0.01	0.01	0.01	-0.01	23.2	2.3
0.03	0.05	0.03	-0.04	25.8	3.7
0.04	0.01	0.05	0.03	27.4	4.2

Table 2: *Summary effects estimate*

Factor	Effect Estimates; Var.:Temperature; R-sqr=1. (Spreadsheet3) 4 factors, 1 Blocks, 10 Runs DV: Temperature Effect	Coeff.
Mean/Interc.	22.4827	22.4827
(1)Vertical Offset Value(L)	-23.7423	-11.8712
Vertical Offset Value(Q)	-14.1846	-7.0923
(2)Vertical Angular Value(L)	0.9038	0.4519
Vertical Angular Value(Q)	9.6154	4.8077
(3)Horizontal Offset Value(L)	22.2769	11.1385
Horizontal Offset Value(Q)	9.2462	4.6231
(4)Horizontal Angular Value(L)	2.1231	1.0615
Horizontal Angular Value(Q)	-10.8000	-5.4000
1L by 2L	9.1192	4.5596

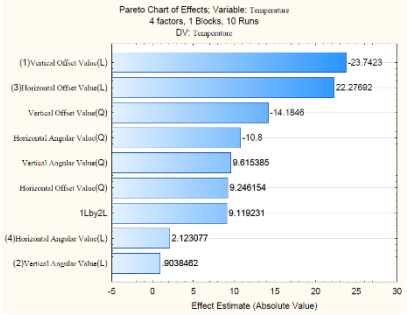

Fig.9. *Pareto chart of effects on Temperature*

Table 3: *Summary effects estimate*

Factor	Effect Estimates; Var.:Vibration level; R-sqr=1. (Spreadsheet3) 4 factors, 1 Blocks, 10 Runs DV: Vibration level Effect	Coeff.
Mean/Interc.	1.2265	1.22646
(1)Vertical Offset Value(L)	-19.6250	-9.81250
Vertical Offset Value(Q)	-11.2767	-5.63833
(2)Vertical Angular Value(L)	0.3967	0.19833
Vertical Angular Value(Q)	7.4950	3.74750
(3)Horizontal Offset Value(L)	17.2900	8.64500
Horizontal Offset Value(Q)	7.1000	3.55000
(4)Horizontal Angular Value(L)	2.0250	1.01250
Horizontal Angular Value(Q)	-7.9762	-3.98812
1L by 2L	6.8917	3.44583

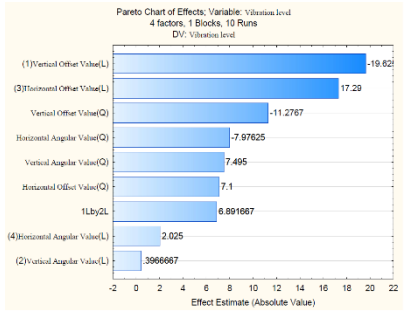

Fig.10. *Pareto chart of effects on Vibration level*

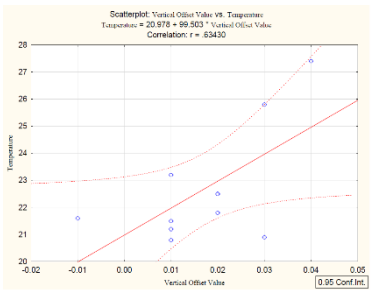

Fig.11. *Scatterplot: Vertical offset Value vs Temperature*

8. Conclusions and recommendations

Coming from the conducted experiment, it is possible to do the followings conclusions:

Based on the results of the analysis of the experimental data, it can be seen that the vertical and horizontal misalignments have the most influence on the temperature (see Fig.9 and Fig.11, and Table 2) and vibration level (see Fig. 10 and Table 3). It is also important to note that the temperature and vibration level are directly proportional to the amount of vertical and horizontal misalignment. Angular deviations in the vertical and horizontal planes have less

effect on temperature and vibration levels. This can be explained by the fact that the clutch between the worm gear is able to compensate for angular deviations in a wider range of values, compared to misalignment values.

As recommendations it is possible to mark following:

When operating worm gearboxes, as well as other rotary equipment, it is necessary to organize constant monitoring of such important parameters as: temperature and vibration level. Regular alignment checks of gearboxes and other rotary equipment should be carried out using laser alignment equipment. At the enterprise, it is necessary to organize a service whose tasks include measures for comprehensive control over the state of the equipment. The ISO 10816 standard [8] can be used as recommendations for assessing the vibration level.

9. References

1. A Practical Guide to Shaft Alignment. PRUFTECHNIK LTD. Edition 4; 4-03.007. - LUDECA Inc., 2002. – 63 p.,

2. McMillan R.B., Rotating Machinery: Practical Solutions to Unbalance and Misalignment. – New York: Marcel Dekker,Inc., 2004. – 228 p.,

3. Mobley R. Keith., Plant engineer's reference book. - Oxford: Butterworth-Heinemann, 2001. – 1189 p.,

4. Girdhar P., Practical Machinery Vibration Analysis and Predictive Maintenance. – Oxford: Elsevier, 2004. – 256 p.,

5. Монтгомери Д.К. Планирование эксперимента и анализ данных: Пер. с англ. – Л.:Судостроение, 1980. – 384с.,

6. Барков А.В., Баркова Н.А., Азовцев А.Ю., Мониторинг и диагностика роторных машин по вибрации. – Санкт Петербург: Изд. Центр СПбГМТУ, 2000. -159с.

7. Measurement and alignment systems «Easy Laser». Manual 05-0100 Rev.7// Damalini AB, - 2005.p. A2-F8.,

8. ISO 10816-1:1995. "Mechanical vibration – Evaluation of machine vibration by measurement on non-rotating parts,

9. Ļitvinovs, D., Priževaitis, A., Geriņš, Ē. *Thermal Growth Influence on the Shaft Alignment and Vibration of Centrifugal Pump*. In: 9th International Congress "Machines,Technologies, Materials 2012" (MTM 2012): Scientific Proceedings of the Scientific-Technical Union of Mechanical Engineering. Year XX, Vol.6, Bulgaria, Varna, 19-21 September, 2012. Varna: 2012, pp.59-60. ISSN 1310-3946,

10. Ļitvinovs, D., Priževaitis, A., Geriņš, Ē. *Analysis of Thermal Growth Influence on V-Belt Transmission Alignment Precision*. Journal of Mechanics Engineering and Automation (JMEA), 2013, Vol. 1, No. 1, pp.52-56. ISSN 2159-5275,

11. Современные средства центровки, балансировки и виброконтроля при монтаже и наладке роторного оборудования. Сборник методических материалов семинара.// Санкт-Петербург: ООО «Балтех». – 2003.– 85 с.,

12. Litvinov D., Priževaitis A., *Defects Detection in gear using direct spectrum analysis of vibration*, International Scientific Journal „Machines. Technologies. Materials", Vol. 9 (2015), Issue 11, pg(s) 34-35, PRINT ISSN 1313-0226,

13. Ļitvinovs, D., Priževaitis, A. *Spectral Analysis of Vibration Application for the Metallurgical Electric Furnace Main Fan Bearings Condition Evaluation.* In: International Scientific Conference "Machines. Technologies. Materials 2020": Proceedings. Year III, Iss.1. Vol.1, Bulgaria, Borovets, 11-14 March, 2020. Sofia: Scientific Technical Union of Mechanical Engineering Industry-4.0, 2020, pp.18-20. ISSN 2535-0021. e-ISSN 2535-003X,

14. Ļitvinovs, D., Priževaitis, A., Geriņš, Ē. *Thermal Growth Influence on V-Belt Transmission.* In: ICBBM 2013: Proceedings of the 9th Baltic-Bulgarian Conference on Bionics and Prosthetics, Biomechanics and Mechanics, Mechatronics and Robotics, Latvia, Rīga, 17-21 June, 2013. Rīga: 2013, pp.119-124. ISBN 978-9934-8409-0-6,

15. https://www.flir.eu/products/tg297/- termocamera FLIR TG297,

16. https://vibrotek.ru/products/sd21/%D0%A1%D0%94-21%20%D1%80%D1%83%D0%BA%D0%BE%D0%B2%D0%BE%D0%B4%D1%81%D1%82%D0%B2%D0%BE%20%D0%BF%D0%BE%20%D1%8D%D0%BA%D1%81%D0%BF%D0%BB%D1%83%D0%B0%D1%82%D0%B0%D1%86%D0%B8%D0%B8.pdf

17. https://www.skf.com/binaries/pub39/Images/0901d1968039ea10-15303RU_TKSA41_tcm_39-227817.pdf,

18. https://www.sterlingsensors.co.uk/pdfs/TGLEA.pdf

ИЗМЕРВАНЕ И ОЦЕНКА НА МАГНИТНИ ПОЛЕТА В ЕЛЕКТРИЧЕСКИ АВТОМОБИЛИ

Магдалена Гарванова[1], Владимир Иванов[2], Иван Гарванов[1], Даниела Борисова[2]
[1]Университет по библиотекознание и информационни технологии, София, България
m.garvanova@unibit.bg, i.garvanov@unibit.bg
[2]Институт по информационни и комуникационни технологии – БАН, София, България
ivanov.vladi@gmail.com, danbor@iit.bas.bg

Резюме: *За решаването на проблема с вредните емисии, емитирани от превозни средства с вътрешно горене като въглероден двуокис, азотни окиси, сажди и др., се предлага използване на електрически автомобили. Тези устройства работят с помощта на електричество, което индуцира „електромагнитно замърсяване“ в или в близост до тях. Въздействието на електромагнитните полета върху живите организми е безспорно, но все още не е напълно ясно доколко е вредно за човека. В електрическите превозни средства пътниците седят много близо до електрическа система, работеща със значителна мощност и в продължение на голям период от време. Това означава, че потребителите са изложени на въздействието на изкуствени магнитни полета. Производителите на електрически автомобили са добре запознати с тези проблеми и предлагат различни технологични решения при проектирането и производството им. В настоящата статия ще бъдат проведени експериментални измервания на магнитните полета, генерирани от електрически автомобил, който работи в различни режими на работа, и ще бъдат дадени препоръки за правилната му експлоатация.*

Ключови думи: *електрически автомобили, електромагнитно излъчване, излагане на магнитно поле*

1. Въведение

Електрическите превозни средства и хибридните електрически превозни средства придобиват широка популярност през последните години. Електрическите автомобили зависят изцяло от електричеството, а хибридните модели частично се захранват с електричество. Електрическите превозни средства притежават много предимства в сравнение с конвенционалните автомобили с вътрешно горене. Двигателите на електрическите автомобили са много бързи и в същото време не замърсяват околната среда с вредни за природата химични вещества. Електрическите превозни средства са особено привлекателни за градски условия, където има голяма нужда от намаляване на вредните въглеродни емисии от автомобилите [1].

Задвижването на електрическите автомобили се осъществява с помощта на електродвигатели, захранвани с електроенергия с висока мощност от порядъка на 5–200 kW, в зависимост от типа превозно средство. Понастоящем повечето електрически превозни средства работят с напрежение под 400 V, което предполага ток от порядъка на стотици ампера. Това води до генериране на магнитни полета (МП) в електрическите автомобили с много високи стойности в сравнение с полетата от електроуредите в бита. Както е известно, магнитните полета затихват в пространството, но разстоянията между генераторите на тези магнитни полета и пътниците в автомобилите са сравнително малки, от порядъка на сантиметри, и полето остава сравнително мощно [2]. Това означава, че в непосредствена близост до пътниците циркулира ток в размер на стотици ампера, генериращ силни магнитни полета. Тези полета могат да имат нежелани ефекти както върху електронните устройства, така и върху пътниците, намиращи се в превозното средство или в близост до него.

Влиянието на електромагнитните полета (ЕМП) върху електронните устройства е добре известно в практиката и проблемите от електромагнитните смущения се решават чрез електромагнитната съвместимост на електроните устройства в съответната електромагнитна среда. Въздействието на генерираното електромагнитно излъчване върху човека предизвиква ефекти, принадлежащи към областта на биоелектромагнетизма [3]. Електромагнитната радиация обикновено се класифицира на йонизиращо и нейонизиращо лъчение в зависимост от способността й да йонизира атомите. Този ефект е възможен само ако радиацията носи голямо количество енергия [4]. Границата между нейонизиращо и йонизиращо електромагнитно поле се намира в ултравиолетовия обхват на електромагнитния спектър. Всичко казано дотук означава, че електромагнитната радиация, излъчвана от електрическите превозни средства, е нейонизираща [5].

Експозицията на електромагнитните полета може да предизвика различни ефекти в зависимост от честотата на електромагнитното поле. Това е причината в Директивата за електромагнитните полета на Европейския съюз да се формулират различни гранични стойности на експозиция за: нетоплинни ефекти, предизвикани за ниски честоти (0–10 MHz) и топлинни ефекти, получавани при високи честоти (100 kHz – 300 GHz) [6]. Видно е, че двата обхвата се припокриват. Следователно при средния честотен обхват (100 kHz –10 MHz) може да възникнат както топлинни, така и нетоплинни ефекти, и затова трябва да се имат предвид и двете гранични стойности на експозиция. При прекомерни облъчвания с нискочестотни електромагнитни полета могат да се предизвикат различни въздействия върху тъканите, нервната система и мускулите на човек, а при високочестотни полета се получава нагряване на тъканите. Получените ефекти от облъчването се разделят на краткосрочни и дългосрочни. Дългосрочните ефекти са много трудни за регистриране, тъй като те отнемат десетилетия да се появят и оценят. Краткосрочните нейонизиращи ефекти са известни и добре проучени. Тези ефекти се появяват веднага щом експозицията започне, и изчезват, когато тя спре или малко след това. Тези биологични ефекти се получават от силни електромагнитни полета с много ниска честота (до няколкостотин kHz) и/или силни средночестотни ЕМП (радиовълни и микровълни до 300 GHz) [7], [8]. Тези ефекти се класифицират в две основни групи: електростимулиращи ефекти и термични ефекти. Топлинните ефекти обикновено са незначителни за честоти на полето под 100 kHz, но стават все по-значими с нарастването на честотата.

Както бе споменато по-горе, електрическите автомобили се състоят от електрически машини с висока мощност, инвертори, захранващи кабели с високо напрежение и батерии, работещи в ниския честотен диапазон от 0–100 kHz. Следователно, експозицията на магнитно поле е неизбежна. Експозицията на магнитни полета с ниска честота се разглежда от Международната агенция за изследване на рака (IARC) като вероятно канцерогенна за хората и е тясно свързана с появата на левкемия [9]. Международната комисия за защита от нейонизиращи лъчения (ICNIRP) предлага насоки за установяване на гранични стойности за безопасност при експозиция на магнитни полета с ниска честота [10].

Настоящата статия има за *цел* да измери и анализира магнитно поле в електрически превозни средства при различни

режими на работа и посочи евентуални препоръки за правилното експлоатиране на електрическите автомобили.

2. Електрически и магнитни полета

Електрически и магнитни полета съществуват навсякъде, където протича електрически ток – в електропроводи и кабели, жилищно окабеляване и електрически уреди. Електрическите полета възникват от електрически заряди, измерват се във волта на метър (V/m) и са екранирани от общи материали като дърво и метал. Магнитните полета възникват от движението на електрически заряди (т.е. ток) и се изразяват в тесла (T). Тези полета не са защитени от повечето разпространени материали и лесно преминават през тях. И двата вида полета са най-силни близо до източника и намаляват при увеличаване на разстоянието [11].

3. Уреди за измерване на ЕМП

Измерването на електромагнитните замърсявания, генерирани от електрическите автомобили, работещи при различни условия и режими на работа, е възможно да се установи с измервателни уреди. В нашия случай е използван уред ME3830B Analyser в честотния диапазон от 16 Hz до 100 kHz на немската фирма Gigaherz (фиг. 1.). Измервателният диапазон за плътността на магнитния поток е в диапазона 1–1999 ηT, а за силата на електрическото поле е в диапазона 1–1999 V/m [12].

Фиг. 1. Измервателни уреди ME3830B Analyser

Уредът е честотно компенсиран, т.е. нито един честотен диапазон не е надценен, подценен или игнориран. Измервателният уред установява магнитната индукция и интензивността на магнитното поле, като показва стойността на „сумарния сигнал“ в зададения честотен диапазон. Нормите на електромагнитните полета за спални помещения са показани на фиг. 2. От нея се вижда, че нива над 500 ηT са екстремно високи и биха оказали неблагоприятни ефекти за здравето на човек. Тези норми са препоръчителни за помещения за сън, докато в работни помещения се допускат и по-високи стойности на магнитното поле.

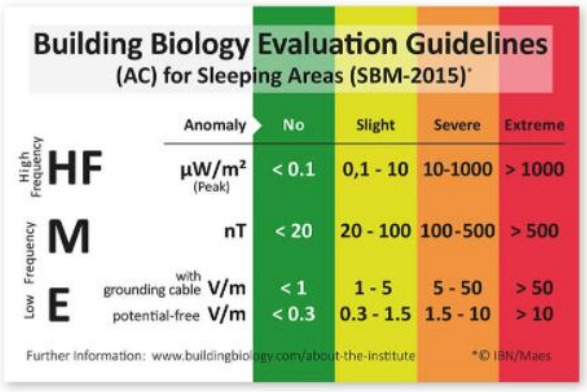

Фиг. 2. Нива на магнитния поток в помещения за сън

Международната комисия за защита от нейонизиращи лъчения (ICNIRP) предлага да се използва силата на индуцирано електрическо поле като основно ограничение, докато силата на магнитното поле (H) и плътността на магнитния поток (B) се задават като референтни нива при оценката на експозицията [9]. Референтните нива на полето са получени от основните ограничения с помощта на модели, които представляват стоящ човек, изложен на равномерно разпределение на полето в открита среда. Това е много различно от средата в превозното средство, където пътниците са седнали и са в непосредствена близост до източниците на полето. Референтните нива на полето са пространствено осреднени стойности по цялото тяло на експонирания индивид, но с уговорката, че не се превишават основните ограничения за локална експозиция [13]. Референтните нива на плътността на магнитния поток обикновено намаляват с увеличаване на честотата (за честоти 8–25 Hz се получават стойности 0.625–0.2 mT, за честоти 25–400 Hz се получава 0.2 mT, за честоти 400–3000 Hz МП е 0.2–0.0267 mT). Тези стойности се базират главно на краткосрочни експозиции. В близост до определени електроуреди стойностите на магнитното поле могат да бъдат от порядъка на няколкостотин µT. Под електропроводите магнитните полета могат да бъдат около 20 µT, а електрическите полета могат да бъдат няколко хиляди волта на метър. Въпреки това средните магнитни полета в домовете са много по-ниски – около 0.07 µT в Европа и 0.11 µT в Северна Америка. В [5] се посочва, че годишната експозиция на МП с честоти 50 и 60 Hz и нива на МП над 0.3–0.4 µT може да доведе до повишен риск от детска левкемия.

4. Описание на проблема

Специфичните характеристики на електрическите автомобили като: високи нива на тока, водещи до генерирането на мощни магнитни полета, много малките разстояния между оборудването на автомобила и пътниците, в съчетание с дълготрайната експозиция на пътниците, е от изключително значение за здравето на хората. Както бе споменато по-горе, нивата на мощност в електрическите превозни средства са от порядъка на десетки и стотици kW, докато нивата на напрежение рядко надвишават 600 V. Това означава, че текущите нива на тока обикновено достигат стотици ампера. В практиката не се срещат много ситуации, в които хората да са на сантиметри до проводници или устройства, работещи с толкова високи стойности на тока. Настоящата тенденция при производството на електрически автомобили се състои в намаляване на нивата на напрежение, доколкото е възможно, което предполага дори по-високи стойности на тока. Разстоянията между пътниците и електрическите компоненти на електрическите автомобили (батерия, кабели, електрически двигател и др.) е от порядъка от 0.2 до 3.0 метра, което е предпоставка за наличие на мощни магнитни полета.

5. Резултати

С помощта на уреда ME3830B Analyser са проведени измервания на МП, генерирани от електрически автомобил. Марката и видът на автомобила няма да бъдат споменати с цел да се защити търговският интерес на производителя. Измерванията са проведени в различни режими на работа и на различни места в електрическия автомобил. Интензитетът на магнитното поле, измерено в областта на водача, мястото до водача и на задната седалка са показани в табл. 1. Измерванията са проведени при различни режими на работа на автомобила. При зареждане на автомобила и в режим на контакт нивата на МП са много ниски. При работещ на място автомобил се забелязва покачване на стойностите на МП до 60–80 ηT за предните седалки и около 30 ηT за задната седалка. В режим на зареждане на електрическия автомобил интензитетът на магнитното поле около зарядна станция е 600 ηT, което е много силно магнитно поле.

Таблица 1. Стойности на магнитни полета, генерирани от електрически автомобил (на място)

Режим на работа	Място на измерване		
	Място на шофьора	Място до шофьора	Задна седалка
	Магнитно поле [ηT]		
Зареждане	14	17	22
На контакт	14	17	9
Работещ на място	70	80	30

При многобройните измервания се установи, че нивата на МП са най-високи в областта между първите две седалки и за тази цел бе взето решение измерванията да продължат на мястото, показано на фиг. 2.

Фиг. 2. Измерване на магнитно поле в електрически автомобил

Нивата на МП при шофиране в градски условия се променят непрекъснато в границите около 100–200 ηT. При тръгване и спиране нивата са сравнително високи от порядъка на 170–230 ηT. При спрял автомобил на светофар нивото на МП е от порядъка на 165–200 ηT.

При движение на електрическия автомобил по магистрала със скорости 50, 80 и 100 km/h се получават нива на МП от порядъка на 100–300 ηT. Резултатите от измерването са показани в табл. 2.

Таблица 2. Стойности на магнитни полета, генерирани от електрически автомобил, който се движи по магистрала с постоянна скорост

Скорост на движение на автомобила	Място на измерване		
	Място на шофьора	Място до шофьора	Задна седалка
	Магнитно поле [ηT]		
50 км/h	100	90	60
80 км/h	230	230	220
100 км/h	260	280	290

От таблица 2 се вижда, че при по-ниски скорости на движение на автомобила се получават по-ниски стойности на МП. С увеличаване на скоростта на движение нивото на МП се увеличава. Резултатите са получени след осредняване на повече от 30 измервания в дадения режим на работа на автомобила и за трите места на измерване.

6. Изводи

От получените резултати се вижда, че в купето на автомобил, работещ в различни режими на работа, нивата на МП са в норма. Това е постигнато благодарение на инженерните решения, използвани при производството на електрическия автомобил. Прави впечатление, че при ускорение и спиране на автомобила се забелязват сравнително високи стойности на МП, но това е за много кратки периоди от време. По-притеснителен е фактът за продължителна експозиция и сравнително високи стойности на МП при високи скорости на движение на електрическия автомобил. Върху силата на МП, генерирано в купето на автомобила, оказват влияние мощността, теглото, ускорението и скоростта на движение на автомобила. При зареждане на електрическия автомобил е препоръчително хората да са извън автомобила и на колкото се може по-голямо разстояние от него. Трите фактора, влияещи най-силно върху здравето на човека, са: високи нива на електромагнитните полета, малки разстояния между генераторите на тези полета и пътниците, както и сравнително продължителната експозиция.

Благодарности

Статията е реализирана по проект „Синтез на динамичен модел за оценка на психологически и физически въздействия от прекомерна употреба на смарт технологии”, КП-06-Н 32/4/07.12.2019, финансиран от ФНИ–МОН.

Използвана литература

1. Yang, L., Lu, M., Lin, J., Li, C., Zhang, C., Lai, Z., & Wu, T. (2019). Long-term monitoring of extremely low frequency magnetic fields in electric vehicles. International Journal of Environmental Research and Public Health, 16 (19), 3765, doi: https://doi.org/10.3390/ijerph16193765.
2. Frieske, B., Kloetzke, M., & Mauser. F. (2013). Trends in vehicle concept and key technology development for hybrid and battery electric vehicles. World Electric Vehicle Symposium and Exhibition (EVS27), Barcelona (Spain).

3. Garvanova, M., Garvanov, I., & Borissova, D. (2020). The influence of electromagnetic fields on human brain. Proceedings of the XXI International Symposium on Electrical Apparatus and Technologies (SIELA 2020), 3-6 June 2020, Bourgas, Bulgaria, pp. 111-114, doi: 10.1109/SIELA49118.2020.9167099.
4. Garvanova, M., Garvanov, I., Trapkova, D., Nedelchev, K., Borissova, D., Dimitrov, G., Kerimbaev, N., Tkach, G., & Zeinullayeva, I. (2021). Effects of mobile phone electromagnetic fields on human brain activity. Proceedings of the Tenth International Conference on Telecommunications and Remote Sensing – ICTRS'21, 15-16 November 2021, Sofia, Bulgaria. ACM International Conference Proceeding Series, pp. 31-36. New York: ACM, doi: https://doi.org/10.1145/3495535.3495541
5. Garvanova, M., Garvanov, I., & Kashukeev, I. (2020). Business processes and the safety of stakeholders: Considering the electromagnetic pollution. Business Modeling and Software Design. BMSD 2020. Lecture Notes in Business Information Processing, vol. 391, pp. 386-393. Springer Nature Switzerland AG, doi: https://doi.org/10.1007/978-3-030-52306-0_28.
6. Директива 2013/35/ЕС на Европейския парламент и на Съвета от 26 юни 2013 г. относно минималните изисквания за здраве и безопасност, свързани с експозицията на работниците на рискове, дължащи се на физически агенти (електромагнитни полета) (Двадесета специална директива по смисъла на член 16, параграф 1 от Директива 89/391/ЕИО) и за отмяна на Директива 2004/40/ЕО. Достъп: https://eur-lex.europa.eu/legal-content/BG/TXT/?uri=celex%3A32013L0035.
7. Garvanov, I., & Garvanova, M. (2021). New approach for smart cities transport development based on the Internet of Things concept. Proceedings of the 17th Conference on Electrical Machines, Drives and Power Systems ELMA 2021, pp. 1-6. IEEE, doi: 10.1109/ELMA52514.2021.9503084.
8. Garvanov, I., Garvanova, M., Borissova, D., Vasovic, B., & Kanev, D. (2021). Towards IoT-based transport development in smart cities: Safety and security aspects. Business Modeling and Software Design. BMSD 2021. Lecture Notes in Business Information Processing, vol. 422, pp. 392-398. Springer, Cham, doi: https://doi.org/10.1007/978-3-030-79976-2_27.
9. World Health Organization (WHO). (2007). Electromagnetic fields and public health: Exposure to extremely low frequency fields. Available at: http://www.who.int/peh-emf/publications/facts/fs322/en/.
10. International Commission on Non-Ionizing Radiation Protection (ICNIRP). (2010). Guidelines for limiting exposure to time-varying electric and magnetic fields (1 Hz to 100 kHz). Health Physics, 99 (6), pp. 818-836. Available at: https://www.icnirp.org/cms/upload/publications/ICNIRPLFgdl.pdf.
11. Гарванова, М., Станева, К., Гарванов, И. (2020). Вторично използване на безжичните технологии. Proceedings of the XVII International Scientific Congress "Machines. Technologies. Materials" – Winter Session, 11-14.03.2020, Borovets, Bulgaria, vol. 1, issue 1 (16), pp. 85-88.
12. Гарванова, М., Борисова, Д., Гарванова, Г. (2021). Измерване на електромагнитните полета в работната среда. Proceedings of the IX International Scientific Conference "Technics. Technology. Education. Safety" – TTES 2021, 7-10 June 2021, Borovets, Bulgaria, vol. 1, issue 1 (11), pp. 55-57.
13. Item Media. (2014). Assessing low frequency magnetic field exposure in hybrid and electric vehicles. Available at: https://interferencetechnology.com/assessing-low-frequency-magnetic-field-exposure-in-hybrid-and-electric-vehicles/.

On pressure drop and airflow directivity ability of air vents on automobile cabinets

Kaan Mumcuoglu[1], Yesim Yazici Beyhan[1], Emre Bingol[1], Hakan Serhad Soyhan[2 3]
[1]Ecoplas Automotive, R&D Division, Kocaeli, Turkey
[2]Sakarya University, Department of Mechanical Engineering, Sakarya, Turkey
[3]Team-San Ltd. Sti., Esentepe Campus, Sakarya University, Sakarya, Turkey
kmumcuoglu@ecoplas.com.tr, yyazici@ecoplas.com.tr, ebingol@ecoplas.com.tr, hsoyhan@sakarya.edu.tr

Abstract: *In this study, airflow directivity ability and pressure drop values of air vents where placed on the front console of automobile cabinet were investigated with computational fluid dynamics analysis. One of the aims of these studies is the airflow performance impact of design changes on air vents. Therefore, parametric studies were conducted with diffuser structures having 3, 4, 5 blades and 16mm, 20mm, 24mm blade width and 3mm, 4mm blade thickness. These variations were created to determine the effects of the number of blades, blade width and blade thickness on air flow and pressure drop performances of automobile diffusers. The impact of automobile diffusers on thermal comfort inside of the cabinet has been detected—correlations which give pressure drop and airflow angle were obtained according to analysis results. Thus, equations giving airflow direction angle and pressure drop within specific parameters were obtained without computational fluid dynamics analysis. In this way, a faster approach was provided to reach related performance values on automobile diffuser design.*
Keywords*: COMPUTATIONAL FLUID DYNAMICS, DIFFUSER, AUTOMOBILE, AIR FLOW, BLADE, PRESSURE*

1. Introduction

Nowadays, Diffuser types are used on thermal conditioning systems of automobile cabinet as circular, conventional, split types. Visuality, structural strength, soundless working, low-pressure drop and airflow directivity of automobile diffusers are important performance indicator parameters. Airflow directing to desired angle significantly affects thermal comfort inside of automobile cabinet. Diffusers having high-pressure drop value blocks to the desired airflow also influence the considerable efficiency of air conditioning. Therefore, Diffusers with high airflow directivity and low-pressure drop are needed for increasing the thermal comfort of passengers inside the automobile. One of this study aims is examining to design of attributions for diffusers having high airflow directivity ability and low-pressure drop value. Many studies are made related subject in the literature.

Somnath and Mayur investigated thermal comfort and airflow distribution in automobile cabinets and detected that directed airflow to passengers significantly affected thermal cooling load in their study [1]. Myoung Su Oh et al. studied energy recovery on automobile compartments and investigated automobile diffuser locating effects over the thermal comfort [2]. Air directing ability is critically important on diffusers for obtaining airflow distribution in automobile cabinets and increasing the thermal comfort of passengers in a cabinet. Zhang et al. analyzed airflow path and temperature in automobile cabins for with and without passenger conditions [3-4] experimentally. Nissan Hagino and Hara examined to affecting parameters of air temperature and airflow path for the purpose of understanding the thermal sensations of passengers [5]. Many studies in the literature have been seen that many investigations have been made about airflow distribution airflow direction for detection of thermal comfort. In this study, the effects of diffuser blade dimensions are examined in detail by computational fluid dynamics analysis.

2. Modelling

Automobile diffusers are produced with different dimensions, blade width, blade thickness and blade quantity by companies. Figure 1 shows a sample automobile diffuser. Analyzed parameters with computational fluid mechanics are shown in Figure 2.

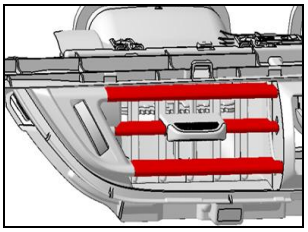

Fig. 1 *Automobile diffuser sample*

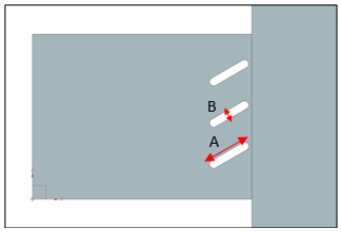

Fig. 2 *Geometric parameters*

A parameter shows blade width, B parameter shows blade thickness. Also, the effect of different blade quantities having 3, 4, and 5 blades on diffuser performance was investigated. The angle of blades with the horizontal plane is kept constant 30° for each case.

3. Governing Equations

Mathematical equations should be exhibited for solving problems and understanding physical principles. Boundary conditions and eliminate parameters must be given according to the physical structure of modeling for numerical solving of differential equations. Continuity and momentum equations used in this study are given below. Since the conditions examined in the study are turbulent flow, the RANS form of the continuity and momentum equations was used. Diffuser structure modeled with mesh structure in computational fluid mechanics was solved with the below equations.

Continuity equation indicates mass conservation during flow motion. In this study, density-dependent to the derivative of time can be eliminated due to steady-state flow. In addition, since the density is considered constant, it can be taken out from the local derivative, and in this case, the equation will be as follows.

$$\frac{\partial \bar{u}}{\partial x}+\frac{\partial \bar{v}}{\partial y}+\frac{\partial \bar{w}}{\partial z}=0$$

The components of X, Y, and Z direction of momentum equation in the Cartesian coordinate system are as follows. In this study, the flow is considered a steady-state. In addition, since the density is considered constant, it can be taken out from the local derivative and in this case, the equation will be as follows.

The x-direction momentum equation

$$\bar{u}\frac{\partial \bar{u}}{\partial x}+\bar{v}\frac{\partial \bar{u}}{\partial y}+\bar{w}\frac{\partial \bar{u}}{\partial z}+\frac{1}{\rho}\frac{\partial \bar{P}}{\partial x}=$$

$$\left(\frac{\partial^2 \bar{u}}{\partial x^2}+\frac{\partial^2 \bar{u}}{\partial y^2}+\frac{\partial^2 \bar{u}}{\partial z^2}\right)-\frac{\partial \overline{(u')^2}}{\partial x}-\frac{\partial \overline{(u'v')}}{\partial y}-\frac{\partial \overline{(u'w')}}{\partial z}$$

The y-direction momentum equation

$$\bar{u}\frac{\partial \bar{v}}{\partial x}+\bar{v}\frac{\partial \bar{v}}{\partial y}+\bar{w}\frac{\partial \bar{v}}{\partial z}+\frac{1}{\rho}\frac{\partial \bar{P}}{\partial y}=$$

$$\nu\left(\frac{\partial^2 \bar{v}}{\partial x^2}+\frac{\partial^2 \bar{v}}{\partial y^2}+\frac{\partial^2 v}{\partial z^2}\right)-\frac{\partial \overline{(u'v')}}{\partial x}-\frac{\partial \overline{(v')^2}}{\partial y}-\frac{\partial \overline{(v'w')}}{\partial z}$$

The z-direction momentum equation

$$\bar{u}\frac{\partial \bar{w}}{\partial x}+\bar{v}\frac{\partial \bar{w}}{\partial y}+\bar{w}\frac{\partial \bar{w}}{\partial z}+\frac{1}{\rho}\frac{\partial \bar{P}}{\partial w}=$$

$$v\left(\frac{\partial^2 \bar{w}}{\partial x^2}+\frac{\partial^2 \bar{w}}{\partial y^2}+\frac{\partial^2 w}{\partial z^2}\right)-\frac{\partial(\overline{u'w'})}{\partial x}-\frac{\partial(\overline{v'w'})}{\partial y}-\frac{\partial(\overline{w'})^2}{\partial z}+g_z$$

4. Numerical Results

In this study, Pressure drop and airflow direction angle values were detected by using 3, 4 and 5 blade quantities with 3 mm blade thickness. Computational fluid mechanics result of pressure and velocity contours were shown in figures as below.

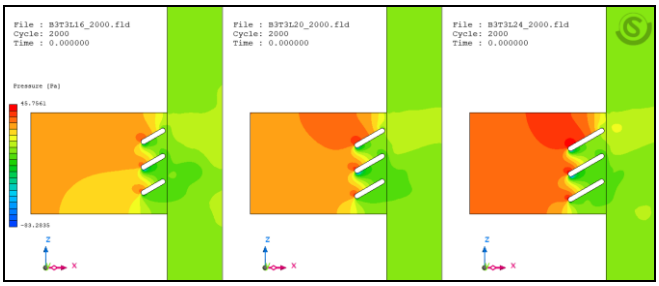

Fig. 3 *Pressure drop contour of 3 blades and 3 mm blade thickness (16 mm, 20 mm, 24 mm, blade width, respectively)*

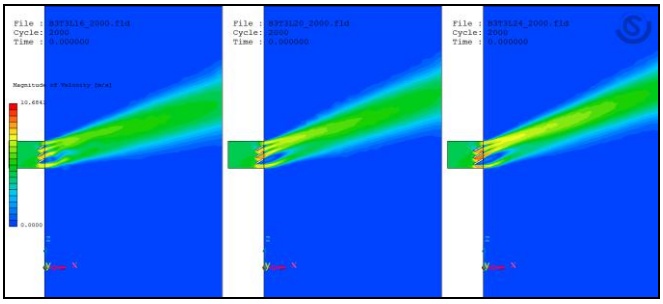

Fig. 4 *Velocity contour of 3 blades and 3 mm blade thickness (16 mm, 20 mm, 24 mm, blade width, respectively)*

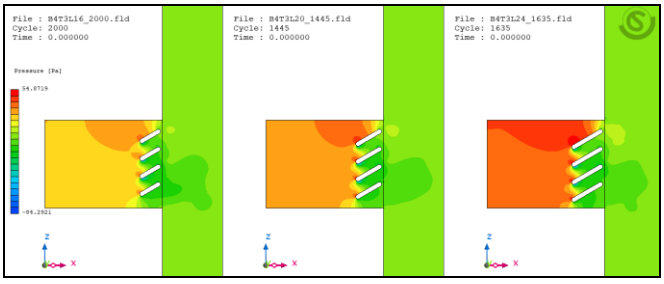

Fig. 5 *Pressure drop contour of 4 blades and 3 mm blade thickness (16 mm, 20 mm, 24 mm, blade width, respectively)*

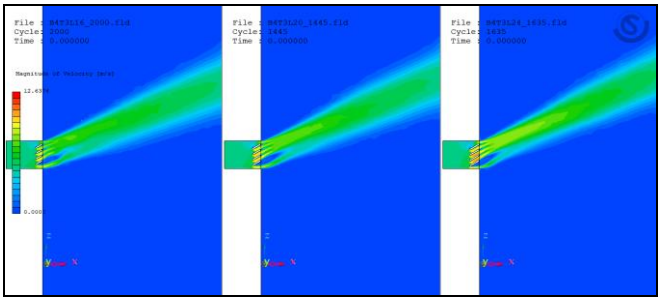

Fig. 6 *Velocity contour of 4 blades and 3 mm blade thickness (16 mm, 20 mm, 24 mm, blade width, respectively*)

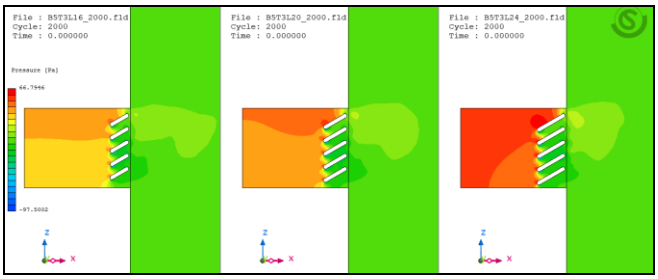

Fig. 7 *Pressure drop contour of 5 blades and 3 mm blade thickness (16 mm, 20 mm, 24 mm, blade width, respectively)*

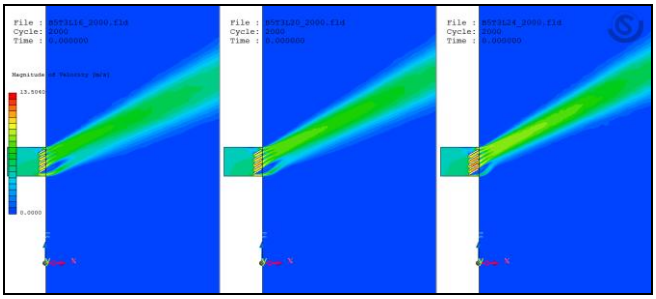

Fig. 8 *Velocity contour of 5 blades and 3 mm blade thickness (16 mm, 20 mm, 24 mm, blade width, respectively)*

The effect of blade thickness on airflow directing ability and pressure drop performances in automobile diffusers has been investigated, and contours that are the output of computational fluid mechanics analysis are given in the figures below.

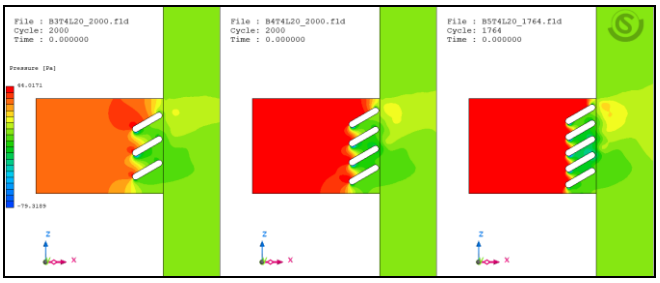

Fig. 9 *Pressure drop contour of 3, 4, 5 blades and 4 mm blade thickness (20 mm blade width)*

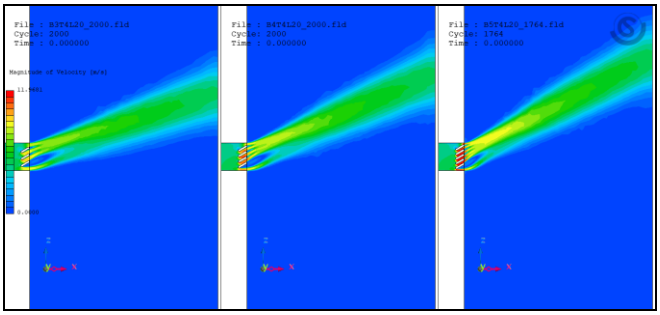

Fig. 10 *Velocity contour of 3, 4, 5 blades and 4 mm blade thickness (20 mm blade width)*

Pressure drop and airflow direction angle obtained from computational fluid dynamics analysis were listed as below Table 1 according to blade quantity, blade thickness, blade width.

Table 1: *Numerical pressure drop and airflow angle values for different blade thickness, quantity, and width*

Blade Quantity	Blade Thickness	Blade Width	Pressure Drop (Pa)	Air Flow Angle (°)
3	3 mm	16 mm	20,7 Pa	16°
3	3 mm	20 mm	25,5 Pa	19°
3	3 mm	24 mm	31,3 Pa	21°
4	3 mm	16 mm	26,4 Pa	21°
4	3 mm	20 mm	32,5 Pa	23°
4	3 mm	24 mm	40,2 Pa	24°
5	3 mm	16 mm	33,9 Pa	25°
5	3 mm	20 mm	41,6 Pa	27°
5	3 mm	24 mm	52,1 Pa	28°
3	4 mm	20 mm	29,7 Pa	19°
4	4 mm	20 mm	41,5 Pa	23°
5	4 mm	20 mm	59,2 Pa	27°

Correlations giving pressure drop and airflow direction were created according to obtained results. Thus, equations giving pressure drop and airflow angle-dependent to blade quantity and blade width were obtained for automobile diffusers.

$$\Delta \boldsymbol{P} = (0{,}3046x^2 + 0{,}186x + 5{,}76).\, e^{(0{,}001x + 0{,}0487)y}$$

$$\Delta P = Pressure\ drop \quad x = Blade\ quantity \quad y = Blade\ width$$

$$3 \leq x \leq 5 \quad 16 \leq y \leq 24$$

$$\boldsymbol{F°} = (2{,}461x^2 - 22{,}149x + 56{,}67).\ln(y) + (-7{,}3303x^2 + 69{,}972x - 162{,}17)$$

$$F° = Air\ flow\ angle \quad x = Blade\ quantity \quad y = Blade\ width$$

$$3 \leq x \leq 5 \quad 16 \leq y \leq 24$$

5. Conclusion

In this paper, automobile diffuser airflow directivity and pressure drop performances are presented. Context of this study results, some approaches were obtained for automobile diffuser performance improvement. According to the computational fluid dynamics analysis, it has been observed that as the blade width is increased, the airflow directing ability also increases, but this situation increases the pressure drop. Another of the findings obtained in the studies is that the airflow directing ability of automobile diffusers increases when the number of blades is increased, but in this case, pressure drop also increases and it affects diffuser performance in a negative way. When these two situations are compared, it has been determined that increasing the number of blades in automobile diffusers increases the pressure drop less than increasing the blade width and affects the airflow directing ability more positively. Increasing the number of blades is more efficient than increasing the blade width in order to achieve the ability to direct airflow during the design of automobile diffusers. Increasing the fin thickness in the diffusers does not affect the airflow directing ability and increases pressure drop and negatively affects diffuser performance was detected on studies. In line with the studies, two correlations giving the angle of directing the airflow and the pressure drop were obtained. Thus, performance values can be obtained according to the desired number of blades, and blade width were determined without the need for computational fluid dynamics analysis.

6. References

1. S. Somnath, S. Mayur, Numerical simulation and validation of cabin aiming and cool-down of a passenger car. *SAE Technical Paper Series*, (2016)

2. M. Oh, J. Ahn, D. Kim, D. Jang, Y. Kim, Thermal comfort and energy saving in a vehicle compartment using a localized air-conditioning system, *Appl. Energy*, **133** (2014)

3. H. Zhang, L. Dai, G. Xu, Y. Li, W. Chen, W.Q. Tao, Studies of air flow and temperature field inside a passenger compartment for improving thermal comfort and saving energy. Part I: test/numerical model and validation, *Appl. Therm. Eng*., **29** (2009)

4. H. Zhang, L. Dai, G. Xu, Y. Li, W. Chen, W.Q. Tao, Studies of air flow and temperature field inside a passenger compartment for improving thermal comfort and saving energy. Part II: simulation results and discussion, *Appl. Therm. Eng.*, **29** (2009)

5. M. Hagino, J. Hara, Development of a method for predicting comfortable airflow in the passenger compartment, *Worldwide Passenger Car Conference and Exposition*, (1992)

Techno-Economic aspects of small PV plants up to 2MWp in Albania.

Ilirian Konomi, [b]Jonida Teta, [b]Lorenc Malka, [a]Ermonela Rrapaj,
[a]Department of Hydraulics & Hydrotechnics, Faculty of Civil Engineering, Polytechnic University of Tirana, Albania
[b]Department of Production and Management, Faculty of Mechanical Engineering, Polytechnic University of Tirana, Albania
[c]Department of Energy, Faculty of Mechanical Engineering, Polytechnic University of Tirana, Albania
ikonomi64@gmail.com

Abstract: *The economic benefits have been also addressed, evaluating the energy production and distribution throughout the year and cost of electricity generation for small PV plants up to 2MW. Renewable energy sources, including solar, wind, hydropower, biofuels and other renewable sources that may be developed in the future are the main focus of the energy transition ensuring a safe step on the path to an intensity system. low energy, with minimal impact of greenhouse gases (GHG) and with a minimal cost for end users. Over the last two years PV systems have attracted a large amount of monetary and investment globally, especially in EU countries. The responsible ministry (MEI) and its subordinate institutions have drafted and approved the "National Strategy of Energy 2018-2030 ", consisting of 6 possible scenarios of energy transition towards a sustainable, reliable and diversified energy system. The national strategy seeks to meet its objectives based on Renewable Energy Sources (RES) and Energy Efficiency (EE). Hence, the economic aspects and identification of the most influenced parameters is identified and highlighted.*
Keywords*: PVWP, PVsyst, RES, Irrigation*

1. Introduction

PV power generation is very essential in today's society development. As the cost of wind power technologies are falling lots of wind power systems have been developed and installed around the globe. Electricity costs from renewables have fallen sharply over the past decade, driven by improving technologies, economies of scale, increasingly competitive supply chains and growing developer experience [1]. Effects of environmental, economic, social, political and technical factors have led to the rapid deployment of various sources of renewable energy-based power generation.
Increased demand for energy, indiscriminate use of fossil fuels/ energy reserves coupled with environmental pollution problems around the globe, have increased the demand for large-scale commissioning of energy production capacities based on solar energy. On the other hand, the installation of photovoltaic systems is associated with high demand for land area. Consequently, in order to conserve valuable terrestrial resources, it may be very promising to install photovoltaic systems on the salty soil found in the region of Divjaka. This study presents the overall economic-financial analysis, profitability and limitations of the photovoltaic plant with a capacity of 2MW built in the village of Tërbuf, part of Divjaka Municipality. The development of renewable energy sources as a means of meeting the global energy demand and simultaneously replacing fossil fuels as one of the key drivers of climate change has become one of the major societal challenges of our time.

2. *Energy planning and the role of RES to the road map of diversification of energy system.*

First of all, a comprehensive long term energy system analysis is aimed at ensuring a good energy-related policy and to enable the right investment decision. Planning increases the nation's capacity to anticipate and respond to changes and opportunities arising in the sector. Like other instances of public energy policy, it has been informed mainly by recourse to analytical models. Energy modelling is key in the energy sector, it happens to be data intensive which is a challenge for several countries. Hence in this work RETScreen Expert tool for precise economic simulation for the case of Terbuf PV plant is chosen.

3. Materials and Methods

Actually, there are several models available for conducting a set of analysis including environmental impact and benefits. RETScreen Expert is a clean-energy awareness, decision-support and capacity-building tool [2].

Figure 1: *RETScreen Expert tool overview and conceptualization [2].*

This model helps us as energy planers in national level to determine the annual reduction in the emission of greenhouse gases stemming from using the proposed technology in place of the base case technology. The model uses a computerized system with integrated mathematical algorithms and top to bottom approach which has been developed to overcome the barriers to clean energy technology implementation at the preliminary feasibility stage. It provides a cost analysis, GHG emission reduction analysis, financial summary, sensitivity analysis, provides a low-cost preliminary assessment of RES projects with a small set of a detailed information. Methodology 2 as the more suitable to perform the techno-economic analysis is chosen [2-3].
One of the primary benefits of using the RETScreen software is that it facilitates the project evaluation process for decision-makers.The Financial Analysis worksheet, with its financial parameters input items (e.g. discount rate, debt ratio, etc.), and its calculated financial viability output items (e.g. IRR, simple payback, NPV, etc.), allows the project decision-maker to consider various financial parameters with relative ease.

4. Economic Analysis Methods

Economic analysis can be conducting using neither "**Absolute analysis"** by checking if the costs are higher or lower than the benefits? or "**Relative analysis"** especially for RES projects such defining the rank of the proposed wind farm in terms of costs and benefits.

- ***Cost-benefit analysis:*** A time period is chosen and the sum of all costs and benefits in that period is determined. The net benefit is determined by subtracting total benefits and total cost in that time period.

$$\text{Total Benefit}=\sum(benefits)-\sum(costs) \quad (1)$$

- ***Benefit to cost ratio (BCR):*** A time period is chosen then the sum of all costs and benefits in that period is determined. The ratio of benefit to cost gives the benefit to cost ratio.

$$\text{BCR}=\frac{\sum(benefits)}{\sum(costs)} \quad (2)$$

- **Simple payback period (SPB):** This is one of the most common ways of finding the economic value of a wind energy project. Payback considers the initial investment costs and the resulting annual cash flow. The payback time (period) is the length of time needed before an investment makes enough to recoup the initial investment.

$$\text{SPS}=\frac{\sum(\text{investment costs})}{(\text{yearly benefits}-\text{yearly cost})} \quad (3)$$

However, the payback does not account for savings after the initial investment is paid back from the profits (cash flow) generated by the investment (project). This method is a "first cut" analysis to evaluate the viability of investment. It does not include anything about the longevity of the system.

- ***Initial rate of return:*** This is the opposite of simple payback period. The value makes the investment look too good.

$$\text{Initial rate of return}=\frac{(\text{yearly benefits}-\text{yearly cost})}{\sum(\text{investment cost})}*100\% \quad (4)$$

This initial rate of return acts as a minimum threshold indicator for the investment. If the internal rate of return is below this minimum threshold there is no need to proceed with the investment.

- **Levelized cost of energy (LCOE):** All the costs are added during a selected time period which is divided by units of energy. A net present value (NPV) calculation is performed and solved in such a way that for the value of the LCOE chosen, the project's NPV becomes zero. This means that the LCOE is the minimum price at which energy must be sold for an energy project to break even.

$$\text{LCOE}=\frac{\sum costs/\text{no. years}}{annual\ yield\,(\text{kWh})} \quad (5)$$

- **Cash flow analysis:** One of the most flexible and powerful way to analyze an energy investment is the cash-flow analysis. This technique easily accounts for complicating factors such as fuel escalation, tax-deductible interest, depreciation, periodic maintenance costs, and disposal or salvage value of the equipment at the end of its lifetime. In a cash flow analysis, rather than using increasingly complex formulas to characterize these factors, the results are computed numerically using a spreadsheet. Each row of the resulting table corresponds to one year of operation, and each column accounts for a contributing factor. Simple formulas in each cell of the table enable detailed information to be computed for each year along with very useful summations. Cash flow is always positive.

$$\sum cashflow_n=\sum benefits_n-\sum costs_n \quad (6)$$

where ***n*** is the number of years of operation from the start system operation.

- **Discounted cash flow (DCF)**: DCF analysis uses future free cash flow projec- tions and discounts them to arrive at a present value, which is used to evaluatethe potential for investment. If the value arrived through DCF analysis ishigher than the current cost of the investment, the opportunity may be a goodone. The purpose of DCF analysis is to estimate the money one would receive from an investment and to adjust for the time value of money.
-

$$Discount\ cash\ flow_n=\frac{\sum benefits_n-\sum costs_n}{(1+r)^n} \quad (7)$$

r=the discount rate represents the interest rate used in calculating the present value of future cash flows and n = the years from the system starts operation. The present worth factor in the above equation is given $1/(1+r)^n$. The value that is chosen for **r** shows that "weigh" the decision towards one option or another, so the basis for choosing the discount rate value must clearly be carefully evaluated. The discount rate depends on the cost of capital, including the balance between debt-financing and equity-financing, and an assessment of the financial risk must be applied.

- **Net present value (NPV):** NPV compares the value of a dollar today to the value of that same dollar in the future, taking inflation and returns into account. If the NPV of a prospective project is positive, it should be accepted. However, if NPV is negative, the project should probably be rejected because cash flows will also be negative. To calculate NPV; choose the time period for the project and sum all the discounted cash flows in that time period.

$$Discount\ cash\ flow_n=\frac{\sum benefits_n-\sum costs_n}{(1+\text{i})^n}=NPV \quad (8)$$

- **Internal rate of return (IRR)**: This is perhaps the most persuasive measure of the value of a wind energy project. The IRR allows the energy investment to be directly compared with the return that might be obtained for any other competing investment. IRR is the discount rate that makes the NPV of the energy investment equal to zero. When the IRR is less than discount rate, it is a good indicator for the project.

$$\text{IRR}\rightarrow\text{NPV}=0\ \text{ i.e}\frac{\sum benefits_n-\sum costs_n}{(1+\text{i})^n}=0 \quad (9)$$

5. Data inputs and assumption

Tabele 1: Distribution of costs of PV plant in (€/kW) according to components of PV plant with capacity 2MW, Terbuf village, Divjaka municipality.

	%	€/kW	€
PV Panels	47	349	698462
Inverter	11	82	163470
Rack installation	13	97	193192
Electrical parts	12	89	178331
Civil & Installation	12	89	178331
Development	5	37	74304
TOTAL	100%	743	1 486 089

From table 2 the main techno-economic parameters and assumptions used as primary indicators in the study are given. Power capacity range, electricity export rate, and other financial parameters in the country context are accepted. The grid extension cost (25-55000 €/km) per 35 km is taken in the sensitivity analyses

and O&M cost are identified and taken into consideration in this study. Based on these recommendations we have calculated the monetary values that are expected to be spent during the operation phase (O&M) of the 2MW project, at €50 000 per year.

Table 2: *Financial parameters and assumptions.*

Components	Value	Unit
Installed Capacity	2	MW
Electricity export rate	65	€/MWh
Investment Cost	743	€/kW
Discount Rate	5-7-11	%/ year
Debt rate	70	%
Debt interest rate	5.5	%
Inflation Rate	3.0	%
Debt term	15	year
Reinvestment rate	0	%
GHG reduction credit rate	25	€
Module Lifespan	25	year
(O&M) Cost	15	€/MWh
Land lease	Not applicable	Not applicable

The technical aspects of PV type selection directly affect the annual revenue generated by each module. The total investment cost assumed in this study is considered 1 626 089€ and the results below is fully based on this investment.

6. Results and analysis

From the simulation of the proposed PV system the final results for the efficiency of the system and other techno economic features.

Table 3: *The equity payback of the proposed PV plant for the chosen financial parameters given in table 2.*

Electricity export rate (€/MWh)	↓35%@105 6957€	↓17.5%@1 341 523€	0%@1 626 089€	↑17.5%@1 910 654€	↑35%@2 195 220€
42.5 (€/MWh)	7.0	16.4	25.0		
53.63(€/MWh)	4.0	6.8	13.4	19.1	24.3
65 (€/MWh)	2.9	4.4	6.7	11.1	16.8
76.38(€/MWh)	2.2	3.2	4.6	6.6	10.0
87.75(€/MWh)	1.8	2.6	3.5	4.8	6.6

The model calculates the equity payback, which represents the length of time that it takes for the owner of a facility to recoup its own initial investment (equity) out of the project cash flows generated. The equity payback considers project cash flows from its inception as well as the leverage (level of debt) of the project, which makes it a better time indicator of the project merits than the simple payback. In our case study for a given electricity export rate of 65 (€/MWh) and total installation cost of 1 626 089€ the payback results 6.7 year (see table 3 number highlighted in red). For the supposed investment and suggesting a rise to 17.5% and 35% of the electricity export rate the payback time is reduced to 4.6 and 3.5 respectively.

The model calculates the energy (electricity) production cost per kWh (or MWh), this value (also called the Levelized Cost of Electricity or LCOE) represents the electricity export rate required in order to have a Net Present Value (NPV) equal to 0. The GHG reduction revenue, the "Other" revenue (cost) and the Clean Energy (CE) production revenue are not included in this calculation. From the graph in figure 3 it is clearly shown that LCOE is affected by the interest rate applied on the investment in the period of 15 years considered in our study.

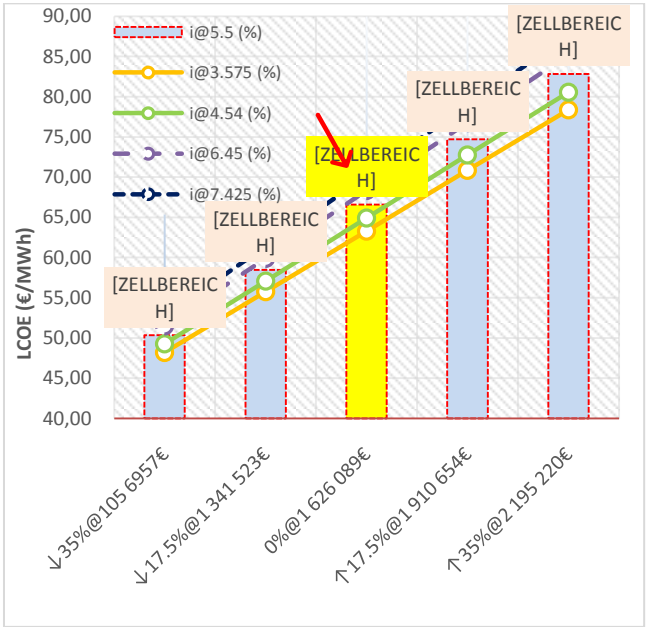

Figure 3: *LCOE (€/MWh) as a function of the total investment cost (€) and the interest rate in the range ±35% and constant discount rate 8%.*

The reference interest rate is taken 5.5% and the sensitivity analyses is extended on ±35% of the total investment cost and interest rate.

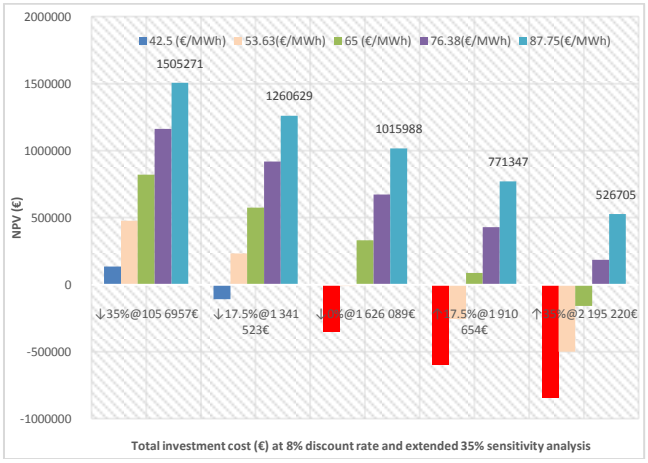

Figure 4: *NPV variation at a range of sensitivity analysis ±35%.*

The model calculates the Net Present Value (NPV) of the project, which is the value of all future cash flows, discounted at the discount rate of 8%, in today's currency. NPV is related to the internal rate of return (IRR). NPV is thus calculated at a time 0 corresponding to the junction of the end of year 0 and the beginning of year 1. Under the NPV method, the present value of all cash inflows is compared against the present value of all cash outflows associated with an investment project. The difference between the present value of these cash flows, called the NPV, determines whether or not the project is generally a financially acceptable investment. Positive NPV values are an indicator of a potentially feasible project. The model calculates the NPV using the cumulative after-tax cash flows. In cases where the user has selected not to conduct a tax analysis, the NPV calculated will be that of the pre-tax cash flows. For electricity export rate €42.5MWh NPV results negative and payback period is more than 25 years reaching the maximum time period of the PV.

For the chosen total investment cost of 1 626 089€ and electricity prices equal or more than €65/MWh the project is profitable and NPV results positive.

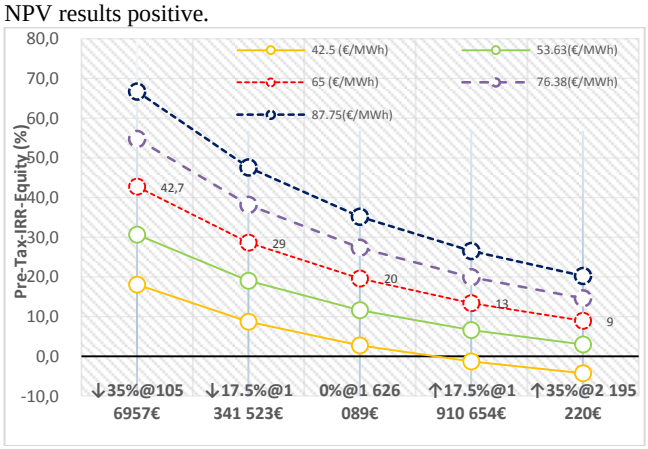

Figure 5: *Pre-Tax-IRR-Equity (%) distribution at a range of sensitivity analysis ±35%.*

In figure 5 Pre-Tax-IRR-Equity (%) distribution is given. The model calculates the pre-tax internal rate of return (IRR) on equity (%), which represents the true interest yield provided by the project equity over its life before income tax. It is calculated using the pre-tax yearly cash flows and the project life. It is also referred to as the return on equity (ROE) or return on investment (ROI) or the time-adjusted rate of return. It is calculated by finding the discount rate that causes the net present value of the equity to be equal to zero. The most obvious advantage of using the internal rate of return indicator to evaluate a project is that the outcome does not depend on a discount rate that is specific to a given investment. In our case study IRR at reference condition results 20%.

7. Conclusion

The economic analysis of the PV project of 2MWp is focused on estimating the total investment cost, the price of electricity generation (LCOE), factors influencing investment as well as a detailed sensitivity analysis and financial risk. In the sensitivity analysis, the effects of changes in financial parameters in the range of ±35% on the values of self-repayment period (VAT), NPV, IRR, LCOE, O&M were checked.

In order to perform economic aspects at a high accuracy level Methodology 2 in RETScreen Expert is chosen. Sensitivity and Risk Analysis (Monte Carlo simulation) is performed on sensitivity of important financial indicators in relation to key technical and financial parameters.

From the simulation the annual electricity generated, and export rate and total cost are the main parameters influencing the potential of small PV plants.

The PV plant of 2MW of installed capacity, at the proposed location can generate an annual electricity of 3319MWh, NPV=1015988 € and payback time 6.7 years.

The cost of manufacturing solar panels has plummeted dramatically in the last decade, making them not only affordable but often the cheapest form to replace the existing power systems. Solar panels have a lifespan of roughly 30 years and come in variety of shades depending on the type of material used in manufacturing.

As a conclusion by installing 10 times more capacities it can not only reduce the electricity import by 11% but in other hands helps in the diversification of the Albanian Energy sector requested on [6].

References

[1] IRENA (2020), Renewable Power Generation Costs in 2019, International Renewable Energy Agency, Abu Dhabi

[2] RETScreen. Financial and risk analysis, 2004. Retrieved: July 20, 2015 from URL:http://www.retscreen.net/ang/financial_and_risk_analysis_with_retscreen.php

[3] Malka, Lorenc et al. 2020. "An Approach to the Large-Scale Integration of Wind Energy In Albania." 10(5): 327–43

[4] Renewable, International, and Energy Agency. 2020. Renewable Energy and Jobs – Annual Review 2020

[5] Malka, L., Konomi, I., Alcani, M., Gjeta, A., & Bebi, E. (2020). Off-grid hybrid PV plants used to supply autonomuos internet base stations supporting the mitigation of GHG in Albania Case study: Bulqiza district, Albania. 178(4), 174–178. https://stumejournals.com/journals/i4/2020/4/174

[6] Strategjia Kombëtare e Energjisë. (2018-2030), Available from: http:// www.kesh.al/admini/pdflinks/86.pdf

Environmental aspects and GHG credits impact on LCOE and key indicators for small installed PV plants in Albania.

[a]Ilirian Konomi, [b]Lorenc Malka, [a]Ermonela Rrapaj
[a]Department of Hydraulic & Hydrotechnic, Faculty of Civil Engineering, Polytechnic University of Tirana, Albania
[c]Department of Energy, Faculty of Mechanical Engineering, Polytechnic University of Tirana, Albania
ikonomi64@gmail.com, lmalka@fim.edu.al

Abstract: *A lot of techno-economic analyses have been conducted to seek the most cost-effective solution for electricity generation applied in the interval time of 25 years of project life. The actual benefits taken from small PV plants up to 2MW have been identified, as well as the effects of the most sensitive parameters, such as installation price, incentives and other credit options such as carbon credit rate or feed in tariff. The output carried out from the simulation performed in RETScreen Expert tool shows that PV system represents the best solution to provide free carbon and costless electricity to run the water pump for sprinkler irrigation in the agriculture sector in Albania. The environmental benefits have been also addressed, evaluating the CO2 emissions saving achievable from the PV system operation and some financial aspects such as simple payback period (SPP), NPV, IRR. The annual electricity production from PV plant located in the village of Tërbuf, Divjaka Municipality with an installed capacity of 2MW results 3319MWh and would avoid 3253 tCO2. The effects of ETS schemes on the LCOE from small PV plants are highlighted.*
KEYWORDS: *PV, RETSCREEN EXPERT, CO2, SPP, CREDITS.*

1. Introduction

Several trends are shaping an unfolding energy transition and giving an indication of its direction. **First**, the costs of renewable technologies have plummeted to the point that new fossil-based electricity is no longer an attractive option. **Second**, the progress in the power sector is spilling over to end uses, allowing a re-imagining of possibilities with the abundance of renewable options at hand. **Third,** a consensus has formed that an energy transition grounded in renewable sources of energy and efficient technologies is the only way to give us a fighting chance of limiting global warming by 2050 to 1.5°C [1]. The integration of distributed renewable energy can demonstrate various technical benefits to the energy sector but at the same time to the owners of the facilities. Benefits include the reduction of fossil fuel use and associated GHG emissions, the improvement of grid reliability and limitation of power outages, protection of critical loads, independence of foreign supply, and increased energy security coupled with a fixed energy cost which is immune to future tariffs and fossil fuel costs increases. The carbon intensity of PV power varies between technologies according to the materials and processes used and module efficiency.

In the other hand the depletion of fossil fuel and the negative effect on the environment as well as the potential techno-economic merits of "*hybrid combinations*" identified as a good solution moving towards reliable and more feasible energy systems based on renewables [2]. As the need for clean, sustainable energy increases, and renewable technologies get ever more advanced, more projects had been developed in greater sizes and complexities, including on-grid and off-grid solutions based on renewables.

Smart electrification with renewables focuses on the potential synergies between major increases in renewable power generation, electrification and digitalisation, and looks to create the conditions for the unprecedented co-ordination of their deployment and more efficient use across end-use sectors – power, transport, industry and buildings [3].

Growing shares of those jobs are off-grid, supporting productive use in farming, food processing and healthcare in previously remote, isolated, energy-poor communities. In parallel, rural areas benefit from the feedstock production that underpins bio-energy and which accounts for the bulk of about 3.6 million jobs in that segment. Renewables accounted for an estimated 11.5 million jobs worldwide in 2019. Using solar PV to power mini-grids is an excellent way to bring electricity access to people who do not live near power transmission lines, particularly in developing countries with excellent solar energy resources and reducing the negative effect on environmental. Continued emissions of greenhouse gases will cause further warming and changes in all components of the climate system. Limiting climate change will require substantial and sustained reductions of greenhouse gas emissions [4].

1.1 Site location

The 2MW photovoltaic plant will be installed on the ground in Tërbuf. The property is located 14.8 km from the city of Divjaka, 73.6 km from the Albanian capital, Tirana.

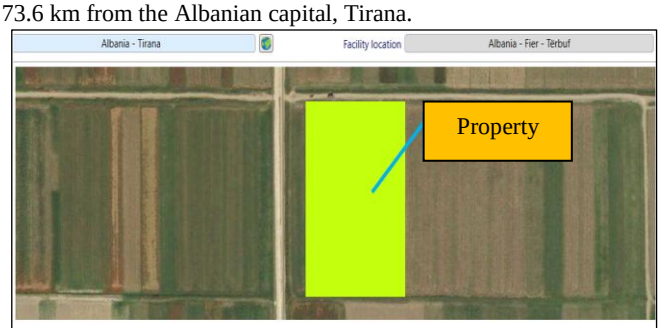

Figura 1: *Location of the 2MW PV project. Village of Tërbuf, Divjakë Municipality, Albania.*

2. *Materials and methods*

Actually, there are several models available for conducting a set of analysis including environmental impact and benefits. RETScreen Expert is a clean-energy awareness, decision-support and capacity-building tool [5]. This model helps us as energy planers to determine the annual reduction in the emission of greenhouse gases stemming from using the proposed technology in place of the base case technology. The model uses a computerized system with integrated mathematical algorithms and top to bottom approach which has been developed to overcome the barriers to clean energy technology implementation at the preliminary feasibility stage. It provides a cost analysis, GHG emission reduction analysis, financial summary, sensitivity analysis, provides a low-cost preliminary assessment of RES projects with a small set of a detailed information. Methodology 2 as the more suitable to perform the emission analysis is chosen [5]

3. GHG summary in Albania and global trends

Albania is the largest producer and exporter of oil in the South-East Europe region, most oil extracted in Albania is exported as unrefined crude oil [6]. A further contributor to net energy imports is the country's rising demand for petroleum products, largely fuelling the transport sector. Greening the transport sector by taking up biofuels blending and introducing electric mobility could lower the country's energy imports and positively contribute to the national economy.

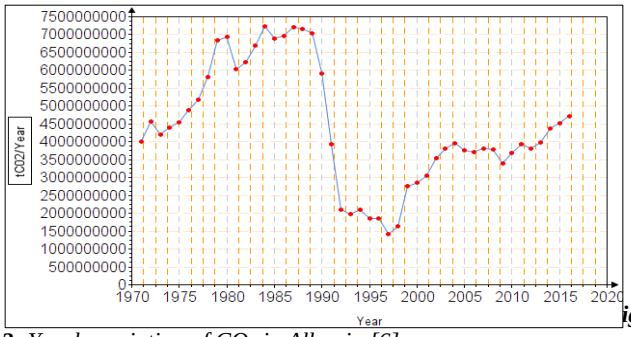

Fig. 2: *Yearly variation of CO_2 in Albania [6].*

In 2019, CO2 emissions per capita for Albania was 1.93 tons of CO2 per capita. Albania CO_2 emissions per capita fluctuated substantially in recent years, showing an increasing trend from 1970 up to 2019 period. By the end of 2019 the specific emission reached a value of 1.93 tons of CO_2 per capita.

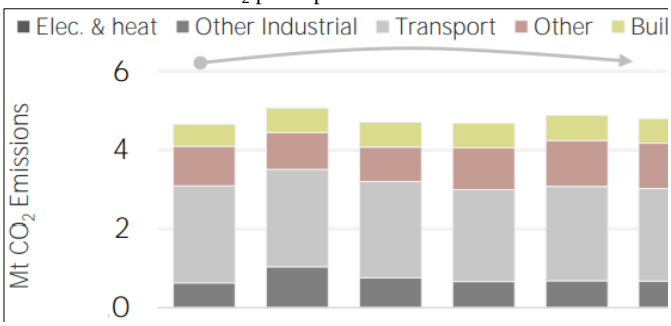

Fig. 3: *Energy related CO_2 emission by sector in Albania [6].*

Renewable energy sources, including solar, wind, hydro, biofuels and other future renewable sources are at the centre of the energy transition towards a less carbon-intensive and more sustainable energy system [7] In the context of GHG emissions, Albanian's electricity sector is zero emitter in the region as the share of electricity from renewable sources in total electricity generation is almost 100%, while EU-27 countries together have a RES share of 32.3% and the border countries Greece (30.3%), North Macedonia (35.1%), Montenegro (59.2%) and Kosovo highly depended on lignite has only 5.1% [8]. Under the Planned Energy Scenario, annual emissions reach 36.5 $GtCO_2$ in 2050. To achieve the 1.5°C Scenario, emissions would have to drop to net zero in all sectors. Additional efforts in sectors such as power, heat and industry would be needed, with negative emissions delivering the necessary additional carbon reductions [1]. Aligned with the IPCC's special report on limiting global warming to no more than 1.5°C by 2050 [9], IRENA's 1.5°C Scenario starts with the goal of reducing global CO_2 emissions by following a steep and accelerated downward trajectory from now to 2030 and a continuous downward trajectory thereafter, reaching net zero by 2050. Because the energy sector is currently responsible for around 80% of anthropogenic CO2 emissions, it has a central role to play in delivering the required decarbonisation. This is achievable but extremely challenging, requiring urgent action on multiple fronts. Fossil fuel use would have to decline by more than 75% by 2050 (Figure 4).

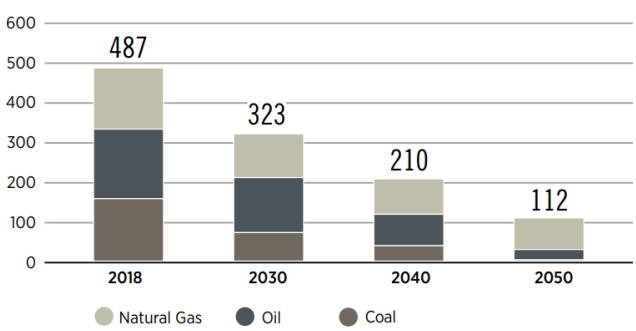

Fig. 4: Primary fuel supply (EJ) road map [Source IRENA].

Fossil fuels would still have roles to play, mainly in power and to an extent in industry, providing 19% of the primary energy supply in 2050. Oil and coal would drop the fastest, while natural gas would peak around 2025 and decline thereafter. The global production of oil in 2050 is expected to be 85% lower than today. Most of it would be used in industry for petrochemicals (non-energy uses, close to 40%), and in aviation and shipping. Coal production would decline even more drastically, from around 5 750 million tonnes in 2018 (160 exajoules [EJ]) to 240 million tonnes per year (7 EJ) in 2050. In the power sector, coal generation would be cut in half by 2030, in half again by 2040 and phased out by 2050. The remaining coal demand would be largely restricted to industry, mostly for steel production (coupled with carbon capture and storage) and to a certain extent in chemicals production. Natural gas would be the largest remaining source of fossil fuel in 2050, making up 70% of total fossil fuel supply and 13% of total primary energy supply (down from 26% in 2018). In 2050, natural gas would primarily be used in industrial processes, blue hydrogen production (coupled with carbon capture and storage) [10] and power plants.

4. Emission reduction analysis in RETScreen Expert model

The model performs a GHG emission reduction analysis depending on whether the clean energy system under consideration generates electricity or provides other energy requirements.

The only difference lies in transmission and distribution losses, which are incurred only by electricity generating systems. The reduction Δ_{GHG} is calculated as follows in equation 1:

$$\Delta_{GHG} = \left(e_{base} - e_{prop}\right) E_{prop} (1-\lambda_{prop})(1-e_{cr}) \quad (1)$$

where e_{base} is the base case GHG emission factor, e_{prop} is the proposed case GHG emission factor, E_{prop} is the proposed case annual electricity produced, λ_{prop} is the fraction of electricity lost in transmission and distribution for the proposed case, and e_{cr} the GHG emission reduction credit transaction fee. For both the base case and proposed case system, the transmission and distribution losses are deemed to be negligible for on-site generation, such as off-grid and water-pumping PV applications.

5. GHG emission factor – base case electricity system

For the base case electricity generation system is strictly required the calculation of the GHG emission factors, defined as the mass of greenhouse gas emitted per unit of energy produced. For a single fuel type, the following formula in equation (2) is used to calculate the base case electricity system GHG emission factor, e_{base}:

$$e_{base} = \left(e_{CO_2} GWP_{CO_2} + e_{CH_4} GWP_{CH_4} + e_{N_2O} GWP_{N_2O}\right) \frac{1}{\eta} \frac{1}{1-\lambda} \quad (2)$$

where e_{CO2}, e_{CH4}, and e_{N2O} are respectively the CO_2, CH_4 and emission factors for the fuel/source considered, GWP_{CO2}, GWP_{CH4}, and GWP_{N2O} are the global warming potentials for CO2, CH_4 and N_2O, η is the fuel conversion efficiency and λ is the fraction of electricity lost in transmission and distribution. The GHG emission factor will vary according to the type and quality of the fuel, and the type and size of the power plant. In cases for which there are a number of fuel types or sources, the GHG emission factor e_{base} for the electricity mix is calculated as the weighted sum of emission factors calculated for each individual fuel source given in equation (3):

$$e_{base} = \sum_{i=1}^{n} f_i e_{base,i} \quad (3)$$

where n is the number of fuels/sources in the mix, f_i is the fraction of end-use electricity coming from fuel/source i, and e_{base}, *i* is the emission factor for fuel *i*, calculated through a formula similar to equation (2):

$$e_{base,i} = \left(e_{CO_2,i} GWP_{CO_2} + e_{CH_4,i} GWP_{CH_4} + e_{N_2O,i} GWP_{N_2O}\right) \frac{1}{\eta,i} \frac{1}{1-\lambda,i} \quad (4)$$

where $e_{CO_2,i}$, $e_{CH_4,i}$ and $e_{N_2O,i}$ are respectively the CO2, CH4 and N2O emission factors for fuel/source i, η,i is the fuel conversion efficiency for fuel i, and λ,i is fraction of electricity lost in transmission and distribution for fuel i.

The GHG emission factor for the electricity mix will apply from year 1 up to the year of change in baseline, as specified by the user, unless no changes are specified; in this case, the emission factor will apply throughout the life of the project. When a change in the baseline emission factor is specified, the new factor for the year that the change in baseline takes place, and the years that follow will be determined by (e*):

$$e^*_{base} = e_{base} r_{change} \quad (5)$$

where r_{change} is the percentage change in the base case (baseline) GHG emission factor for the year that the change in baseline takes place, and the years that follow.

6. GHG emission factor – proposed case electricity system

The calculation of the proposed case electricity system GHG emission factor, e_{prop}, is similar to that of the base case GHG emission factor, with the exception that for off-grid systems the fraction of electricity lost in transmission and distribution is set to zero. e_{prop} is therefore calculated through equation (2) with λ=0, in the case of a single fuel/source, or through equations (3) and (4) with all λ_i=0, in the case of a mix of fuel/sources.

7. Silmulation of the PV system in RETScreen Expert

Emission factors will vary for different types and qualities of fuels, and for different types and sizes of power plants.. The electricity mix factors thus account for a weighted average of the fuel conversion efficiencies and T&D losses of the different fuel types. For fuel type selected, diesel 2, 100% single fuel mix, units are given in (kg/GJ) as it is shown in table 2. The other financial parameters are transferred directly once the energy PV model is created such as inflation rate 3%, discount rate 8%, fuel escalation rate 2% and project life 25 years.

Table 2: *Emission factors for the chosen fuel type taken in the study (Diesel 2)*

Fuel Type (Base case)	Fuel Mix	CO_2 emission factor (kg/GJ)	CH4 emission factor k(g/GJ)	N_2O emission factor (kg/GJ)	Electricity Generation efficiency (%)	T&D losses (%)	GHG emission factor (tCO_2/MWh)
Fuel Mix (%)	100	70	0.002	0.0006	35	7	0.777
Electric Mix (%)	100	215	0.0063	0.0018		7	0.777

In this study the plant efficiency of 35% and 7% T&D losses are considered. The default factors provided are those which are representative of large power plants that feed a central electricity grid such as CO_2 gas emission factor 70 kg/GJ, CH4 emission factor 0.002 kg/GJ and N2O levell 0.0006 kg/GJ. The model calculates the GHG emission factor for for the chosen fuel type considered Diesel#2. Values are calculated based on the individual emission factors, the electricity generation efficiency and the T&D losses. The weighted GHG emission factor for the total electricity mix is calculated 0.777 tCO_2/MWh as it is given in table 2.

Table 3: *Calculation of fuel consumption and GHG emission (the base case system).*

Fuel consumption	GHG emission factor	GHG emission
MWh	tCO_2/MWh	tCO_2
3,319	0.777	2,578
3,319	0.777	2,578

In the table 3 the GHG emission for the base case system by multiplying the fuel consumption by the GHG emission factor. The model also calculates the GHG emission for the base case system by multiplying the annual system losses by the global warming potential. The model calculates the gross annual reduction in GHG emissions estimated to occur if the proposed case is implemented. The calculation is based on emissions of both the base case and the proposed case systems on an annual basis.

The annual GHG base case results 2578 tCO_2 and the proposed 180 tCO_2. The proposed GHG emission is calculated by multiplying the annual fuel consumption,GHG emission factor and the accepted T&D losses (7%). The gross annual GHG reduction results 2397 tCO_2.

8. GHG reduction credit

In this case study the optional GHG reduction credit, per equivalent ton of CO_2 (tCO_2) is considered. It is used in conjunction with the net GHG reduction to calculate the annual GHG reduction revenue. Prices for GHG reduction credits, per equivalent ton of CO_2 (tCO_2), vary widely depending on how the credit is generated and how it will be delivered. Other factors which have an impact on price may include voluntary or mandatory emissions reduction; private or public purchase of credits; credits traded within, for example, the European Union Greenhouse Gas Emission Trading Scheme (EU ETS), other national, transnational, or regional schemes; type of technology used to generate the emissions reductions; and others. As of May 2014, prices including rates for carbon taxes varied between $1 to $168 per ton of CO_2 [11].

The model escalates the GHG reduction credit rate yearly according to the GHG reduction credit escalation rate starting from year 1 and throughout the GHG reduction credit duration as it is given in the table 4.

Table 4: *Carbon credit revenue calculation.*

	€/tCO2	*14*
Net GHG reduction	tCO2/yr	2349
Net GHG reduction-25yrs	tCO2	58729
GHG reduction credit rate	€/tCO2	14
GHG reduction revenue	€	32889
GHG reduction credit duration	yrs	15
Net GHG reduction-15yrs	tCO2	35238
GHG reduction credit escalation rate	%	2

Carbon credit instruments often coexist with other heterogeneous policies that may directly or indirectly contribute to reducing GHG emissions by addressing areas such energy or infrastructure. In our study they have to be planned to interact and complement other strategic priorities at local and national levels. The GHG reduction credit duration is acceped to be applied all into the whole lifetime of the proposed PV system with a reduction credit escalation rate of 2%. The credit transaction fee is accepted 2%. In the graph in figure 3 the results of the simulations of the PV system compared to that of the base case (diesel#2 powered) is given. The proposed system, PV offers the lowest possible scenario for the mitigation of GHG emissions resulting to 180 tCO2 compared to baseline scenario 2578tCO_2.

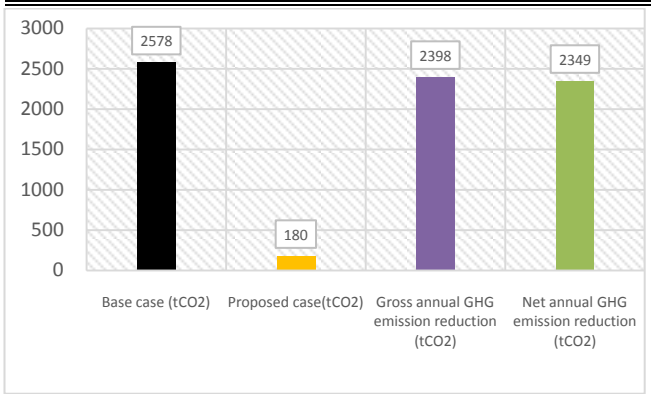

Figure 5: *Results of the simulation of the baseline scenario and proposed PV system.*

Assuming that the annual electricity produced (3319MWh/year) by the photovoltaic plant (PV) with a capacity of 2MW located in the village of Tërbuf, Divjaka Municipality would be produced through the use of fuel Diesel#2.

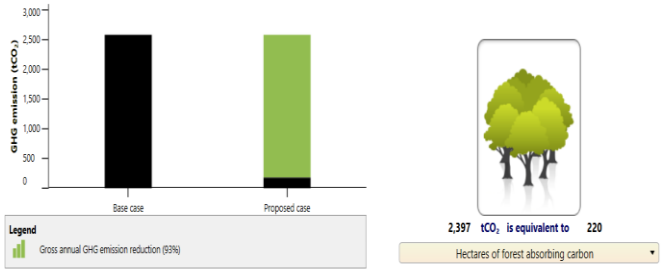

Figure 6: *Results of the simulation of the baseline scenario and proposed PV system.*

As it is clearly shown in figure 6 the proposed PV system can avoid 2349 tCO_2/year equivalent to 220 hectares of forest absorbing carbon.

The model calculates the equity payback, which represents the length of time that it takes for the owner of a facility to recoup its own initial investment (equity) out of the project cash flows generated. The equity payback considers project cash flows from its inception as well as the leverage (level of debt) of the project, which makes it a better time indicator of the project merits than the simple payback. The model uses the year number and the cumulative after-tax cash flows in order to calculate this value.

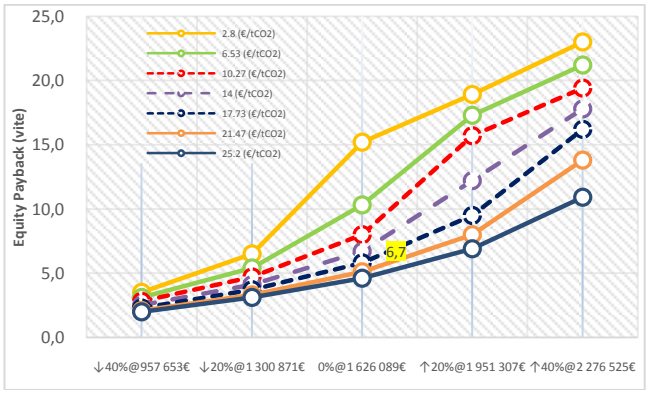

Figure 7: *Graphical presentation of sensitivity analysis (± 40%) for investment repayment period (years) as a function of total installation cost (€) and carbon credits (± 80%) (€ / tCO_2).*

The graph in figure 7 shows the graphical representation of the sensitivity analysis (±40%) for the investment repayment period (years) as a function of the total cost of installation (€) and the selling price of carbon credits (€/tCO_2) in the range (±80%). In our analysis the selling price of carbon is accepted €14/tCO2 and the fixed price of electricity €65/MWh.

If the selling price of carbon is 14-25 (€/tCO_2) and the fixed price of electricity €65/MWh then the self-repayment period is reduced to 3.3 years for the assumed selling price of electricity €65/MWh.

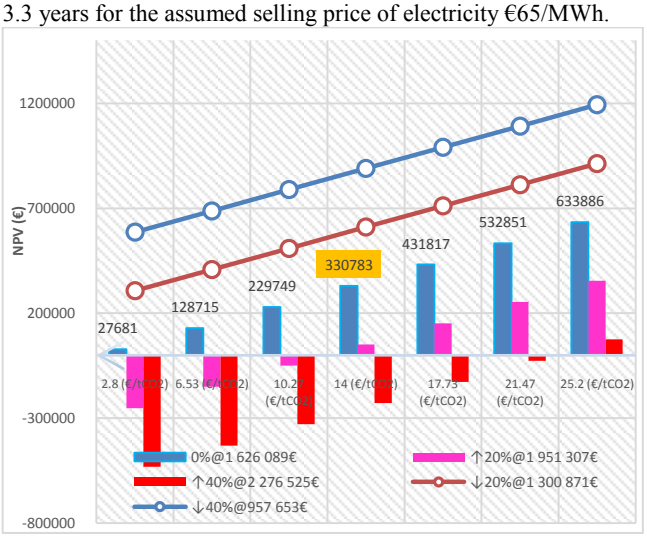

Figure 8*: Variation of NPV in function of total investment cost (€) for discount rate 8%, interest rate 5.5% fixed price of electricity 65 €/MWh @ ± 40% of sensitivity analysis and sale price of carbon credits (€/tCO_2) @ ± 80%.*

The graph in Figure 8 clearly shows the effect of the economic performance of the photovoltaic system under the application of carbon credit trading schemes.

Worst case scenario, increase of installation cost by 40% (red columns give negative NPV in all cases), while pink scenario with increase of installation cost by 20% brings benefit only with credit values carbon (€/tCO_2) in the interval of [14→ + ∞ [.

Baseline scenario, for discount rate 8%, interest rate 5.5% fixed price of electricity 65 €/MWh and sensitivity analysis of installation cost @ ±40% and sale price of carbon credits (€/tCO2) @ ± 80% (blue columns) show in all cases of lending positive values of NPV. NPV in the baseline scenario reaches the value of € 330780 and doubles when the selling price of carbon credits increases (€/tCO_2).

9. Conclusion

The effects of carbon credits for the photovoltaic project with an installed capacity of 2MW, located in the village of Tërbuf, Divjaka Municipality were considered at the level of €14/tonCO_2. The analysis and the results of the study according to the scenario of application of carbon credits showed that it has a positive effect on the main indicators of the system by reducing the repayment period to 3.3 years from 6.7 years.

Emission trading systems are suitable to accelerate the transition of clean energy in the energy sector. Currently, the energy sector around the world is moving towards a decarbonised system, due to falling costs of low carbon technology and low risks from competition, but this is not happening at a satisfactory pace to meet the objectives of " "The Paris Agreement." The electricity sector is very convenient to be regulated under an emissions trading system.

First, it is a large emitting sector with proven technologies, with low GHG levels that are available in the market.

Second, the availability of data on electricity generation is moderately strong across all jurisdictions, which is needed to set allocation standards. Furthermore, some jurisdictions already have experience in implementing energy sector mitigation activities with carbon price support, for example through lending mechanisms such as the Clean Development Mechanism.

The energy sector is involved in almost all emissions trading operating systems worldwide, as well as in the jurisdictions that are developing or considering the development of an emissions trading system. It is recommended that in our country to regulate by law, especially in the RES sector, the application of carbon credit schemes at least at the level of 14÷25 (€/tCO_2).

References

[1] IRENA. (2021). World energy transitions outlook: 1.5 degrees pathway. In Irena. https://irena.org/publications/2021/March/World-Energy-Transitions-Outlook

[2] Malka, L., Gjeta, A., Konomi, I., Alcani, M., Bebi, E., & Kaci, S. (2020). Off-grid hybrid PV configuration' s role to supply internet access points antenna in remote areas. Case study: " Ostren i vogël - Trebisht " villages, Bulqiza district, Albania. 226(5), 218–226 https://stumejournals.com/journals/i4/2020/5/218

[3] Renewable, I., & Agency, E. (n.d.). ELECTRIFICATION Driving the transformation. https://www.irena.org/publications/2022/Feb/Smart-Electrification-with-Renewables

[4] Malka, Lorenc et al. 2020. "An Approach to the Large-Scale Integration of Wind Energy In." 10(5): 327–43 https://www.econjournals.com/index.php/ijeep/article/view/9917/5291

[5] RETScreen. Financial and risk analysis, 2004. Retrieved: July 20, 2015 from http://www.retscreen.net/ang/financial_and_risk_analysis_with_retscreen.php

[6] IRENA (2021), Renewables Readiness Assessment: Albania, International Renewable Energy Agency, Abu Dhabi

[7] IEA. (2020), Renewable Power. Paris: IEA. Available from: https://www.iea.org/reports/renewable-power

[8] Malka, L., Konomi, I., Bartocci, P., & Rrapaj, E. (2021). An Integrated Approach toward a sustainable transport sector using EnergyPLAN model: case of Albania. 147(4), 141–147. https://stumejournals.com/journals/innovations/2021/4/141.full.pdf

[9] IPCC (2018), Global Warming of 1.5°C: An IPCC Special Report on the Impacts of Global Warming of 1.5°C above Pre-Industrial Levels and Related Global Greenhouse Gas Emission Pathways, in the Context of Strengthening the Global Response to the Threat of Climate Change, Intergovernmental Panel on Climate Change, Geneva

[10] ICEF (2018), "Direct Air Capture of Carbon Dioxide–ICEF Roadmap 2018", ICEF – Innovation for Cool Earth Forum, Tokyo, December, www.icef-forum.org/pdf/2018/roadmap/ICEF2018_DAC_Roadmap_20181210.pdf.

[11] World Bank. 2014. State and Trends of Carbon Pricing 2014. Washington, DC: World Bank

The effect of different heat treatments on the mechanical properties of the steel forgings

Srba Mladenović[1], Jasmina Petrović[1]
[1]Technical Faculty in Bor University of Belgrade, VJ 12 19210 Bor Serbia[1]
smladenovic@tfbor.bg.ac.rs

Abstract: *The effect of different heat treatments on the microstructure and mechanical properties of the C45 and S355J2 steel forgings has been presented. Samples of the same forgings, but subjected to the different heating treatments, were prepared and tested by using optical microscopy, tensile machine, and hardness tester. It was observed that the requested mechanical properties of the forgings and uniform structure can be achieved by determining the appropriate heating treatment parameters.*
Keywords*: S355J2, C45 STEEL, FORGINGS, HEAT TREATMENT, PROPERTIES, MICROSTRUCTURE*

1. Introduction

Forging is a process in which the final shape of the work piece is obtained by compressive forces. This forces are applied through dies and tools by hammering or pressing the metal billet.

Classification of forging processes can be based on the temperature of the work piece and on arrangements of dies. When the temperature of the billet is above its recrystallization temperature than we have a hot forge process. Forging at room temperature is referred as cold, and forging at elevated, but below recrystallization temperatures is called warm. Open die forging is a process in which the flat dies of simple shape are used to deform material. In this process, there is no constraint to material flow in lateral direction. When the material is shaped to fill a die cavity formed by the upper and lower die halves, which are not completely closed and allow some material to escape (flash), than we have an impression die forging. Forging in which the material is fully constrained in the cavity formed by the die halves is define as closed die forging.

The grain microstructure of low and medium steels is dependent on recovery, recrystallization and grain growth mechanisms that occurs during the hot forging process. This mechanisms are affected by key forging parameters such as degree of plastic deformation, temperature, time and design of deformation passes [1]. Plastic deformation is responsible for the closure of the internal voids and for the reduction of non-metallic inclusions by breaking them into smaller particles and redistribute them uniformly [2]. High plastic deformation levels also contribute to reduce the thickness of segregated bands microstructure which is a common phenomenon in rolled-steel bars [3]. However there are some concerns regarding the microstructure of the forgings. Grain flow is preferentially oriented depending on the severity of the plastic deformation on the longitudinal or transverse axis of the forging. Furthermore, due to cooling rate variations a heterogeneous microstructure could be formed along the wall-thickness. Coarse grain structure can also be produced in the forgings.

Further improvement of the forgings mechanical properties can be achieved by heat treatment. The heat treatment (e.g. normalization, quenching, tempering) determines final microstructure and mechanical properties of the forgings. Normalization reduces the heterogeneity and microstructural anisotropy developed after the hot forging and refined the coarse structure. This treatment involves heating the material above it upper critical point (A_{c3}), holding it at austenitizing temperature until complete austenitization before being cooled in air. Quenching can be describe as follows: initially the material is heated to its austenitic range, then after the soaking time is over, the material is immersed in a quench medium to promote fast cooling in order to transform austenitic structure into meta-stable structures (martensite or bainite). This heat treatment can be regarded as a key technological process used in the forging industry to tailor the microstructure and properties of low and high alloy steels [4]. Tempering treatment is required after quenching process since the as-quench martensite is brittle, hard and consequently not suitable for structural applications. Tempering consists of heating the previously obtained martensitic structure to a determined temperature for a specific time period and the cooling in still air. The tempering time is calculated based on the thickness of the part, while the selection of the tempering temperature depends on the desired mechanical properties [5].

Design of heat treatment is consists in the definition of crucial parameters such as heat rate, temperatures, soaking times and cooling rates. The purpose of the present work is to show the effect of different heating treatment parameters on the mechanical properties and microstructure of the forgings made from hot rolled C45 and S355J2 steel bars.

2. Experimental

2.1. Forging

Hot rolled round steel bars were used as a starting material. The grade of the material was C45 and S355J2 according to EN10204/3.1. Chemical composition and mechanical properties of the material are given in table 1 and 2.

Table 1: *Chemical composition and mechanical properties of C45 steel bars*

Element	C	Mn	Si	P	S	Cr	Ni	Cu	Mo
Wt%	0,43	0,61	0,26	0,01	0,01	0,1	0,12	0,29	0,01
Tensile strength, MPa		Yield strength, MPa			Elongation, %		Impact toughness, KV, J (-20°C)		
677		434			22		73,3		

Table 2: *Chemical composition and mechanical properties of S355J2 steel bars*

Element	C	Mn	Si	P	S	Cr	Ni	Cu	Mo
Wt%	0,17	1,01	0,2	0,01	0,02	0,08	0,09	0,29	0,01
Tensile strength, MPa		Yield strength, MPa			Elongation, %		Hardness, HB		
517		369			28		197		

For the production of the forgings, impression die forging process was used. Three identical forgings were produced. First forgings was produced from C45 steel and the other two was produced from S355J2 steel.

2.2. Heat treatment

Finished forgings were subjected to different heat treatments. The first one was subjected to normalization treatment. It was heated in the chamber furnace, holded for some period of time and then slow air-cooled until its temperature drop to the room temperature. The temperature-time diagram of heating and holding of the first forgings is presented at fig 1.

Second forgings was normalized at 905°C, and then air-cooled, and third forgings was heated at 860°C, oil-cooled and after that it was subjected to tempering process in which it was heated at 420°C and then air-cooled.

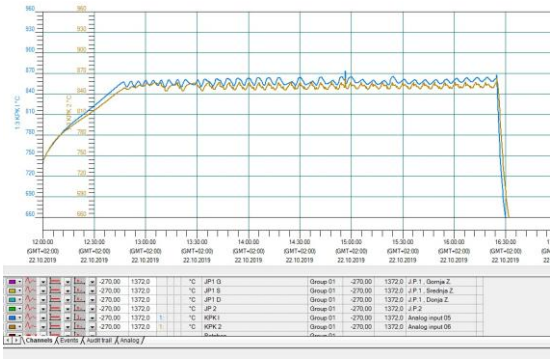

Fig 1. Heat treatment graph

2.3. Structure characterization

Tested forgings were cutted in small pieces and the samples were prepared from the surface and the central parts of the forgings (fig. 2.).

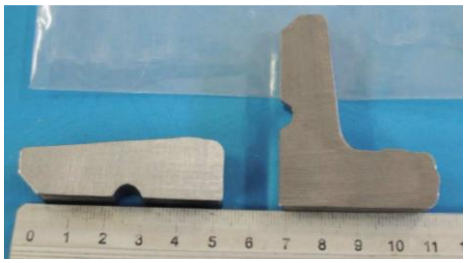

Fig. 2. Metallographic specimens

The preparation of the metallographic specimens for microstructural studies was carried out according to standard methods. The grinding papers of different roughness were used and polishing was carried out on a Al_2O_3 suspension with a polishing particle size of 0,3μm. The specimen were etched with a 4% solution of HNO3 in alcohol in order to reveal and identify its microstructure morphology. The exposure time was 4s, followed by washing and drying.

Microstructure analyses, for the first forgings, was performed with *„Leica DM 2700M“* light microscope equipped with Leica Grain & Phase Expert software package for materials analysis (fig. 3.).

Fig. 3. Leica DM 2700M light microscope

Microstructure of other two forgings samples were analyzed with Carl Zeiss Jena EPITYP 2 light microscope and for this samples average grain size was evaluated by applying the linear intercept method.

2.4. Tensile test and hardness measurements

Tensile test of the heat treated steel forgings were conducted on the cylindrical samples with a 6 mm diameter (type II following ISO 6892:1998) (fig 4). The tests were carried out at an ambient temperature.

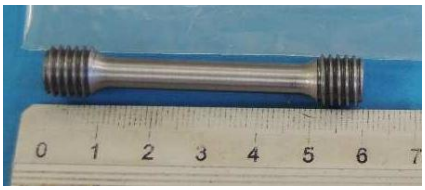

Fig. 4. Specimens for tensile testing

The mechanical properties, namely the yield strength (YS), tensile strength (TS), plasticity (elongation), and hardness for the investigated steel forgings after the heat treatment, are given in table 3.

The tensile and hardness measurements were conducted at Technical faculty in Bor in laboratory for mechanical testing of the metal materials.

3. Results and discussion

The microstructure of the forgings 1 is shown in Fig. 6.

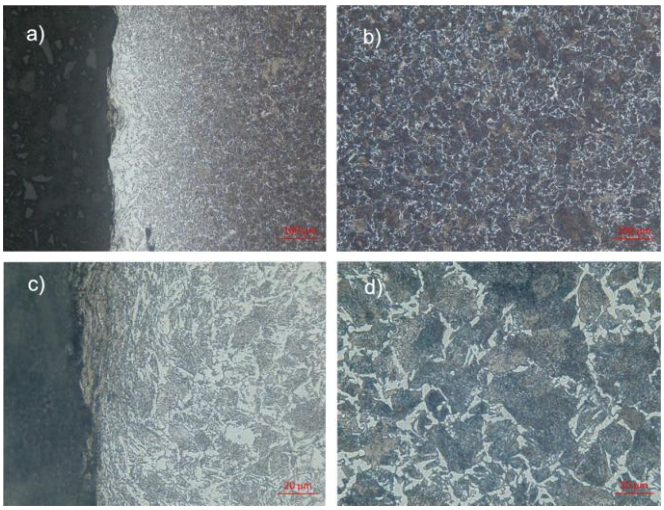

Fig. 6 Microstructure of first forgings a)100x and c)500x near the surface, b)100x and d)500x near the center of the sample, normalized at 860^{o}C for 4,5h and cooled in slow air

The sample has a predominantly pearlitic normalized structure with partially reticular arranged perlite. The microstructure are homogenized and pure. Light area at the surface of the sample (shown at figure 6a), can indicate that in this region maybe it came to the decarburization process. Blaoui et al. [6] studied the influence of cooling rate during the heat treatment on microstructure of the C45 steel. They found that the sample quenched in air after it was heated to 900^{o}C has combination of ferrite and pearlite with a low amount of spheroidal graphite. But the holding time was only 30min. Fadare et al. [7] investigated the efect of heat treatment on the microstructure of NST 37-2 steel. The steel samples were heat treated at different temperature levels and holding times, and then cooled in different media. It was observed that beside pearlitic matrix the structure contains graphite flakes.

After forging process a coarse grain structure is produced in the parts thanks to high forging temperature that was employed during the hot working operations. Coarse structure is refined after normalizing process. Average grain size, for forgings 1, evaluated by Leica Grain & Phase Expert image analyzer software is found to be 11 as it can be seen on photos that are presented on figure 7a. and 7b. for sample near the surface and near the center of the forgings, respectively.

The strength values for forgings 1 presented in table 3 are higher than those obtained for the starting material. The mechanical properties of the normalized specimen were found to be 780MPa, 489MPa and 21% for tensile strength, yield strength, and percentage elongation, respectively. The increase in tensile strength as compared to starting materials was due to proper normalization parameters which resulted in formation of pearlitic matrix structure.

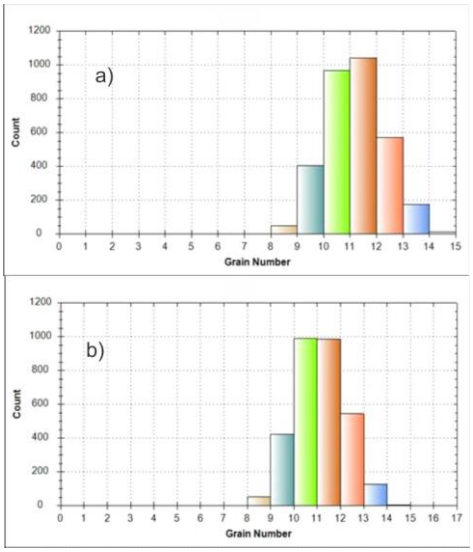

Fig 7. Determination of grain size by Leica Grain & Phase Expert software

The microstructure of forgings two and three are shown in figure 8 and 9 respectively.

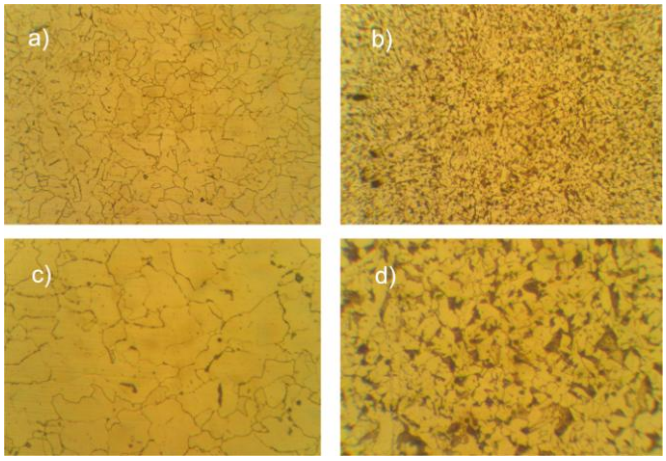

Fig. 8. Microstructure of second forgings a)100x and c)500x near the surface, b)100x and d)500x near the center of the sample, normalized at 905^{o}C, 1h for itch 2,5cm of forgings thickness and cooled in slow air

Microstructure of forgings 2, presented on figure 8 consists of ferrite and pearlite. The samples material was clean regarding nonmetallic inclusions.

The strength values for forgings 2 are presented in table 3. The limited values requested from the customer were 490-630MPa, min. 345MPa, min.20% and hardness 140-187HB for tensile strength, yield strength, percentage elongation, and hardness respectively. Obtained values, after the heat treatment, were on lower limit for tensile strength and hardness, and lower for yield strength.

Considering that forgings 3, was heated at 860^{o}C and then cooled in oil at intermediate cooling rate, microstructure was probably a mixture of lower bainite and martensite. Tempering process, conducted after the heating and oil cooling of the forgings 3 has influenced on transformation of martensite and formation of ferrite and carbide (fig. 9).

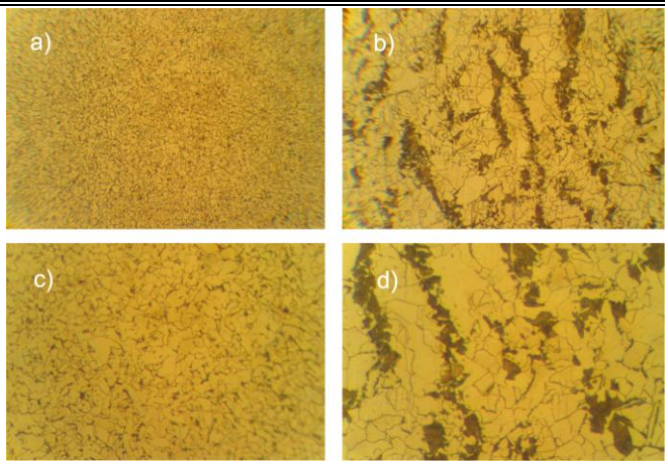

Fig. 9. Microstructure of second forgings a)100x and c)500x near the surface, b)100x and d)500x near the center of the sample, heated at 860^{o}C, 1h for itch 2,5cm of forgings thickness, oil-cooled, and tempered at 420^{o}C and finally air-cooled.

The strength values for forgings 3 are presented in table 3. The limited values requested from the customer were 490-630MPa, min. 345MPa, min.20% and hardness 140-187HB for tensile strength, yield strength, percentage elongation, and hardness respectively. Obtained values, after the heat treatment, were are higher than those requested from the customer.

Table 3: *Mechanical properties of forgings after heat treatment*

	Tensile strength, MPa	Yield strength, MPa	Elongation, %	Hardness, HB
Forgings 1	780	489	21	
Forgings 2	495	297	34,3	145
Forgings 3	520	366-	33,3	168

4. Conclusions

The effect of the high-temperature heat treatment on the mechanical properties and microstructure of the C45 and S355J2 steels forgings have been presented. Despite the improvement on its properties after forging, sometimes forgings cannot be used in the "as-forged" condition since the microstructure and mechanical properties are still not within the specification requirement.

Applying the heat treatment leads to increase the strength of low and medium carbon steels. Different cooling rates result in different phases during a treatment process. The tensile strength, yield strength and hardness decrease with the increase of the holding time.

However, if all the heat treatment parameters are design properly the inappropriate heat treatment conditions (control of temperature and atmosphere inside the furnace e.g.) can be a cause for developing undesired mechanical properties and processes (decarburization e.g.).

5. Acknowledgment

This work was supported by the Ministry of Education, Science and Technological Development of the Republic of Serbia (Grant Agreement No 451-03-9/2021-14/200131).

6. References

1. Q. Ma, Z.-q. Lin and Z.-q. Yu, Int. J. Adv. Manuf. Technol., **40**, **3**, 253-260, (2009)
2. R. Neves Penha, J. Vatavuk, A. A. Couto, S. A. de Lima Pereira, S. A. de Sousa, L. d. C.F. Canale, Eng Fail Anal., **53**, 59-68, (2015)
3. A. Nagode, A. Resnik, R. Vertnik, M. Bizjak, B. Kosec, M. Gojić, G. Kosec, B. Šarler, B. Zorc, Kovove Mater., **55**, 51–56, (2017)

4. N. Kozlov and O. Keßler, Int. J. Therm. Sci., **101**, 133-142, (2016)
5. G. E. Totten, Ed., Steel Heat Treatment Handbook, (CRC Taylor & Francis Group, (2007)
6. M. M. Blaoui, M. Zemri, and A. Brahami, Mech. Mech. Eng., **22**, **4**, 909-918, (2018)
7. D. A. Fadare, T. G. Fadara, O. Y. Akanbi, J Miner Mater Char Eng., **10**, **3**, 299-308, (2011)

Monolayer FeSe Superconductor on Si(001): Electronic Structure Calculations

Karel Carva[1,*], Jan Honolka[2]
Charles University, Faculty of Mathematics and Physics, Department of Condensed Matter Physics, Ke Karlovu 5, 121 16 Prague 2, Czech Republic[1]
Institute of Physics ASCR, Na Slovance 2, CZ-18221 Prague, Czech Republic[2]
karel.carva@mff.cuni.cz

Abstract: *Iron-based unconventional superconductors have attracted intense interest after the critical temperature of FeSe was enhanced by more than one order of magnitude. This was achieved for FeSe placed on top of an insulating oxide substrate with its thickness reduced to the nanometer limit. There are numerous indications of the critical importance of specific features of the FeSe electronic structure in the vicinity of the Fermi surface. Here, we explore how the FeSe band topology changes when located on a Si(001) surface, by first-principles calculations based on the density functional theory. We determine which interface arrangement is preferred and what is the optimal distance between FeSe and Si. Our calculations reveal interesting effects of Si proximity on the FeSe band structure. Bands corresponding to hole pockets at the Γ point in NM FeSe are generally pushed down below the Fermi level. We explain these changes by a redistribution of electrons between different Fe orbitals rather than charge transfer to/from Si.*

Keywords*: SUPERCONDUCTIVITY, INTERFACE EFFECTS, THIN LAYERS , FIRST PRINCIPLES CALCULATIONS*

1. Introduction

FeSe superconductor has been attracting attention in recent years due to its simple structure, open questions regarding its magnetism and pressure dependence of superconducting transition temperature. Furthermore, the critical temperature has been shown to increase dramatically when FeSe with nanoscale thickness is situated on oxide substrates, up to 100 K for monolayer FeSe on $SrTiO_3$ substrate [1].

Superconductivity strongly depends in these compunds on detailed band fillings, and information about the change of electronic structure could help to predict whether superconducting transition temperatures may increase or not [2]. The Fermi surface (FS) of bulk FeSe indicates nesting between hole pockets at Γ and electron pockets near M points [3]. However, the electronic structure of FeSe on $SrTiO_3$ undergoes a Lifshitz transition, during which the hole pockets at Γ vanish [1]. It was found that for FeSe on SrTiO3 , an even higher T_C can be achieved by the deposition of potassium atoms onto FeSe, which leads to electron doping [4]. This increase in T_C is associated to another Lifshitz transition, where electron pockets appear at Γ [5]. Connections between Lifshitz transitions and an increase in T_C have already been discovered for other Fe-based superconductors.

The physical mechanism of superconductivity of FeSe SC at the interface to non-conductive perovskite-type oxide substrates is under intense debate, but only few other substrates have been studied for comparison. In this work, we study the interface between FeSe and semiconductingve Si(001) by ab initio DFT methods. Like $SrTiO_3$, Si(001) has an in-plane lattice constant, which is comparable to that of FeSe (mismatch 1%), and thus might allow a large-scale single-crystalline interface growth without formation of azimuthally rotated FeSe domains as observed on unmatched substrates [6]. We examine here the electronic structure of FeSe monolayers interfaced to Si with a special attention to features considered important for supeconductivity. We show changes in the energetical distribution of individual bands that can be tracked in atom-resolved densities of states as well as in occupations of individual Fe 3d orbitals.

2. Methods

The full-potential linear augmented plane wave (FP-LAPW) method implemented in the band structure program ELK [7] has been employed in density funtional theory calculations. The generalized gradient approximation (GGA) parametrized by Perdew-Burke-Ernzerhof [8] has been used to determine the exchange-correlation potential. Spin-orbit coupling (SOC) is known to play key role in FeSe electronic structure near the Fermi level [9] and has been included in the calculation. Calculations presented here assumed nonmagnetic state, e.g. zero spin-polarization for all atoms.

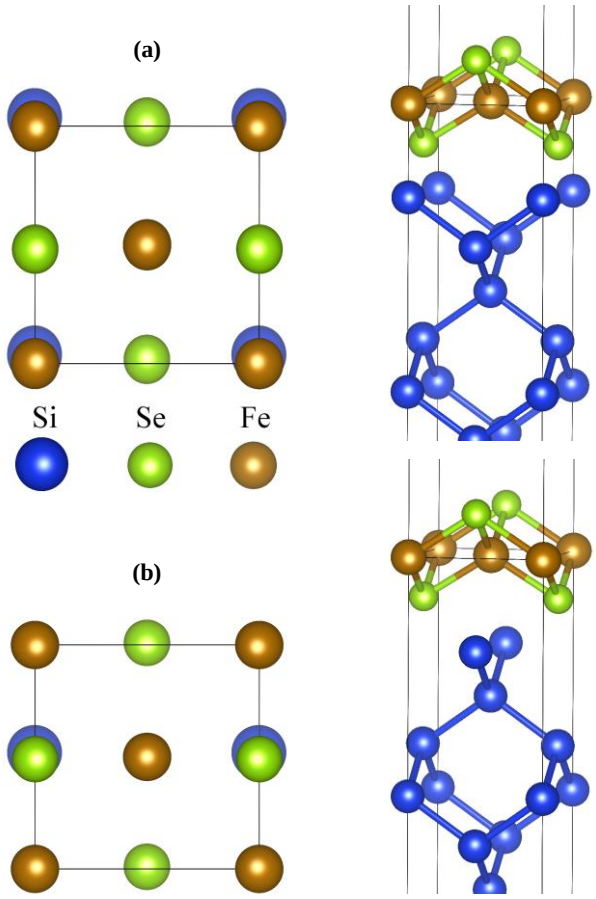

Fig. 1 *Atomic structure of an FeSe monolayer on the Si(001) surface with two possible interface configurations: (a) IC1, (b) IC2. For both the top view and side view is shown. Top view includes Si atoms from the interfacial layer plus Fe and Se atoms. Images were drawn using the 3D visualization program for structural models, VESTA.*

The FeSe adlayer on Si has been modelled using 8 Si(001) layers. Within the supercell an 8 Å thick vacuum spacer was included to simulate the surface. The full Brillouin zone has been sampled by 10 x 10 x 1 *k*-points. For each magnetic and interface configuration we have found the optimal distance $d_{Si\text{-}Se}$ between the interfacial Si plane and its neighboring Se plane with respect to the total energy. The results were compared to the free-standing FeSe

monolayer serving as a special idealized limiting case, in order to elucidate which properties originate from the Si interface and which are due to the FeSe thickness reduction down to the monolayer limit. The free-standing monolayer is not expected to be stable according to DFT calculations [10].

In our bandstructure plots we show only bands with a significant projection onto FeSe atomic orbitals. Fe and two non-equivalent Se atoms are distinguished by colors, while the respective color intensity indicates the amount of projection to these atoms.

Notably the presence of FeSe on Si(001) leads also to a small straining as compared to the bulk FeSe case. In our calculation the FeSe lattice constant is accomodated to that of Si, a = 3.85 Å, which means its enlargement by 2.5% (slightly less than in the case of $SrTiO_3$).

3. Results and discussion

There are two plausible relative arrangements of the Si surface w.r.t. the FeSe ML, denoted as interface configurations IC1 and IC2 (see Fig. 1). IC1 introduces a larger difference in the environment of the two Fe atom sublattices, resulting possibly in a difference of the corresponding magnetic moments. IC1 is energetically more favorable according to our calculations [11].

One of the key parameters affecting the electronic structure of FeSe adlayers is the distance from the substrate. The optimal distance differs between the studied cases, being larger for IC2 compared to IC1 configurations (see Fig. 2). In all cases the distance was smaller than the value found for the $SrTiO_3$ interface [12], probably due to the low atomic density of the Si lattice and the tendency of Si to form covalent bonds. For NM IC1 we obtain the shortest interplane distance $d_{Si\text{-}Se}$=1.47 Å, which is slightly larger than the chalcogen plane distance from the Fe plane.

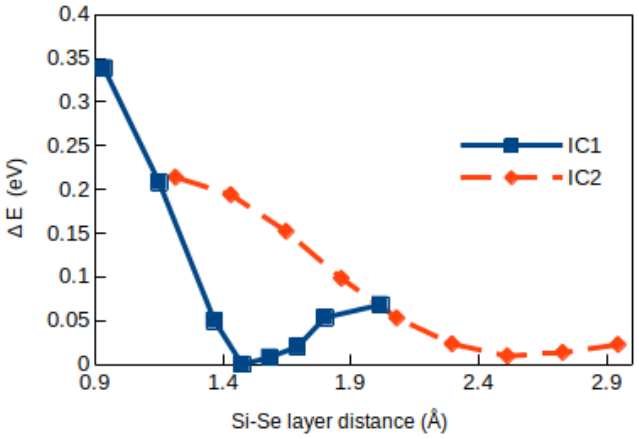

Fig. 2 *Total energy relative to its minimum value ($\Delta E = E - E_{min}$) as a function of the distance $d_{Si\text{-}Se}$ between Si and Se layers for a FeSe monolayer on the Si(001) surface with two possible interface configurations IC1 and IC2.*

There is not too big difference between band structures of free-standing monolayer FeSe and bulk FeSe regarding features near the Fermi level (Fig. 3 (a) and (b)). In both cases, similar hole pockets near Γ and electron pockets near M are present, with only quantitative differences between them, in approximate agreement with previous calculations [13]. Comparing Fig. 3 (b) for the free-standing ML FeSe and Fig. 3(d) for the most favorable IC1 configuration we observe that the Fermi level is positioned differently w.r.t. bands. Some bands originally crossing the Fermi level are pushed below it, with only a small hole pocket at Γ remaining. However, our calculations do not show a significant charge transfer between Si and FeSe. For FeSe on Si, in the case of IC1 configuration (Fig. 3 (d)), there is apparently very strong hybridization with Si interfacial bands indicated by the loss of Fe/Se character at some points of the Brillouin zone. It is much stronger than for IC2 (Fig. 3 (c)) due to the smaller distance of FeSe to the substrate. Especially the Fe band located below −2 eV with energy minimum at Γ is affected. To understand the shift of the Fermi level relative to different bands, we have also extracted the orbital-resolved DOS for Fe atoms. For FeSe on Si the occupation of d_{yz} is increased, while that of d_{xy} and d_{z2} is reduced. the degeneracy between d_{xz} and d_{vz} orbitals is lifted due to the reduced symmetry in the system. The two FeSe electron pockets located at the M point became flatter and the outer one of them (mostly of d_{xy} character) is strongly hybridized with Si [11].

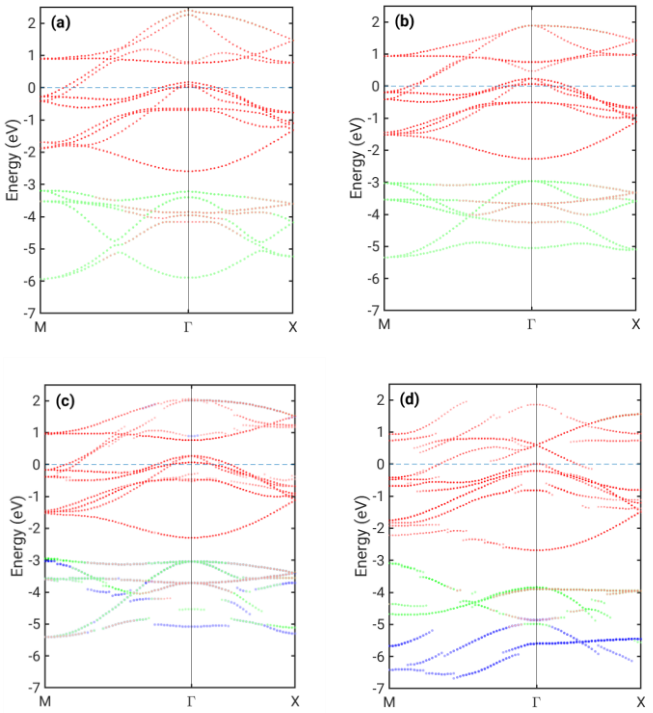

Fig. 3 *Bandstructure cuts of (a) bulk FeSe, (b) free-standing FeSe ML, (c) 1ML FeSe on top of Si, IC2 (d) 1ML FeSe on top of Si, IC1, Colors indicate atomic character: red (Fe), blue (Se in the plane closer to the surface), green (Se in the plane closer to Si). .*

Our theoretical contribution on FeSe - Si(001) interfaces is not only interesting from a fundamental physics point of view, but may have an impact on future nanotechnological applications or in the area of quantum computing [12]. The Si(100) surface is the most important facet for silicon-based metal–oxide semiconductor device fabrication. Moreover, we want to mention that instead of serving as a substrate, silicon may also become important to terminate and protect FeSe-based heterostructures from deterioation in air: most studies on SC in FeSe/$SrTiO_3$ heterostructures use scanning-tunneling spectroscopy (STS) and angle-resolved photoemission spectroscopy (ARPES) studies performed under ultra-high vacuum conditions, but FeSe is found to be susceptible to contaminants like water, reducing Tc drastically [15].

4. Conclusions

We have predicted the optimal interface configuration and interlayer distance for FeSe monolayer on Si(001). Calculated electronic structure shows that some FeSe bands originally crossing the Fermi level are pushed below it due to Si proximity, and the remaining hole pocket around Γ is significantly suppressed.

Complete removal of hole pockets from the Fermi surface, as observed for the $SrTiO_3$ interface, appears to be possible. Bands corresponding to electron pockets centered at M were flattened and one of them strongly hybridized with Si. This is connected to a redistribution of charge between different Fe 3*d* orbitals, during which also the degeneracy between d_{xz} and d_{yz} orbitals is lost.

Acknowledgements

We acknowledge financial support by the Czech Science Foundation (Grant No. 19-13659S).

References

1. X. Liu, et al., J. Phys.: Condens. Matter **27**, 183201 (2015)
2. A.I. Coldea and M.D. Watson, Annu. Rev. Condens. Matter Phys. **9**, 125 (2018)
3. P.J. Hirschfeld, M.M. Korshunov, I.I. Mazin, Rep. Prog. Phys. **74**, 124508 (2011)
4. Y.Miyata, et al., Nat. Mater.**14**, 775 (2015)
5. X. Shi, et al., Nat. Commun. **8**, 14988 (2017)
6. J. Fikáček, et al. New J. Phys. **22**, 073050 (2020)
7. The ELK Code. Available online: http://elk.sourceforge.net/
8. J. P. Perdew, K. Burke, M. Ernzerhof, Phys. Rev. Lett. **77**, 3865 (1996)
9. R.M. Fernandes, O. Vafek, Phys. Rev. B **90**, 214514 (2014)
10. S. Haastrup, et al. 2D Mater. **5**, 042002 (2018)
11. K. Carva, P. Vlaic, and J. Honolka, Nanomaterials **12**, 270 (2022)
12. K. Liu, et al., Phys. Rev. B **91**, 045107 (2015)
13. A. Subedi, et al., Phys. Rev. B **78**, 134514 (2008)
14. D. Castelvecchi, Nature **541**, 9 (2017)
15. I. Bozovic, C. Ahn, Nat. Phys. **10**, 892 (2014)

Microstructure and hardness of Cu-Al-Ni-Fe alloy after precipitation hardening

Ivana Marković[1,*], Marko Banković[2], Ljubiša Balanović[1], Dragan Manasijević[1], Jasmina Petrović[1]
University of Belgrade, Technical Faculty in Bor, Bor, Serbia[1]
Serbia Zijin Copper RBM Branch Majdanpek, Majdanpek, Serbia[2]
[*]imarkovic@tfbor.bg.ac.rs

Abstract: *Nickel aluminum bronze with the composition CuAl9Ni3Fe3 was investigated in this paper. After casting, the alloy was annealed at 900 °C followed by quenching. Thermodynamic calculation of the existing phases was performed using the ThermoCalc software. Quenched NAB samples were further aged for 1 h at 300 °C, 350 °C, and 400 °C. During the experiment, the values of hardness and microhardness were examined using standardized Vickers measurement methods. Microstructural analysis was performed using scanning electron microscopy equipped with an energy-dispersive spectrometer. During the precipitation hardening, β' martensite eutectoidly decomposed into α and κ phases causing an increase in mechanical properties.*

Keywords*: NICKEL ALUMINUM BRONZE, MICROSTRUCTURE, PRECIPITATION HARDENING*

1. Introduction

Nickel-aluminum bronzes (NAB) are copper-based alloys with aluminum, nickel, and iron as alloying elements [1]. They have high strength, good resistance to wear, and corrosion, which makes them suitable as engineering materials for propellers, gears, bearings, valves, and dies. The commercial NAB usually have a microstructure consisting of α phase which is a copper-based solid solution, some β phase, and intermetallic κ phases [2, 3]. Due to the relatively low solubility of alloying elements in a metallic matrix, designed of the α and β phases, it is characterized by dendritic micro segregation [4]. The precipitation processes of the κ phases were described in [5]. During cooling the melt, the κ_I phase rich in iron precipitates the first. It is formed in a liquid alloy in the shape of a large rosette. A κ_{II} phase precipitates next. Particles of the κ_{II} phase are smaller than the κ_I particles and have a shape as rosettes or globules. Further, a κ_{III} phase rich in nickel precipitates at the α/β boundaries. The κ_{III} particles are small with a plate shape. A κ_{IV} phase precipitates the last. Particles are smaller than the κ_I and κ_{II} particles but as well rich in iron.

To improve the mechanical properties of the NAB, some techniques have been used for refining grains and changing the microstructure: friction surfacing, equal channel angular extrusion, friction stir processing, etc. However, these techniques are expensive and have low efficiency. Because of that, heat treatment is usually used to improve the mechanical properties of the NAB [6, 7].

There are a limited number of papers in the literature that analyze the microstructural changes in the NAB during heat treatment. Brezina found that the optimal quenching temperature for the NAB was about 900 °C, while the optimal temperatures for the precipitation hardening treatment were about 400 °C - 500 °C [8]. Liu et al. confirmed that precipitation began at lower temperatures [9]. Therefore, in this paper, the precipitation hardening was performed at the lower temperatures: 300 °C, 350 °C, and 400 °C to follow the influence of aging temperatures on the properties of CuAl9Ni3Fe3 alloy.

2. Experimental part

The alloy CuAl9Ni3Fe3 was obtained by a casting method. After measuring the calculated amount of copper and alloying elements, their melting was performed in a flame furnace with a silicon carbide pot. The casting of melt was performed in a sand-clay mold. Chemical analysis by the "Thermo Scientific Niton XL 3T Gold+" spectrophotometer showed 8.996 wt.% Al, 2.619 wt.% Ni, 3.309 wt.% Fe and rest copper in the composition of an ingot. The ingot was cut on samples with dimensions 43 mm x 15 mm x 6 mm, which were subjected to further heat treatment. Cutting was performed using the cutting machine "Mesotom – Struers".

For further heat treatment, there was not found in the literature the vertical cross-section of a Cu-Al-Ni-Fe phase diagram with 3% nickel and 3% iron. Because of that, the thermodynamic calculation of the phase diagram of a CuNi3Fe3-Al system was performed using the ThermoCalc software. Table 1 shows the phases and their calculated composition of the investigated CuAl9Ni3Fe3 alloy at 878 °C.

Table 1: Phases and their composition in the CuAl9Ni3Fe3 alloy at 878 °C.

Phases	Phase's content, wt.%	Composition, wt.%	
B2_BCC#1 (κ_{III})	3.64868	Ni	68.270
		Al	31.730
BCC_B2#1 (κ_I or κ_{II})	2.19779	Fe	84.280
		Al	12.272
		Cu	3.358
		Ni	0.089
BCC_B2#2 (β)	15.74899	Cu	87.959
		Al	9.320
		Fe	2.699
		Ni	0.021
FCC_L12#1 (α)	78.40454	Cu	90.649
		Al	7.787
		Fe	0.922
		Ni	0.642

The samples were heated in the "T 40/600" tube furnace in the atmosphere of pure hydrogen at 900 °C for 1 h. After solid-solution annealing, the samples were quenched in cold water. The quenched samples were aged in the electric resistance furnace "Heraeus K 1150/2" without the protective atmosphere at three temperatures (300 °C, 350° C, and 400 °C) for 1 h.

After the casting, quenching, and aging, hardness and microhardness of phases were measured, and microstructure analysis was conducted. The Vickers hardness test was performed using the load of 10 kgf (98 N) during 15 s, on the "VEB Leipzig" hardness tester. The microhardness was measured using the "PMT 3" microhardness tester; at the load of 100 gf (0.98 N) during 15 s. Microstructural changes were analyzed using the scanning electron microscope (SEM) "Tescan Vega 3LMU" equipped with an energy-dispersive spectrometer (EDS) "Oxford Instruments X-act". After standard metallographic preparation by grinding and polishing, the samples were etched with an alcoholic solution of ferric chloride.

3. Results and discussion

The microstructure of as-cast CuAl9Ni3Fe3 alloy was shown in Fig.1. Since cooling speed was higher than that in equilibrium condition, the microstructure of the alloy was composed of an α solid solution (light phase), a residual β phase (dark phase), and different κ phases rich in iron and nickel which appeared in the rosette, spherical or platelet shapes. Four types of the κ phase denoted as κ_I, κ_{II}, κ_{III}, and κ_{IV} can be found in the literature [10, 11]. The κ_I phase appears as large rosette form particles which consist of Fe_3Al with copper and nickel. The κ_{II} phase has similar composition

but the particles are smaller and globular in form. The κ_{IV} are very fine particles (significantly smaller than the κ_I and κ_{II}) based on Fe_3Al within grains. The κ_{III} phase has a plate or lamellar shape and it is rich in nickel [12].

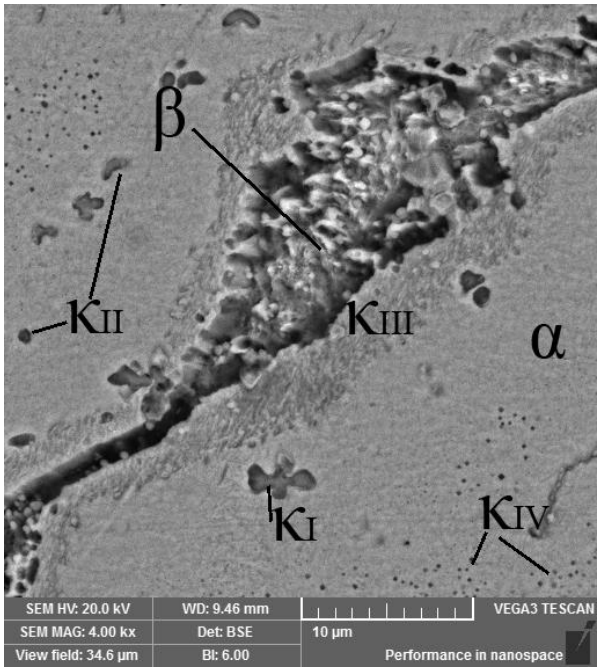

Fig. 1 *Microstructure of as-cast CuAl9Ni3Fe3 alloy.*

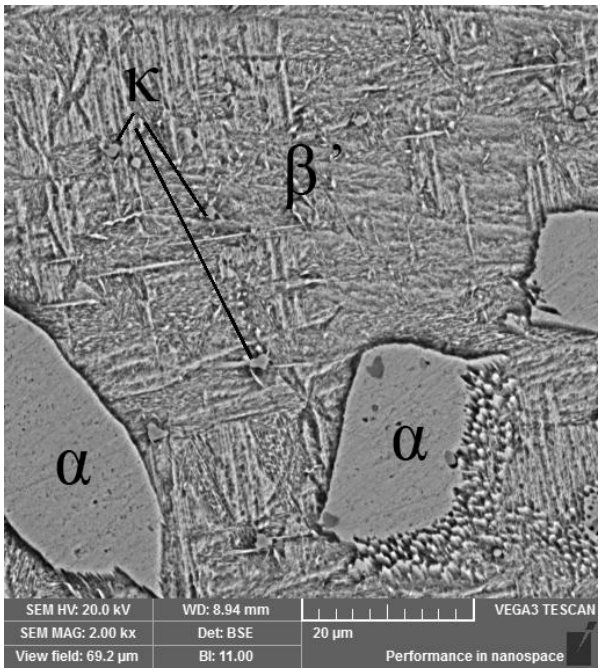

a)

Phases	Al	Fe	Ni	Cu
α	8.2	3.38	2.43	85.99
β’	10.94	3.49	3.52	82.05

b)

Fig. 2 *Microstructure of quenched CuAl9Ni3Fe3 alloy (a) and EDS analysis of the α and β’ phases (b).*

Fig. 2a shows the SEM microphotograph of the CuAl9Ni3Fe3 alloy after quenching from 900 °C. It is noticed that the quenching contributed to a significant change in the microstructure in comparison to the as-cast sample (Fig. 1). The amount of the α phase significantly decreased due to an increase in β’ martensite content. The α phase gradually dissolved into the β phase, which led to a decrease in the volume fraction of the α phase [10]. There was no more the κ_{III} phase and fine precipitates of the κ_{IV} phase because they were dissolved in the α solid solution at 800°C and 850°C, respectively [12]. In the microstructure of the quenched sample, the α and β’ phases were presented together with un-dissolved precipitates of the κ_I and κ_{II} phases. A phases’ composition of the main α and β’ phases from Fig.2a was shown in Fig. 2b.

The hardness of CuAl9Ni3Fe3 alloy after different stages of thermal treatment was shown in Fig. 3. The hardness of cast alloy was around 152 HV10. After quenching from 900 °C, it increased up to 185 HV10. Quenched samples were isochronally annealed at 300 °C, 350 °C, and 400 °C. After precipitation hardening of the quenched sample at 300 °C, the hardness reached a value of 220 HV10. After aging at 350 °C, the hardness increased to 232 HV10, while the maximum value of the hardness was reached at the aging temperature of 400 °C when the hardness increased to 244 HV10. The aging at 400 °C for 1 h caused an absolute increase in the hardness for 59 HV10 compared to the quenched state, or 92 HV10 compared to the cast state, which corresponded to a relative increase in the hardness for 32 % and 60 %, respectively.

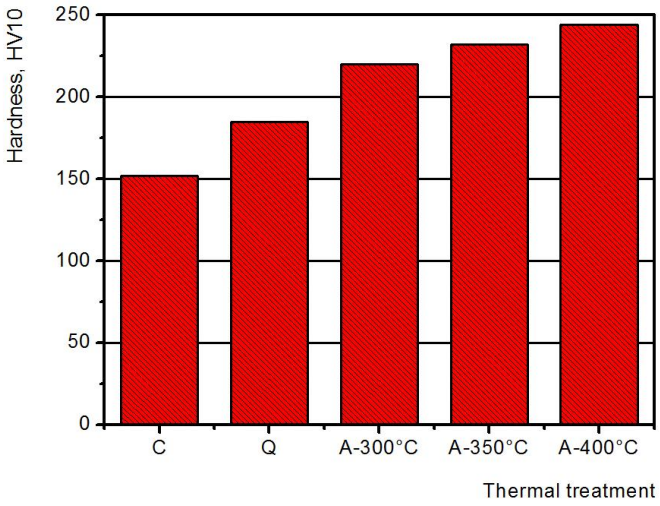

Fig 3. *The hardness of CuAl9Ni3Fe3 alloy after different stages of thermal treatment (C – casting; Q – quenching; A-300°C – aging at 300°C; A-350°C – aging at 350°C; A-400°C – aging at 400°C).*

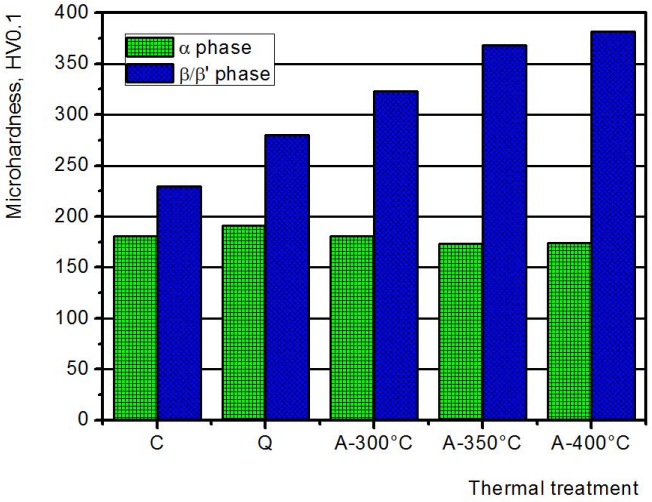

Fig 4. *Microhardness of α and β/β’ phases of CuAl9Ni3Fe3 alloy after different stages of thermal treatment (C – casting; Q – quenching; A-300°C – aging at 300°C; A-350°C – aging at 350°C; A-400°C – aging at 400°C).*

The microhardness of the α and β/β’ phases in CuAl9Ni3Fe3 alloy after different stages of thermal treatment was shown in Fig. 4. The quenching of the cast sample caused an increase in microhardness values of the β phase from 230 HV0.1 to 280 HV0.1,

due to its transformation to martensite β' phase. Further, the microhardness of the β' phase increased during aging in comparison to the quenched state. During the aging at 300 °C, the microhardness value increased to 323 HV0.1. After the aging at 350 °C, the microhardness of the β' phase increased intensively to 368 HV0.1, while its maximum value was achieved after the aging at 400 °C, and it was 382 HV0.1. The aging at 400 °C for 1 h caused an absolute increase in the microhardness of a dark phase for 102 HV0.1 compared to the quenched state, or 152 HV0.1 compared to the cast state, which corresponded to a relative increase in the microhardness for 36 % and 66 %, respectively.

Quenching of the cast sample caused an increase in the microhardness values of the α phase from 181 HV0.1 to 191 HV0.1, However, the results of measuring the values of the microhardness of the α phase during the aging showed different tendencies. It was noticed that the values of the microhardness of the α phase were lower after the aging compared to the quenched state. With an increase in aging temperature, there is the tendency to a slight decrease in the microhardness of the α solid solution. It decreased to 181 HV0.1, 173 HV0.1, and 174 HV0.1 after the aging at 300 °C, 350 °C, and 400 °C, respectively.

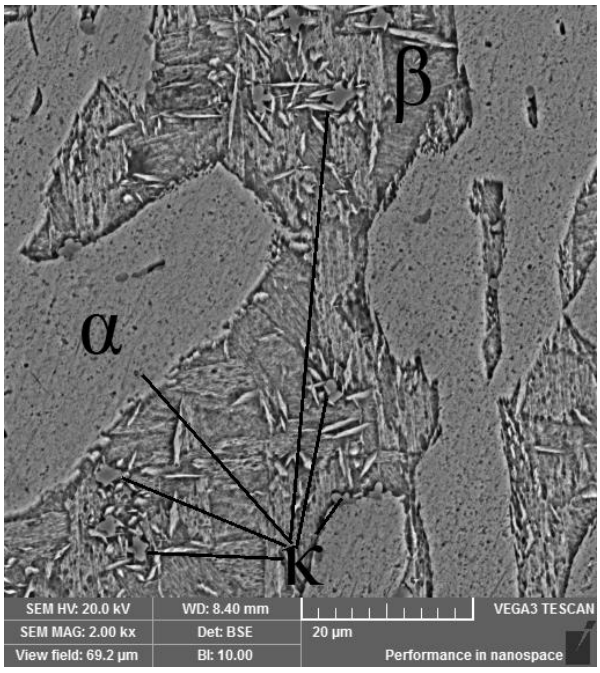

a)

Phases	Al	Fe	Ni	Cu
α	7.57	2.81	2.54	87.09
β'	10.55	3.67	3.78	82.00

b)

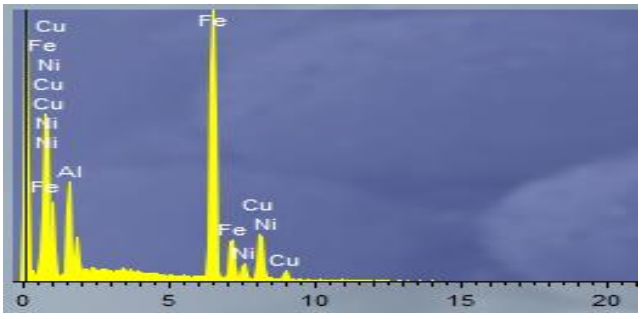

c)

Fig. 5 *Microstructure of quenched CuAl9Ni3Fe3 alloy after aging at 300 °C (a) results of EDS analysis of α and β' phases (b) EDS analysis of one κ phase particle (c).*

During the aging, fine particles of the κ phases precipitated from the martensite β' phase [13]. The κ precipitates formed during the aging were finer compared to those formed during casting. The κ phases were harder than β'martensite. However, the contribution of the α phase increased with an increase in the aging temperature. Two opposite effects occurred during the aging. The first effect is a decrease in the hardness due to an increase in the contribution of the α phase, and the second effect is an increase in the hardness due to the precipitation of the fine particles of κ phases [14]. The second effect became more dominant in comparison to the first one, consequently, the hardness increased with increasing the aging temperature.

Fig. 5a shows the SEM microphotograph of CuAl9Ni3Fe3 alloy after quenching from 900 °C and aging at 300 °C. The β' martensite needles with the κ phases spherical or rosette in a shape were still observed. The needle martensite formed by the quenching at 900 °C did not change its morphology into the banded martensite after the aging at 300 °C. However, the martensite's structure started to transform into the α phase.

A phases' composition of the main α and β' phase from Fig.5a was shown in Fig.5b. The content of the alloying elements in the β' martensite is higher than in the α solid solution therefore, phase changes that occurred in the β' phase were the main causes of an increase in the mechanical properties during the aging. The precipitation of the fine κ particles in the β' martensite is most likely to occur [2, 10]. The EDS analysis of one κ phase particle from Fig.5a was shown in Fig.5c.

4. Conclusions

Based on the experimental results on the investigation of the effect of precipitation hardening on the microstructure and hardness of the CuAl9Ni3Fe3 alloy, the following conclusions can be drawn:

• The microstructure of as-cast CuAl9Ni3Fe3 alloy consisted of the α solid solution, the residual β phase, and the κ_I, κ_{II}, κ_{III}, and κ_{IV} phases.

• The quenching has caused microstructural changes. The amount of the α solid solution decreased due to an increase in the content of the β'martensite. The eutectoid rich in the κ_{III} phase and fine precipitates of the κ_{IV} phase were dissolved. Only the precipitates of κ_I and κ_{II} pha'ses have remained.

• The aging of the quenched alloy further increased the values of hardness and microhardness of the β' phase due to the precipitation of the fine κ particles from the β' phase. The content of aluminum in the β' martensite was higher than in the α solid solution, so phase changes that occurred within the β' phase were the main causes of an increase in the mechanical properties during the aging.

• Maximum values of hardness (244 HV10) and microhardness of the β' phase (382 HV0.1) were achieved after the aging at 400 °C.

• The aging caused a decrease in the microhardness value of the α solid solution. Due to the precipitation of the κ phase, the content of alloying elements in the α solid solution decreased, causing a decrease in the microhardness value.

• The martensite lamellas were still observed in the aged state, which eutectoidically decomposed into the α and κ phases.

Acknowledgment

This work was supported by the Ministry of Education, Science and Technological Development of the Republic of Serbia (Grant Agreement No 451-03-9/2021-14/200131).

5. References

1. Jain P., P. K. Nigam, J. Mech. Eng., **4** (6) (2013) 16-21.
2. Chen R., Z. Liang, W. Zhang, D. Zhang, Z. Luo, Y. Li, T. Nonferr. Metal Soc., **17** (2007) 1254-1258.
3. Ding D., Z. Pan, S. van Duin, H. Li, C. Shen, Materials, **9** (2016), 652.
4. Pisare B. P., Arch. Foundry Eng., **12** (2012), 187-204.
5. Łabanowski J., T. Olkowski, Arch. Foundry Eng., **14** (2014), 73-78.
6. Lv Y., M. Hu, L. Wang, X. Xu, Y. Han, W. Lu, J. Mater. Res., **30** (20) (2015) 30401-30408.
7. Fuller M.D., S. Swaminathan, A.P. Zhilyaev, T.R. McNelley, Mater. Sci. Eng. A, **463** (2007) 128-137.
8. Brezina P., Int. Mater. Rev., **27** (1) (1982) 77-120.
9. Liu Y., J. Mazumder, K. Shibata, Metall. Mater. Trans. A, **25** (1) (1994) 37-46.
10. Lin G., H. Wang, Y. Wei, Z. Zhang, K. Zhou, J. Mater. Res., **31** (24) (2016) 3832-3840.
11. Thossatheppitak B., S. Suranuntchai, V. Uthaisangsuk, A. Manonukul, P. Mungsuntisuk, Adv. Mat. Res., **683** (2013) 82-89.
12. Sláma P., J. Dlouhý, M. Kövér, Mater. Tehnol., **48** (2014) 599-604.
13. Lv Y., L. Wang, X. Xu, W. Lu, Metals, **5** (2015) 1695-1703
14. Shirazabad M.M., A. Karimi, A. Babakhani, *Proceedings of 3th International Conference on Materials Heat Treatments*, 2012, 51.

Geopolymers based on natural zeolite clinoptilolite with addition of metakaolin

Aleksandar Nikolov
Institute of Mineralogy and Crystallography, Bulgarian Academy of Sciences (IMC-BAS)
Sofia, Bulgaria
E-mail: drsashko@imc.bas.bg

Abstract: *Geopolymers based on natural zeolite clinoptilolite and addition of up to 50% metakaolin were synthesized using binary sodium/potassium alkali activator. The influence of metakaolin addition was evaluated on apparent density, water absorption, relative mass loss after watering and microstructure (XRD) of the prepared geopolymers. The addition of metakaolin greatly influenced the physical and mechanical properties of the obtained geopolymers. Minimal/optimal metakaolin addition was estimated to 30% in the respect of sufficient strength (11 MPa) and the high price of metakaolin. The resulted geopolymer based on natural zeolite and metakaolin (30%) contained residual unreacted clinoptilolite which could be beneficial for properties of future geopolymer products. Potential applications of obtained geopolymer-clinoptilolite agglomerates are: waste or radioactive water decontamination, passive cooling systems, plasters in residential buildings, etc.*

Keywords*: GEOPOLYMER, NATURAL ZEOLITE, CLINOPTILOLITE, METAKAOLIN*

1. Introduction

Carbon dioxide (CO_2) emissions are one of the most significant challenges encountered by humanity nowadays. In 2020, slightly reduced CO_2 emissions were triggered by the ongoing COVID-19 pandemic [1]. Still, Portland cement industry is responsible for 8% of global CO_2 emissions of which 55% of decarbonisation of limestone and 40% of heating the kilns to temperature about 1450 ° C [2]. In recent years, ecological building materials are in the focus of the global research. A potential alternatives of Portland cement are geopolymers. Geopolymers are synthetic inorganic polymers which act as binder to produce monolith stone-like materials. Usually, the geopolymers are comprised of two components– aluminosilicate powder precursor and activator solution. The precursor could be a raw material or industrial by-product consist of high amount of reactive Al_2O_3 and SiO_2. The breakthrough precursor was metakaolin from which first geopolymers was synthesized by Joseph Davidovits in the late 1970s [3]. The metakaolin is a calcined kaolinite clay at temperature about 750 ° C. Geopolymer cements do not rely on limestone and generate much less CO_2 during manufacture, i.e. a reduction in the range of 40% to 80-90%, compared to Portland cement materials [4]. The properties of the geopolymers are similar to Portland cement and even superior as better fire and chemical resistance [5–7]. High strength [8,9] and rapid hardening geopolymers [10] are also reported. This allow geopolymers to partially or entirely replace Portland cement materials.

In general, aluminosilicate binder materials activated by alkali hydroxides or silicates under high-pH conditions are classified as geopolymers [11]. Nowadays, the focus of potential geopolymer precursors is aimed to industrial by-products such as fly ash and slags from heavy metal productions. The benefits of utilizing industrial waste are of ecologic and economic aspects. One of the main drawbacks is the non-persistent chemical and mineralogical composition. Moreover, the industrial waste often consists of undesirable elements such as iron, magnesium, heavy or radioactive metals. Numerous studies reported geopolymer immobilization of hazardous elements [12], but still such materials should not be used in residential buildings. Geopolymer precursors could be of natural origin such as volcanic tuffs, perlite, zeolite, clay, rock dust, etc. Geopolymers based on natural materials are more suitable for residential buildings.

One of potential ecological geopolymer precursorc are natural zeolites. Zeolite rocks are composed of zeolite minerals, such as clinoptilolite, mordenite, phillipsite, chabazite, etc - over 30 species. The major world deposits are located in USA, Cuba, Japan, Bulgaria, Russia, China, Italy, Mexico, Slovakia and others [13]. The natural zeolite deposits in Bulgaria are mostly clinoptilolite type – located in Eastern Rhodopes. The only commercially available is near Beli Plast village (Kardzhali region). The quality is very good, as the amount of clinoptilolite reaches 90% of the rock composition. The zeolites are crystalline, hydrated, aluminosilicates with lattice structure. Their three dimensional network is composed of SiO_4 and AlO_4 tetrahedra sharing oxygen atoms. The zeolite structure contains channels and connected cavities of different sizes, where water molecules and cations are located, necessary to balance the negative balance of the structure. The cations are mobile and could be exchanged [14]. The density of zeolites varies from 1.9 to 2.3 g/cm^3 depending on the type of cations. The structure of clinoptilolite contains micropores with dimensions corresponding to molecular diameters. This gives the zeolite function of a molecular sieve. The water molecule can enter the network of channels, but other, heavier (large) molecules remain "locked" in. The pores of clinoptilolite are heterogeneous, with two types of pores observed. The main porosity is microporosity (0.5 nm - 2.5 nm) composed of the clinoptilolite three-dimensional aluminosilicate lattice, which forms a nanosystem of channels. The second type of pores are mesopores and macropores (2.5 nm – 50 nm), which may contain water [15]. The specific structure of zeolites gives a variety of useful properties in different areas of application. Zeolites are used as molecular sieves, ion exchangers, catalysts and others. Based on these characteristics, devices and technologies with high efficiency and diverse focus have been created: enrichment of the air with oxygen, extraction of radioactive elements from solutions [16], purification of wastewater and domestic water [17], removal of ammonia from wastewater, extraction of acidic components from wastewater, separation of gases, separation of normal and aromatic hydrocarbons, extraction and separation of rare alkaline (Rb, Cs, Li), colored (Cu, Zn, Pb), heavy (Ag) and alkaline earth (Sr) elements. Zeolite is also used in various fields of catalysis [18]. In many countries, from ancient times zeolite rocks are used as a building material [19]. Recently, zeolite raw material has been used to produce new, non-traditional building materials such as geopolymers [20–22].

In previous studies the potential of natural zeolite as geopolymer precursors was evaluated [23–25]. The results showed that geopolymers based on natural zeolite possess excellent adhesion to concrete [26]. However, geopolymers based on natural zeolite slowly gain strength at normal temperature and undergo high shrinkage [27]. The aim of the present work is to study the influence of metakaolin addition to properties of geopolymers based on natural zeolite.

2. Materials and methods

2.1. Method of analysis

The density was measured by hydrostatic weighing method and calculated using Equation 1:

$$D = \frac{m_d}{m_w - m_{w,w}}, g/cm^3$$

, where:

m_d – mass of dried specimens after watering

m_w – mass of water absorbed specimens

$m_{w,w}$ – mass under water of water absorbed specim*ens*

Equation 1. Calculation of density by hydrostatic weighing method

The relative mass loss was calculated based on dried mass before and after watering of the specimens.

The mechanical properties were evaluated using 3 cubic specimens with side area 10 cm^2 each series.

The XRD patterns were obtained by Panalytical Empyrean at 40 kV and 30 mA. The chemical composition was analyzed by X-ray fluorescence apparatus - Rigaku Supermini 200 using 30 mm pressed tablets.

3.1. Materials

The main geopolymer precursor in the present experiment was natural zeolite from Beli Plast, Bulgaria, provided by Imerys, a commercially available product with particle size < 0.15 mm. The chemical composition of the natural zeolite is presented in Table 1.

Commercial metakaolin, provided by Kaolin EAD, Bulgaria, was used in order to enhance the properties of the geopolymer. The metakaolin is produced by calcination of local kaolinite clay. The wet residue on 45 μm sieve of the metakaolin is 0.40%. The chemical composition of the natural zeolite is presented in Table 1.

Table 1. Chemical composition of the geopolymer precursor - natural zeolite clinoptilolite(NZ) and metakaolin (MK)

	SiO_2	Al_2O_3	CaO	K_2O	MgO	Fe_2O_3	Na_2O	TiO_2
MK	53.94	43.2	0.15	0.62	0.09	1.14	0.11	0.74
NZ	78.89	11.71	3.43	3.09	1.13	1.11	0.44	0.19

The activator solutions were prepared by using solid KOH pellets, sodium water glass with molar modulus about 3 and tap water. The ingredients were mixed by magnetic stirrer a day prior the synthesis of geopolymers.

2.3. Geopolymer synthesis

Total of 6 series were prepared with different concentration of the activator. The composition design is presented at Table 2 in molar ratios. Sample ZM20 was designed with higher SiO_2/Al_2O_3 by addition of more water glass. The recipes are based on best results from previous studies on geopolymers based on natural zeolite [26] and metakaolin [28], separately.

The geopolymer precursor and activator solution were mixed and homogenized with mechanical stirrer for 1 min. The mixtures were rested to mature for 5 min, then mixed again for 30 seconds. From each series certain amount of the geopolymer paste was taken for microstructural examination (XRD). To determine mechanical and physical properties the fresh geopolymer paste was mixed with quartz sand (zeolite to sand = 1:2 by mass) and homogenised mortar was poured in steel cubic moulds. The samples were stored in plastic bags for three days at laboratory conditions (20 ^oC), then placed at 80 ^oC for 24 hours.

Table 2. Composition design in molar ratios and water to solid ratio (w/s) of the prepared geopolymers

Series	Molar ratio			w/s
	SiO_2/Al_2O_3	Al_2O_3/M_2O	H_2O/M_2O	
ZM5	11.70	0.32	10.19	0.51
ZM10	10.43	0.36	10.43	0.52
ZM20	8.55	0.43	10.90	0.54
ZM20W	9.41	0.40	10.91	0.54
ZM30	7.23	0.51	11.40	0.56
ZM50	5.51	0.65	12.37	0.59

3. Results and Discussion

3.1. Physical and hydrophysical properties

The outside appearance of the geopolymer series was characterized by visible with bare eye cracks in decreasing manner with the addition of metakaolin. The physical and hydrophysical properties of the prepared geopolymer mortars are presented at Table 3. The apparent density of the geopolymers increased with the increase of metakaolin addition up to 30%, then at 50% slight decrease was observed. The water absorption was lower at 20% metakaolin addition, then steady increased and the value was about 20% at 50% metakaolin. The lack of straightforward correlation between metakaolin addition and density and water absorption is probably due to different water to solid ratio of the series. However, the relatively high water absorption (about 14-20%) and relatively low density is a sign for well-developed porous structure.

The relative mass loss was very high at low level of metakaolin additions. The samples lost mass probably because they contained water soluble unreacted activator and/or partial disintegration due to low strength. The relative mass loss was about 1% or less at 30% or more metakaolin addition.

The usage of more water glass (ZM30W) led to higher density and lower water absorption.

Table 3. Apparent density, water absorption and relative mass loss after watering of the prepared geopolymers

Series	Density, g/cm^3	Water absorption, %	Relative mass loss, %
ZM5	1.56	18.0 ± 0.1	8.0 ± 0.4
ZM10	1.63	16.3 ± 0.1	6.0 ± 0.3
ZM20	1.69	15.4 ± 0.3	3.1 ± 0.3
ZM20W	1.72	13.6 ± 0.2	3.3 ± 0.1
ZM30	1.70	17.5 ± 0.1	1.3 ± 0.1
ZM50	1.65	20.4 ± 0.1	0.7 ± 0.1

3.2. Compressive strength

The results of compressive strength tests of the prepared geopolymer mortars are presented at Figure 1. The addition of metakaolin up to 20% showed no beneficial effect on strength, thus geopolymers was characterized by only about 3 MPa. Significant strength increase was observed with addition of 30% and 50% metakaolin, respectively – 11 and 20 MPa. Minimal/optimal metakaolin addition is determined at 30% in the respect of sufficient strength and the high price of metakaolin, respectively minimal amount of addition.

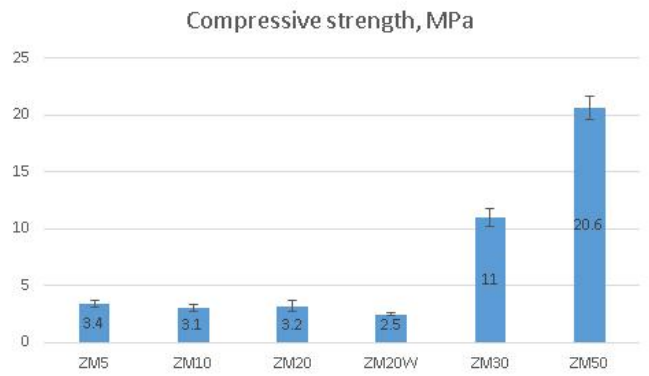

Figure 1. Compressive strength of the prepared geopolymers

3.3. Powder XRD

The natural zeolite, metakaolin and the prepared geopolymers were examined by Powder X-ray diffraction. The results are presented in **Грешка! Източникът на препратката не е намерен.**. The natural zeolite was comprised of clinoptilolite (~80%) and opal-cristobalite. Metakaolin showed amorphous structure presented by broad halo between 15 – 30 2θ° , and quartz inclusion. The geopolymer samples ZM30 showed characteristic amorphous halo for geopolymers between 22 – 37 2θ° . Opal-cristobalite presented in the natural zeolite was completely dissolved to take part of geopolymerization process. The clinoptilolite reacted partly thus geopolymer contains residual clinoptilolite which could be beneficial for the future properties of the geopolymer product.

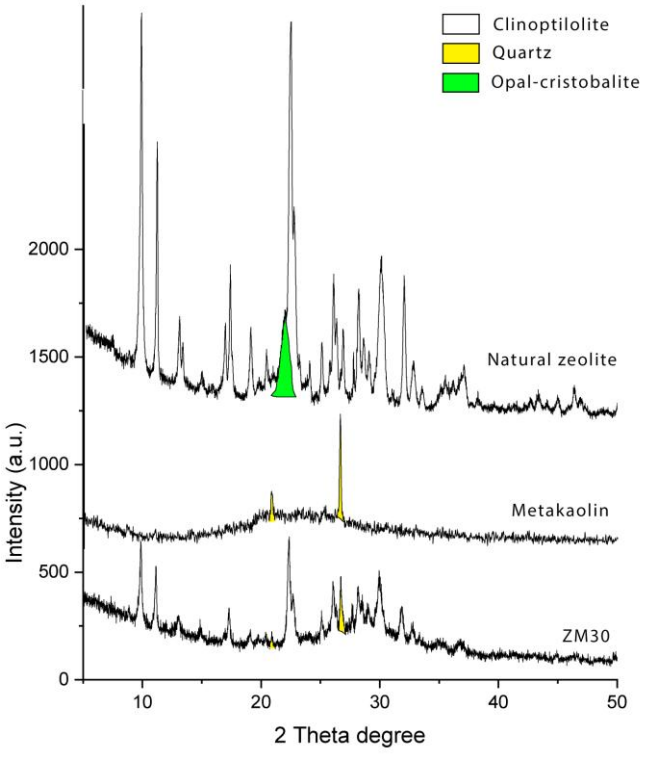

Figure 2. Powder XRD diffractograms of the precursors and geopolymer series ZM30

4. Discussion on possible applications

The different metakaolin addition to the synthesized geopolymers greatly influenced the physical and mechanical properties of the final material. The addition of 30% or more metakaolin guarantees satisfactory integrity of the synthesized geopolymers clinoptilolite agglomerates. The result was synthetic geopolymer-clinoptilolite agglomerate consist of geopolymer gel phase and unreacted clinoptilolite. Moreover, the filler from quartz sand could be replaced with fractionized crushed natural zeolite in order to increase the zeolite content. The shape of the geopolymer-clinoptilolite agglomerates could be designed from irregular - produced in moulds, to spherical shapes fabricated by granulation techniques, or layered plaster on surface. Both clinoptilolite and geopolymer gel possess sorption and ion-exchange properties [16,29,30]. Consequently, geopolymer-clinoptilolite agglomerates probably could be utilized in waste water treatment for heavy metal and radioactive decontamination. However, the high pH and high alkali content of the geopolymer must be also considered. More studies are needed to evaluate sorption capacity and selectivity of the synthetic geopolymer-clinoptilolite agglomerates.

Rising temperatures in big cities are an increasing problem, especially at arid areas, or in summer. This effect arises from the increasing amount of heat generated by human activities and cumulative surface areas covered by artificial materials with high solar absorption capacity. This warming phenomenon is known as “heat island effect”. One of the possible methods for counteracting the “heat island effect” is application of passive cooling systems using evaporation of water absorbed by porous material [31]. Both natural zeolites and geopolymers are suitable for passive cooling materials [31,32]. The synthesized geopolymer-clinoptilolite agglomerates appears to be candidate for materials with passive cooling properties. More studies are required to evaluate application of the synthetic geopolymer-clinoptilolite agglomerates in passive cooling systems.

5. Conclusion

The metakaolin greatly influenced the physical and mechanical properties of prepared geopolymers based on natural zeolite clinoptilolite. The addition of up to 20% metakaolin did not bring beneficial effect to the properties of the prepared geopolymers. Minimal/optimal metakaolin addition was estimated to 30% in the respect of sufficient strength (11 MPa) and the high price of metakaolin. The resulted geopolymer based on natural zeolite and metakaolin (30%) contained residual unreacted clinoptilolite which could be beneficial for the future properties of the geopolymer product. Potential applications of obtained geopolymer-clinoptilolite agglomerates are: waste or radioactive water decontamination, passive cooling systems, plasters in residential buildings.

6. Acknowledgement

The results in this work have been achieved in fulfilment of a project financed by the National Science Fund of Bulgaria under contract **No. КП-06-М47/1 from 26.11.2020**. The author acknowledges the technical support (XRD) from the project PERIMED BG05M2OP001-1.002-0005 /29.03.2018 (2018–2023). Special thanks to PhD Liliya Tsvetanova for XRF measurements.

6. Literature

[1]. B. Li, N. Haneklaus, Reducing CO2 emissions in G7 countries: The role of clean energy consumption, trade openness and urbanization, Energy Reports. 8 (2022) 704–713.
[2]. N. Müller, J. Harnisch, A blueprint for a climate friendly cement industry, Gland WWF Lafarge Conserv. Partnersh. (2008).
[3]. J. Davidovits, Solid-phase synthesis of a mineral blockpolymer by low temperature polycondensation of alumino-silicate polymers: Na-poly (sialate) or Na-PS and characteristics, in: Proc. IUPAC Symp. Long-Term Prop. Polym. Polym. Mater. Stock. Sweden, 1976.
[4]. J. Davidovits, Geopolymer cement a review, published in geopolymer science and technics, Technical paper\# 21, Geopolymer Institute Library, (2013).
[5]. M. Lahoti, K.H. Tan, E.-H. Yang, A critical review of geopolymer properties for structural fire-resistance applications,

Constr. Build. Mater. 221 (2019) 514–526. https://doi.org/10.1016/J.CONBUILDMAT.2019.06.076.
[6]. T. Bakharev, Resistance of geopolymer materials to acid attack, Cem. Concr. Res. 35 (2005) 658–670.
[7] W.G. Valencia Saavedra, D.E. Angulo, R. de Gutiérrez, Fly ash slag geopolymer concrete: Resistance to sodium and magnesium sulfate attack, J. Mater. Civ. Eng. 28 (2016) 4016148.
[8]. H.W. Nugteren, V.C.L. Butselaar-Orthlieb, M. Izquierdo, High strength geopolymers produced from coal combustion fly ash, Glob. NEST J. 11 (2009) 155–161.
[9]. A. Nikolov, Characterization of geopolymer based on fayalite waste and metakaolin with standard consistence, Comptes Rendus l'Acad_emie Bulg. Des Sci. 74 (2021) 1461–1468. DOI:10.7546/CRABS.2021.10.05.
[10]. A. Nikolov, R. Titorenkova, N. Velinov, Z. Delcheva, Characterization of a novel geopolymer based on acid-activated fayalite slag from local copper industry, Bulg. Chem. Commun. 50 (2018) 54–61.
[11]. J.L. Provis, J.S.J. Van Deventer, Geopolymers: structures, processing, properties and industrial applications, Elsevier, 2009.
[12]. Z. Ji, Y. Pei, Bibliographic and visualized analysis of geopolymer research and its application in heavy metal immobilization: A review, J. Environ. Manage. 231 (2019) 256–267.
[13]. W.S. Wise, MINERALS | Zeolites☆, in: Ref. Modul. Earth Syst. Environ. Sci., Elsevier, 2013. https://doi.org/10.1016/B978-0-12-409548-9.02906-7.
[14]. Ullmann's encyclopedia of industrial chemistry, Verlag Chemie, 1991.
[15]. N. Mansouri, N. Rikhtegar, H.A. Panahi, F. Atabi, B.K. Shahraki, Porosity, characterization and structural properties of natural zeolite-clinoptilolite-as a sorbent, Environ. Prot. Eng. 39 (2013).
[16] N. Lihareva, O. Petrov, L. Dimowa, Y. Tzvetanova, I. Piroeva, F. Ublekov, A. Nikolov, Ion exchange of Cs+ and Sr 2+ by natural clinoptilolite from bi-cationic solutions and XRD control of their structural positioning, J. Radioanal. Nucl. Chem. 323 (2020) 1093–1102.
[17]. N. Popov, T. Popova, J. Rubio, S.R. Taffarel, Use of natural and modified zeolites from Bulgarian and Chilian deposits to improve adsorption of heavy metals from aqueous solutions, Bull. Mineral. Petrol. Geochemistry. 49 (2012) 83–93.
[18]. Д.Т. Рустамова, Э.А. Дж, Ф.М. Насири, С.А. Байрамова, С.А. Алиев, С.И. Мамедов, К.А. Мансурова, Цеолиты-условия образования в природе, свойства и применение / Zeolites--formation conditions in the nature, properties and applications, 2018, 1000 Kopii. 67.
[19]. C. Colella, M. de' Gennaro, R. Aiello, Use of zeolitic tuff in the building industry, Rev. Mineral. Geochemistry. 45 (2001) 551–587.
[20]. A. Nikolov, I. Rostovsky, H. Nugteren, Geopolymer materials based on natural zeolite, Case Stud. Constr. Mater. (2017). https://doi.org/10.1016/j.cscm.2017.03.001.
[21]. C. Villa, E.T. Pecina, R. Torres, L. Gómez, Geopolymer synthesis using alkaline activation of natural zeolite, Constr. Build. Mater. 24 (2010) 2084–2090.
[22]. S. Özen, B. Alam, Compressive strength and microstructural characteristics of natural zeolite-based geopolymer, Period. Polytech. Civ. Eng. 62 (2018) 64–71.
[23]. А. Николов, Геополимери на основа естествен зеолит за приложение в строителството. състав, структура, свойства, София, 2018, ISBN 978-619-188-201-4.
[24]. A. Nikolov, Geopolymers based on Bulgarian raw materials – preliminary studies, Int. Sci. J. "Machines, Technol. Mater. XIII (2019) 197–199.
[25]. A. Nikolov, I. Rostovsky, Sodium-silicate geopolymers based on natural zeolite – clinoptilolite, Comptes Rendus L'Academie Bulg. Des Sci. 70 (2017).
[26]. A. Nikolov, B. Barbov, E. Tacheva, Geopolymer mortars based on natural zeolite., Rev. Bulg. Geol. Soc. 82 (2021).
[27]. A. Nikolov, H. Nugteren, I. Rostovsky, Optimization of geopolymers based on natural zeolite clinoptilolite by calcination and use of aluminate activators, Constr. Build. Mater. 243 (2020). https://doi.org/10.1016/j.conbuildmat.2020.118257.
[28]. A. Nikolov, Geopolymers based on metakaolin – literature review and prelimenary studies, VSU, Proceeding, ISSN 1314-071X,2018, Sofia, 2018.
[29]. J.R. Gasca-Tirado, A. Manzano-Ramirez, P.A. Vazquez-Landaverde, E.I. Herrera-Diaz, M.E. Rodriguez-Ugarte, J.C. Rubio-Ávalos, V. Amigó-Borrás, M. Chávez-Páez, Ion-exchanged geopolymer for photocatalytic degradation of a volatile organic compound, Mater. Lett. 134 (2014) 222–224.
[30]. N. Ariffin, M.M.A.B. Abdullah, M.R.R.M.A. Zainol, M.F. Murshed, M.A. Faris, R. Bayuaji, Review on adsorption of heavy metal in wastewater by using geopolymer, in: MATEC Web Conf., 2017: p. 1023.
[31]. K. Okada, A. Ooyama, T. Isobe, Y. Kameshima, A. Nakajima, K.J.D. MacKenzie, Water retention properties of porous geopolymers for use in cooling applications, J. Eur. Ceram. Soc. 29 (2009) 1917–1923.
[32]. Z. Emdadi, N. Asim, M.A. Yarmo, R. Shamsudin, Investigation of more environmental friendly materials for passive cooling application based on geopolymer, APCBEE Procedia. 10 (2014) 69–73.

Analysis of mechanical properties and microstructure of ti-al-c composites after spark plasma sintering

Kandrotaitė Janutienė Rasa[1], Yogesh Ragupathy, Mažeika Darius[1], Syzonenko Olha[2], Lypian Evhen Vasylovych[2], Torpakov Andrii Serhiiovych[2], Prystash Mykola Serhiiovych[2], Dlouhý Jaromír[3]
Faculty of Mechanical Engineering and Design – Kaunas University of Technology, Lithuania[1]
Institute of Pulse Processes and Technologies of the National Academy of Sciences of Ukraine – Mykolaiv, Ukraine[2]
COMTES FHT, Dobřany, Czechia[3]
E-mail: raskand@ktu.lt, darius.mazeika@ktu.lt, jaromir.dlouhy@comtesfht.cz

Abstract: *Titanium rich alloys of Ti-Al-C and Ti-Al-B system was synthesised by Spark Plasma Sintering (SPS) and Field Activated Pressure Assisted Sintering (FAPAS) methods with altering sintering temperatures in the range of 950°C-1020°C with different current for the duration of 5 minutes. The initial powders of the composite 85%Ti and 15%Al was processed by High Velocity Energy Distribution (HVED) in a solution of kerosene at the specific energy of 25MJ/kg to reduce the size of the particles to nano-scale. This method of using different parameters of production technology have helped to analyse the most efficient, energy saving, and less waste generation technological process with improved mechanical properties. The metal-based samples were examined by optical and electron microscopy. Mechanical properties of composites were determined by measuring microhardness.*

The aim of the investigation was to determine the dependence between parameters of production technology and properties of Ti-AlC composites.

Keywords: TI-AL-C COMPOSITE, MICROSTRUCTURE, OPTICAL ANALYSIS, SEM, HVED.

1. Introduction

The method of production of the Ti-Al-C composite is directly proportional to the mechanical properties of the composite. The most common way of producing the composite by conventional casting was used in the early stages but however the occurrence of microstructural defects such as pores or cracks will lower the mechanical properties of the composite. To make it more stable, powder metallurgy was carried out by the scientists in which during gas atomization Ti-Al fine grain metallic powders will be obtained with homogeneous composition. Afterwards with the process of spark plasma sintering, the powdered particles will be compacted with the help of high intensity current and stress. A lot of industries are attracted to this because of its several advantages like speed, cheap and simplicity [1]. P Wang et al. [2] synthesized ternary layered carbide Ti2AlC by spark plasma sintering using elementary powder mixtures which showed great mechanical properties. D Wang et al. [3] synthesized Ti-Al-Cr-Nb alloy by spark plasma sintering with different sintering temperatures and stresses showed good mechanical properties. C Magnus et al. [4] synthesized a dual max phase composite by spark plasma sintering under vacuum condition by altering the composition of the raw materials showed good mechanical properties. It is clear that to obtain good mechanical properties, importance should be provided to the parameters of the production phase such as sintering temperature, current, inclusion particles, time etc.

The tests which are conducted to determine structure and properties of metal-based composites are Vickers hardness nano-indentation test for hardness property, microstructure analysis with the help of scanning electron microscope (SEM) and energy dispersive X-ray spectrometer (EDS) for determining the plastic deformation and other properties, etc. The phase analysis can be a key to determine the certain phases formed in the composite because of sintering temperature and chemical composition. The test results from X-ray diffraction can show the intensity of peaks of phases by which we can come to conclusion whether the composite material is stable or not [5].

In this paper, analysis of the tests such as Vickers hardness test, microstructural analysis and chemical composition were discussed in detail to compare the results with the experimental results obtained.

2. Methodology

The raw materials such as titanium (99.9% purity) and aluminum (99.9% purity) were used in the preparation of samples for the testing. These samples were prepared with varying sintering temperature, current, and time which is explained in detail in the Table 1. Spark plasma sintering and field activated pressure assisted sintering methods are opted for the preparation of samples. These methods are chosen since it is a high energy saving technology with less processing time and procedure. A technique of high voltage electric discharge W1=1kg and Wsum=25MJ/kg being applied on the powders rather than using an addition of inclusion particles. By this method, the Ti-Al-C and Ti-C powders are synthesised by the reaction between the discharge and the initial powders to result in homogeneous mixing of compounds.

The mixture obtained is compacted by the sintering process and the preservation of reinforcing phases takes place in the matrix.

The whole process of producing the sample was done in the Institute of Pulse Processes and Technologies, National Academy of Science of Ukraine with the help of Dr. Olha Syzonenko and coauthors.

Table 1: *Parameters of production technology for evaluating the properties*

Sample	Initial powders	Sintering methods	Sintering temperature, °C	Current, A	Time, min
13.2	15%Al+85%Ti	SPS	985	995	5
14.4	15%Al+85%Ti	SPS	1020	915	5
G13.2	15%Al+85%Ti	FAPAS	950	840	5
G14.2	15%Al+85%Ti	FAPAS	960	770	5

Preparation of metal-based composite samples for microscopic analysis was performed according to ASTM E3-11: 2017 [6]. The mounted, ground samples were polished using aqua-pol-diamond suspension (3μ, and then, 1μ grain size). After the process of polishing, the samples are immersed in the alcohol for few minutes to further remove the traces of debris.

After polishing the surface of the sample, experimental tests were conducted on it to determine the mechanical properties of the composite. The microhardness test was carried out on Innova test machine (Fig. 1). This machine is a universal machine which has the built-in option of choosing any kind of hardness testing method. The Vickers hardness test method was opted with load being 2.5kgf and dwell time of 10 seconds. The diamond indenter was used in this nano-indentation microhardness test. For each sample 30 indentations were performed, and the hardness values were noted down.

The structure of the samples was examined using:

- Optical microscope Nikon equipped with video camera Nikon DS-2 16 MP and objectives Nikon TU Plan Fluor 10×/0.30 and Nikon TU Plan Fluor 100x/0.90. NIS-Elements D software was used to analyze the photographs.
- Scanning electron microscope (JEOL IT 500 HR) equipped with an EDS analyzer (EDAX Octane Elite

Super). EDS was used for determining the chemical composition of phases.

a *b* *c* *d*

Fig. 1. *Experimental setup: grinding of samples with Lamplan machine, b – prepared samples, c - the Innova test machine for determining hardness value, d – examination of the structure using optical microscope Nikon*

3. Results and Discussion

3.1. Vickers hardness nano-indentation test analysis

The Vickers hardness nano-indentation test was carried out in the Innova test machine with load and dwell time being 2.5kgf and 10 seconds respectively. The samples were indented in 30 different spots with the diamond indenter to analyze the hardness values to a full extent. The figure 2 (a) and (b) shows the hardness values of the sample 13.2 and 14.4. These samples are sintered by SPS process at two different temperatures such as 985°C and 1020°C. There is almost a constant range of values all over the surface of the specimen 13.2. A peak of 668.7 HV is recorded when the nano-indentation was carried out on small network structures of phases near the edges. But it does not affect the other mechanical properties of the composite. The presence of very small pores in the sample 13.2 was the reason for achieving a less hardness value of 407.4 HV. The values of the sample 13.2 shows that there is a good densification achievement happened.

On reviewing the hardness values of the sample 14.4, there is wide range of difference between some points. A maximum value of 764.9 HV is achieved in the test where the indentation was carried out on the large network structure of hard phases. To contrast, some minimum hardness values such as 243 HV and 323.4 HV was achieved is some places around the clusters where a non-uniform distribution of particles surrounded. On comparing the two samples sintered by SPS process, the sample 13.2 has a good hardness value throughout the sample. Even though the sample 14.4 has the highest hardness value than 13.2, there are some places with poor hardness value range.

In the samples G13.2 and G14.2, the raw materials underwent an initial process in HVED solution before sintered by FAPAS method. The sintering temperature of 950°C and 960°C was used to sinter the sample G13.2 and G14.2 respectively. The result showed a minimum value of 439.2 HV (Fig. 2, c and d). The drop in value may be because of the unreacted hard particles accumulated near the areas which caused pores while sintering. The values remained in a good range in the other spots of the sample where nano-indentation was performed. A peak value of 1335.5 HV was identified at the place of clusters formed by the over allocation of particles at a same place. When the sample G14.2 was tested, it showed good hardness values throughout the whole readings. The slight increase in temperature may be the reason for uniform distribution of particles and formation of very few pores of small lengths than the big pores formed in the sample G13.2. A hardness of value of 879.2 HV was recorded which is lesser than the peak of G13.2 but the overall values show that the composite has good hardness values.

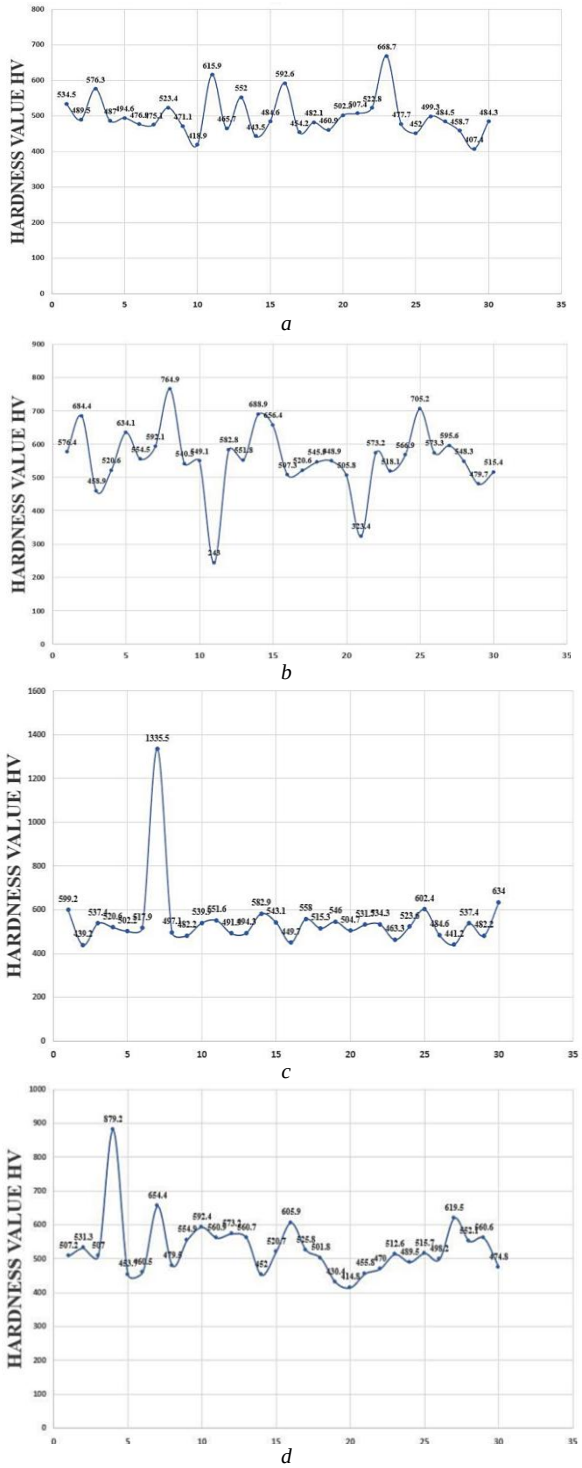

Fig. 2. *Hardness value graph for the Ti-Al-C composites treated by HVED and sintered: a – SPS, 985°C, 995 A; b – SPS, 1020°C, 915 A; c – FAPAS, 950°C, 840 A; d – FAPAS, 960°C, 770 A*

3.2. Optical analysis of the microstructure of composites

The optical micrographs of the polished un-etched surface of the as-synthesized Ti-Al-C composites are shown in the Fig. 3.

The microstructure of sample 13.2 consists of very few pores/voids not bigger than the length of 20.13µm (Fig.3, a). Also, the hardness values of the sample 13.2 which was taken in 30 different spots are almost between the range of 407.4- 668.7 HV. Hence a uniform densification has taken place. This adds an extra support to the statement regarding the density. In a recent study involving Ti-Al-C composite, the author S. Riaz et.al [7] results on the microstructure were almost similar to this project. By using 85%Ti, 10%Al and 5%C as initial powders, the composite was sintered by arc furnace method at 1050°C. The microstructure was composed of elongated plate-like structured β-Titanium as matrix, the carbides spread over the matrix as small dendritic structure and Ti_3AlC (P phase) as dark phase.

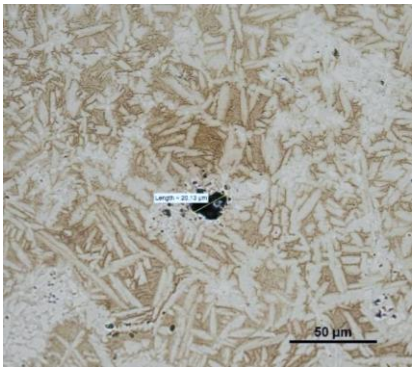

a

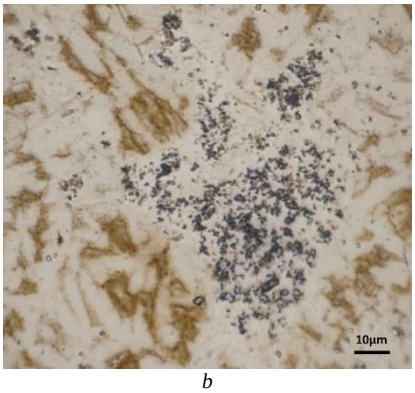

b

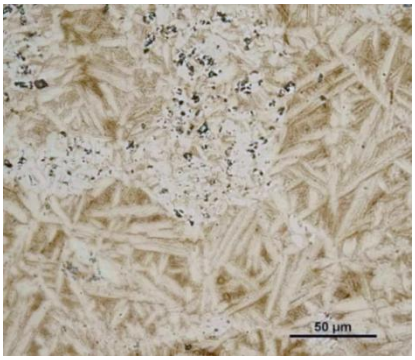

c

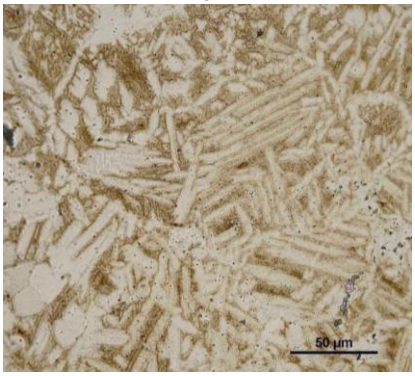

d

Fig. 3. *Optical micrographs of Ti-Al-C composites after such treatment: a – SPS, 985°C, 995 A; b – SPS, 1020°C, 915 A; c – FAPAS, 950°C, 840 A; d – FAPAS, 960°C, 770 A. Here – elongated β-Ti crystals, slightly brown – possible Ti-Al-C chemical compounds, and dark carbides*

According to author Syzonenko O. et.al [8], the same case of experimenting with 15%Al and 85% of Ti at 1100°C for 5 minutes by SPS with HVED is discussed. The results showed that due to the presence of phases C60 and C70 after the HVED process, the composite had the formation of Ti_2AlC max phase and Ti_3AlC in it. The optical microscopy results of the author's specimens depict that the dark phase formed in the composite as Ti_3AlC which also consisted of few traces of TiC. The light phase is formed of Ti, and it has some traces of the Ti_2AlC phases. In the present work with Ti-Al-C composite, the reaction between the HVED solution and the initial powders, a solid-liquid reaction takes place which forms the C. When comparing the results obtained from the literature, the microstructure consists of elongated needle like shapes all over the sample which may be the β-Ti matrix (Fig. 3, a-d)., the dark phase formed in the samples may be of Ti_3AlC or similar carbides is visible on the surface of the matrix (Fig. 3, b, c).

3.3 SEM analysis of Ti-Al-C composites

The electron microscopic analysis of the composite samples was carried out by Scanning electron microscope (SEM) at scientific institute COMTES Fht., Czech.

The Fig. 4 shows secondary electron scanning images of the sample 13.2 which was sintered by SPS method at 985°C for 5 minutes with current 995 A. The figure (a) shows the presence of small pores in the surface of composite. Due to the effect of sintering or poor compaction of materials these small pores could have generated. But in the figure (b) there is presence of cracks in the surface of hard carbides. In case of poor binding of materials in some places due to the effect of sintering and over allocation of particles in a place. According to the author S. Riaz et.al [7], the proper allocation of the particles is dependent on the current which is applied during the sintering process.

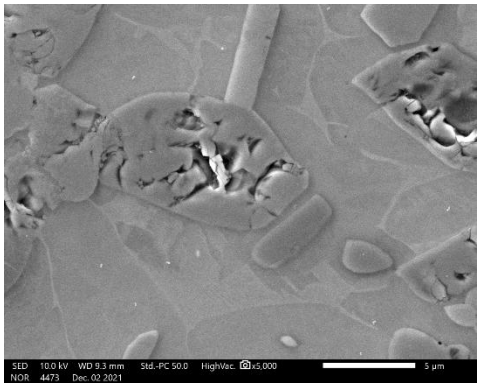

a

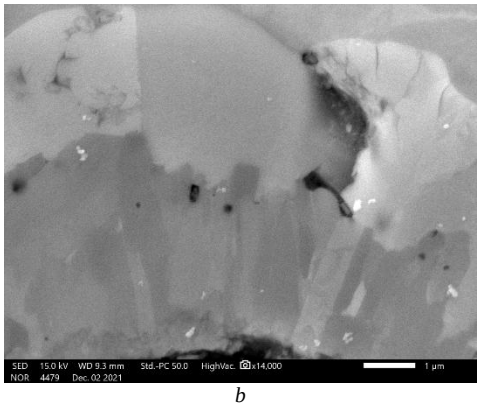

b

Fig. 4. *Secondary electron scanning image of Ti-Al-C sample: a – porous carbides are visible inside β-Ti matrix; b – small cracks inside carbides (at the upper right corner of the image)*

The back scattered electron images show the clear formation of matrix, dark phases, and light phases. As discussed before in the optical microscope analysis, the elongated needle shaped structures

are the β- Titanium, the dark spots like pores are the presence of carbides and the light phase is Ti_3AlC. It is evident from the author S. Riaz work that the occurrence of martensitic transformation of β-Ti to α-Ti occurs when the sintering temperature is above 1250°C or when the ratio of Al powders increased. The other way of transformation is the quenching of water or cooling for some time after the sintering process. Now it is clear that the sample of Ti-Al-C composite sintered at 985°C temperature has not gone through the martensitic transformation of β-Ti to α-Ti. The uniform distribution of the elongated needle shaped β-Ti acts as the matrix which is evident in the Fig. 5 (a). The Fig. 5 (b) shows the grain growth of carbides into irregular dendritic form. Titanium inside the composite is more precipitative in the carbides when the sintering temperature is less than 1050°C. By the action of sintering parameters and the precipitation of titanium carbides tends to form porous structured dark phases at the grain boundaries of elongated β-Ti crystals.

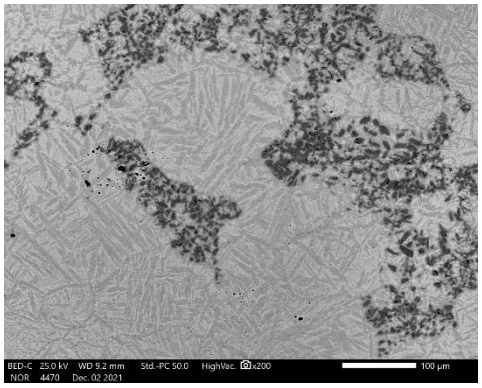

a

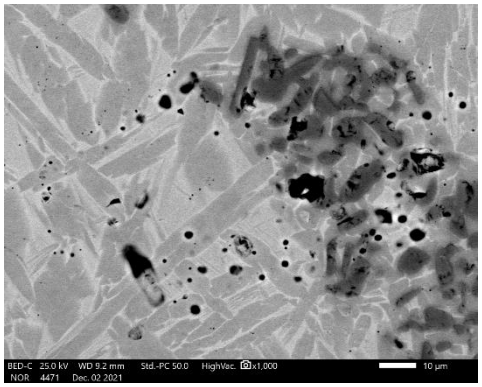

b

Fig. 5. *Back scattered electron image of Ti-Al-C sample: dark carbides, slightly grey β-Ti and light particles – possible Ti_3AlC*

Further studies of Ti-Al-C composite materials sintered by different technologies are planned, as well, as the initial powder treatment by HVED process is going to be investigated in more detail. The following X-ray experiments will show exact phase composition of these composites allowing to collect more data about structure and properties of Ti-Al-C composites.

4. Conclusions

Investigation of the dependencies between the parameters of production technology and the mechanical properties of the Ti-Al-C composite was successfully carried out letting the formulation of such conclusions:

1. The hardness values of nano-indentation test shows that the samples such as 13.2, 14.4, G13.2, and G14.2, possess the peak hardness values of 668.7 HV, 764.9 HV, 1335.5 HV, and 879.2 HV, respectively. When comparing the values, the samples sintered by FAPAS method possess a range of good hardness values followed by the samples of SPS. A hard brittle nature on the surface of some areas of samples tends to provide a very high peak of values but the overall values is poor because of the formation of voids and cracks.

2. The optical microscopic analysis showed the formation of β-Ti in the shape of elongated needle-shaped formation distributed all over the surface as matrix. The hard black surface in the shape of small dendritic structures on the matrix are the carbides which are over accumulated in some grain boundaries of the 13.2 and 14.4 samples of Ti-Al-C composite. The slightly brown phase may be the Ti_3AlC phase. The samples 13.2 and 14.4 has comparatively less pores in the surface of the composite than the sample G13.2, G14.2.

3. The electron microscopic analysis on the sample 13.2 showed a clear imaging of the elongated needle-shaped structures of the β-Titanium, the dark spots are the presence of carbides and the white phase can be Ti_3AlC. The composite 13.2 has not gone through the martensitic transformation of β-Ti to α-Ti. Depending on sintering parameters and the precipitation character of titanium carbides, it tends to form porous structured dark phases at the grain boundaries.

5. References

1. VENKATESH, B.; and HARISH, B. Mechanical Properties of Metal Matrix Composites (Al/SiCp) Particles Produced by Powder Metallurgy. International Journal of Engineering Research and General Science, 2015, vol. 3, no. 1. pp. 1277-1284.

2. WANG, Ping, et al. Fabrication of Ti_2AlC by Spark Plasma Sintering from Elemental Powders and Thermodynamics Analysis of Ti-Al-C System. Journal of Wuhan University of Technology-Mater.Sci.Ed., 2007, vol. 22, no. 2. pp. 325-328.

3. WANG, Dongjun; YUAN, Haoand QIANG, Jianming. The Microstructure Evolution, Mechanical Properties and Densification Mechanism of TiAl-Based Alloys Prepared by Spark Plasma Sintering. Metals, 2017, vol. 7, no. 6. pp. 201.

4. MAGNUS, Carl, et al. Microstructural Evolution and Wear Mechanism of Ti_3AlC_2 – Ti_2AlC Dual MAX Phase Composite Consolidated by Spark Plasma Sintering (SPS). Wear, 2019, vol. 438-439. pp. 203013. Available from <https://www.sciencedirect.com/science/article/pii/S0043164819307227>. ISSN 0043-1648.

5. GALYSHEV, S. N., et al. High-Temperature Firing of Composite Based on the MAX-Phase of the Ti–Al–C System. Refractories and Industrial Ceramics, 2018, vol. 58, no. 5. pp. 557-561.

6. ASTM E3-11:2017. Standard Guide for Preparation of Metallographic Specimens, ASTM International, West Conshohocken, PA, 2017, www.astm.org.

7. RIAZ, S.; FLOWER, H. M.and WEST, DRF. Phase Relationships Involving TiC and Ti_3AlC (P Phase) in Ti–Al–C System. Materials Science and Technology, 2000, vol. 16, no. 9. pp. 984-992.

8. SYZONENKO, O., et al. High-Energy Synthesis of Metalomatric Composites Hardened by Max Phases of Ti-Al-C System. Machines.Technologies.Materials., 2018, vol. 12, no. 10. pp. 395-397.

ACKNOWLEDGEMENTS

This paper was developed thanks to the project No. P-LU-22-5 "Application of high-concentrated energy flows for producing nanostructured polyfunctional composite materials (NAPOCOM)" supported by the Lithuanian-Ukrainian bilateral cooperation in the field of science and technology by Research Council of Lithuania and Ministry of Education and Science of Ukraine.

Temperature regime in obtaining $BaTiO_3$-$BaSnO_3$ system and study of dielectric properties

Mihaela Aleksandrova[1] , Lyuben Lakov[1], Vladimir Blaskov[1], Yordan Marinov[2]

[1]Bulgarian Academy of Sciences, Institute of Metal Science, Equipment and Technologies with Hydro- and Aerodynamics Centre "Acad. A. Balevski", Shipchenski Prohod Blvd. 67, 1574 Sofia, Bulgaria, e-mail: mihaela.krasimirova@mail.bg

[2]Bulgarian Academy of Sciences, Institute of Solid State Physics "G. Nadjakov", 72 Tzarigradsko Chaussee, Blvd., 1784 Sofia, BULGARIA

***Abstract**: A system based on $BaTiO_3$ – $BaSnO_3$ (BT-BS) has been developed in search of highly efficient lead-free piezoelectric ceramics. The powder samples were mixed and homogenized in a ratio of 50%: 50% and 15%: 85%. From the compositions thus obtained, tablets with the presence of a PVA plasticizer were formed, which were further annealed in a furnace with a corundum backfill. The temperature regime is in two steps. Drying time up to 800oC with a delay of 1h 30min. and additional heating to 1150°C with one hour delay. The results were characterized by XRD analysis, the relative dielectric constant of the two samples was determined.*

***Keywords:** CERAMIC, $BATIO_3$, $BASNO_3$, HIGH PERMITIVITTY*

I. Introduction

Alkaline earth mites are interesting compounds in terms of their dielectric properties. Solid solutions in the $BaTiO_3$-$BaSnO_3$ (BT-BS) system have attracted attention in recent years in the field of nanocapacitors.

Synthetic $BaTiO_3$, prepared by conventional solid phase method shows great performance with high ε_r value of ~ 1900 at room temperature (30°C), low dielectric loss δ ~ 0,01 and piezoelectric constant d_{33}~ 191 pC/N [1]. $BaTiO_3$ has five polymorphic structures showing different phases that vary with temperature [2]. The phase transition of $BaTiO_3$ at the Curie temperature (Tc) significantly changes its properties, which are ferroelectric and non-ferroelectric. The $BaTiO_3$ nepheroelectric shows a hexagonal structure at 1460°C and a cubic structure at over 120°C [3]. On the other hand, the ferroelectric properties of $BaTiO_3$ exist in three different polymorphic crystal structures, which are tetragonal, orthorhombic and rhombohedral. Zheng et al. [4] studied the effect of grain size on the dielectric constant and piezoelectric properties of $BaTiO_3$. They report that the dielectric constant and piezoelectric properties increase significantly by reducing the grain size. The maximum grain size was reached around 0.94 μm due to the density of the domain structure and the area decreased with decreasing grain size.

$BaSnO_3$ has a cubic perovskite structure that exhibits n-type semiconductor behavior at room temperature [5, 6]. $BaSnO_3$ is thermally stable up to 2000°C, but has a high absorption of moisture compared to other species [6]. Thus, it is currently used for thermally stable capacitors and humidity sensors [7, 8]. Meanwhile, completely dense $BaSnO_3$ ceramics can be achieved by synthesizing them at temperatures above 1594°C [6]. Huang reported that in order to obtain single-phase $BaSnO_3$, it is necessary to heat it to 1200°C and achieve a significant amount of grain porosity [9, 10]. In addition, Azad confirmed that grain porosity can be reduced by milling $BaSnO_3$ at 1600°C [11]. The initial report on materials based on the findings found that $BaSnO_3$, synthesized at 1200°C, has a dielectric constant ε_r~ 14 at 25°C [6]. Kumar reported that $BaSnO_3$ was sintered at 1200°C for 12 hours using the solid state method. A huge dielectric behavior of $BaSnO_3$ has recently emerged, where the dielectric constant εr value reaches ~ 6000 when measured at 220°C and at a frequency of 1 kHz. The εr value of $BaSnO_3$ is two orders of magnitude higher than previously reported studies [12, 13]. However, the dielectric constantεr decreases with decreasing temperature. Therefore, it is assumed that the lack of oxygen leads to a reduction of Sn^{4+} to Sn^{2+} in $BaSnO_3$ samples, which contributes to an anomaly in the value of the giant dielectric constant εr when the samples were sintered at very high temperatures of T°C≥1450°C [13-16].

II. Experimental part

The raw materials used to prepare the $BaSnO_3$ and $BaTiO_3$ systems by the sol-gel method are described in a previous publication by the authors. [17] They are synthesized by sol-gel method and the final product is in the form of a powder mixture. The synthesis was carried out at 1100°C. They were initially tested by XRD and TG with DSC. Two press specimens were formed, in a ratio of 50% $BaSnO_3$ - 50% $BaTiO_3$ and 15% $BaSnO_3$ - 85% $BaTiO_3$ tablets using a surfactant, which acts as a binder. The samples were further annealed until the plasticizer burned at 1250°C. The relative dielectric constant was determined on the obtained materials and the two results were compared.

III. Results and discussion

The phase and the purity of the as-prepared powder were characterized by X-ray diffraction (XRD), using Cu Kα radiation фиг. 1 и фиг. 2. XRD analysis shows that the synthesis temperatures of $BaTiO_3$ powders have a nanostructured nature and good crystallinity. In addition to the crystalline nature, XRD showed a cubic structure.

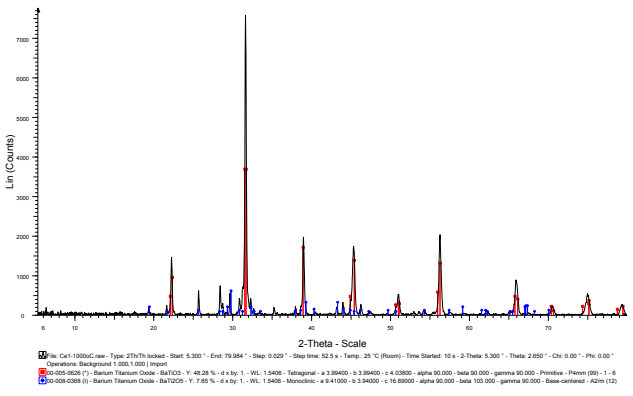

***Fig. 1** XRD diagram of synthesized $BaTiO_3$ by sol-gel method.*

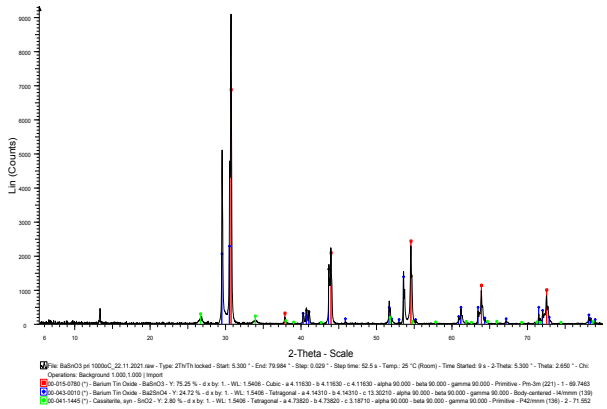

Fig. 2 *XRD diagram of synthesized $BaTiO_3$ by sol-gel method.*

Figure 2 shows an XRD model of $BaSnO_3$ nanoparticles. All vertices are indexed with a cubic structure indicating a high XRD model for BaSnO3 nanoparticles. All peaks are indexed to a cubic structure. For $BaSnO_3$, which show that the formation of the $BaSnO_3$ phase was completed during the combustion process itself without the need for a calcination step. It was found that the crystal size, calculated from half the maximum of the full width, using Scherer's formula for the main reflection is~25 nm. It can be noted that the single-phase $BaSnO_3$ material can be obtained by the solid state reaction path only after prolonged calcination of the reaction mixture at 1100°C with repeated intermediate homogenization.

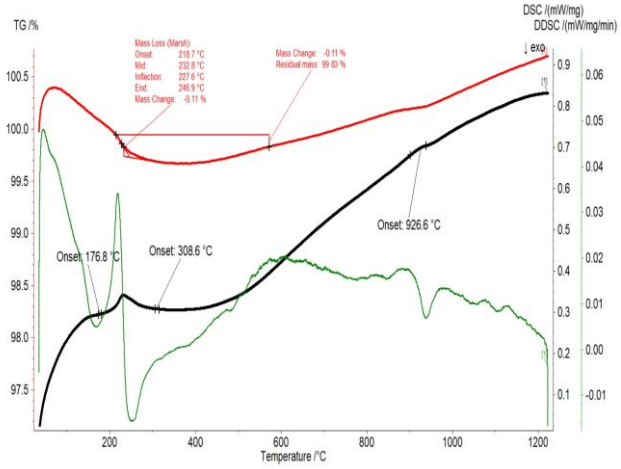

Fig. 3*. TG-DSC of the system $BaTiO_3$ - $BaSnO_3$*

Simultaneous analysis of TG-DSC was performed at a heating rate of 10°C / min of the mixed powder to a temperature of 1200°C. A characteristic peak is seen at about 250°C. The DSC curve shows a strong endothermic peak at about 828.5°C, corresponding to the chemical reaction between barium titanate and tin titanate. The small endothermic peak of 900 to 1000°C may be due to the formation and decomposition of a small amount of intermediate phase Ba_2SnO_4. There are no mass losses, only 0.11%. The main information we get from the diagram is a clean temperature bar (black). There are no characteristic changes of the sample in the range up to 1200°C.

Determination of relative dielectric constant of BT-BS system in two different ratios. On the samples prepared in this way, the measurement of the relative dielectric constant was performed in order to evaluate and optimize the composition and the technological regime.Since the dielectric properties of ferroelectric materials are usually described by relative dielectric constant (ε_r), which may vary depending on the change in temperature. In the presented results the difference between the two compositions is made.

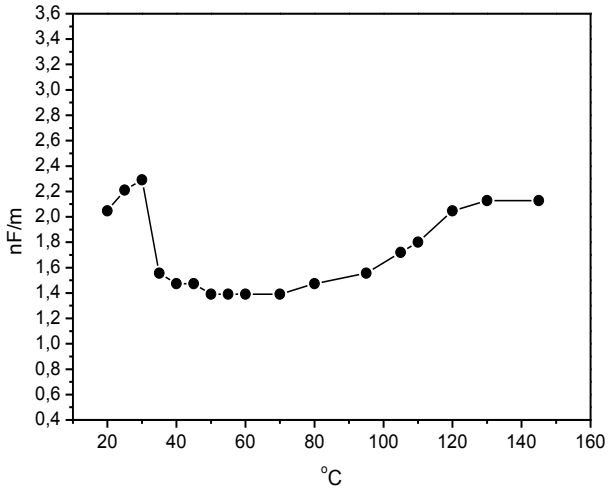

Fig. 4*. ε_r of $BaTiO_3$ - $BaSnO_3$ ratio 50:50 ceramic pellet vs the temperature of the pellet.*

The effect of the heating on the dielectric permittivity ($\boldsymbol{\varepsilon_r}$) was proven by capacitance measurement of the $BaTiO_3$-$BaSnO_3$ ceramic sample upon temperature variation (Figure 4). Under the experimental conditions (20ºC to 150ºC), a considerable change of $\boldsymbol{\varepsilon_r}$ was not observed. The value of $\boldsymbol{\varepsilon_r}$ is staying in the range 1.4 ÷ 2.3 nF/m. Slight reduction of $\boldsymbol{\varepsilon_r}$ followed by it's restoration is visible in Figure 4. This effect needs further considerations.

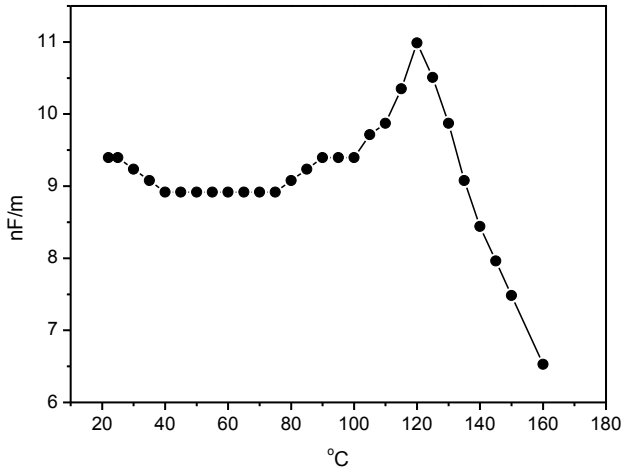

Fig. 5*. ε_r of $BaTiO_3$ - $BaSnO_3$ in ratio (85%:15%) ceramic pellet vs the temperature of the pellet.*

Figure 5 presents the results of $\boldsymbol{\varepsilon_r}$ of $BaTiO_3$ - $BaSnO_3$ in ratio (85%:15%) ceramic pellet.
Compared to Figure 4, this graph shows a clear peak at 120°C. After this temperature the material changes from ferromagnet to paramagnetic.
The maximum measured value of the relative dielectric constant is 11,000, which is higher than that of pure $BaTiO_3$ - of the order of 6000. Thus, we can conclude that BT-BS ceramics have better dielectric properties compared to pure $BaTiO_3$.

IV. Conclusion:

As a result of the performed researches, the following conclusions can be made: Synthesis of barium-titanate - barium-static ceramics with high dielectric constant using the sol-gel method for synthesis of the initial barium-titanate powder. Technology has been developed for the creation of ceramic tableted test specimens in two

different proportions. Radiographic analyzes of $BaTiO_3$ - $BaSnO_3$. The sintering temperature was determined by DSC at 1200°C. Ceramics can find application in the development of dielectrics for supercapacitors.

Acknowledgements

The authors are grateful to the financial support of Bulgarian National Science Fund at the Ministry of Education and Science, Contract No КП-06-Н 37/26 18.12.2019.

All equipment and experimental units used in this work was funded by the European Regional Development Fund within the OP "Science and Education for Smart Growth 2014 - 2020", project CoE "National center of mechatronics and clean technologies", № BG05M2OP001-1.001-0008-C08.

References:

1.H. Jafe, Piezoelectric ceramics. J. Am. Ceram. Soc. 41(11), 494–498 (1958).

2.M.J. Pan, C.A. Randall, A brief introduction to ceramic capacitors. IEEE Electr. Insul. Mag. 26(3), 44–50 (2010)

3.M.M. Vijatović, J.D. Bobić, B.D. Stojanović, History and chal lenges of barium titanate: part I. Sci. Sinter. 40(2), 155–165 (2008)

4.P. Zheng, J.L. Zhang, Y.Q. Tan, C.L. Wang, Grain-size efects on dielectric and piezoelectric properties of poled BaTiO3 ceramics.

5. N.F. Muhamad, R.A.M. Osman, M.S. Idris, M.N.M. Yasin, Physi cal and electrical properties of $SrTiO_3$ and $SrZrO_3$. EPJ Web Conf. 162, 01052 (2017).

6. W.W. Cofeen, Ceramic and dielectric properties of the stan nates. J. Am. Ceram. Soc. 36(7), 207–214 (1953)

7. T. Maekawa, K. Kurosaki, S. Yamanaka, Thermal and mechani cal properties of polycrystalline BaSnO3. J. Alloys Compds. 416(1), 214–217 (2006)

8. Y. Shimizu, Y. Fukuyama, T. Narikiyo, H. Arai, T. Seiyama, Perovskite-type oxides having semiconductivity as oxygen sen sors. Chem. Lett. 14(3), 377–380 (1985)

9. C. Huang, X. Wang, X. Liu, M. Tian, T. Zhang, Extensive analysis of the formation mechanism of BaSnO3 by solid-state reaction between $BaCO_3$ and SnO_2. J. Eur. Ceram. Soc. 36(3), 583–592 (2016)

10. S. Upadhyay, O. Parkash, D. Kumar, Preparation and characteri zation of barium stannate BaSnO3. J. Mater. Sci. Lett. 16(16), 1330–1332 (1997)

11. A.M. Azad, N.C. Hon, Characterization of $BaSnO_3$-based ceramics: part 1. Synthesis, processing and microstructural development. J. Alloys Compds. 270(1), 95–106 (1998)

12. E. P. Kashchieva, V. D. Ivanova, B. T. Jivov and Y. B. Dimitriev, „Nanostructured borate glass ceramics containing $PbMoO_4$", Physics and Chemistry of Glasses, 41 (6), 2000, pp. 355-357.

13. Elena P. Kashchieva, Vanya D. Ivanova, Bojidar Tzv. Jivov, Plamen K. Petkov, Yanko B. Dimitriev, „Structure-Property Correlation in Lead-Borate Composites with Participation of $PbMoO_4$", In: Proceedings of the 13th Conference on Glass and Ceramics, 29 September - 1 Oktober 1999, Varna, Bulgaria, Vol. 1 (Glass), Varna, Eds B. Samuneva et al. (Science Invest, Sofia, 1999), pp. 159-164.

14. V. D. Ivanova, E. P. Kashchieva, B. T. Jivov, Y. B. Dimitriev, „Electron Microscopic Study of Lead-Borate Composites Containing $PbMoO_4$ Nanocrystals", Nanostructured Materials Application and Inovation Transfer, Heron Press Science Series, Sofia, 2001, pp 30-32.

15. A. Kumar, B.P. Singh, R.N.P. Choudhary, A.K. Thakur, Fer roelectric phase transition in Te-modifed $BaSnO_3$. Mater. Lett. 59(14–15), 1880–1888 (2005)

16. K.N.D.K. Muhsen, R.A.M. Osman, M.S. Idris, Giant anomalous dielectric behaviour of $BaSnO_3$ at high temperature. J. Mater. Sci. 30(8), 7514–7523 (2019)

17. Blaskov V., lakov lyuben., Aleksandrova M.,"PREPARATION OF SN-DOPED $BATIO_3$ BY SOL-GEL METHOD ",. Journal of Materials Science. Non Equilibrium Phase Transformations Year VI, 3, 3, Scientific Technical Union of mechanical Engeneering Industry 4.0, 2020, 267-268.

Numerical analysis of metallographic preparation effect on the hardness of titanium alloy

Slokar Benić Lj.[1], Dr Ivec I.[1], Šimić K.[1], Dr Jandrlić I.[1]
University of Zagreb, Faculty of Metallurgy – Sisak, Croatia[1]
E-mail: slokar@simet.unizg.hr, iivec@simet.unizg.hr, klaras0206@gmail.com, ijandrli@simet.unizg.hr

Abstract: *Titanium alloys due to their good properties are increasingly used in biomedicine. However, in order to improve certain properties, titanium-based alloys with new chemical compositions are designed. In order to be characterized in a satisfactory manner, they must first be adequately prepared. In this paper the two most influential parameters were varied: grinding time and force, while the speed of rotation of the grinding wheel was constant. After grinding with the highest gradation of grind paper, the samples were observed under a light microscope to determine the condition of the surface. Then their hardness was determined by the Vickers method with different indenter loads. After that, the samples were polished under the same conditions, and their hardness was determined again. The obtained hardness values were numerically analyzed and the corresponding functional dependences of the measured hardness on the grinding parameters (time and force) and on the indentation force were determined.*
Keywords*: TITANIUM ALLOY, METALLOGRAPHIC PREPARATION, HARDNESS, VICKERS METHOD*

1. Introduction

Musculoskeletal disorders are the most common health problems. It is estimated that about 90% of the world's population over the age of 40 suffers from degenerative diseases such as arthritis, and their number in the total population has been increasing significantly recently. Biomaterials are solutions to such problems, because their surgical implantation helps to restore the function of otherwise functionally endangered structures [1].

Biomaterials are artificial or natural materials which are used to make implants for the purpose of replacing a damaged or diseased structure with the aim of restoring its original shape and function. Biomaterials are used in various parts of the human body and are implanted as stents in blood vessels, dental implants, orthopedic implants in joints, knees, hips, elbows, ears.

Ever since it was first recognized in 1969 at Clemson University in South Carolina, the field of biomaterials has continued to receive increasing attention. Biomaterials used as implants are divided into 4 groups: metallic, composite, polymeric and ceramic biomaterials. Due to higher strength and hardness and better biocompatibility, metallic biomaterials are used much more in biomedical applications. An alloy Ti-6Al-4V, discovered in the United States in 1954, thanks to its optimal biomechanical properties, became the standard metallic biomaterial in dental implantology. Titanium and its alloys are often described in the literature as "dental metals of the future". This is supported by the large number of new titanium alloys that are being discovered every day. Namely, titanium and its alloys as biomedical materials can improve the quality of human life and life expectancy and therefore in the last few decades have become increasingly used in dentistry and orthopedics [1-4].

1.1. The goal of the paper

With the development of new materials, the methods of their metallographic preparation are being developed or modified in order to obtain as accurate and reliable results as possible using various methods of determining their characteristics. Recently, more and more emphasis has been placed on the economy of the procedure, i.e. on saving resources. Therefore, this paper will study the influence of metallographic preparation of alloys, i.e. grinding and polishing, on the measured hardness values of experimental titanium alloy $Ti_{80}Cr_{15}Co_5$ designed for use in biomedicine [3], in order to determine the optimal conditions for its metallographic preparation. This will be assessed using a numerical analysis of the measured hardness values measurement results. For this purpose, by cutting the alloy into 12 equal parts, samples will be obtained which will be inserted into the epoxy mass, ground and polished. After grinding using various parameters, the surface condition will be recorded and the hardness of all samples measured by the Vickers method. Hardness will be measured on all samples also after polishing. From the obtained results, the influence of metallographic preparation on the measured hardness values of the experimental titanium alloy will be concluded.

2. Prerequisites and means for solving the problem

2.1. Preparation of samples

In order to determine the influence of metallographic preparation on the measured hardness values of the alloy $Ti_{80}Cr_{15}Co_5$ using a numerical analysis, the combination of parameters shown in Tab. 1 was selected. The rotation speed of the grinding wheel was kept constant at 200 rpm.

Table 1. *Grinding parameters of titanium alloy*

Force / time	3 min	6 min	9 min
5 N	sample 1	sample 5	sample 9
10 N	sample 2	sample 6	sample 10
15 N	sample 3	sample 7	sample 11
20 N	sample 4	sample 8	sample 12

In order to obtain the appropriate number of samples for metallographic preparation with different parameters according to Tab. 1, it was necessary to obtain twelve approximately equal parts of titanium alloy. Therefore, the cutting was performed on a JET HVBS-56M.

After cutting, the samples were inserted into the polymer mass. The samples were placed in a mold each separately and overflowed with a viscous two-component polymer resin CEM1000, a mixture of polymer in powder form and liquid catalyst.

Grinding and polishing of the samples were performed by standard procedure. Titanium alloy samples were grinded with a force of 5 N, 10 N, 15 N or 20 N for 3, 6 or 9 minutes, i.e. one of 12 possible combinations was applied to each sample. Grinding was performed with sandpapers of different grain sizes, from the coarsest (120) to the finest (1200). The grinding machine speed was set to 250 rotations per minute. During grinding the samples were constantly cooled with water to prevent possible changes in the microstructure due to the action of heat generated by friction between the grit paper and the surface of the metal sample and to remove / wash impurities and grinding products.

2.2. Light microscopy

A light microscope was used to obtain information about the appearance of the surface and phenomena in the samples, such as inclusions, porosity, cracks and others. For that purpose, samples that were metallographically prepared were used.

In this paper the samples were observed at 200 times magnification using an Olympus GX 51 light microscope. The surfaces of the experimental alloy samples after different conditions of metallographic preparation were recorded using an Olympus DP 70 digital camera connected to the said light microscope.

2.3. Hardness measurement

Hardness is a mechanical property that represents the resistance of a material to the penetration of another, harder material into its surface or structure. Hardness is affected by the chemical composition of the material, mechanical and heat treatment. Further, hardness is closely related to the yield strength, modulus of elasticity, fracture strength, tensile strength and toughness [5,6].

In this paper the hardness of the experimental alloy samples was measured by the Vickers method on a Mitutoyo hardness testing machine with different indentation forces: 50 N, 100 N and 300 N. Hardness measurements with each indentation force were performed 3 or 5 times at random spots on the polished surface. After that, all samples were polished again on a microfiber fabric (so-called felt) to a mirror surface (without scratches) at a speed of 200 rpm with occasional addition of aqueous suspension of Al_2O_3. The polishing time was 10-15 minutes. The hardness of HV5, HV10 and HV30 was also measured on the polished samples. The indentation time was 10 s, and the magnification of the microscope for the imprint diagonals measurement was 200 x.

2.4. Statistical analysis of hardness measurement results

In this paper 12 samples of titanium alloy were examined. All samples were grinded with four different grinding forces (5 N, 10 N, 15 N, 20 N), during three different times: 3 min, 6 min and 9 min.

Hardness was measured by the Vickers method using indentation forces of 50 N, 100 N and 300 N. Each measurement was repeated for 3-5 times and the average values were calculated. Values that deviated from the average by more than one standard deviation were excluded. After measuring the hardness with all the chosen indentation forces the samples were polished, and then all measurements were repeated. In repeated measurements, besides indentation forces of 50 N, 100 N, 300 N, a force of 500 N was also used to check the dependence of the measured hardness value on the indentation force obtained before polishing.

3. Results and discussion

3.1. Light microscopy results

Images of the surface of the samples after grinding in different conditions are shown in Fig. 1.

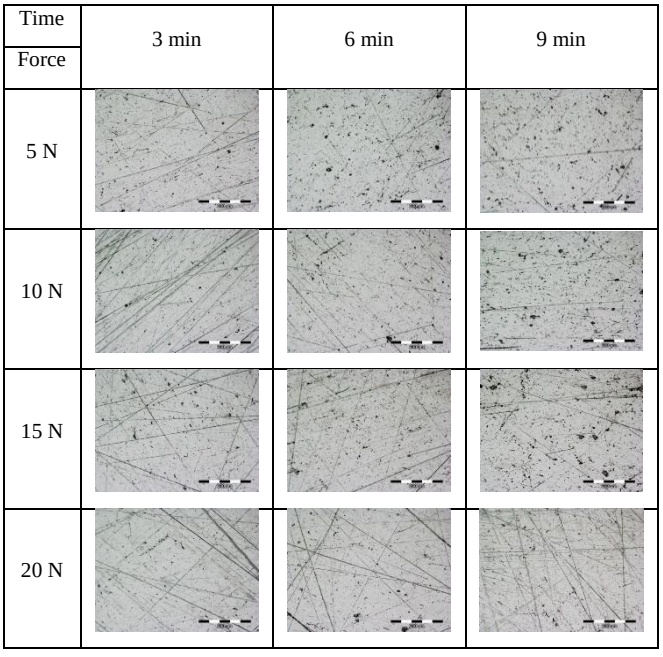

Fig. 1. *The condition of the surface of the samples after grinding by applying different forces for different times*

They show that grinding with the greatest force (20 N) results in the roughest and most numerous cuts / scratches, which become thinner with longer grinding. In the images shown it can be noticed that a longer grinding time leads to the smoothing of deeper cuts and a significant reduction in their number. When comparing the images taken after grinding for 3 and 6 minutes, a significant difference in the number and roughness or fineness of the scratches can be noticed. However, this difference after 6 and 9 minutes of grinding is not so noticeable. From the economic point of view, it follows from the above that the optimal grinding conditions would be the mean grinding time (6 min) and the mean grinding force (10 - 15 N).

3.2. Hardness measurement results

Tab. 2 shows the measurements before polishing while Tab. 3 shows results of measurement after polishing. Excessive deviations are marked in red and these measurements are not included in the calculation of the mean hardness value, which is indicated by the bold font for each sample and for each indentation force.

Table 2. *Hardness measurement results after grinding*

sam-ple	grind. force (N)	grind. time (min)	$HV5$	deviation (sigma)	$\overline{HV5}$	$HV10$	$\overline{HV10}$	$HV30$	$\overline{HV30}$
1	5	3	346,9	0,878	**328,4**	309,2	**313,6**	303,2	**307,6**
			322,1	-0,721		315,9		311,2	
			352,8	1,258		315,6		308,4	
			318,4	-0,959					
			326,2	-0,456					
2	10	3	317		**315,0**	311,3	**305,9**	313,9	**310,8**
			314,7			304,7		310	
			313,4			301,6		308,6	
3	15	3	315,4	-0,085	**312,6**	306,6	**309,2**	317,8	**315,0**
			330,9	1,451		312,2		311	
			320,9	0,460		308,8		316,3	
			306,4	-0,977					
			307,7	-0,849					
4	20	3	317		**315,5**	302,2	**305,5**	307,5	**302,2**
			314,2			301,6		300,4	
			315,3			312,6		298,8	
5	5	6	304,2		**308,4**	321,6	**321,1**	312,5	**315,1**
			311,6			318,1		315,1	
			309,5			323,7		317,7	
6	10	6	322,1	0,964	**315,5**	304,8	**306,6**	310	**312,5**
			320,8	0,839		301,5		309,2	
			298,3	-1,316		313,5		318,4	
			314,8	0,264					
			304,2	-0,751					
7	15	6	311,8	-1,384	**311,3**	320,6	**316,2**	307,7	**304,6**
			302,4	-1,990		317,2		300,9	
			324,3	-0,579		310,9		305,1	
			319,7	-0,875					
			293,6	-2,557					
8	20	6	321,6	0,463	**297,0**	309,6	**309,3**	304,6	**307,6**
			295,7	-3,148		306,7		314,2	
			275,1	-6,019		311,6		304	
			297,7	-2,869					
			297,6	-2,883					
9	5	9	315,6	0,384	**309,1**	316,6	**310,1**	313,8	**312,3**
			311,1	-0,348		306,9		312	
			298,5	-2,397		306,9		311,1	
			309,3	-0,641					
			306,8	-1,047					
10	10	9	299,7	-1,921	**309,5**	312,3	**311,7**	302,7	**306,6**
			312,3	-0,036		310,2		312	
			314,2	0,248		312,5		305,1	
			308,2	-0,649					
			307,9	-0,694					
11	15	9	316,3		**310,9**	312,3	**307,8**	311,9	**307,7**
			314,3			303,2		307,3	
			302			307,8		304	
12	20	9	309,5		**309,6**	314,2	**311,3**	311,8	**309,1**
			309			306		308,3	
			310,4			313,7		307,1	

In general, the results in Tab. 2 show relatively similar values of the measured hardness under all conditions of metallographic preparation. However, considering the grinding parameters (time and force) it can be seen that the grinding time has a more significant role, because after grinding the samples for 9 minutes almost identical hardness values were measured, while after grinding for 3 and 6 minutes the measured values show larger deviations.

Table 3. *Hardness measurement results after polishing*

sam-ple	grind. force (N)	grind. time (min)	$HV5$	deviation (sigma)	$\overline{HV5}$	$HV10$	$\overline{HV10}$	$HV30$	$\overline{HV30}$
1	5	3	322,4		**319,7**	314,1	**319,1**	310,2	**310,5**
			321,2			322,1		309,5	
			315,5			321,2		311,9	
2	10	3	346,2	1,292	**315,8**	309,6	**304,0**	309,8	**306,2**
			335,1	0,790		306		301,2	
			310,4	-0,325		296,4		307,6	
			294,4	-1,048					
			301,9	-0,709					
3	15	3	302,1		**311,9**	307,6	**304,2**	310,4	**309,9**
			316,1			303,4		308,9	
			317,6			301,5		310,4	
4	20	3	315,9		**321,6**	301,6	**299,8**	310,9	**305,5**
			326,7			296,7		306,6	
			323,1			301,2		299,1	
			320,8						
5	5	6	331,6	1,492	**309,9**	310,2	**311,3**	317,6	**312,3**
			310,1	-0,482		314,8		309,2	
			308,5	-0,629		308,9		310,2	
			311,2	-0,381					
6	10	6	307,7		**308,2**	303,8	**308,1**	311,3	**311,2**
			300,3			312,2		316,2	
			316,5			308,4		306,1	
7	15	6	318,9	-0,546	**314,6**	317,6	**308,0**	313,1	**311,5**
			324,8	-0,112		302,7		313,8	
			312	-1,054		303,6		307,7	
			313	-0,981					
8	20	6	304,9		**297,5**	309,2	**305,0**	305,7	**304,4**
			291,2			294,7		305,4	
			296,3			311,2		302,2	
9	5	9	329,1	2,301	**329,6**	322,9	**318,5**	307,8	**305,1**
			340,3	3,703		316,3		303,9	
			343,2	4,066		316,3		303,5	
			319,5	1,099					
			316,3	0,699					
10	10	9	299,6		**306,0**	313,8	**316,7**	302,3	**310,1**
			307			316,9		312,1	
			311,4			319,5		316	
11	15	9	325,5	1,164	**307,8**	297,2	**303,0**	319,9	**309,6**
			325,3	1,144		304		303,8	
			305,2	-0,859		307,7		305	
			306,3	-0,750					
			311,9	-0,191					
12	20	9	322,4	0,694	**315,0**	309,3	**308,2**	308,1	**311,0**
			327,7	1,200		306,7		316,1	
			312,1	-0,289		308,7		308,8	
			310,5	-0,441					

3.3. Statistical analysis of hardness measurement results

After measuring the hardness of all samples with different indentation forces, statistical analysis of the results was performed. First, the mean hardness value was calculated and also the standard deviation from the mean value, for all 12 samples together, depending on the indentation force, before and after polishing. The obtained results are shown in Tab. 4:

Table 4. *Comparison of calculated mean hardness values and standard deviations*

HV		HV5	HV10	HV30	HV50
Before polishing	mean	311,9	310,7	309,3	-
	standard deviation	7,2	4,6	4,0	-
After polishing	mean	313,1	308,8	309,0	306,9
	standard deviation	8,3	6,4	2,8	4,7

The results given in this table show that the differences in the measured hardness before and after polishing are much smaller than the standard deviation of the measurement series, which means that the polishing process does not significantly affect the measured hardness values of the experimental titanium alloy.

Furthermore, the standard deviations are slightly higher for the indentation force of 50 N (although measurements with excessive deviation have already been omitted), which means that the indentation force of 50 N is too small to measure the hardness of the experimental titanium alloy, i.e. measurements with this force result in excessive statistical errors. This is quantified by taking the first three measurements for each sample (regardless of deviations) and calculating the relative measurement error (RME) according to the expression:

$$(1) \quad RME = \frac{maximum\ \ hardness\ - minimum\ \ hardness}{mean\ \ hardness\ \ value}.$$

This term was used due to the fact that the standard deviation is not reliable information because it was calculated from a series of only three measurements. The mean value for RME was then calculated for all 12 samples and the results are shown in Tab. 5.

Table 5. *Relative measurement error*

Indentation force		50 N	100 N	300 N	500 N
Before polishing	RME	0,053	0,025	0,023	-
After polishing	RME	0,051	0,034	0,033	0,032

The results shown in Tab. 5 show that the RME is much higher for a force of 50 N than for other applied forces. For this reason, it is recommended to use an indentation force of at least 100 N to measure the hardness of the experimental titanium alloy.

From the results obtained by measuring the hardness, a decrease in the measured hardness (HV) with an increase in the indentation force (F) is also observed. For the values obtained after grinding (before polishing) the following formula is obtained:

$$(2) \quad HV = 309.105 + 4.9404 \cdot e^{-0.011F},$$

with the R^2 value equal to 1, which means a perfect match. The quality of this model was checked by measuring the hardness of all samples after polishing with an additional indentation force of 500 N and the following formula was obtained:

$$(3) \quad HV = 306.68 + 7.2185 \cdot e^{-0.006F},$$

with the R^2 value equal to 0.8306, so still a good match, which is clearly shown by the graph shown in Fig. 2:

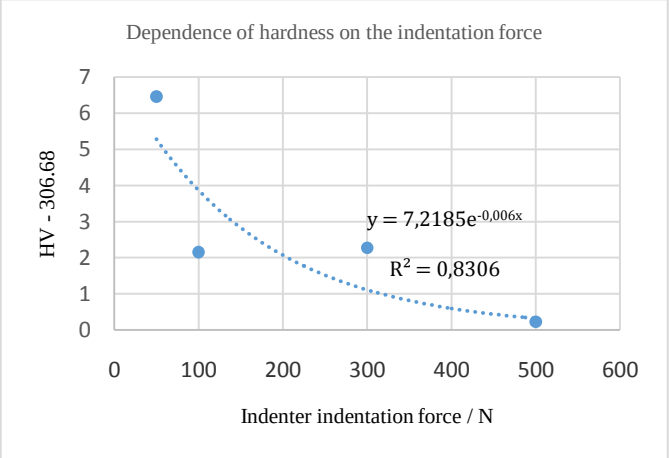

Fig. 2. *Dependence of hardness measured after polishing on the indentation force*

The dependence of the measured hardness on the grinding parameters was also determined. However, the standard deviation for only three measurements is mostly in the range of 3 to 7 HV, so statistically significant deviations from the mean values are only those greater than 10 HV. Statistically significant deviations are considered to be those that deviate from the mean by at least two standard deviations. There were very few such large deviations in these measurements, so unfortunately no clear conclusion can be drawn in this direction. Therefore, it is recommended that a higher number of measurements be performed during the hardness test, with fewer variable parameters.

However, it can be observed that the hardness decreases with the grinding force because such a trend is obtained both before and after polishing, as shown in Fig. 3 and 4 (a mean hardness value of measurements for all grinding times is considered here).

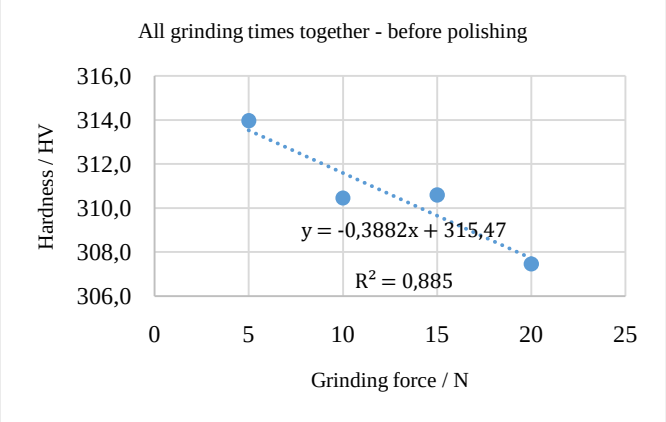

Fig. 3. *The trend of decreasing hardness with increasing grinding force - before polishing*

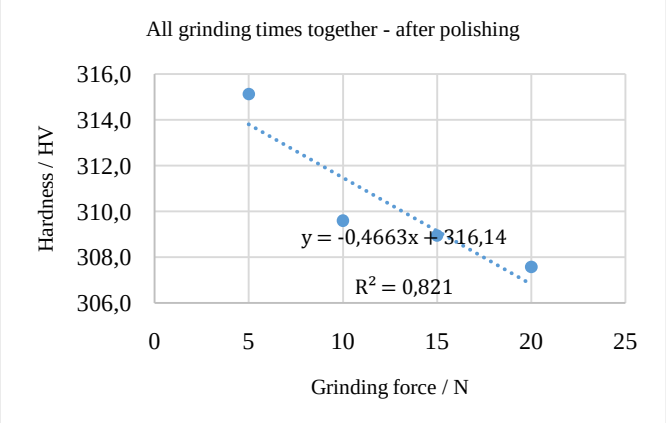

Fig. 4. *The trend of decreasing hardness with increasing grinding force - after polishing*

4. Conclusion

In this paper we measured the hardness of 12 samples of experimental titanium alloy $Ti_{80}Cr_{15}Co_5$ by the Vickers method with different indentation forces (50 N, 100 N, 300 N) after grinding for 3, 6 and 9 minutes with grinding forces of 5, 10, 15 and 20 N, in order to determine the influence of metallographic preparation on the measured hardness values of the alloy. The measurements are done both before and after polishing.

Based on the results obtained in this paper, the following conclusions can be drawn:

- After grinding the samples for the longest time (9 min) almost all samples have no cuts / scratches or are they slightly visible. The exception is sample 12, which was ground with the greatest force, and this obviously led to significant damage to the surface, which was not smoothed even after 9 minutes of grinding.
- The measured hardness values are very similar (uniform) which can be explained by the homogeneous microstructure of the experimental alloy.
- The measured hardness values decrease as the surface of the samples becomes finer.
- The values of hardness measured during indentation with higher forces do not depend on the surface condition, i.e. on the metallographic preparation of the samples.
- The hardness values measured during indentation with lower forces increase with increasing surface roughness of the samples.
- The measured values of the hardness of the samples of the experimental titanium alloy decrease with increasing indentation force.
- The measured hardness values decrease with increasing applied grinding force in the metallographic preparation of samples.
- The polishing process does not have a significant effect on the measured hardness values of the experimental titanium alloy.
- Indentation force of 50 N is not recommended since the standard deviations are slightly higher than with higher indentation forces.
- From the aspect of economy, in order to save resources (grinding material, water, electricity), it is enough to use the average grinding force (10-15 N) for the average time (6 min), after which the relevant hardness values are obtained.

5. References

1. M. Geetha, A.K. Singh, R. Asokamani, A.K. Gogia, Ti based biomaterials, the ultimate choice for orthopaedic implants - A review, Progress in Materials Science, 54 (2009) 3, 397–425.
2. J. Živko-Babić, D. Stamenković, Titan i legure titana-metali budućnosti u stomatologiji, Stomatološki materijali, knjiga 2, Stomatološki fakultet u Beogradu, Beograd, 2012.
3. Lj. Slokar, Utjecaj kobalta i niobija na stabilnost beta faze u biomedicinskim titan-krom legurama, Doktorska disertacija, Sveučilište u Zagrebu Metalurški fakultet, Sisak, 2010.
4. A. Pandey, A. Awasthi, K. Saxena, Metallic implants with properties and latest production techniques: A review, Advances in Materials and Processing Technologies, 6 (2020) 2, 1-36.
5. Mechanical Testing and Evaluation, ASM Handbook Volume 8, ASM International, Materials Park, (2000)
6. P.M. Talarico, Y.W. Kwon, Hardness and tensile properties of metals subjected to aging conditions, Multiscale and Multidisciplinary Modelling, Experiments and Design (2020) 3:187-200

Obtaining abrasives on the base of composite Ni-P coatings for surface treatment of rock materials

Veselina Chakarova, Maria Petrova
Institute of Physical Chemistry, Bulgarian Academy of Sciences,
"Acad. G. Bonchev" Str., Blok 11, 1113 Sofia, Bulgaria
e-mail: vchakarova@ipc.bas.bg

Abstract: *The electroless deposition of Ni-P coatings is well known classic method for production of metal coatings on polymers. The addition of dispersed particles of different types and sizes to the base solution for electroless deposition significantly improves the properties of the coating by increasing its wear resistance and micro-hardness. Thereby, the metallized polymers find new and different applications. By using a device, designed and developed in IPC-BAS, tribological tests of composite Ni-P coatings deposited on substrate of polyethylene terephthalate (PET) are performed. Three types of dispersed particles (diamond (D), BN and SiC) are co-deposited in the Ni-P coatings. Their application as abrasive material for surface treatment of rock materials is evaluated. The structure, morphology and elemental composition of Ni-P coatings are characterized by SEM and EDS.*
KEYWORDS*: COMPOSITE ELECTROLESS NI-P COATINGS, PET, DISPERSED PARTICLES (D, BN, SIC), SEM, EDS.*

1. Introduction

The electroless deposition of Ni-P coatings is a method for surface modification of materials of different types and compositions. The coatings have a number of advantages, such as: good corrosion and wear resistance, hardness and evenly distribution, regardless of the complexity of the detail. The co-deposition of a non-metallic element (P) largely determines the structure and hence the properties of these coatings [1, 2].

Improvement of the basic properties of the electroless Ni-P coatings is achieved by addition of dispersed particles of different types and sizes to the base solution and hence, composite coatings are deposited [3-8].

The most commonly used dispersoid are synthetic diamond particles. They are cubic or octahedral crystals. A significant number of studies are devoted to the preparation of composite Ni-P coatings containing diamond particles of different sizes (Ni-P/D). The comparison with the Ni-P coatings shows better properties in terms of micro-hardness, wear resistance, abrasiveness, corrosion protection, etc. [3, 7, 9, 10].

Boron nitride (BN) is not present in nature as a mineral. Three of its crystal modifications are known: alpha modification (denoted as hBN due to the hexagonal graphite-like structure), beta modification with diamond-like cubic crystal structure of a sphalerite type (denoted as cBN) and gamma-BN with hexagonal crystal structure (wurtzite type). The last two modifications show hardness close to that of a diamond. The modification hBN is used as a solid lubricant. It is embedded into composite materials and the produced details show antifriction properties [3, 11].

Carbides are difficult to melt and insoluble solids. As a typical representative of covalent carbides, SiC (also called carborundum) is characterized by high hardness (about 9 on the Mooc scale), high melting temperature and chemical inertness. The addition of SiC particles as a second phase to the electroless coatings has been shown to be one of the methods for improving their basic characteristics (micro-hardness and corrosion resistance) [12-14].

Common between the three types of particles is that they find application in obtaining tools for abrasive treatment of different materials [15, 16].

The aim of the present study is to obtain composite Ni-P coatings with the three types of particles (D, BN and SiC) on a flexible substrate of PET, and to study their possible application for surface treatment of rock materials. Polyethylene terephthalate (PET) is a linear homo-polymer with a dominant composition of polyester fibers. It can be heated and processed into various forms, such as fibers, sheets, etc. [17, 18].

2. Experimental

Non-woven cloth of PET subjected to reinforcement by additional pressing was used as a substrate in these investigations. The samples were pre-treated employing the following technological scheme [19]: etching in alkaline solution OA-84-2 (a commercial product of Technical University-Sofia) at T = 65 ˚C and τ = 15 min; pre-activation in 3M HCl at T = 25 ˚C and τ = 5 min; activation in colloidal solution of $PdCl_2$ A-75-12 (a commercial product of Technical University-Sofia) at T = 25 ˚C and τ = 5 min; acceleration in alkaline solution X-75-4 Accelerator (a commercial product of Technical University-Sofia) at T = 25 ˚C and τ = 5 min.

After the above pre-treatment, the samples were immersed in the solution for electroless nickel plating [18], presented in Table 1.

Table 1. *Composition of the solution and working conditions*

Composition of the solution	
$NiSO_4.7H_2O$, g l^{-1}	25.0
$NaH_2PO_2.2H_2O$, g l^{-1}	22.0
CH_3COONa, g l^{-1}	20.0
Lactic acid (80 %), g l^{-1}	20.0
Stabilizer 2, mg l^{-1}	1.0
Working conditions	
pH	4.6 – 4.8
T,°C	82-85

As dispersoids were used particles of: diamond with dimensions of 3/7 μm (corresponding to a mixture of D particles sized from 3 to 7 μm) and 63/75 μm; cBN – 63/80 μm and hBN 1/5 μm; SiC - 7/10 μm and 60/70 μm. Prior to addition to the solution, all particles were subjected to preliminary treatment in aqueous solution of sodium laurylsulphonate (SLS) with concentrations of 0.01 g l^{-1} at room temperature.

The composite coatings were deposited with different time duration to ensure the incorporation of the different sized particles. For more evenly distribution, the solution was stirred by air flow agitation (100 ml min^{-1} for 250 ml solution) under different modes, respectively noted in the experimental results.

The mass of the deposited nickel coating (Δm) was determined gravimetrically – based on the difference in the weights of the samples prior and after the deposition of the coating.

The morphology and the structure of the coatings, as well as the particles' distribution over their surface were studied by means of scanning electron microscopy (SEM) (JSM 6390, Japan). The average amount of co-deposited particles (N cm^{-2}) was determined by the counting in three arbitrarily chosen zones at a magnification 200x.

A device, designed and manufactured at IPC-BAS was used to perform tribological tests [20]. The specimens with a diameter of 7 cm were fixed on a support disk, flat-parallel to the surface of the counter body of limestone. The load on the working disk was 1 kg; the speed of rotation 1000 rpm, and a successive change of the disks in the direction from larger to smaller size of the dispersed particles. The working time of the every disk was 1 min.

The roughness parameters R_a and R_z were measured by a profilograph-profilometer Perthometer C3A (Dr. Ing. Perthen GmbH).

3. Results and discussion

3.1. Conditions for obtaining composite Ni-P coatings on PET

In our previous papers [8, 15, 16], the influence of the concentration of the dispersoid in the solution, the deposition time and the hydrodynamic regime on the inclusion of the particles, as well as their adhesion to the coating were studied. In this section are presented only the conditions for obtaining the composite Ni-P coatings with which the tribological tests are performed.

All composite coatings were deposited at a dispersoid concentration of 5.0 g l^{-1} regardless of the particle size.

Data on the mass of composite coatings and the number of the incorporated particles during 1 h deposition time are given in Table 2.

Table 2. *Influence of the type and the size of the particles on the Mass of the composite coating (Δm, g) and number of deposited particles (N/cm^{-2}) at a deposition time of 1 h.*

	D	**D**	**hBN**	**cBN**	**SiC**	**SiC**
μm	**3/7**	**63/75**	**1/5**	**63/80**	**7/10**	**60/70**
Δm, g	0.3937	0.4355	0.4360	0.2964	0.5014	0.4739
N/cm^{-2}	-	2200	-	11600	-	1200

For the small particles, the time of stay of the specimens in the solution of 1 h is quite sufficient to obtain coatings with good characteristics. No attempt is made to estimate their number because of their small size and the coverage of some of them by Ni-P coating. For the larger particles, the composite coating deposited at that time has a mass insufficient to obtain good attachment of the particles to the coating. Therefore, for composite coatings with larger particles, the time of deposition of 5 h is more appropriate (Table 3).

Table 3*. Influence of the type of the particles on the mass of the composite coating (Δm, g) and number of the deposited particles (N/cm^{-2}) at a deposition time of 5 h.*

	D 63/75 μm	**cBN 63/80 μm**	**SiC 60/70 μm**
Δm, g	0.7937	0.7027	0.5292
N cm^{-2}	222600	240500	90000

Composite Ni-P coatings with small particles were deposited by constant air stirring. This hydrodynamic regime is not suitable for large particles. An appropriate interrupted hydrodynamic regime for the large particles was turned out to be 2 min of stirring and 10 min without stirring according to [16, 20].

SEM images of Ni-P coatings obtained on PET under the selected composition and operating conditions of the nickel solution (Fig. 1).

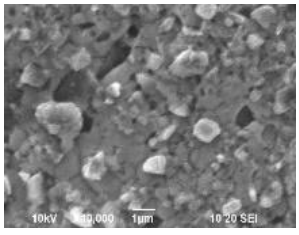

a)

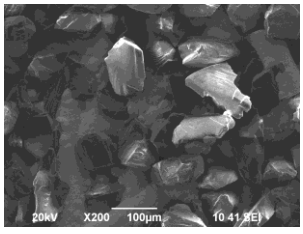

b)

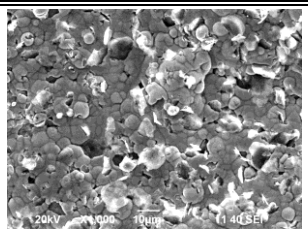

c)

d)

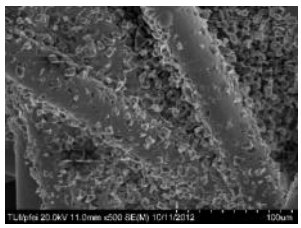

e)

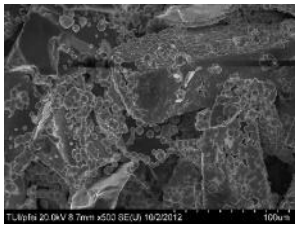

f)

Fig.1. *SEM images of composite Ni-P coatings deposited in the presence of: Diamond particles - a) 3/7 μm and b) 63/75 μm; c) hBN particles 1/5 μm; d) cBN 63/80 μm; SiC particles - e) 7/10 μm and f) 60/70 μm.*

3.2. Tribological testing of samples with different dispersoids

The object of treatment is the limestone material with dimensions 10x10x10 mm.

The change in the mass (Δm) of the limestone samples before and after treatment with the tested disks is shown in Table. 4.

Table 4*. Influence of the type and size of the dispersoid in the composite coating on the loss of limestone mass (1000 rpm/1 min/1 kg).*

Type of the dispersoid	Δm, g
D 3/7 μm	0.008
D 63/75 μm	0.067
SiC 7/10 μm	0.001
SiC 60/70 μm	0.056
hBN 1/5 μm	0.001
cBN 63/80 μm	0.011

The results show that larger particles take away more mass, with the strongest effect in the case of diamond particles

The abrasive effect of the composite coatings is determined by the change of the values of the parameters characterizing the surface roughness (R_a and R_z) (Fig. 2) and the weight loss (Table 4).

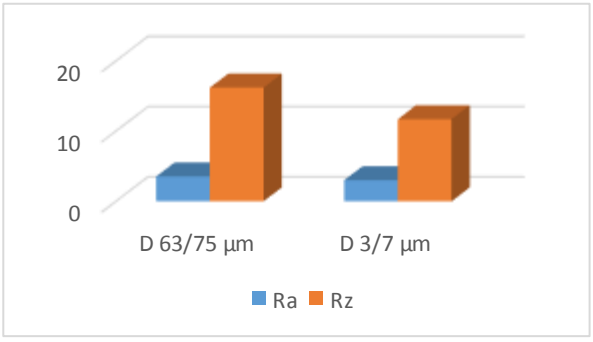

a)

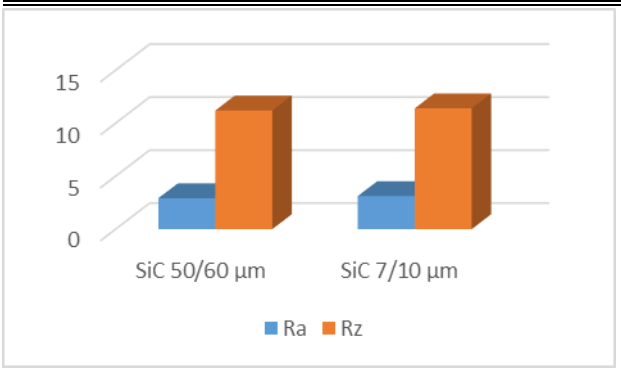

b)

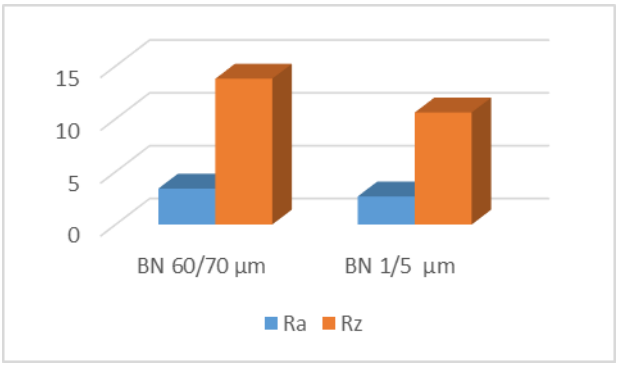

c)

Fig. 2: *Change of the roughness parameters Ra and Rz after treatment of the limestone samples with disks with different types and sizes of the particles: a) Diamond particles; b) SiC; c) BN. Values of R_a and R_z before treatment - 3.96 µm and 17.6 µm, respectively.*

4. Conclusions

Composite Ni-P coatings with three types of particles - diamond (D), boron nitride (BN) and silicon carbide (SiC) of different sizes are deposited on a flexible substrate of polyethylene terephthalate (PET). The deposited samples are characterized by good adhesion of the particles to the coating and to the substrate. Tribological studies show that composite coatings are promising in terms of their use in abrasive tools for surface treatment of rock materials. The next step would be to optimize the tribological conditions - load on the abrasive disk and duration of the treatment.

Acknowledgment: The investigations are conducted with the support of the Project DN 19/1, "Metallisation of dielectric materials using innovative environmental solutions", funded by the Bulgarian National Science Fund and Project_INFRAMAT (National Roadmap for Scientific Infrastructure) under contract D01-284/17.12.2019 of Ministry of Education and Science is gratefully acknowledged.

5. References

1. G. Gavrilov, Ts. Nikolov, "Chemical nickel plating and disperse coatings", (1985).
2. Hr. Petrov, "Galvanization of plastics", (1982).
3. J.N. Balaraju, T.S.N. Sankara Narayanan, S.K. Seshadri, J. Appl. Electrochem. 33, 807–816 (2003).
4. A. Sharma, A. K. Singh, J. Mater. Eng. Perform, 22, 176-183 (2013).
5. V.V.N. Reddy, B. Ramamoorthy, P. Kesavan Nair, Wear, 239, 111-116 (2000).
6. V. Chakarova, M. Georgieva, M. Petrova, Special Issue of Bulg. Chem. Commun., 49 (F), 30-36 (2017).
7. H. Xu, Z. Yang, M.-Ke Li, Y.-Li Shi, Y. Huang, H.-Lin Li, Surf. Coat. Technol, 191, 161-165 (2005).
8. M. Petrova, M. Georgieva, V. Chakarova, Ek. Dobreva, Arch. Metall. Mater., 61 (2), 493-498 (2016).
9. Y.L. Shi, Z. Yang, H. Hu, M.K. Li, H.L. Li, J. Mater. Sci., 39, 5809-5815 (2004).
10. H. Mazaheri, S. Reza Allahkaram, Appl. Surf. Sci., 258, 4574–4580 (2012).
11. O.A. Leoh, M.H. Staila, H.E. Hintermann, Surf. Coat. Technol., 108-109, 461-465 (1998).
12. M. Islam, M.R. Azhar, N. Fredj, T. David Burleigh, Surf. Coat. Technol., 236, 262-268 (2013).
13. Y.S. Huang, X.T. Zeng, X.F. Hu, F.M. Liu, Electrochim. Acta, 49, 4313-4319 (2004).
14. M. Islam, M.R. Azhar, Y. Khalid, R. Khan, H.S. Abdo, M.A. Dar, O.R. Oloyede, T. David Burleigh, J. Mater. Eng. Perform, 24, 4835-4843 (2015).
15. M. Georgieva, M. Petrova, Ch. Jakob, M. Fritz, V. Chakarova, WoMag, 10 (3), 26-27 (printed, short version) and 6 pages (on-line) (2014).
16. V. Chakarova, M. Georgieva, M. Petrova, E. Dobreva, D. Stoychev, Trans. Inst. Metal Finishing, 94 (5), 269-264 (2016).
17. J. Karl Fink, Book Chapter, 347-390 (2008).
18. M. Georgieva, M. Petrova, V. Chakarova, Bulg. Chem. Commun., 45 A, 116-121 (2013).
19. BG Patent № 65604 (2009).
20. D. Stoychev, E. Dobreva, N. Razkazov, M. Stoycheva, N. Koteva, Bulg. Chem. Commun., 46 (2), 283 (2014).

Effect of work hardening and recrystallization annealing on structure and properties of low-carbon steel wire

Kaverynskyi V.V., Bagliuk G.A., Verbylo D. G.
Institute for problems in material science NAS of Ukraine

Abstract: *In this work it was studied the influence of low-carbon steel wire annealing at different temperatures from 500 to 750 °C that was obtained by cold drawing on its structure and properties. It was sown that bigger work-hardening during the drawing process leads to the decreasing of collective recrystallization starting temperature, which could resulting in obtaining less plastic properties than are appear after lower annealing temperatures with additional loss of strength. The found effects give valuable information for cases when it is desirable to obtain the minimal strength or the maximum plasticity of the wire.*
Keywords: WIRE, COLD DEFORMATION, ANNEALING, LOW-CARBON STEEL, *RECRYSTALLIZATION*.

1. Introduction

Low strength properties are rather often needed from low-carbon steel wire. For instance, wire for fastening nails in pneumatic tools should have tensile strength on the level less than 350…360 MPa with not very high plasticity, because it ought to be able easily tear. Sometimes wire is obtained in several stages of cold drawing with intermediate annealing. For this case the wire condemned to the following high cold deformation must be primary as more plastic as it possible. High plasticity is also desired for many cases of ready product, for example, it is crucial for knitting wire and sometimes for welding wire. Low strength at this situation is also may be needed but not as much as for the first example. Moreover, very low strength is not desired for welding wire to prevent its bending and twisting when feeding from a welding machine. So the optimal tensile strength here is on the level about 400 MPa or even some more.

Industrial experience meets a problem that properties of low-carbon wire after recrystallization annealing are not always simply predictable. The desirable level of properties is obtained in some cases but in others is not in spite of the same annealing time and temperature. Also it was noticed that properties sometimes could be highly nonlinearly and spasmodically depend on the annealing temperature. Thus it was deiced that the problem needs a detailed investigation.

It is known, that the main cause of strength decreasing of cold-worked metal during annealing are such structural phenomena as recovery and recrystallization processes [1]. There could occur primary and collective recrystallization [2]. The first one is proceeding at deformed material and resulting in obtaining equiaxial grains instead of deformed ones. These grains could be even smaller than the parent ones [3]. Another process is collective recrystallization. It could appear even in not deformed or annealed materials and may be described like coagulation and Ostwald ripening of the grains [4]. Recrystallization is accompanied with recovering process which is decreasing of dislocation density that leads to the loss of material strength [2]. Recovering could appear even without noticeable recrystallization, especially at lower temperatures [5]. It is distinguished dynamic and static recrystallization [2]. The first one proceeds simultaneously with deformation and is mostly has to do with hot deformation processes which are not under the consideration in this study. So here we have static recrystallization that occurs during annealing after deformation.

The aim of this study is to determine dependence between previous work hardening and mechanical properties of low-carbon steel wire after annealing at different temperatures and also to specify influence of structure changes on them.

2. Materials and experimental details

The first supposed reason of different behavior of the material under the same annealing regime that ought to be considered is its chemical composition. However, the statistical analysis of the industrial protocols did not reveal a significant influence of any element of the composition in its present variation range on strength properties after annealing. It was found a slight dependence of tensile strength in the deformed state on Cr, N, and As impurities amount, but even them are not very valuable and low statistical reliability. It only could be noticed that Cr and N might lead to some increase of deformed metal strength and As may slightly decrease it. Thus the most reasons in this case are not in chemical composition, moreover it could be considered as averagely same for all the studied specimens. The averaged chemical composition of the studied samples material is given in table 1.

***Table 1. Chemical** composition of the studied material (mass %)*

Elements, %							
C	Mn	Si	S	P	Cr	Ni	Cu
0,04 – 0,06	0,31 – 0,37	0,026 – 0,080	0,004 – 0,026	0,008 – 0,017	0,02 – 0,07	0,02 – 0,13	0,03 – 0,05
As	N	Ti	B	V	Mo	W	Sn
0,002 – 0,005	0,005 – 0,011	0,001 – 0,005	< 0,0004	0,001 – 0,005	< 0,01	< 0,027	0,003 – 0,005

It is a low-carbon steel that contains only some amount of Mn as alloying element. Other elements are just on the typical level of impurities.

For the main process where the final properties of the material are forming is annealing, an experimental study was carried out which consist in annealing of the wire specimens at different temperatures during different keeping times. The initial samples were taken directly after cold deformation (drawing) which is wire production process. They have different initial level of work hardening and different diameter. Here are the diameters and the average values of ultimate tensile strength: 3.0 mm, 849±17 MPa; 2.0 mm, 882±8 MPa; 1.2 mm, 1040±18 MPa. Initial tensile strength before the cold deformation was similar to all the samples, about 360…380 MPa. The studied annealing temperatures were following: 500, 600, 650, 700, and 750 ºC with temperature hysteresis about ±15 ºC. The annealing time varied from 2 to 5,5 hours. The annealed samples were used to study tension mechanical properties and microstructure.

Also additional experiments were carried out, where the samples of wire were undergo heating at 930 ºC (to austenite area) during about 5 – 7 minutes and then cooled in the air or salt water (~10 % of NaCl solution). After cooling some of the specimens were tempered at 650 and 700 ºC during about an hour.

3. The results of the experiments and their discussion

The obtained results showed that considered varying of annealing time does not make a valuable impact on the mechanical properties. But according to the industrial data lesser times could significantly affect them, especially first 30 minutes. Rather more important factors are the annealing temperature and work hardening made through drawing deformation. The effect of ultimate tensile strength (a) and yield strength (b) on the annealing temperature are shown on figure 1. A plot are given for every of the specimens type.

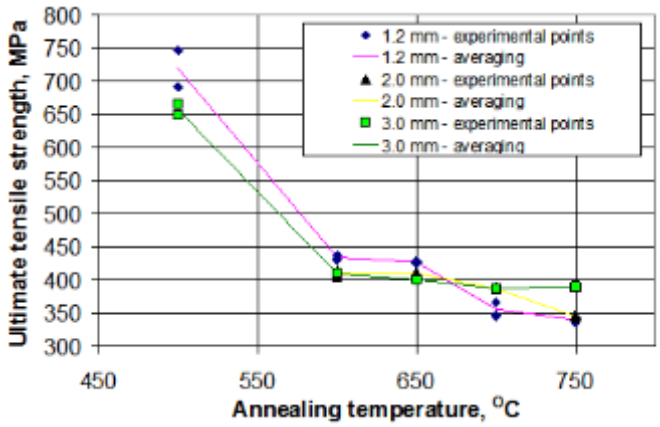

a)

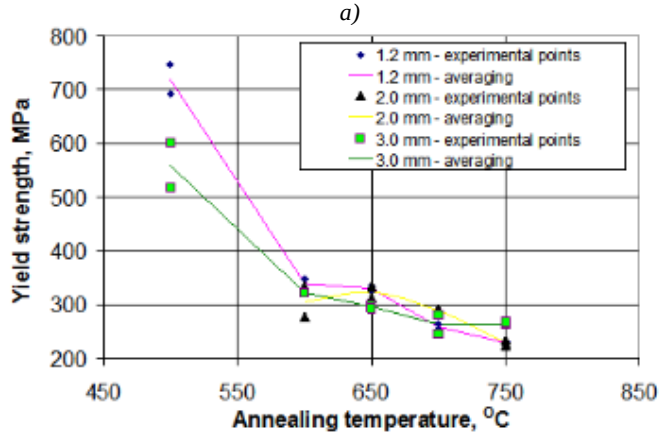

b)

Fig. 1. *Effect of annealing temperature on strength properties of the low-carbon steel wire*

From the obtained data it is clearly perceptible some difference in regularity of changing strength with annealing temperature alteration for different types of the samples, which are distinguished only with their work hardening, but not the composition.

After 500 ºC annealing the obtained strength is already significantly less than in the corresponding deformed state but yet rather high. It is notable that for this case the higher work hardening is resulting in somewhat bigger strength after annealing. More distinctly this effect is observed for the yield strength property, there the gap between average values for the samples with initial 849±17 MPa and 1040±18 MPa correspondently after annealing becomes about ~ 160 MPa (~ 550 and 710 MPa correcpondently).

The same tendency remains at annealing temperatures 600 and 650 ºC – more work hardened metal has higher strength also after annealing. It is noteworthy that at this temperature range there is no statistically significant difference in tensile strength obtained after annealing at 600 and 650 ºC for the corresponding specimens types. Only for the less work hardened samples there might be a slightly decrease in yield strength.

Higher annealing temperatures give the most notable results. Fore the least work hardened samples ultimate tensile strength remains almost at the same level as it has been obtaining after 600 and 650 ºC annealing. There may be only just insignificant decline. The decrease in yield strength here is some more significant, however, it is almost linear without any leaps. In contrast to that for the most work hardened samples we can see an abrupt additional decline of tensile strength after annealing at 700 ºC comparing with one obtained after 600 and 650 ºC annealing. Almost the same strength level remains also after annealing at 750 ºC, may be just slightly less. Wire samples of Ø 2 mm which are some more work hardened than Ø 3 mm ones shows the same behavior, but only at 750 ºC annealing. At lower annealing temperatures only insignificant tensile strength decrees could be observed and the values are close to ones for Ø 3 mm specimens.

It is remarkable that after annealing at 750 ºC strength values (both ultimate tensile strength and yield strength) for the Ø 1.2 and Ø 2 mm samples appear very similar: ~ 340 MPa vs. ~ 346 MPa and ~ 229 MPa vs. ~ 230 MPa correspondently. Taking into account that ultimate tensile strength values for the most work hardened wire (Ø 1.2 mm) are almost not change in the range of annealing temperatures 700 – 750 ºC, there is a reason to suppose that these values are ultimate least that could be obtained after recrystallization low-temperature annealing for this material.

Not the less interesting looks the dependence of relative extension, which is a measure of material plasticity, on the annealing temperature. The corresponding plot is given on figure 2.

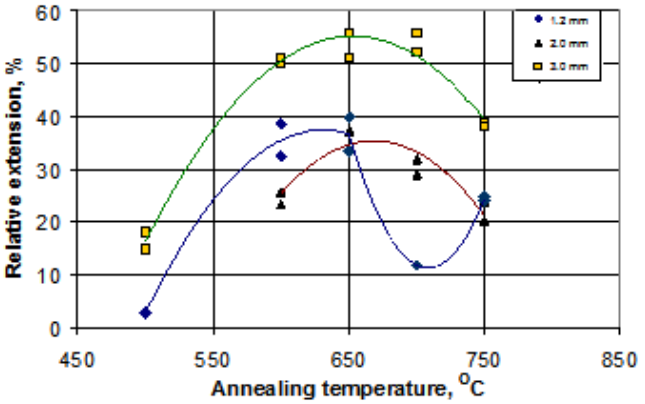

Fig. 2. *Effect of annealing temperature on relative extension of the low-carbon steel wire*

The first notable feature here is that the least work hardened wire (Ø 3 mm) shows the highest relative extension values for each corresponding annealing temperature. However, just more hardened wire (Ø 2 mm) demonstrates the least of its values fore the most of the considered annealing temperatures. The most worth notable at this case is that for the most hardened wire (Ø 1.2 mm) is observed a collapse of plasticity after annealing at 700 ºC, but 750 ºC annealing leads to its higher values. The common thing for all of the considered samples types is that the maximum values of relative extension could be obtained after annealing at about 650 ºC. Then, at higher temperatures, it anyway tends to decline. Annealing temperature does not the same significantly affect the values of constriction ratio (another plastic property).

The observed behavior of plasticity, especially for the samples type of the most work harden, were the plasticity collapse is present, is to be compared with mentioned above dependence of strength on the annealing temperature. As we can see, the plasticity decline after annealing appears at 700 ºC, at the same temperature in these specimens also occurs the additional strength decrease, which is more clearly seen for the yield strength for Ø 1.2 and 2 mm samples and also for ultimate tensile strength for Ø 1.2 samples. So we have simultaneous decrease of both strength and plasticity at rising annealing temperature to 700 ºC and higher comparing with properties that could be obtained at lower annealing temperatures.

As it was mentioned above and is seen from the plots, the dependence of strength and plasticity on annealing temperature for different specimen types is not the same. And the only difference between the types is the level of work hardening. To make this dependence more clear, plots are given on the figure 3, which demonstrate an influence of initial ultimate tensile strength in cold-worked state on one obtained after annealing at different temperatures. Data for 500 ºC annealing are not given on this plot because of comparably higher values, which could make the plot system less clear.

For the temperatures 600 and 650 ºC we observe almost linear dependences which show that the more work hardened the material was, the higher its strength appear after annealing. And here the difference in the dependences is almost absent for both of these temperatures. For the temperatures 700 and 750 ºC the

dependencies appear quite different, and the most specific fact in these cases is that they change their directions – higher strength in a work hardened state leads to less one after the annealing.

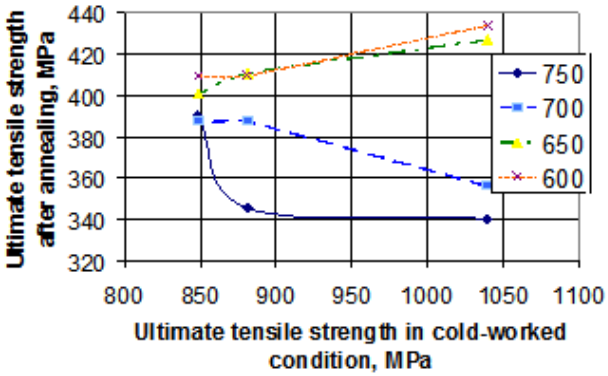

Fig. 3. *Effect of initial strength after drawing deformation on the strength obtained after annealing*

For the annealing temperature 700 ºC increase of the initial strength in cold-worked state from 849 to 882 MPa almost does not affect the resulting one obtained after the annealing. However, hardening up to 1040 MPa does – the resulting tensile strength appears significantly less. For 750 ºC annealing even work hardening to 882 MPa is enough to obtain significantly lesser strength after annealing than it could be received for hardened to 849 MPa specimens. Additional work hardening leads to just slight decrees of the strength obtained after annealing at this temperature.

It seemed that the causes of the observed behavior are in recrystallization that has a place during the annealing processes. Therefore it was carried out an exploration of the annealed metal microstructure. Figure 4 shows the microstructure of deformed metal for each type of the samples.

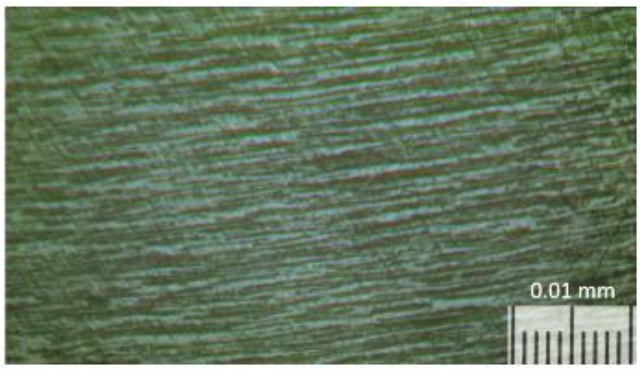

a)

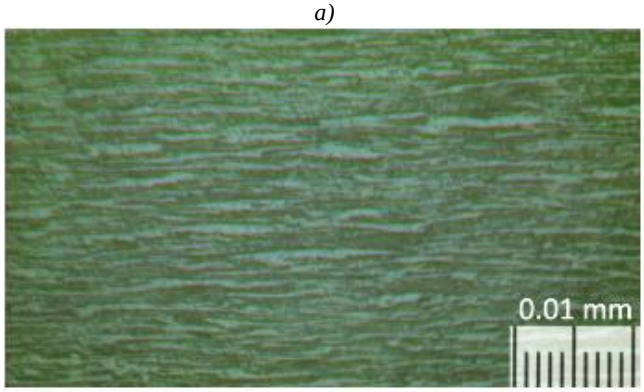

b)

c)

Fig. 4. *Microstructure of the of low-carbon steel wire in work hardened state: a) 1.2 mm, 1040±18 MPa; b) 2.0 mm, 882±8 MPa; c) 3.0 mm, 849±17 MPa*

The structure in the deformed state is quite ordinary. It consists of elongated ferrite grains, as longer and thinner as more significant drawing deformation the metal was affected. It is noteworthy that the structure after 500 ºC annealing remains rather qualitatively similar. As we can see from figure 5, there also observed the same elongated grains.

a)

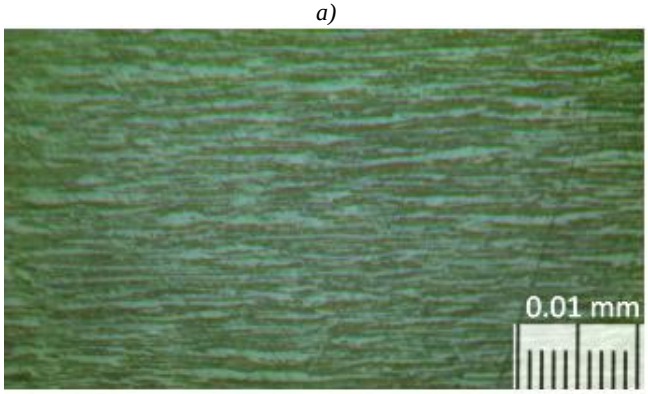

b)

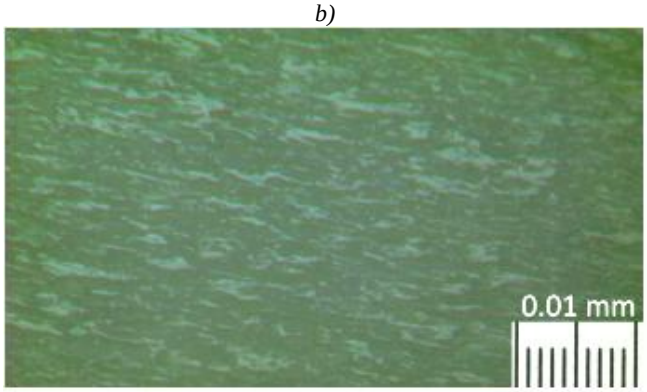

c)

Fig. 5. *Microstructure of the of low-carbon steel wire after annealing at 500 °C: a) 1.2 mm, 1040±18 MPa; b) 2.0 mm, 882±8 MPa; c) 3.0 mm, 849±17 MPa*

Photos taken at bigger magnification (×1000) and shown at figure 6 suggest supposing that some initial recrystallization might occurred near the grain boundaries even during annealing at this temperature. However, it seems like the main cause of the observed some strength loss in this case is merely recovering, but not recrystallization.

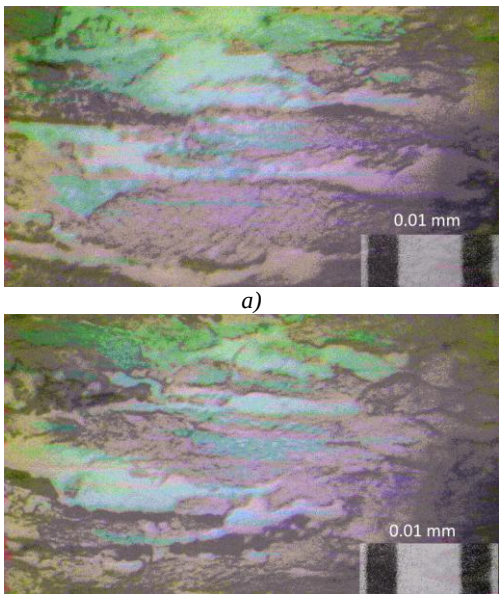

a)

b)

Fig. 6. *Microstructure of the of low-carbon steel wire after annealing at 500 °C, ×1000*

Annealing at 600 ºC leads to an active primary recrystallization. As it seen from figure 7 the structures is formed by almost equiaxial small grains. The grains are the smaller the higher was the work hardening.

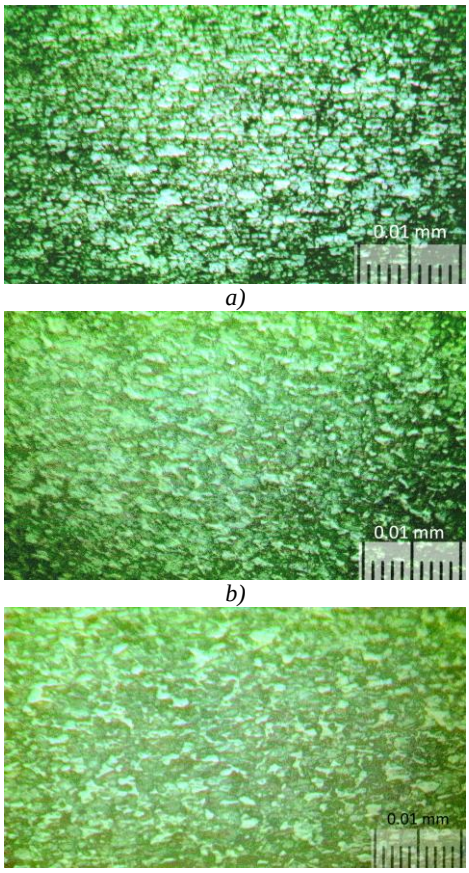

a)

b)

c)

Fig. 7. *Microstructure of the of low-carbon steel wire after annealing at 600 °C: a) 1.2 mm; b) 2.0 mm; c) 3.0 mm*

From the structures just above and more clearly from the figure 8, where are shown structure photos of larger magnification, in seams like in Ø 1.2 samples the primary recrystallization is rather complete, but in the other types is not.

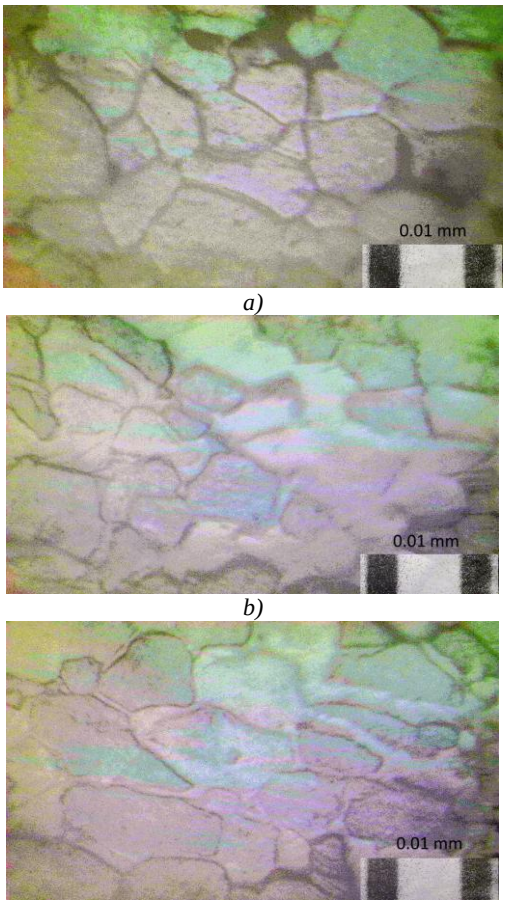

a)

b)

c)

Fig. 8. *Microstructure of the of low-carbon steel wire after annealing at 600 °C: a) 1.2 mm; b) 2.0 mm; c) 3.0 mm*

The difference in the structure parameters between the corresponding samples annealed at 600 and 650 °C is insignificant. We also have small equiaxial grains of similar size. However, it could be mentioned, that at this temperature has a place more complete primary recrystallization and grains appear more equiaxial than they were after 600 °C annealing, especially for less initially work hardened samples.

During annealing at 700 °C starts collective recrystallization – grains become lager. Its appearing highly depends on the level of work hardening of the material, so, as we can see from photos on figure 10, it could vary through the cross-section of the wire.

Figure 10 (a) shows the surface layer of the wire, which is more work hardened that its core. So collective recrystallization near the surface goes more actively, which is resulting in obtaining larger grains in that place. In the Ø 3 mm wire, which was least deformed, collective recrystallization process almost not started, but primary recrystallization is complete. Only in a thin surface layer, not more than 50 microns, which is likely was the most work hardened, some signs of collective recrystallization might be seen. Collective recrystallization occurs in Ø 2 mm wire at this temperature. However, its work hardening does not significantly vary through the cross-section, so the grain size in it is close to one in the core of Ø 1.2 mm wire. Thickness of the collective recrystallized layer in Ø 1.2 mm wire is up to 0.45…0.50 mm, which is a significant part of the cross-section. Hence we observe the mentioned abrupt strength and plasticity loss. In contrast, more evenly deformed Ø 2 mm wire shows more facile strength decrease by rising the annealing temperature.

Annealing at 750 °C initiates collective recrystallization in all of the specimens types. In Ø 1.2 mm samples in this case it touches

almost all the cross-section, as in could be seen from figure 11 (a), but inner layers still have somewhat smaller grains than the surface ones.

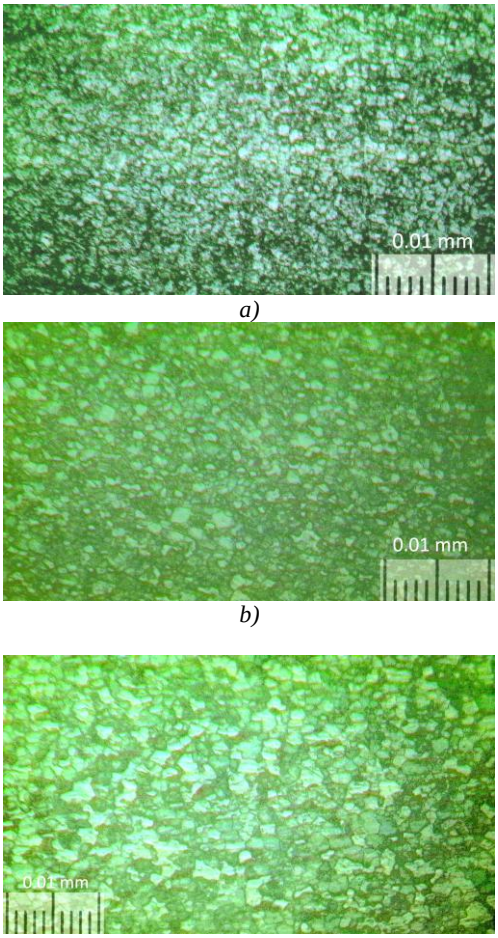

a)

b)

c)

Fig. 9. *Microstructure of the of low-carbon steel wire after annealing at 650 °C: a) 1.2 mm; b) 2.0 mm; c) 3.0 mm*

Significant collective recrystallization in this case appear through all the cross-section of Ø 2 mm wire (figure 11 – c, d). Certainly that results in additional loss of strength to the level close to one that is been obtained for Ø 1.2 mm wire after annealing at 700 and 750 °C.

Collective recrystallization also has a place in Ø 3 mm specimens. However, it occurs only in the surface layer with thickness not more than 0.5 mm, which is likely was the most deformed and work hardened. In contrast to Ø 1.2 mm wire in this case it forms significantly lesser part of the cross-section. Hence, we do not observe such additional loss of strength as it was for Ø 1.2 mm at 700 °C, where the similar situation appears. Although a decrease of the plasticity is definitely seen.

The hypothesis that work hardening facilitates collective recrystallization is additionally proofed by micro hardness measurement, which change through the cross-section in a deformed state strongly correlates with structural layers after annealing. Figure 12 shows the micro hardness variation from the surface to the core of the wire in a work hardened sate.

In Ø 1.2 and Ø 3.0 mm wire surface layer appear significantly harder, Ø 2.0 mm wire does not have such difference, and its hardness only slightly decreases from the surface to the core. Thus in Ø 1.2 and Ø 3.0 mm wire after a certain annealing temperature we obtain a surface layer in which a collective recrystallization evolves rather more significantly, but in Ø 2.0 mm wire we do not observe such behavior.

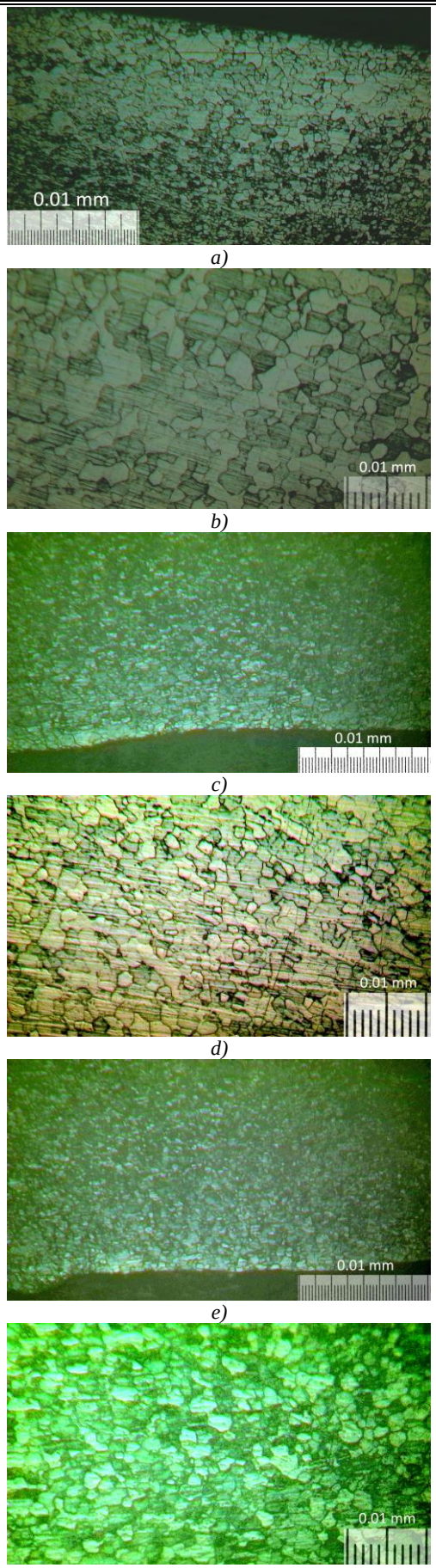

a)

b)

c)

d)

e)

f)

Fig. 10. *Microstructure of the of low-carbon steel wire after annealing at 700 °C:a) 1.2 mm, ×40; b) 1.2 mm, ×100; c) 2.0 mm, ×40; d) 2.0 mm, ×100; e) 3.0 mm, ×40; f) 3.0 mm, ×100*

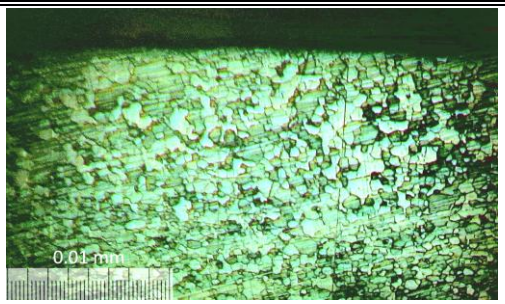

a)

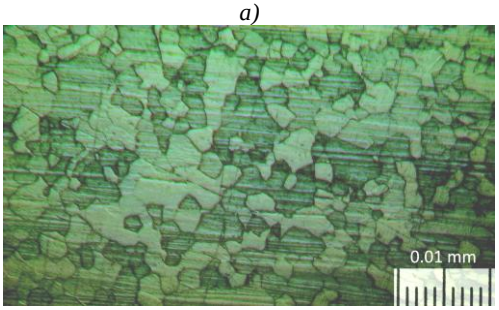

b)

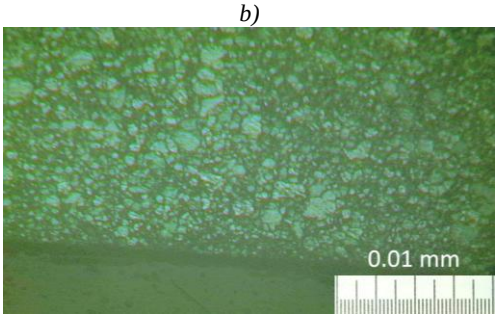

c)

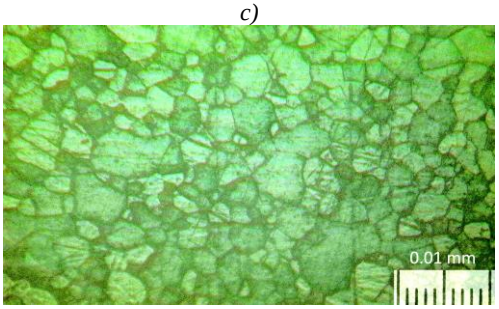

d)

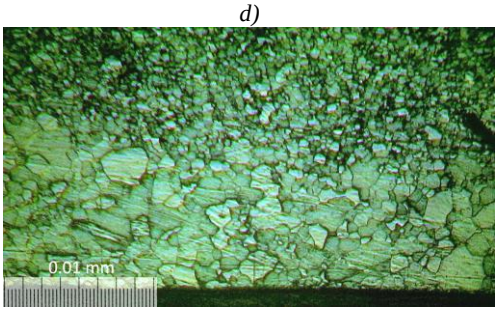

e)

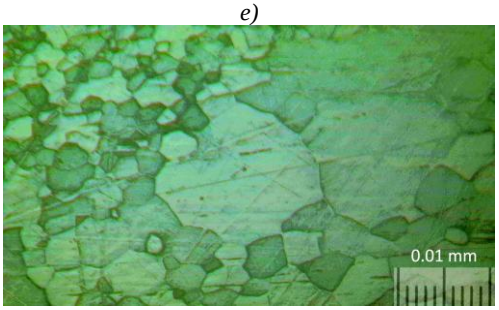

f)

Fig. 11. *Microstructure of the of low-carbon steel wire after annealing at 750 °C: a) 1.2 mm, ×40; b) 1.2 mm, ×100; c) 2.0 mm, ×40; d) 2.0 mm, ×100; e) 3.0 mm, ×40; f) 3.0 mm, ×100*

Such low-carbon steels are not much susceptible to quenching, but extreme cooling from the austenite area could have some effect, which was studied for the case if this wire. Work hardened samples were quenched in a ~10 % NaCl water solution, which could provide a fast cooling of rate up to 1000 °C/s or even more. Measurement of the mechanical properties showed that this material after quenching has less strength than in a work hardened state, but it is significantly more than after annealing. Moreover, it was also found a dependence of tensile strength after quenching from one in deformed state. The values are following, the values for the work hardened state are given in parentheses: Ø 3.0 mm – 471 MPa (849 MPa), Ø 2.0 mm – 501 MPa (882 MPa) and Ø 2.0 mm – 663 MPa (1040 MPa). The dependence is almost linear, which could be seen from the figure 13 (a). So we can see that more work hardened material has bigger strength also after quenching. The qualitatively similar to quenching is the dependence for the air cooling but the values are less and rather close to those after annealing at 600 °C.

Tempering at 650 °C after quenching decline strength and the decrease is the more the higher strength was after quenching. This tempering almost neutralizes the effect of work hardening, and only a weak dependence might remain. Rising the tempering temperature to 700 °C leads to a significant strength decline for the quenched samples. The direction of the dependence changes as it was previously observed for annealing. The values are also close to those after the corresponding annealing temperature, may be somewhat higher. So we observe the same effect of greater strength deceasing after more significant previous work hardening.

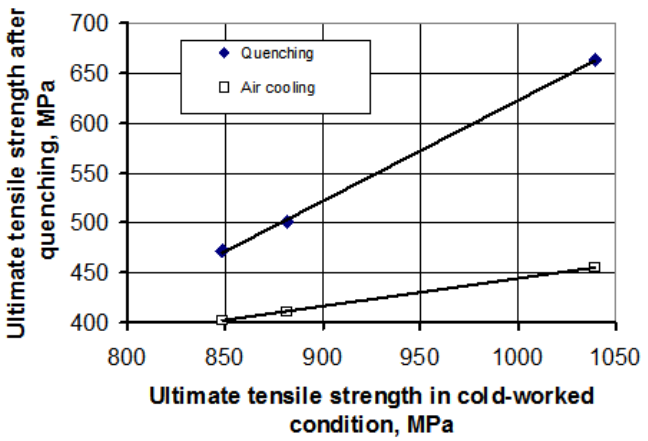

a)

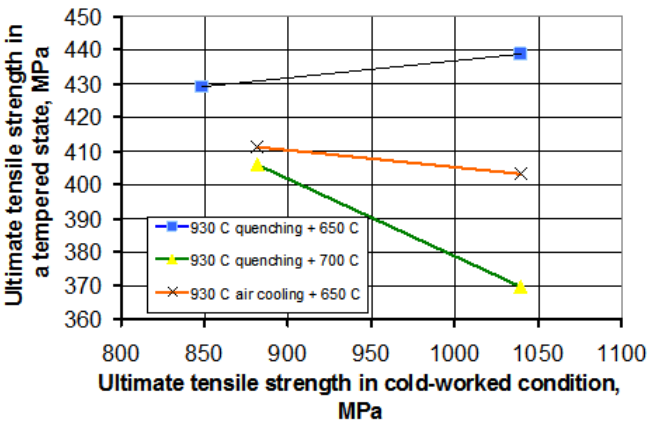

b)

Fig. 13. *Effect of initial strength after drawing deformation on the strength obtained after quenching and air cooling (a) and after subsequent tempering (b)*

Tempering after air cooling also neutralizes the effect of work hardening and even slightly demonstrates an effect of additional strength decreasing for more work hardened material. There is almost no effect on the specimens that had strength 882 MPa in deformed state. Their strength remains at about 410 MPa, which

could be obtained directly from air cooling. For the samples that had after work hardening strength about 1040 MPa and 455 MPa after air cooling from the austenite area tempering gives its noticeable additional decline down to 400 MPa. Thus, for air cooling even 650 °C is enough to evoke the effect of turning the dependence of obtained strength from one in work hardened state into opposite direction.

The driving force for recrystallization is energy stored within the metallic material, which arises during the lattice strains and accumulates on the crystalline imperfections generated during deformation [1]. According to [6] dislocations are the major contributor into the stored deformation energy. A cold working deformation process could increase the dislocation density in a metal to an estimated $10^{16}m^{-2}$ from about $10^{10}m^{-2}$ in annealed state. Each dislocation is a crystal defect that generates lattice disturbances in form of strains within its vicinity. The increased lattice strain is associated with the increase in strain energy in the metal [1, 7]. If deformation is performed at rather low temperature the defect accumulation to occur resulting in an increase in the stored energy [8]. The deformed state due to defect accumulation and work hardening is thermodynamically unstable, and there is a natural tendency to revert to the or annealed state to minimize its overall energy. However it often requires heating.

The recrystallization that eliminates almost all the deformation induced dislocations in worked metallic materials is known as the primary recrystallization, which is the process merely formation and growth in a deformed matrix of new grains which are distortion free and appreciably more perfect than the proper matrix [1, 9]. This process is propelled by the excess volume energy accumulated during the plastic deformation [10].

Collective recrystallization process isn't conjugated with neither new grains nucleation nor extra grain boundaries formation. It consists in grain growth when the boundaries are disappear (coagulation) and some larger grains consumes the smaller ones (Ostwald ripening). So this process does not need the stored in lattice defects energy that primary recrystallization does, but its driving force is surface energy of grain boundaries [11].

It is known that because more intensive deformation forms more lattice defects, especially dislocations, smaller grains in greater amount appear during primary recrystallization. Thus larger amount of stored in grain boundaries surface energy will be obtained, which is, as was mentioned, is the driving force of collective recrystallization. Hence, the observed effect becomes more clear: more developed grain boundaries obtained after primary recrystallization of more work hardened material also enforce collective recrystallization, which in this case actively starts at lower annealing temperature.

The effect of lowering recrystallization start temperature is described in [12], although for steels of different composition. According to that paper, the recrystallization temperature of this material can be considered to be ~670 °C despite the fact that it has a dependency of cold deformation degree. With increasing of the deformation degree, the recrystallization temperature declines. This data are in very qualitative and numerical accordance with our results. More work hardened metal has lesser temperature of the active collective recrystallization start. So the same annealing temperature could be enough for initially more deformed sample to start the collective recrystallization in it, but for other this temperature still not enough, so we do not observe so active collective recrystallization in it, or in may go partially – only in the surface layer, which work hardening is already enough to collective recrystallization be started in these conditions.

The critical points for the considered steel chemical composition were estimated by the method described in our previous work [13] that consists of primary estimation using empirical formulas from [14] with subsequent elaboration of them by a CALPHAD-like method. The obtained values are as follows: A_1 = 722 °C, A_3 = 918 °C. Hence, annealing at 750 °C actually was performed higher than the pearlitic transformation temperature, although there amount of pearlite is such kind of steel is very small. According to the transformation kinetics calculations, performed by the method from [3333], after slowly cooling (~0.01 °C/s) there may be about 4.6 % of pearlite. Thus, most of the structure even during such annealing actually was ferrite, so the results for the 750 °C annealing might be considered to some extent comparable to those for lower temperatures.

Heating up to 930 °C is heating to the purely austenite area for this steel, according to the given values of critical points. A calculated using the technique from [13] and the corresponding software [15] CCT-diagram for the given steel is given on figure 14.

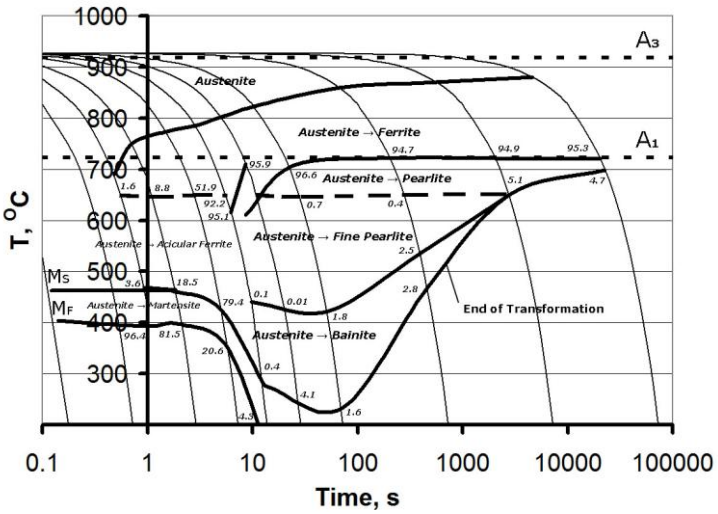

Fig. 14. *Calculated CCT-diagram for the steel of the given composition*

Even though the presented CCT-diagram is merely a simulated estimation it does not much contradict observed behavior of such steel and could be used fore appraisal judgments. Salt water cooling for such small diameter samples is able to give the cooling rate about 1000 °C/s or even more that visually looks like almost immediate. As we can see, such cooling is resulting in purely martensite structure. However, such low-carbon and not alloyed steels do not form hard martensite, here we have so called lath martensite, which is not very hard, although, according to the experimental results the quenched samples have significantly grater strength than annealed or air cooled ones, but their strength is even less than in a work hardened state.

Refrigeration after annealing of a raw bar or ready product in industrial conditions is a rather long term process, which is cooling of several tones of metal with in a quite large furnace (actually with the furnace). It lasts for many hours and the average cooling rate is less than 0.02 °C/s. Hence, it is close to the most right (the lowest) cooling rate of the CCT-diagram. So in such case is obtained a nearly equilibrium structure that consists mostly of globular ferrite with an insignificant amount of coarse pearlite, which could be presented in the structure even like structurally free carbides in ferrite matrix located mostly near ferrite grains boundaries. The part of this pearlite in the structure is less than 4.7 %. No martensite, bainite, acicular ferrite or fine pearlite are not able to form in such conditions.

Analysis of the transformation processes that occur during air cooling seems to be some more complicated. The first reason is presence of various possible transformation types for intermediate refrigeration rates range; the second problem is that for the considered case size (diameter) of the samples may significantly affect cooling process. Also it should be taken into the account that real cooling rate is not constant but slowing with decreasing of temperature difference between a sample surface and environment. Heat transfer coefficient also somewhat changes during the cooling process, actually, as was estimated for this case it varies from 6.6 to 41.6 $W/m^2 \cdot K$ depending on temperature difference and specimen diameter. It is rather difficult to directly measure a cooling curve for such thin samples, but it could be estimated, which is quite enough for a coarse valuation. A model used for the cooling curve

estimation has the following assumptions: during the air refrigeration process only convection heat exchange between the specimen and environment has a place; no forced air fluxes are present; temperature gradient inside the sample is neglected owing to low value of Biot criterion (from $3.3 \cdot 10^{-4}$ to $1.9 \cdot 10^{-3}$); the heat flux is proportional to temperature difference according to Newton's law of cooling; heat transfer coefficient is estimated from the Nusselt criterion, which value is calculated using Prandtl and Grashoff criterions. The calculated cooling curves are shown on figure 15.

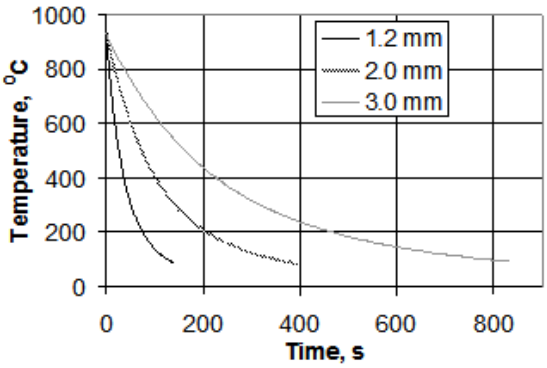

Fig. 14. *Estimated cooling curves for air cooling of the samples*

As we can see, the cooling curves for the wire of different diameter seem quite different. Austenite decomposition kinetics simulation was performed to estimate the influence of this difference of cooling curves on obtained structure. According to the calculations the fallowing final structure characteristics were predicted to be obtained after air cooling:

Ø 1.2 mm wire: 96.1 % ferrite; ~0.5 % fine pearlite; 1.8 % bainite; 1.6 % lath martensite

Ø 2.0 mm wire: 96.2 % ferrite; 1.6 % fine pearlite; 2.2 % bainite

Ø 3.0 mm wire: 95.0 % ferrite; 2.3 % fine pearlite; 2.7 % bainite

Thus, we can see that in spite of visually valuable difference between cooling curves, there is no cardinal difference in the samples structure. For all of the cases it is mostly ferritic with small amount of harder phases. However, there is some difference in the ratio of this phases. In the Ø 1.2 mm wire small amount of lath martensite might be formed, which is not predicted for the thicker specimens. Those may have some fine pearlite and bainite. Nevertheless, this small distinction seems not to make a significant contribution into mechanical properties difference that has been observed. So, there is a reason to believe, that exactly work hardening during deformation is the most valuable factor for the considered cases.

Conclusions

From the observed results, it can be concluded that increased work hardening promotes grain growth at higher annealing temperatures, when collective recrystallization occurs. This is evidenced by the presence of a coarse-grained surface layer, which was hardened to a greater hardness, and the fact that in specimens of Ø 1.24 mm, which had a higher strength in the initial state and underwent a greater degree of deformation than specimens of 3.0 mm, is observed a slightly greater average grain size after annealing. The fact that the mentioned coarse-grained layer in 3.0 mm samples appears at a higher annealing temperature suggests that a large degree of work hardening reduces the temperature of active collective recrystallization start. For this case, exactly occurrence of collective recrystallization at most of the wire material (over the cross section) makes it possible to achieve an additional softening, which is required in some cases from annealing. However, this reduces the resulting ductility and is therefore not desirable in intermediate stages (between drawings). This effect of work hardening on the properties obtained after annealing remains also after quenching and air cooling from austenite area.

For the minimal strength obtaining after annealing the material should to be previously work hardened up to 1000…1200 MPa and then annealed at temperature higher 700 °C during not less than 2 – 3 hours. The complex of mechanical properties in this case will be as fallows: σ_u = 325 – 350 MPa, σ_y = 250…270 MPa, δ = 20…30 %, ψ > 45 %.

To obtain maximal ductility, there are the following recommendations: initial tensile strength of the material condemned to the annealing should be not more than 780 – 850 MPa; the optimal annealing is to be performed at temperature about 640 – 670 °C during not less than 2 – 3 hours. The expected mechanical characteristics after annealing are as follows: $\sigma_u \approx 400$ MPa, σ_y = 300…350 MPa, $\delta \geq 50$ %, ψ = 70…80 %.

References

1. Alaneme K.K. Recrystallization mechanisms and microstructure development in emerging metallic materials: A review / K. K. Alaneme, E. A. Okotete // Journal of science: Advanced materials and devices. – 2019. – Vol. 4. № 1. – P. 19–33.

2. Соколов С.Ф. Исследование и моделирование эволюции микроструктуры и сопротивления деформации сталей при горячей обработке давлением // Диссертация на соискании степени к.т.н. – Санкт-Петербург: Политехнический университет: 2013.

3. Lefevre-Schlick F., Brechet Y., Zurob H.S., Purdy G., Embury D. On the activation of recrystallization nucleation sites in Cu and Fe. /. F. Lefevre-Schlick, Y. Brechet, H.S. Zurob, G. Purdy, D. Embury // Mater. Sci. Eng. A. – 2009. – Vol. 502. – P.70–78.

4. Humphreys F.J. Recrystallization and related annealing phenomena. / F. J. Humphreys, M. Hatherly // Oxford, U.K.: Pergamon Press Ltd. – 1997. – 333 p.

5. Золоторевский Н.Ю. Моделирование структурных превращений в металлических материалах / Н. Ю. Золоторевский // СПбГПУ. – 2007. – 164 с.

6. Martin J. W. Stability of microstructure in metallic systems. / J. W. Martin, R. D. Doherty, B. Cantor // Cambridge : Cambridge University Press. – 1997. – 442 p.

7. Hansen N. New discoveries in deformed metals. / N. Hansen // Mater. Trans. – 2001. – Vol. 32A. № 12. – P. 2917 – 2919.

8. Effect of cold rolling and annealing on mechanical properties of HSLA steel / [I. Schindler, M. Janošec, E. Místecký, M. Rùièka et. all.] // Arch. Mater. Sci. Eng. – 2009. - Vol. 36. № 1. – P. 41 – 47.

9. Humphreys F.J. Nucleation in recrystallization / F.J. Humphreys // Mater. Sci. Forum. – 2004. – P. 107 – 116.

10. Haasen P. Physical metallurgy / P. Haasen // Cambridge : Cambridge University Press. – 1997. – 2740 p.

11. Горелик С.С. Рекристаллизация металлов и сплавов. / С. С. Горелик, С. В. Добаткин, Л. М. Капуткина // М.: Изд-во МИСИС – 2005. – 432 с.

12. Tavakoli M. Static recrystallization kinetics of ferrite in cold-deformed medium carbon steel / M. Tavakoli, H. Mirzadeh, M. Zamani // Mater. Res. Express. – 2020. – Vol. 6. № 12. – P. 1265 – 1273.

13. Каверинский В.В. Моделирование кинетики распада переохлаждённого аустенита в легированных сталях / В. В. Каверинский, А. И. Троцан, З. П. Сухенко // Металлофизика и новейшие технологии. – 2017. - № 8. – С. 1051 – 1068.

14. Соколов Д.Ф. Эмпирические формулы для расчёта температур и концентраций углерода, отвечающих параравновесию основных фаз в сталях / Д. Ф. Соколов, А. А. Васильев, Н.Г. Колбасников, С. Ф. Соколов // Вопросы материаловедения. – 2012. – Т. 69. № 1. – С. 5 – 13.

15. Каверинський В.В. Математичне моделювання і комп'ютерний аналіз процесів структуроутворення легованих сталей в ході фазових перетворень // Київ: КІМ. – 2019. – 212 с.

Influence of heat treatment on metallographic and mechanical properties of ductile iron

Ivan Opačak[1], Nikolina Berić[1], Valnea Starčević[2], Aleksandar Bašić[1]
Faculty of Mechanical Engineering, University of Slavonski Brod, Trg Ivane Brlić-Mažuranić 2, Slavonski Brod, Croatia [1]
Đuro Đaković Termoenergetska postrojenja d.o.o., Dr. Mile Budaka 1, Slavonski Brod, Croatia [2]

iopacak@unisb.hr, nberic@unisb.hr, valnea.starcevic@ddtep.hr, abasic@unisb.hr

Abstract: *Due to the mechanical properties (toughness, elongation, tensile strength) that characterize ductile iron, its application in foundry technology is becoming more pronounced every day. The chemical composition and heat treatment of ductile iron have a great influence on the required mechanical properties. Given the operating conditions, the main purpose of heat treatment of ductile iron is to change the desired mechanical properties. Since the specific mechanical properties of ductile iron are generally related to the regularity of the mined graphite nodules, the main objective in production is to produce ductile iron with the highest possible percentage of ductility. In the experimental part of the paper, microstructure and hardness tests were carried out on specimens of ductile iron NL 400 and NL 700 before and after heat treatment by soft annealing (ferritization) and improvement. It was found that the type and corresponding parameters of heat treatment significantly affect the microstructure and the achieved hardness values of the ductile iron test specimens.*

Keywords: *DUCTILE IRON, HEAT TREATMENT, STRUCTURES, HARDNESS*

1. Introduction

Casting is considered one of the oldest and most widely used technologies for forming metal objects. The principle of casting technology is based on molten metal, which solidifies by pouring into the mold, thus maintaining the internal dimensions of the mold cavity after cooling. The main advantages of this technology are certainly the great repeatability of the process and the possibility to produce the most complicated structural parts by casting. In the production of semi-finished products and products by casting technology, there are certain peculiarities in the process itself, which should be well known in order to obtain the required structure and, consequently, the desired properties. Since metal casting is a continuous process, complete control during the process itself is difficult [1]. Nowadays, ductile iron is increasingly used in casting technology, which is still considered a relatively new type of cast iron. Ductile iron has much higher strength than gray iron, but its workability and vibration damping are lower than those of gray iron. A particular advantage of ductile iron over unalloyed steel, as well as the widely used gray iron, is its high value of yield strength. The good mechanical properties of ductile iron are due to the extraction of graphite beads in the Fe-C alloy, which are still in the casting phase. The properties of ductile iron can be subsequently improved by mechanical and heat treatments [2]. In this paper, the heat treatment soft annealing (ferritization) and improvement (hardening + high temperature tempering) are applied to prepared ductile iron specimens NL 400 and NL 700, after which microstructure and hardness tests were performed.

2. Properties, heat treatment and application of ductile iron

From the second half of the 20th century until today, the production of ductile iron has increased exponentially. The mechanical properties (toughness, elongation, tensile strength) of ductile iron indicated its future successful application. Looking at the mechanical properties, ductile iron is classified between steel and gray iron. Ductile iron belongs to the group of castings with high carbon content, whose mechanical properties are characterized by the carbon precipitated in the form of graphite beads. The extraction of the graphite spheres from the original sheet shape is achieved by adding small amounts of e.g. cerium or magnesium to the melt just before the base melt Fe-C is poured into the mold. If the melt contains small amounts of nodulation inhibitors (e.g. lead, titanium) or more than the allowable amounts of sulfur, the carbon will not be precipitated in the form of pellets and ductile iron will not form [3].

In such a case, gray iron is formed, in which the carbon is formed in the form of flakes. Nodular graphite causes ductile iron to be more ductile and tough than gray iron, but the strength and toughness of such cast iron depends much more on the strength of the Fe-C base than, for example, gray iron. The tensile strength of ductile iron ranges from 400 to 800 MPa, but due to heat treatment and alloying of ductile iron, it can reach 1400 MPa. The properties and microstructure of ductile iron are influenced by various factors such as chemical composition, metallurgical processes in the melt, and cooling rate during solidification and solid cooling [2]. The shape of the graphite and the structure of the Fe-C matrix are significantly influenced by the chemical composition. The declared chemical composition of ductile iron is listed in Table 1.

Table 1: *Declared chemical composition of ductile iron* [4].

Chemical composition, %						
C	Si	Mn	P	S	Mg	Fe
3,2 ÷ 3,8	2,4 ÷ 2,6	0,1 ÷ 0,5	0,005 ÷ 0,045	0,002 ÷ 0,01	0,03 ÷ 0,05	rest

Because of its favorable mechanical properties, ductile iron is used as a substitute for cast steel or steel forgings. Typical examples of ductile iron are crankshafts and camshafts, cylinder liners for engines and compressors, gears, valves, piping, plain bearing caps, parts for wind turbines, pump rotors, etc. In the manufacture of ductile iron products, various heat treatment processes are used to simultaneously increase strength and toughness, such as isothermal and classical improvement (hardening and tempering). Ductile iron improvement processes also increase wear resistance. Also, the amount and shape of graphite formed in ductile iron cannot be affected by subsequent heat treatment. Nodularity is determined as the volume fraction of graphite nodule accumulations relative to the total number of graphite accumulations. During production, the aim is to produce ductile iron with as high a proportion of ductility as possible (usually above 90 %), since the specific mechanical properties of ductile iron are generally related to the regularity of the graphite nodules obtained [1]. The mechanical properties, i.e., tensile strength and dynamic resistance, decrease with decreasing percentage of nodularity. In addition, lower fissility affects the modulus of elasticity, lowers toughness and decreases electrical resistance, but increases the ability to dampen vibrations.

3. Experimental part

In the experimental part of the paper, samples of ductile iron NL 400 and NL 700 were tested. After preparation of the test specimens, heat treatments such as soft annealing (ferritization) and improvement (hardening + high temperature tempering) were performed. Microstructure and hardness tests were also carried out.

3.1. Chemical composition test

The chemical compositions of the test specimens were determined using a spectrometric analyzer. Table 2 shows the measured chemical composition of the NL 400 ductile iron specimen, while Table 3 shows the measured chemical composition of the NL 700 ductile iron specimen.

Table 2: *Measured chemical composition of ductile iron NL 400.*

Chemical composition, %						
C	Si	Mn	P	S	Cu	Mg
3,6	2,1	0,14	0,037	0,009	0,077	0,043
Cr	Ni	Mo	Al	V	Ti	Sn
0,036	0,045	0,007	0,012	0,008	0,018	0,007

Table 3: *Measured chemical composition of ductile iron NL 700.*

Chemical composition, %						
C	Si	Mn	P	S	Cu	Mg
3,54	2,072	0,676	0,035	0,008	0,0673	0,05
Cr	Ni	Mo	Al	V	Ti	Sn
0,055	0,051	0,011	0,010	0	0	0

Specimens made of ductile iron NL 400 and NL 700 with dimensions Φ40x20 mm and specified chemical compositions were selected for the test. Before starting the test, the specimens were cut on a metal cutter, which has the possibility of intensive heat dissipation by means of cold water circulation. The MC-80 specimen cutter is shown in Figure 1.

Fig. 1 *Device for cutting specimens.*

3.2. Heat treatment of ductile iron

After cutting the specimens, they were marked according to Table 4, which also lists the parameters of heat treatment (ferritization and improvement) and the designations of certain specimens made of ductile iron NL 400 and NL 700.

Table 4: *Inscriptions and heat treatment parameters (ferritation and improvement) for the specimens NL 400 and NL 700.*

Specimen	Initial condition (at 20 °C)	Ferritization (at 725 °C, cool in the oven to 345 °C	Improvement (quenching from 870 °C and tempering at 565 °C)
NL 400	1.0	1.1	1.2
NL 700	2.0	2.1	2.2

Before heat treatment, metallographic examinations of the microstructure and hardness tests of the initial condition of test specimens 1.0 NL 400 and 2.0 NL 700 were performed. Test specimens 1.1 NL 400 and 2.1 NL 700 were heat treated by soft annealing (ferritization). These specimens were heated continuously from room temperature to 725 °C, at a heating rate v_h = 250 °C/h. After heating to 725 °C, it was necessary to hold 1 h of 1" thickness at the soft annealing temperature.

After holding at the soft annealing temperature, the specimens were cooled to 345 °C in an oven at a cooling rate of v_c = 55 °C/h and then in still air. Specimens 2.1 NL 400 and 2.2 NL 700 were processed by the heat treatment process of improvement (hardening + high temperature tempering). Quenching consisted of heating the specimens to an austenitizing temperature of 870 °C, holding at this temperature for 1 h, and then quenching in oil. Quenching of ductile iron castings is usually performed in oil because the castings may crack when cooled in water due to the high stresses. High temperature tempering consisted of heating the specimens from room temperature to 565 °C, heating rate v_h = 250 °C/h. The holding time at 565 °C was 2 h, followed by cooling in an oven to 240 °C (with the aim of relieving stresses, but also hardness), cooling rate v_c = 55 °C/h and cooling from 240 °C to room temperature in still air.

3.3. Microstructure test

Microstructure testing was performed using a Leica DM 2500 M laboratory light microscope connected to a computer to save photos after testing, Figure 2.

Fig. 2 *Light microscope Leica DM 2500 M.*

Figure 3.a shows the microstructure of ductile iron in the initial unheated and unetched condition for test specimen 1.0 NL 400, while Figure 3.b shows test specimen 2.0 NL 700. In both cases, it can be seen that the percentage of nodule formation during casting exceeded 90 %.

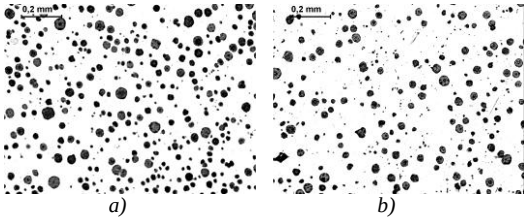

a) *b)*

Fig. 3 *Microstructure of ductile iron*
a) test specimen 1.0 NL 400; b) test specimen 2.0 NL 700.

Figure 4.a shows the microstructure of ductile iron in the initial unheated and etched condition for test specimen 1.0 NL 400, while Figure 4.b shows test specimen 2.0 NL 700. Etching was performed using a three percent solution of nital. Figure 4.a shows the pearlitic structure of ductile iron NL 400 with characteristic ferritic areas around the sphere (the microstructure consists of pearlite and the area around the sphere is called the "bull's eye"). In Figure 4.b, ductile iron NL 700 has a pure pearlite matrix.

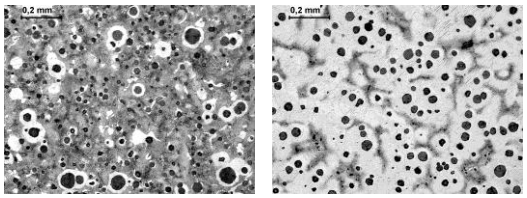

a) *b)*

Fig. 4 *Microstructure of ductile iron*
a) test specimen 1.0 NL 400; b) test specimen 2.0 NL 700.

Figures 5.a and 5.b show the microstructures of ductile iron after soft annealing (ferritization) in the etched condition for specimen 1.1 NL 400, while Figures 5.c and 5.d show specimen 2.1 NL 700. Etching was performed using a three percent solution of nital. In Figure 5.a it can be seen for the specimen of ductile iron 1.1 NL 400 that the size and shape of the nodules did not change after heat treatment by soft annealing (ferritization). A similar, predominantly ferritic microstructure as in Figure 5.a was observed in Figure 5.c for the specimen of ductile iron 2.1 NL 700. Ferrites

with traces of pearlite were observed in Figures 5.b and 5.d for the test specimens of ductile iron 1.1 NL 400 and 2.1 NL 700.

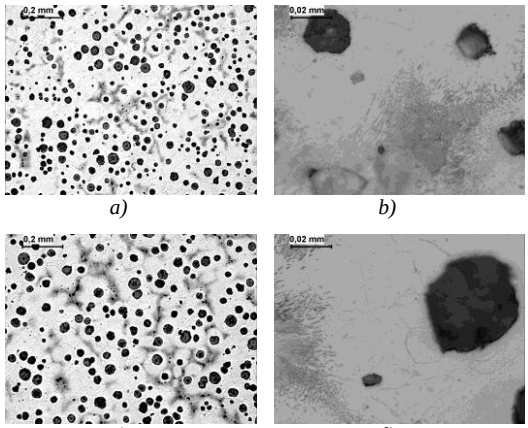

a) *b)* *c)* *d)*

Fig. 5 *Microstructure of ductile iron*
a) b) test specimen 1.1 NL 400; c) d) test specimen 2.1 NL 700.

Figures 6.a and 6.b show the microstructures of ductile iron after heat treatment of the etched improvement for test specimen 1.2 NL 400, while Figures 6.c and 6.d show for test specimen 2.2 NL 700. Etching was performed using a three percent solution of nital. Loose martensite can be seen in the above images.

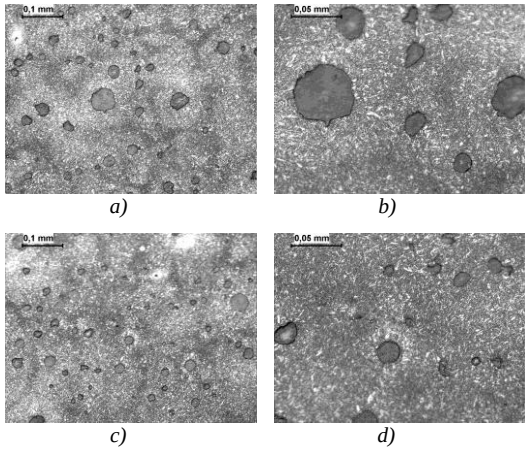

a) *b)* *c)* *d)*

Fig. 6 *Microstructure of ductile iron*
a) b) test specimen 1.2 NL 400; c) d) test specimen 2.2 NL 700.

3.4. Hardness test

The hardness test was performed according to the Brinell method. A steel ball with a 5 mm cross-section was used for the hardness measurements. The diameter of the ball and the injection force in the Brinell hardness measurement are determined using the condition F/D2 = const. which is 30 for steel. The injection force is 750 N for 10 seconds. Table 5 shows the results of hardness measurements on test specimens 1.0 NL 400 and 2.0 NL 700, while Table 6 shows the results of hardness measurements on test specimens 1.1 and 1.2 (NL 400) and 2.1 and 2.2 (NL 700).

Table 5: *Results of hardness measurement on test specimens 1.0 NL 400 and 2.0 NL 700.*

Specimen	Ordinal number of measurements	Hardness HB 5/750/10	Arithmetic value HB
1.0	1	173	172
	2	171	
2.0	1	219	220
	2	221	

Table 6: *Results of hardness measurement on test specimens 1.1, 1.2 (NL 400) and 2.1, 2.2 (NL 700).*

Specimen	Heat treatment	Ordinal number of measurements	Hardness HB 5/750/10	Arithmetic value HB
1.1	Soft annealing	1	143	145
		2	147	
1.2	Improvement	1	288	285
		2	282	
2.1	Soft annealing	1	154	153
		2	152	
2.2	Improvement	1	349	349
		2	349	

4. Analysis of the results and conclusion

In the experimental part of the paper, microstructural investigations and hardness tests were carried out on specimens of ductile iron NL 400 and NL 700 before and after the heat treatment of soft annealing, i.e. subcritical ferritization and improvement. When analyzing the microstructure of ductile iron specimens NL 400 and NL 700 after the heat treatment of soft annealing (ferritization), a change in the size and shape of the ferrite was observed, around which traces of pearlite were observed. Measurement of hardness after heat treatment of soft annealing (ferritization) on test specimens of ductile iron NL 400 and NL 700 showed a decrease in the hardness value compared to the test specimens in the unheated condition. Also, analysis of the microstructure of ductile iron specimens NL 400 and NL 700 after heat treatment of improvement revealed relaxed martensite. Measurement of hardness after heat treatment of improvements on ductile iron specimens NL 400 and NL 700 showed an increase in hardness as a result of formation of the martensitic structure. Particularly high hardness values were observed in ductile iron specimen 2.2 NL 700, where the hardness value after the improvement was 349 HB, compared to heat-treated ductile iron specimen 2.0 NL 700, whose hardness value was 220 HB. In the continuation of the research, the analysis of the influence of certain factors in the improvement (austenitizing temperature and quenching agent) on the microstructure and properties of ductile iron is proposed. As the production of ductile iron castings increases intensively every year, it is important to know how certain chemical elements affect nodule formation and, consequently, the structure of ductile iron. The structure of ductile iron affects the required mechanical properties (toughness, elongation, tensile strength) in certain industries such as automotive. The aim of heat treatment of ductile iron is to change the desired mechanical properties depending on the operating conditions. Heat treatment parameters such as temperature and duration as well as heating and cooling rates determine the type of heat treatment of ductile iron.

5. References

[1] Sahoo, M., Sahu, S.: *Principles of Metal Casting (Third Edition)*., U.S.A., McGraw-Hill, 2014., 816 pp.
[2] Holtzer, M., Górny, M., Dańko, R.: *Microstructure and Properties of Ductile Iron and Compacted Graphite Iron Castings*., Poland, Springer Cham, 2015., 158 pp.
[3] Chaengkham, P., Srichandr, P.: *Continuously cast ductile iron: Processing, structures, and properties.*, Journal of Materials Processing Technology 211 (2011) 8, 1372-1378.
[4] Filetin, T., Kovačiček, F., Indof, J.: *Svojstva i primjena materijala*., Zagreb, Fakultet strojarstva i brodogradnje, 2002., 302 pp.

Structural researching of the inner, primary supporting layer from ductile cast iron with a bimetalic roller shell with high-crome material used as an external (working) layer, during a centrifugal casting method of production with a vertical axis.

Petar Ivanov
"Centromet"AD, Vratza

Abstract: *The processes accompanying the formation of the so called carrier (inner) layer, which is formed in the production of bimetallic castings by the method of centrifugal casting are analyzed. Attention is paid to the structural changes caused by the diffusion processes occurring during the casting and crystallization process. Modification with a spheroidizing modifier with a Cr content in the melt above 0.6% was successfully carried out.*
KEYWORDS: *BIMETALLIC ROLLER SHELL, BEARING LAYER OF DUCTILE CAST IRON, DURABLE LAYER, VERTICAL AXIS CENTRIFUGAL CASTING, MICROSTRUCTURAL STUDIES*

1. Introduction

The technology of production of bimetallic rollers for the ceramic industry by the method of centrifugal casting with vertical axis has proved to be the most successful in terms of the quality of the produced items [1,2,3,4,5] and the facilitation of the subsequent machine processing of the casted product. Compared to stationary produced rollers, centrifugally cast workpieces have an inner (carrier) layer, typically of gray graphite or graphite gray cast iron. In addition to the lower cost and the shorter modes of machine processing, this layer largely bears the loads that are transmitted to it from the outer, wear - resistant layer during the operation of the roller. So it can be argued that for the normal operation of a bimetal roller for the ceramic industry, the quality of the inner (bearing / stabilizing) layer of the workpiece is of great importance.

In the production of a bimetallic mill roller with an outer (working) layer of high chromium material, the selection of a suitable brand of ductile cast iron for the carrier layer is further hampered by the diffusion between the two layers during the molding and crystallization processes of the workpiece. This leads to the formation of chromium carbides in the inner layer. In addition, a high Cr content (0.6 to 1.50%) prevents spheroidization of free graphite. The result of incorrectly selected material for the inner layer is shown in Figure 1.1

Figure 1.1

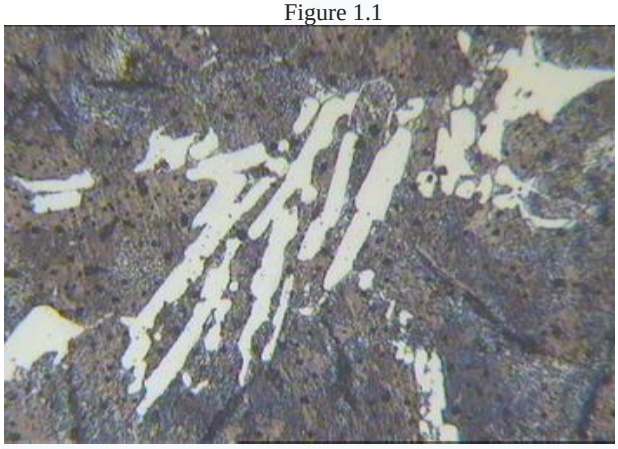

x200- Metal base + carbides + graphite plate
Figure 1.2

Figure 1.2 shows the microstructure of the inner layer:

2. Determination of the optimum amount of the modifier to produce free spheroidal graphite in cast iron with a chromium content of more than 0.6%.

In the production workshop of Centromet JSC, two pieces of sample items (Fig.2.1-Fig.2.3) were cast with the following chemical composition:

Figure.2.1

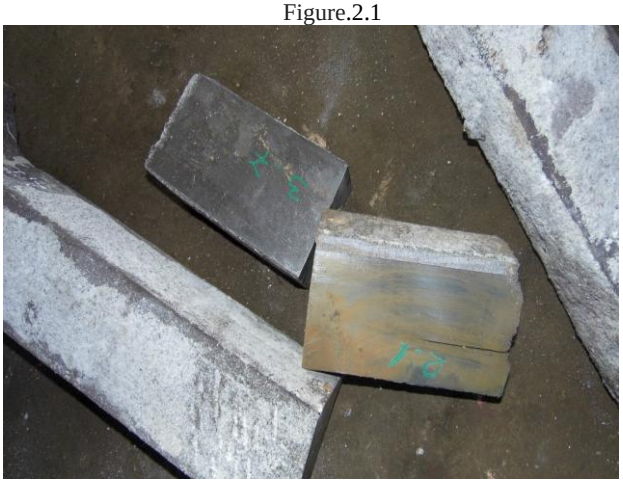

Figure.2.2

Chemical composition in the furnace:
C – 3.44%
Si – 1.96%
Mn – 0.42%
P – 0.05%
S – 0.01%
Cr – 1.02%
Ni – 0.03%
Cu – 0.03%
V – 0.01%
Al – 0.003%

The quantities of the imported VL63M modifier in the two test pieces are as follows:
Trial item №1 – 2.1%
Trial item №2 – 3,7%

Chemical composition of grinding №1:
C – 3.13%
Si – 3.08%
Mn – 0.40%
P – 0.05%
S – 0.01%
Cr – 1.00%
Ni – 0.05%
Cu – 0.04%
V – 0.01%
Al – 0.01%
Mg – 0.06%

Chemical composition of grinding №2:
C – 3.26%
Si – 3.90%
Mn – 0.40%
P – 0.05%
S – 0.01%
Cr – 0.95%
Ni – 0.04%
Cu – 0.04%
V – 0.01%
Al – 0.012%
Mg – 0.12%

The microstructure of grinding №1, is shown in Fig.2.4 and Fig.5.5:

Figure.2.3

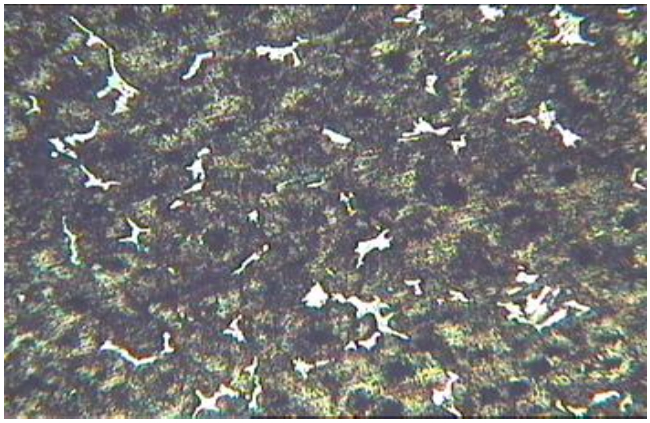

x50- Metal base + carbides + spheroidal graphite
Figure 2.4

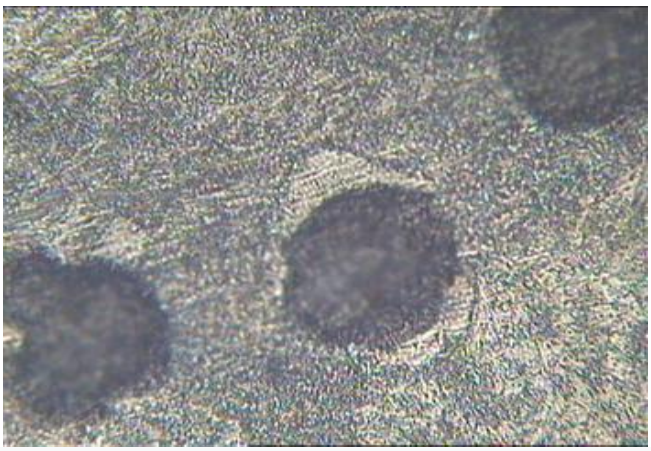

x500- Metal base (perlite) + spheroidal graphite
Figure 2.5

The microstructure of grinding № 2 is shown in Fig.2.6 and Fig.2.7:

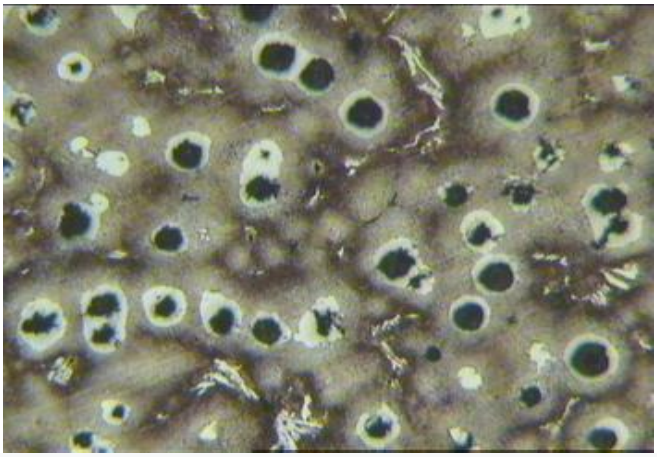

x50- Metal base (perlite) + carbides + spheroidal graphite + ferrite
Figure 2.6

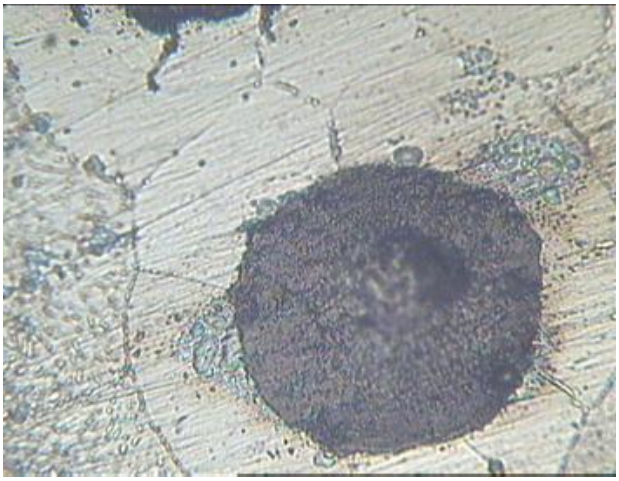

x500- Metal base (perlite) + spheroidal graphite + ferrite
Figure 2.7

The mechanical properties of the two test pieces are:
Hardness:
sample with 2.1% VL63M: 294HB
sample with 3.7% VL63M: 285HB

Tensile strength (Rm):
sample with 2.1% VL63M: 601MPa
sample with 3.7% VL63M: 624MPa

Extension (A):
sample with 2.1% VL63M: 2.19%
sample with 3.7% VL63M: 2.18%

3. Production of bimetallic mill roller with outer layer of material with high content of Cr and inner layer of ductile cast iron.

Based on the results obtained from the two test pieces in the production workshop of Centromet JSC, a prototype of a bimetallic mill roller was produced by the method of vertical axis centrifugal casting. The working, wear-resistant layer is made of a material with a Cr content of more than 20%, and the inner one is a carrier layer, with the chemical composition and percentage of
the embedded modifier corresponding to model # 2.
The finished product is shown in Figure 3.1:

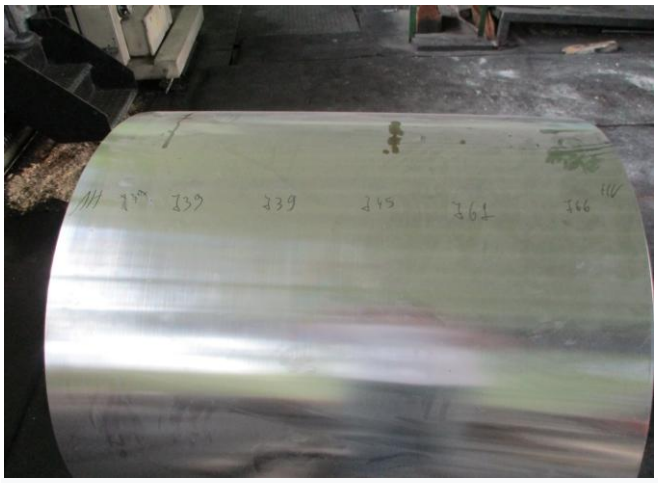

Figure 3.1

The microstructure of the inner layer is shown in Fig.3.2 and Fig.3.3:

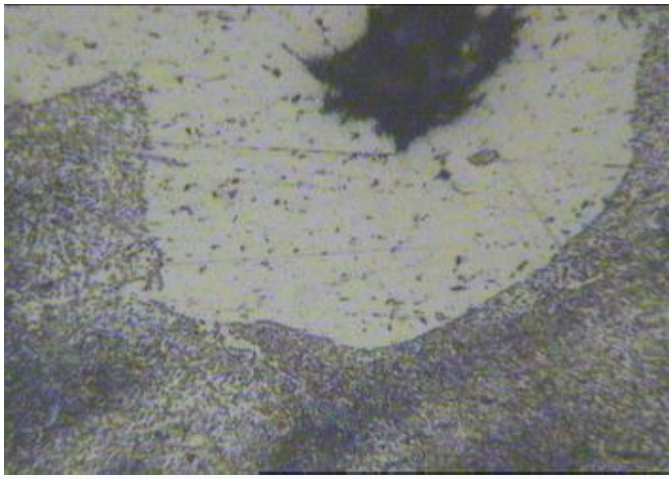

II x200 - Metal base (perlite) + graphite with spheroidal shape + ferrite

Figure 3.2

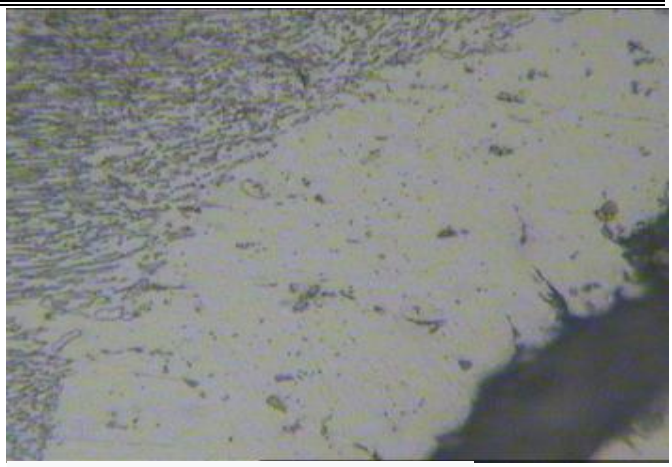

II x500 - Metal base (perlite) + ferrite + graphite

Figure 3.3

4. Conclusions:

1. Theoretical and experimental data of the technological parameters for the centrifugal casting of two-layer castings of high-chromium and spherographic cast iron material were obtained by the method of sequential pouring of the melt casting.

2. Results have been obtained for the structures of the outer and inner layers of the casting, which determine the properties of the cased product.

3. The established technological parameters for the process flow and the implementation of the process guarantee a solid diffusion bond between the two layers,
as well as strength and durability of the outer surface and good workability on the base inner surface.

5.Literature:

1. V. Valkov, I. Georgiev, Investigation of the influence of technological parameters in centrifugal casting of bimetallic castings, Sp. Foundry Bulletin, Issue no. 3/2006, 2 ÷ 4. IMLT - Sofia.

2. Arsov Ya., Bushev S., Valkov V., Georgiev I., Dimitrov M., Stoychev N. Processes in the technological casting system - shape in centrifugal casting, Sp. Engineering Sciences, Vol. 1/2006, 61 ÷ 72, ISSN 1312-5702.

3. Georgiev G., Iv. Georgiev, Art. Bushev, Computer Simulation and Optimization of Multilayer Casting Technologies in Centrifugal Casting, Conference NTSM Scientific Proceedings Proceedings of the XXVI International Conference "Days of Non-Destructive Control 2011", XIX, No. 1 (121), June 2011, 255-260, ISSN 1310-3946.

4. Georgiev G. Eft**.,** Iv. Georgiev, St. Bushev, Mathematical Modeling of The Processes of Casting Formation Occuring in Centrifugal Casting with Vertical Axis of Rotation, J. of Material Science and Technologi, Volume 19 ,2011, Number 3, pp.161-177,ISSN 0861-9786.

5. S. Yudin, M. Levin, and S. Rosenfeld, Centrifugal Casting, Part 1, Moscow, 1972.

Caprolactam distillation: implementation engineering solutions for rotary thin film evaporator

Alexander Vorontsov[1], Valery Sarokin[1], Oleg Lipnitsky[1], Emil Yankov[2], Marina Tarasevich[3]
Yanka Kupala Grodno State University[1] – Grodno, Belarus, University of Ruse, Bulgaria[2],
State establishment «Obuhovo Secondary School»[3] – Grodno region, Belarus
E-mail: a.voroncov@grsu.by, sorvg@ grsu.by, bura_e@mail.ru, eyankov@uni-ruse.bg, tarasevichmarina7@mail.com

Abstract: *The paper proposes a reconstruction of the distillation of caprolactam for more complete removal of water from the finished product, removing the droplet phase during the process in thin-film evaporators, will improve the final product performance by eliminating the inappropriate indicators alkali content and the optical density of the final product and to ensure its stable high quality. The relevance of the work presented directions for improving the process of production of caprolactam - raw ingredient for the preparation of polymeric materials used in various sectors of the economy. Describes the causes affecting the quality characteristics of the finished products produced from caprolactam. the implementation the liquid distributor and the centrifugal separator would reduce 5 - 6 times droplet entrainment to ensure complete removal of moisture from the final product, will reduce the alkali content in the final product, reduce the rate of optical density and thus bring trademark caprolactam by indicators «alkalinity» and «optical density» to the level of the highest quality product.*
KEYWORDS: CAPROLACTAM, DISTILLATION, RECTIFICATION, ROTARY EVAPORATOR, SYNTHESIS, POLYAMIDE FIBER, DEHYDRATION, LYSINE, DROPLET PHASE, DRAINAGE OF THE WATER

1. Introduction

The necessity to improve the technology of organic synthesis and refining industries is caused by environmental, energy and resource saving problems. Partial solution of these problems can be achieved by reducing the number of byproducts, which are waste ones of production [1]. They still do not find qualified use and are mostly incinerated.

Caprolactam is a cyclic amide of ε-aminocaproic acid (white crystals, well soluble in water, alcohol, ether, benzene). Benzene is used as an industrial raw material for caprolactam production. When it is heated in presence of small amounts of water, alcohol, amines, organic acids and some other compounds caprolactam polymerizes to form polyamide resin to make a fiber - capron. Aqueous solutions of acids and alkalis cause hydrolysis of caprolactam to ε-aminocaproic acid [2].

Caprolactam production consists of the oxidation of cyclohexane to cyclohexanone, its conversion to oxime and subsequent regrouping into caprolactam. The oxidation and oxidate conversion processes producing cyclohexanone (more than 99.9%) produce more than 50 different impurity compounds which contribute to contamination of commercial caprolactam.

Caprolactam is a common product in the chemical industry and has a fairly wide range of applications. This material is mainly used in the production of polyamide plastics and fibers. The bulk of global consumption is for yarns and fibers, a significant amount is also consumed in the manufacture of engineering plastics. The remainder is used for the manufacture of packaging films and other materials. Polyamide fibers and yarns are generally used in the production of textiles, carpets and industrial filaments, which are used for the manufacture of tyre cord. Cord yarns are the largest and fastest growing segment of the polyamide market, such as PA6. PA6 resin is also a mainstay in the production of engineering plastics used in the manufacture of electronic and electrical components and automotive parts. The packaging industry uses oriented polyamide films which are also based on PA6 resin. Small amounts of caprolactam are used for lysine synthesis, and also as an agent in polyurethane production [3].

Grodno Azot, JSC produces caprolactam, a valuable chemical product, from which polymer, poly-ε-caproamide (polycaprolactam), widely used in machinery and households, is obtained.

The most important application for polyamide fibers is in the tyre industry. Capron and nylon are used to make cord, the main reinforcing element for car and aircraft tyres.

The main direction of use of nylon fibers in production of consumer goods is fabrics, hosiery and knitwear. Production of knitwear is developing at an accelerated pace, which is explained by the increasing demand and high economic efficiency. Its costs are reduced by 15 % in comparison with the production of cotton and viscose.

The combination of high mechanical strength and lightness with good sliding and electrical insulation properties, as well as corrosion and chemical resistance and the ability to absorb and dampen vibrations have made polyamide plastics an important material for the machinery and instrumentation industry. Important parts of automobiles and aeroplanes are made of them. Despite a wide range of modern plastics, polyamides remain the best material for production of silent gears, bearing inserts, ship propeller blades, fans, impellers of centrifugal and vortex pumps.

Caprolactam serves as a raw material for production of many products of the national economy. Polyamide fibers are produced on the basis of caprolactam. Complex of valuable properties of these fibers defined their wide application in technical products and consumer goods.

Polycaprolactam films are used as packing material, glass substitute in construction of greenhouses, in medicine, etc.

The paper proposes design solutions for caprolactam distillation unit in order to remove moisture from the final product more completely, eliminate dripping during the technological process in thin film evaporators, which will improve the performance of the final product by eliminating the inconsistent alkali content and optical density in the final product, and ensure its stable high quality.

2. Discussion

2.1. Relevance of the topic

The world production of caprolactam is more than three million tons per year and continues to increase [4]. Caprolactam is a monomer of polycaproamide, from the melt of which polyamide fibers are produced. The purity of the monomer is a prerequisite for high quality polymeric materials. This also applies to caprolactam. The consequence of wide application of polyamide fibers is the widespread growth of caprolactam production capacity [5-11].

Properties of polycaproamide highly depend on impurities containing in caprolactam. Their presence affects polymerization process and heat resistance of obtained polymer. The main impurities in commercial caprolactam are amines, alcohols, Schiff bases, ammonium sulphate, iron ions and others. The composition and amount of impurities depend on method of caprolactam production [5].

The purification stage is not only the final step in the multi-step process of caprolactam production, but also lays the foundation for its processing into polyamide products with high technical, economic and qualitative properties. Distillation and rectification of caprolactam [4-11] is the main method completing the purification process. It is preceded by evaporation [6-8].

Since caprolactam is not thermally stable, it is important to ensure the lowest possible thermal impact. This requirement is provided by

rotary-film and heat and mass transfer apparatuses - evaporators and rectifiers.

The essence of work consists of working out of engineering and design decisions on optimization of the technological scheme of distillation and rectification of caprolactam. The work is based on analysis of technological scheme of caprolactam distillation and rectification at Grodno Azot, JSC with implementation of solutions aimed at improvement of physical and mechanical properties of caprolactam and provision of its stable high quality.

2.2. The purpose of our research work

The purpose of our research work is reconstruction of technological scheme of caprolactam distillation and rectification for maintenance of stable high quality of finished product.

To achieve this aim it is necessary to solve the following tasks:

- to offer optimized design of caprolactam distillation unit;
- to analyze developed thin film and rotary thin film evaporators;
- to offer engineering solutions on layout of technological equipment on caprolactam distillation line.

Scientific novelty of the work consists of substantiation of optimal choice of engineering and design solutions at optimization of technological scheme of caprolactam distillation and rectification for getting high quality of finished product.

Practical significance includes obtaining caprolactam distillation unit at Grodno Azot, JSC providing more complete removal of moisture from the finished product, elimination of dripping during the technological process of distillation and allowing to improve physical and mechanical properties of caprolactam, to ensure its consistently high quality.

2.3. Research methodology

The object of the research is the technological scheme of caprolactam distillation and rectification used in caprolactam production at Grodno Azot, JSC.

The methods of computer simulation and design of technical objects on the basis of software products Compass-3D V15 and AutoCAD Mechanical 2013 have been used for modernization of the process flow diagram, optimization of design solutions of thin film rotary evaporators, design and technological documentation. Strength and process calculations of optimized designs of rotary thin film evaporators are performed by the standard methods [8-9].

2.4. Main content of the work

Caprolactam (hexahydro-2H-azepine-2-one) is a cyclic amide (lactam) of ε-aminocaproic acid, colourless crystals; boiling temperature 262.5 °C, melting temperature 68 – 69 °C.

Depending on the grade, caprolactam shall meet the following quality criteria as given in Table 1 [12].

According to the classification of the distillation processes caprolactam is a heavy boiling product [13]. Distillation and distillation of caprolactam are carried out at residual pressure from 260 to 660 Pa. In connection with caprolactam being a thermally unstable product, it is necessary to provide the minimum possible thermal influence, therefore distillation is carried out under deep vacuum. The rotary thin film and thermo mass transfer apparatus – evaporators and rectifiers fulfill this requirement. They have low hydraulic resistance, the residence time of the processed product is a few seconds [3].

The object of our research work is the technological scheme of process of distillation of caprolactam which is presented in fig. 1 [14].

The lactam is distilled at a temperature not exceeding 131 °C and a residual pressure not exceeding 1,1 kPa. A distillate of not more than 50 % of the incoming lactam is distilled in the evaporator. The lactam vapour is condensed in the condenser. The condensate flows by gravity to the lactam collector or to the final product collector (reserve compartment), depending on the quality. The residual pressure in the evaporator and condenser is created by the steam ejectors. The steam ejectors operate with steam pressure not exceeding 1,2 MPa. Water steam from the steam ejectors and lactam carried away from the condenser is condensed in the condensers (total heat transfer area 15 m^2) and drains to the collector. From the bottom of the evaporator, the cube residue enters the pump tank (volume 1.3 m^3).

The lactam is pumped out of the collector by submersible pumps to a storage tank or directly into rail tankers. The lactam is discharged from the operating compartment of the collector by remote controllers. Water drainage, during flushing of evaporators 1, 2 of condensers 3, 4 is carried out to the collector of process water.

During operation of evaporators a number of drawbacks were revealed: dripping; incomplete removal of moisture from the finished product; high alkali content in the finished product; inadequate optical density index [11]. The listed factors do not allow to refer commodity caprolactam produced by Grodno Azot, Jsc to products of the highest quality category, which reduces the efficiency of production of commodity caprolactam fit for further use. The efficiency is about 70%, and the rest of the product in the form of cube liquid is forced to be recycled.

Since caprolactam is a thermally unstable product, in the process of its distillation it is important to ensure the lowest possible thermal impact. Rotor film and heat and mass transfer apparatuses - evaporators and rectifiers - meet this requirement. They have a low hydraulic resistance and the residence time of the product to be processed is only a few seconds.

Table 1 *Quality criteria of caprolactam*

Patented solutions for evaporators and rectifiers for improving the quality of the final product are analysed in this research work.

Name of the indicator	**The norm for a variety**		
	The highest	**The first**	**The second**
1 Permanganate index, units. PI, not more than	4	5	7
2 Colour of an aqueous solution of caprolactam at a mass fraction of 50%, units Hazen, not more than	3,0	4,0	5,0
3 Volatile base content, mmol/kg, no more than	0,4	0,5	0,6
4 Crystallisation temperature, °C, not lower	68,8	68,8	68,8
5 Mass fraction of iron, %, no more than	0,00002	0,00002	0,00002
6 Mass fraction of cyclohexanonoxime, %, max.	0,002	0,002	0,002
7 Optical density of caprolactam solution with mass fraction of 50%, max.	0,04	0,05	0,06
8 Alkalinity, mmol/kg, max.	0,1	0,1	0,05
9 Acidity, mmol/kg, max.	0,05	0,05	0,1
10 pH of a 20% water solution	6,7-8,5	6,7-8,5	6,7-7,5
11 Mass fraction of water, %, max.	0,07	0,07	0,07

There is a design of thin film evaporator protected by patent. 2372129 [15] that contains a vertical drum, a supply line situated in the upper area of the drum for supply of evaporating medium, a heating jacket situated at the drum periphery and generating vapour, an outlet line for discharge of residue left in the lower part of the drum, and a condenser supplied with refrigerant.

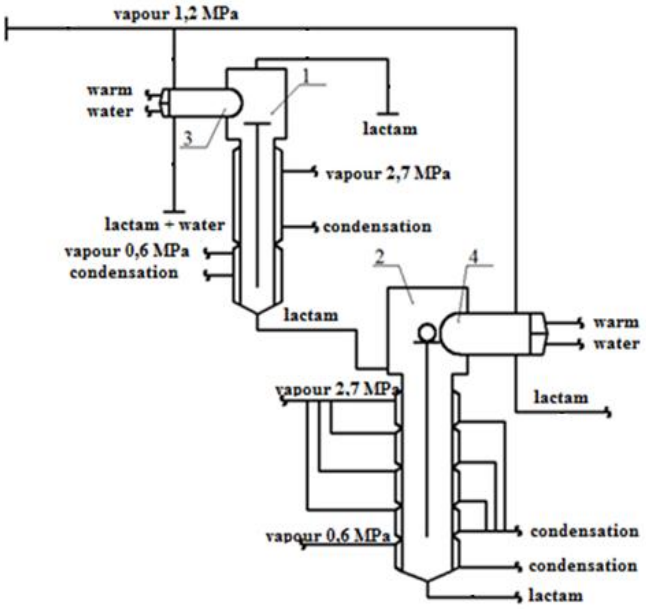

1 - thin-film evaporator; 2 - rotary thin-film evaporator; 3, 4 – condensers

***Fig. 1** Process diagram of a thin film evaporator installation*

Temperature sensitive substances, such as pharmaceutical solutions or food concentrates, can only be heated to boiling point for a short time. To meet this requirement, so called thin film evaporators are used, in which the medium to be evaporated or the solution to be concentrated by evaporation is fed to the evaporator surface only in the form of a thin film. In the case of the thin film evaporator, this objective is achieved according to the invention under consideration by providing an internal device in the vapour path from the heating jacket to the condenser which affects the action of the thin film evaporator, this internal device being preferably of circular cross section and preferably arranged so as to be equidistant from the condenser or directly resting on its outer surface. This internal device serves as a substance transfer zone.

According to the invention [15] the rotary thin-film evaporator is created, characterised by the fact that an internal device between the condenser and the wetting device is provided for the evaporating medium introduced into the drum from above, which can move along the jacket of the drum. This invention can also be used for a downflow evaporator, such an evaporator contains at least two drums.

Design of the rotary thin film evaporator pat. 4370C1 [16] comprises a shell with a heating jacket and process branch pipes, a rotor mounted therein, and a drive, characterized in that the rotor is made as at least one elastically deformed profile extending the length of the shell, and at least one end of the rotor shaft is connected to the drive, allowing uniform distribution of the solution over the heating surface. The rotor is designed as a helical spiral with variable cross section; the rotor shaft is fitted with a disc type eliminator which provides centrifugal separation of liquid droplets and prevents droplet carry over. The casing is arched and tapered in the direction of product flow, which allows the heating surface to expand or contract sharply and, if necessary, reduce the vapour outflow rate from the casing space.

This design allows the treatment both highly mobile and highly viscous suspensions, while improving the quality of the finished product increases the functions of the unit and reduce energy costs.

A tube evaporator design has been developed pat. 2071802 [17], which contains a housing with a heating chamber, bounded by horizontal partitions, on which cylindrical tubes with tape spirals placed inside are fixed, fluid distributors, which are tube bends protruding under the bottom partition, equipped with tapering diaphragms. Separators are fitted on the upper ends of the cylindrical tubes projecting beyond the baffle. This device is designed for distillation of volatile components from liquid mixtures of thermolabile substances during evaporation, distillation and rectification in chemical technology. The aim of invention [17] is increasing of degree of distillation of volatile components in one pass during processing of thermolabile liquids. The aim is achieved by the fact that device contains a housing with a heating chamber, bounded by horizontal partitions, cylindrical tubes with a spiral placed inside them and distributors of liquid. Liquid distributors are located under the lower horizontal partition and are protruding beyond the partition of the tubes, equipped with tapered diaphragms. The advantage of the proposed direct flow tube evaporator over known analogues is the possibility of obtaining a high degree of volatile components distillation in one pass. In addition, it is much easier to manufacture and install a helical coil in the form of a helical strip than a circular coil made of a hollow tube connected to a heating chamber.

The rotary section evaporator design pat. 2108840 [18] is also used in industry. 2108840 [18], which is a vertical cylindrical casing divided in height by sections, the diameter of which decreases from the top to the bottom. Each section is provided with a jacket, which is supplied with heat transfer fluid. Each section is divided into several contact elements consisting of a drain plate, a rotating atomiser with an inlet and a wall mounted drift eliminator which form a single heat transferring surface with the heated casing. Intense circulation of the solution on each contact element is accompanied by multiple dispersion and turbulization of the liquid film on the heat transfer surface. The proposed apparatus design improves the efficiency of the evaporation process and expands the range of liquid phase loads.

Design of film evaporator pat. 2266151 [19], includes a vertical cylindrical body, end covers, upper and lower tube plates, heat exchange tubes, film formers mounted with a gap inside the upper ends of the heat exchange tubes, inlet and outlet connections for the treated liquid, heating, secondary steam and condensate. In the lower part of the shell there is a coil, one end of which is connected with the fluid inlet connection and the other, straight part, is fitted between the tube plates. The fluid inlet connection is mounted in the lower end cap of the evaporator and has two additional tube boards located under the upper and over the lower tube boards respectively, in which the heat exchange tubes and film formers are installed, located concentrically about the central axis of the casing. The mechanism is equipped with pylons placed in the casing and connecting the adjacent heat exchange tubes, as well as the inner and outer walls in each foil forming unit. The pylons in the upper part of the heat exchange tubes and two additional tube sheets contain through holes for passing the treated liquid through the film formers to the heat exchange tubes and further for passing the secondary steam and condensate through the heat exchange tubes and additional tube sheets, respectively. In addition, the evaporator is equipped with a mechanism for axial movement of the film formers, and the film formers and heat exchange tubes in the upper part of the body have sections and reverse cone to regulate the size of the passage gap of the treated liquid.

The invention provides an expansion of technological possibilities by using aggressive media, as well as increasing the efficiency of liquid treatment while changing its physical and chemical properties. Simplicity of construction and possibility of micro miniaturization of the evaporator using non-metallic materials such as quartz glass is provided.

The analysis of patent sources [15–19] has allowed to establish disadvantages of existing technological scheme of distillation, and also applied devices of distillation and to set ways of their elimination. Developments in the sphere of caprolactam production are directed on improvement of quality of caprolactam distillation processes, creation of more perfect designs of evaporators.

The design developed by Stami carbon (Holland) for evaporator "Sako" (fig. 2, a) for purification stage used in caprolactam production at Grodno Azot, JSC (in vertical version) was chosen as an optimization object.

Evaporators in the vertical version are manufactured with a heating surface of up to 24 m^2 with an average internal casing diameter of

up to 1.4 m. It can be up to several minutes in the horizontal apparatus if the residence time of the product in the vertical «Saco» apparatus ranges from 1.6 to 7 s.

The main apparatus for obtaining the finished product caprolactam is a film rotary evaporator [20]. Chemical analysis of commercial caprolactam produced by Grodno Azot, JSC revealed high alkali content and inadequate optical density index. The alkali boils at 128 ºC and enters the finished product in the form of droplets. A rotary ring centrifugal separator design was developed to prevent drip liquid (Fig. 2, b).

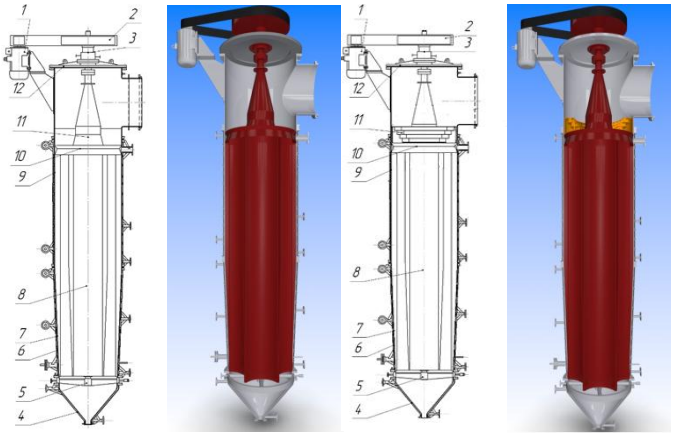

a *b*

1 - electric motor; 2 - V-belt transmission; 3 - mechanical seal; 4 - conical bottom; 5 - bearing pedestal; 6 - jacket; 7 - conical body; 8 - rotor; 9 - cylindrical drum; 10 - distributor; 11 - separating device; 12 - flat lid
a - applied design; b - optimised design
***Fig. 2** Design of the rotary thin-film evaporator*

The column rotary thin-film evaporator (fig. 2) is used for distillation process of caprolactam solution [4, 15–19].

The rotary thin film evaporator is a vertical cylindrical conical body, inside which the hollow vane rotor 8 rotates. Circumferential rotation speed of the blades reaches 12 m/s. The clearance between the blades and the apparatus wall is 0.4 – 1.5 mm. The casing is provided with a heated jacket 6. In this case the surface F = 16 m^2, diameter D = 1250 mm, height H = 6 860 mm.

The caprolactam solution is fed through the top connection to the distributor 10 and by rotating rotor 8 is distributed on the inside surface of the casing as a swirling liquid film flowing downwards. Steam pressure in the evaporator "jacket" is 0,3 to 1,1 MPa.

For operation under vacuum the rotor shaft is sealed by a double acting mechanical seal 3, which allows operating the unit at absolute pressure up to 100 Pa. The rotor lower bearing 5 is a sliding bearing made of graphite with the addition of antifriction materials.

As the film travels along the hot housing, lactam evaporates from the solution. The lactam vapour condenses on the surface of the rotor; the condensate is pushed back onto the heated wall. Multiple evaporation and condensation takes place. The distillation of caprolactam takes place at a temperature not exceeding 131 °C and pressure not exceeding 1.1 kPa.

50 % main product is evaporated. The lactam vapour from the evaporator is sent for condensation. From the lower part of the evaporator, the lactam containing residue is discharged to the collector.

To rotate the rotor 8 in the upper part of the evaporator, there is a self aligning thrust bearing and a thrust ball bearing.

To increase the efficiency of caprolactam distillation unit it is necessary to reconstruct it. It is proposed to install a liquid film distributor in the thin film evaporator (fig. 3) and a rotary ring centrifugal separator in the rotary thin film evaporator (fig. 4).

To eliminate this disadvantage thin film evaporator was equipped with liquid distributor (fig. 3). The distributor of liquid is made in the form of set of vanes 7 turned at angle 30 ° in quantity of 16 pieces and fixed at branch pipe 3 and fixed at pipe 1, located in housing 2. Cone 2 is fixed to the pipe 1 by ribs 5. Liquid distributor is installed in evaporator casing by means of support ring, which is fixed by ribs 6.

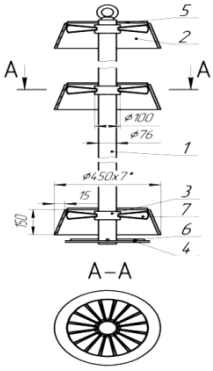

1 - pipe; 2 - conical body; 3 - spigot; 4 - support ring; 5 - fin; 6 - fin; 7 - vane
***Fig. 3** Liquid film distributor*

As can be seen from the process flowchart (Figure 1) the main apparatus for removing residual moisture from caprolactam is the film evaporator, which does not have a rotor. Lactam by means of distribution ring with holes enters into the film evaporator, running down the walls forming streams, reducing the heat exchange surface, which does not provide uniform distribution of the film and sufficient moisture removal from caprolactam.

The apparatus for the finished product is a rotary film evaporator. The inconsistency with the highest product quality for commercial caprolactam is traditionally due to the high alkali content. This leads to deviations in optical density.

Knowing that alkali boils at high temperature, it can enter the product in the form of droplets. To prevent drip liquid, a separator was developed and fitted to the top of the film rotary evaporator (Fig. 4).

The liquid film distributor consists of three swirlers, which give the steam a stream breaking motion, thus ensuring uniform film distribution and sufficient distillation of moisture from caprolactam.

As a separator in a thin film rotary evaporator it is proposed to use a rotary ring centrifugal separator, the installation of which will eliminate the above drawbacks in the evaporator.

Rotor ring centrifugal separator (figure 4) can be used for purification of low pressure gas flows in combination with centrifugal compensation stage. The separation stage is designed as a set of flat rings 3 that form a stepped rotor placed in a shell 2, with curved vanes 4 placed between them. Separation of impurities takes place in two stages: before the separating rotor in the field of centrifugal forces, created by fast rotor, and in rotating curvilinear channels of the rotor.

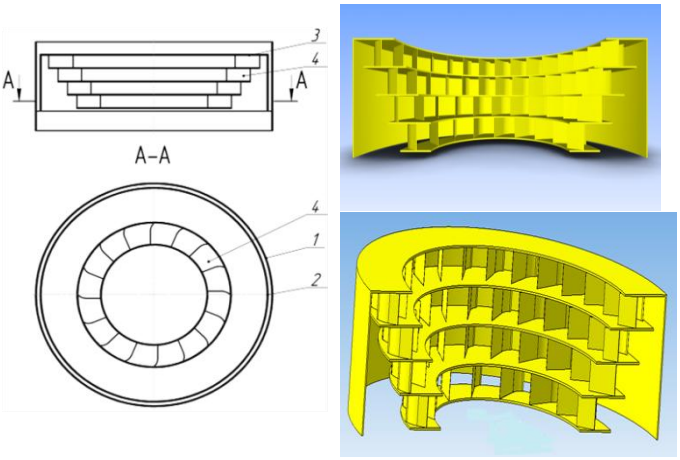

1 - outer shell; 2 - inner shell; 3 - flat ring; 4 - curved blades
***Fig. 4** - Rotary ring separator of counterflow type*

With low economic and operating costs, the reconstruction of the unit will intensify the distillation and rectification of caprolactam and produce high quality caprolactam [21, 22].

3. Conclusion

Development and implementation of design of rotary ring centrifugal separator at caprolactam distillation unit will provide high efficiency of a thin film evaporator in a wide range of gas liquid loadings, will intensify the process of caprolactam distillation and rectification, improve indicators of the final product and provide its stable high quality. This will eliminate subsequent purification of the caprolactam obtained when it is used in the next cycle of the technological process. After the reconstruction the hourly productivity of the unit will increase, while the unit processing cost will decrease.

Implementation of liquid distributor and centrifugal separator will reduce dripping by 5-6 times, provide more complete removal of moisture from the finished product, will reduce the alkali content in the finished product, will reduce the optical density indicator and thereby bring commercial caprolactam by indicators "alkalinity" and "optical density" to the product of the highest quality category. Implementation of the separator will allow to increase selection of commercial caprolactam from 70 % to 75 %, thereby reducing its output in the form of cube liquid for recycling.

5. References

1. Information databases for the chemical industry of the Republic of Belarus / V.S. Kruk [etc.] // Chemical problems of creating new materials and technologies: collected articles / Belarusian State University, Research Institute of Physical and Chemical Problems; editor: O.A. Ivashkevich (responsible editor) [et al.] - Minsk: Belarusian State University, 2003. - Issue. 2. - – P. 231–250.
2. Wikipedia: the Free Encyclopedia. Caprolactam [Electronic resource]. − Access mode: https://ru.wikipedia.org/wiki/Caprolactam.svg. – Access date : 25.04.2021.
3. Furman, M.S. Cyclohexanone and adipic acid production by oxidation of cyclohexane [Proizvodstvo tsiklogeksanona i adipinovoi kisloty okisleniem tsiklogeksana] / M.S. Furman [et al.]. - M .: «Chemistry», 1967. - 235 p.
4. Badrian, A.S. Production of caprolactam [Proizvodstvo kaprolaktama] / A.S. Badrian [et al.]; ed. V.I. Ovchinnikov and V.R. Ruchnskogo. - M .: «Chemistry», 1977. - 264 p.
5. Lebedev, N.N. Chemistry and technology of basic organic and petrochemical synthesis [Khimiia i tekhnologiia osnovnogo organicheskogo i neftekhimicheskogo sinteza] / N.N. Lebedev. - M .: Alliance, 2013. - 592 p.
6. Zharskaya, T.A. The main directions of use of bottoms distillation of caprolactam [Osnovnye napravleniia ispol'zovaniia kubovogo ostatka distilliatsii kaprolaktama] / T.A. Zharskaya, T.S. Korotchenya // Resource and energy saving technologies and equipment, environmentally friendly technologies: materials of the International scientific conference, Minsk, November 26-28, 2014 .: 2 parts, Part 2 / Republic of Belarus Ministry of Education, Educational Institution «Belarusian. State technological University» ; rec .: N.P. Krut'ko, I.M. Astrelin; Ed. N.R. Prokopchuk [et al.]. - Minsk, 2014. - P. 379-383.
7. Sumarchenkova, I.A. Study of methods of processing waste products of caprolactam [Izuchenie metodov pererabotki otkhodov proizvodstva kaprolaktama] : Abstract. Dis. ... Cand. Chem. Sciences: 02.00.13 / I.A. Sumarchenkova; Samara State Technical University. - Samara, 2005. - 26 p.
8. Vessels and apparatuses. Norms and methods of strength calculation. Calculation of cylindrical and conical shells, convex and flat bottoms and lids [Sosudy i apparaty. Normy i metody rascheta na prochnost'. Raschet tsilindricheskikh i konicheskikh obechaek, vypuklykh i ploskikh dnishch i kryshek] : GOST 52857.2-2007. - Enter. 01.04.08. - M .: Standartinform, 2008. - 45 p.
9. Vessels and apparatuses. Norms and methods of strength calculation. Heat exchangers [Sosudy i apparaty. Normy i metody rascheta na prochnost'. Teploobmennye apparaty] : GOST 52857.7-2007. - Enter. 01.04.08. - M .: Standartinform, 2008. - 51 p.
10. Yursha, I.A. Experience of introduction of energy saving technologies in the nitrogen industry [Opyt vnedreniia energosberegaiushchikh tekhnologii v azotnoi promyshlennosti] / I.A. Yursha // Chemical Industry. - 2001. - № 4. - P. 14-16.
11. Karaseva, S.J. To a question about the quality of caprolactam and polyamide [K voprosu o kachestve kaprolaktama i poliamida] / S.Y. Karasev [et al.] // Russian Chemical Journal. - 2006 - T.50, № 3. - P. 54-58.
12. GOST 7850-2013 Caprolactam. Technical conditions. - Introduced on 01.01.2015. - Moscow: Standardinform, 2019. – 4 p.
13. Druzhinina, Yu. A. Methods of processing caprolactam-containing products based on the study of their chemical composition: Ph. Druzhinina Y. A.; Samara State Technical University. - Samara, 2009. - – 23 p.
14. Technological regulations of caprolactam-1 shop Grodno Azot, JSC.
15. Thin film evaporator: Pat. 2372129 Russian Federation, IPC B01D 1/22, B01D 3/00 / Glasl Wolfgang, Siebenhofer Matthäus, Konkar Michel; applicant FTU-Engineering Planungs-und, Beratungsgesellschaft M.B.H., Glasl Wolfgang. - No. 2006114674/15; application form. 01.10.2004; publ. 10.11.2009 // Official Gazette / Federal Service for Intellectual Property. - – 2009. - – № 31. - – P. 156.
16. Rotary thin film evaporator: Patent. 4370C1The Republic of Belarus, MPK B01D1/22 / V.A. Shulyak, D.I. Berezuk, V.N. Basharimova; applicant Mogilev Technological Institute - number a19980340; application. 07.04.1998; publ. 30.03.2002 // Official Newspaper /National Intellectual Property Centre. – 1996. - – № 27. – P. 174.
17. Straight line tube evaporator: patent. 2071802 The Russian Federation, IPC B01D1/06 / N.I. Saveliev, L.K. Zharikov, A.I. Efremov, L.A. Savelieva, V.N. Mayorov, I.A. Militsin, V.G. Shkuro; applicant Cheboksary Production Association "Khimprom". - No.5040944/26; declaration. 06.05.1992; publ. 20.01.1997 // Official bulletin / Federal Service for Intellectual Property. – 1997. – № 2. – P. 125.
18. Rotary section evaporator: Pat. 2108840 The Russian Federation, IPC B01D3/30 / A.F. Sorokopud; applicant Kemerovo Technological Institute of Food Industry. - No. 95113925/25; application. 02.08.1995; publ. 20.04.1998 // Official Gazette / Federal Service for Intellectual Property. – 1998. – № 11. – P. 112.
19. Film evaporator: Patent. 2266151 Russian Federation, IPC B01D1/22 / V.M. Firsov, Y. (NITI-Tesar, JSC). - No. 2004133981/15; Application form. 22.11.2004; publ. 20.12.2005 // Official Bulletin / Federal Service for Intellectual Property. – 2005. – № 35. – P. 86.
20. Zhdanuk E.N. Study of factors influencing the quality of caprolactam / E.N. Zhdanuk E.N., Krutko E.T., Prokopchuk N.R. // Proceedings of BSTU. Series Chemistry, Technology of Organic Substances and Biotechnology. - – 2011. - – №4 (142). - – P. 21–25.
21. Materials speech of the chairman of the Grodno Regional Committee of natural resources and environmental protection of Kazac G.V. [Materialy vystupleniia predsedatelia Grodnenskogo oblastnogo komiteta prirodnykh resursov i okhrany okruzhaiushchei sredy Kazaka G.V.] // Grodno Oblast Committee of Natural Resources and Environmental Protection [Electronic resource]. - 2010. - Access: http://www.ohranaprirody.grodno.by/news/aktualno/materialy-vystupleniya-predsedatelya-grodnenskogo/page-209.html. - Access Date: 10.05.2015.
22. Glazko I. L. Optimization of caprolactam distillation stage / I. L. Glazko [et al.] // Russian Chemical Journal (Journal of Russian Chemical Society named after D. I. Mendeleev). – 2006. – p. 1, № 3. – P. 59-64.

Design of mechanochemical reactions for preparation of advanced materials

Zara P. Cherkezova-Zheleva, Daniela G. Paneva
Institute of Catalysis, Bulgarian Academy of Sciences, Acad. G. BonchevStr., Bld. 11, Sofia 1113, Bulgaria1
zzhel@ic.bas.bg

***Abstract**: Mechanochemical activation is recognized as a green and sustainable method for preparation of different advanced materials, incl. highly active and selective catalysts.*
The study investigates the preparation of advanced materials with unique properties by application of mechanochemical method. Numerous laboratory experiments revealed the possibilities for the design of mechanochemical reactions toward environmentally friendly, sustainable and economical synthesis of target materials. An important part of the investigation is the physicochemical characterization of mechanochemically processed materials. Special attention is paid to follow the changes of material composition at different stages of the treatment.
The paper is a step forwards the development of the scientific foundations of mechanochemistry by studying and modeling the multidirectional processes that take place in mechanochemical treatment of materials. Such investigations are very important for selection of mechanochemical reactions with potential application in practice.
Acknowledgements: Acknowledgements: The authors gratefully acknowledge the financial support of the Bulgarian National Science Fund at the Ministry of Education and Science - Project № КП-06-КОСТ/18/ 2019 and the project COST Action CA 18112 "Mechanochemistry for Sustainable Industry" (Mech@SustInd), supported by COST (European Cooperation in Science and Technology). This article is based on the project activities of H2020-MSCA-RISE-2020 101007669: Chemistry of Platinum Group Metals, CHemPGM.

1. Introduction

Mechanochemical activation is recognized as an alternative attractive greener approach to prepare diverse advanced materials and has become an important synthetic tool in different fields (e.g., physics, chemistry, and material science) since is considered an ecofriendly procedure that can be carried out under solvent free conditions or in the presence of minimal quantities of solvent [1-2]. Being able to substitute, in many cases, classical solution reactions often requiring significant amounts of solvents. These sustainable methods have had an enormous impact on a great variety of chemistry fields, including catalysis, organic synthesis, metal complexes formation, preparation of multicomponent pharmaceutical solid forms, etc. In this sense, we are interested in highlighting the advantages of mechanochemical methods on the obtaining of advanced high- technology materials with new and improved properties.

2. Problem discussion

The old belief that the success of a chemical reaction depends of the presence of large amounts of a solvent is no longer valid [3]. Recently, enormous interest has been focused on the study of ecofriendly and sustainable reactions, with the aim to perform them under solventless conditions or at least with a minimal utilization of solvents. These kinds of reactions fall in the realm of **Green Chemistry**, prioritizing high yields and mild conditions [4]. Green Chemistry is a discipline prone to reduce the utilization of environmentally noxious materials and energetic resources. Green Chemistry promotes the development of benign reactions; limiting the use of solvents and finding the optimization of all resources employed (materials, reactants, reagents, solvents, and energy requirements). Green Chemistry is ruled by twelve lineaments [5-6].

Figure1.*TwelveprinciplesofGreenChemistry.*

Mechanochemistry is a term related with the chemical reactivity promoted by diverse mechanical stimulus, (typically friction, impact, collision, grinding), Fig. 2. A mechanochemical reaction is defined by the IUPAC as: "a chemical reaction that is induced by the direct absorption of mechanical energy" [1-2]. The recent interest in mechanochemical methods is due to diverse advantages compared with the classical-based dissolution reactions. According to Etter: "the absence or at least the minimal usage of solvents during the course of the reactions, often leads by mechanochemical methods to the phase similar to that obtained by solution crystal growth", suggesting that the presence of large amounts of solvent is not necessary for the formation of a new phase [3-4]. Mechanochemical methods are also preferred to be used when the product is not accessible via conventional reactions by classical preparation methods [1-4]. In addition, yields can be improved and reactions may proceed faster than in conventional way [1-4]. Some reactions exhibit a reduced energy consumption due to efficient energy transfer in the mixture reaction (e.g., planetary ball-milling) [1-2].

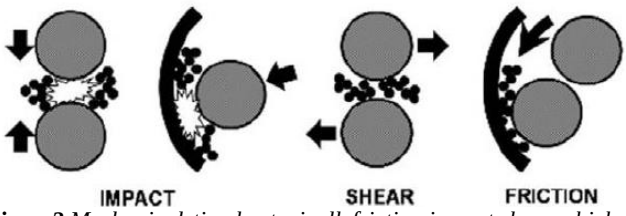

Figure2.*Mechanicalstimulus,typicallyfriction,impact,shear,whichpromotedchemicalreactionduringmechanochemicalprocess.*

3. Objective and research methodologies

Strategies/approaches for development of next generation advanced materials are connected to an improvement / optimization of methods of preparation and processing of new high-technology materials working . Special attention is paid on nanoscale materials - either in the form of bulk nanomaterials or in hierarchically organised structures. The produced new materials come with their new challenges: nanometrology - study of nanoparticles, single and multilayers and *in situ* studies, 3D element mapping, etc.
This study investigates the possibilities for preparation of advanced nanomaterials with unique properties by application of mechanochemical method. Numerous laboratory experiments revealed the potential for the design of mechanochemical reactions toward environmentally friendly, sustainable and economical synthesis of target materials. An important part of such an investigation is the physicochemical characterization of

mechanochemically processed materials in order to reveal the exact mechanism of the reactions. Special attention is paid to follow the changes of material composition at different stages of the treatment in order to move beyond picture-based and story-based experimental characterization.

Key point of advanced materials research is the characterization of materials properties at the macro-, micro-, nanometer and atomic scale using :

- ✓ X-ray analyses - x-ray diffraction and scattering,
- ✓ Electron-optical analytical and imaging (SEM/EDS, TEM/EDS, HRTEM);
- ✓ γ-ray/IR spectroscopies.
- ✓ Surface specific electron spectroscopic (XPS) and spectrometric (SIMS) techniques;
- ✓ Photon spectroscopic (IR and Raman probes) techniques;
- ✓ Scanning probe (AFM) techniques;
- ✓ Light scattering for particle characterisation (particle analysis, dynamic light scattering, centrifugal sedimentation, laser diffraction).

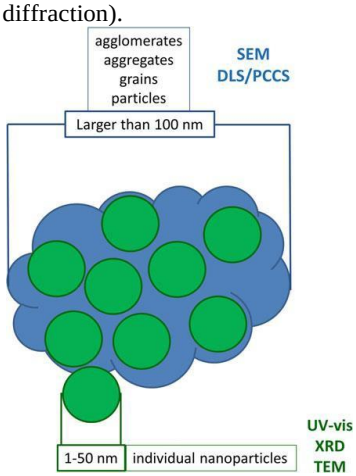

Figure3.*Schematicillustrationshowingwhichtechniquesreportthesize ofindividualnanocrystalsoffewnanometresandthatofagglomerates/gr ainsofsizelargerthan100nm.*

Materials characterization is the use of external techniques to probe into the internal structure and properties of a material or object.

Opportunity to impact the materials development cycle from scientific discovery to technological innovation and deployment.

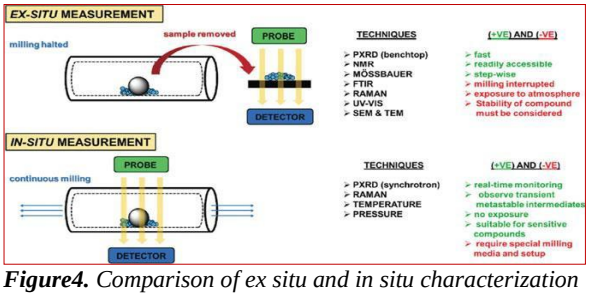

Figure4. *Comparison of ex situ and in situ characterization techniques for mechanochemicalreactions.*

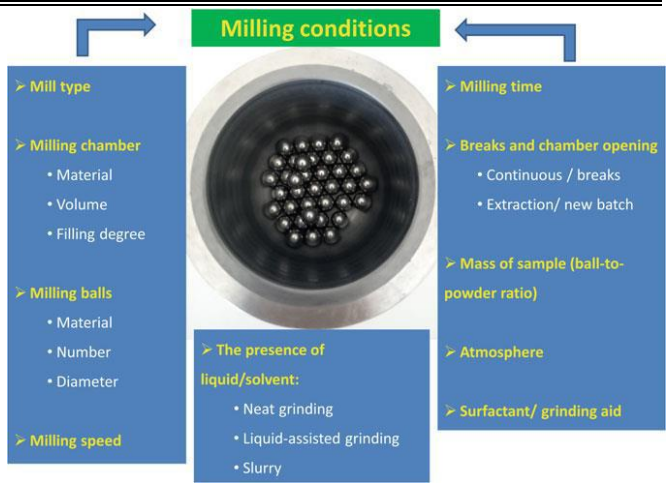

Figure5. *Basic milling conditions which can be optimized to achieve the best outcome*

High-Energy Milling is the Main Mechanochemical Tool

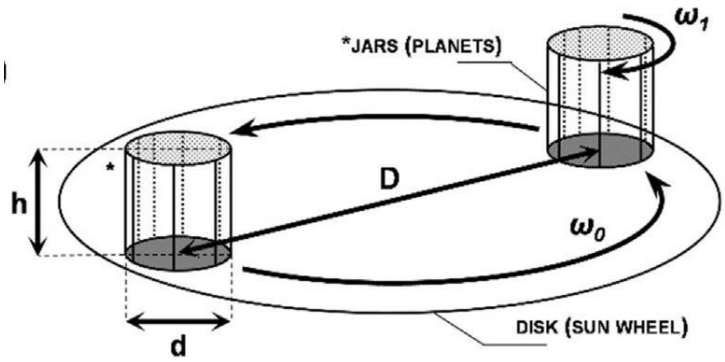

Figure 6. *Schematic representation of high-energy ball milling, where the jars revolve around the centre of the sun wheel (w_0, is the nominal angular velocity) while rotating around their own axis (the corresponding angular velocity, w_1, being not necessarily equal to w_0). In this context, the height (h) and diameter (d) of the vials are important. Combination of shear, friction, and impacts (c) is generated in planetary-type mills.*

3.Conclusion

Progress in materials research passes through the confluence of new theories, novel synthesis and characterization abilities, new computer platforms that extend capabilities to the atomic and nano-scale for the urgent demand for new and improved materials. Mechanochemical synthesis of advanced materials is strongly related to characterization of the materials at different steps during their live cycle (preparation, processing, recycling)

- ➢ Selection of appropriate methods to register the important properties of materials regarding their Application
- ➢ Methods should be combined to obtain information on different levels
- ➢ There is no universal receipt for characterization of each material
- ➢ Use of special conditions in case of unresolved problems, incl. *in situ* techniques, synchrotron beams, etc.

The paper is a step forwards the development of the scientific foundations of mechanochemistry by studying and modeling the multidirectional processes that take place in mechanochemical treatment of materials. Such investigations are very important for selection of mechanochemical reactions with potential application in practice

Acknowledgements:

The authors gratefully acknowledge the financial support of the Bulgarian National Science Fund at the Ministry of Education and Science - Project № КП-06-КОСТ/18/ 2019 and the project COST Action CA 18112 "Mechanochemistry for Sustainable Industry" (Mech@SustInd), supported by COST (European Cooperation in Science and Technology). This article is based on the project activities of H2020-MSCA-RISE-2020 101007669: Chemistry of Platinum Group Metals, CHemPGM. Financial support from the Bulgarian Academy of Sciences (Bilateral grant agreement between BAS and University of Belgrade, ICTM) is gratefully acknowledged.

4.References

1. Baláž, P.; Achimovičová, M.; Baláž, M.; Billik, P.; Cherkezova-Zheleva, Z.; Criado, J.M.; Delogu, F.; Dutková, E.; Gaffet, E.; Gotor, F.J.; et al. Hallmarks of Mechanochemistry: From Nanoparticlesto Technology. Chem. Soc. Rev. 2013, 42, 7571–7637.

2. Baláž, M. Environmental Mechanochemistry, Recycling Waste into Materials Using High-Energy Ball Milling, Springer Nature Switzerland AG, 2021.

3. Ahluwalia, V.K.; Kidwai, M. Organic Synthesis in Solid State. In New Trends in Green Chemistry; Springer: Dordrecht, The Netherlands, 2004; pp. 189–231.

4. Varma, R.S. Greener and Sustainable Trends in Synthesis of Organics and Nanomaterials. ACS Sustain. Chem. Eng. 2016, 4, 5866–5878.

5. Anastas, P.T.; Warner, J.C. Green Chemistry: Theory and Practice; Oxford University Press: Oxford, UK, 1998; ISBN 9780198502340.

6. Tang, S.L.Y.; Smith, R.L.; Poliakoff, M. Principles of Green Chemistry: PRODUCTIVELY. Green Chem. 2005, 7, 761–762.

Electroless metallization of 3D-printed details from PET and PETG

Maria. Petrova [(1)], M. Georgieva [(1) (2)], D. Lazarova [(1)]
[(1)] Institute of Physical Chemistry – Bulgarian Academy of Sciences
e-mail: mpetrova@ipc.bas.bg
[(2)] Technical University of Sofia, Sofia 1797, 8 "Kl. Ohridski" bul

***Abstract**: In recent years, 3D printing of samples of different materials by different technologies is rapidly being used, both in prototyping and becoming a regular production operation in a number of industries, for example: military and aviation industry, automotive industry, architecture, electronics, biotechnology, for receiving medical devices, etc. Using 3D printing, products of complex shapes and various sizes can be made with high precision and with lower raw materials costs, which is a prerequisite for a positive economic and environmental impact.*

The most commonly used 3D printing technology is FDM (Fused Deposition Modeling), in which 3D printed detail grows by successively adding layer by layer of molten material using a computer controlled extrusion nozzle head. FDM is the only additive technology that can be used to make products from thermoplastic materials with excellent mechanical, thermal and chemical characteristics.

A great priority of 3D-technologies is the ability to metallize of the obtained details. Electroless metallization, in which a thin layer of various metal coatings with good adhesion to the base polymer, is generally preferred. The most common materials who is often used for 3D printing and their subsequent metallization are: Acrylonitrile Butadiene Styrene (ABS), Polyethylene Terephthalate (PET), Polylactic Acid (PLA), Glycol-modified PET (PETG) and others.

The aim of the present study is to develop an appropriate pre-treatment and to compare the properties of electroless metallized 3D-printed samples of PETG and PET with different density of filling of the inner layers.

1. Introduction

In recent years, 3D printing of samples of different materials by different technologies is rapidly being used, both in prototyping and becoming a regular production operation in a number of industries, for example: military and aviation industry, automotive industry, architecture, electronics, biotechnology, for receiving medical devices, etc. Using 3D printing, products of complex shapes and various sizes can be made with high precision and with lower raw materials costs, which is a prerequisite for a positive economic and environmental impact.

2. Problem discussion

The most commonly used 3D printing technology is FDM (Fused Deposition Modeling), in which 3D printed detail grows by successively adding layer by layer of molten material using a computer controlled extrusion nozzle head. FDM is the only additive technology that can be used to make products from thermoplastic materials with excellent mechanical, thermal and chemical characteristics.

A great priority of 3D-technologies is the ability to metallize of the obtained details. Electroless metallization, in which a thin layer of various metal coatings with good adhesion to the base polymer, is generally preferred. The most common materials who is often used for 3D printing and their subsequent metallization are: Acrylonitrile Butadiene Styrene (ABS), Polyethylene Terephthalate (PET), Polylactic Acid (PLA), Glycol-modified PET (PETG) and others.

The main problem in the deposition of metal coatings by electroless plating is their roughening of the surface, which is achieved during the pre-treatment of the samples. Until this moment, the most used solutions in practice for etching the surface of the polymer substrate is based on toxic strong chromium acid solutions.

3. Objective and research methodologies

The aim of the present study is to develop an appropriate pre-treatment (и по конкретно операцията байцване) and to compare the properties of electroless metallized 3D-printed samples of PET and PETG with different density of filling of the inner layers.

In this regard, research has focused on replacing a etching solution containing Cr^{6+} (used in practice) which has a detrimental effect on the environment, with a more sparing one..

The studies were conducted with two types of 3D printed samples:

- PET samples - polyethylene terephthalate with a repeating unit /C10H8O10/n and has an amorphous structure, moderate resistance to strongly alkaline environment at room temperature and degrades at high temperature.

3D printed samples of PET produce by FDM (Fused Deposition Modeling) used 3D printer "Stratasys Fortus 250mc" with a print resolution of 0.25 mm and filling density of the inner layers of 100%.

- PETG samples – co-polymer, which combines the properties of PET and glycol. Adding glycol reduces the overheating effect of PET. PETG is an amorphous plastic that can be recycled, with great hardness, impact resistance and chemicals, transparency, elasticity, excellent thermal stability. 3D printed samples of PETG produce by FDM (Fused Deposition Modeling) used 3D printer "Sky-Tech SKYMAKER-A2" with a print resolution of 0.8 mm and filling density of the inner layers of 5%, 10%, 20%, 50% and 100%.

The samples were treated according to the following scheme:

1. Simultaneous degreasing and etching in an alkaline medium (within 100 ÷ 400 g/l NaOH),

T = 40 ÷ 70 °C, time between 3 ÷ 30 min

2. Pre-activation in 3M HCl solution; T = 25±2 °C; τ = 3 min

3. Activation in a colloidal solution of PdCl2 (activator A-75-12 (product of Technical University of Sofia));

τ = 5 min, T = 25±2 °C

4. Acceleration by a commercial X-75-4 accelerator (product of Technical University of Sofia);

τ = 5 min, T = 25±2 °C

5. Electroless nickel plating in solution: 20 g/l $NiSO_4.7H_2O$; 22 g/l $NaH_2PO_2.H_2O$; 10 g/l H_3BO_3; 8 g/l C_6H_5COONa;

τ = 15 ÷ 30 min, pH = 4.6÷4.8, T = 60 ^{0}C

The morphology and structure of the coating was determined by scanning electron microscopy (SEM) with a microscope JEOL JSM 733 (Japan). The elemental composition was analyzed by Energy Dispersive Spectroscopy (EDS / INKA). The thickness of the resulting Ni-P coating was determined by a gravimetric method as well as by X-ray fluorescence analysis (XRF) Fischerscope HDAL.

3.1. 3D printed samples of polyethylene terephthalate (3D-PET)

Table 1: *Dependence of the thickness and elemental composition of Ni-P coatings (deposition time 30 min) on the type of etching solution at T = 60 °C and time for etching 15 min*

Type of etching solution	Thickness of Ni-P coatings, µm	EDS, %At.		
		Ni	P	Pd
Without etching	1.09	5.13	0.9	0.2
CrO_3 and H_2SO_4 (commercial solution)	1.19	15.1	2.8	0.3
NaOH – 100 g/L	1.86	81.0	6.1	0.5
NaOH – 200 g/L	1.90	82.2	6.1	0.5
NaOH – 400 g/L	1.73	31.5	5.2	0.2

Table 2: *Dependence of Ni-P coating thickness (deposition time 30 min) on etching temperature in a solution containing 100 g/l NaOH and time for etching 15 min*

Temperature of etching solution, ^{0}C	Thickness of Ni-P coatings, µm	EDS, %At.		
		Ni	P	Pd
40	1.79	40.5	5.3	0.2
60	1.86	81.0	6.1	0.5
70	1.66	30.1	3.2	0.2

From the obtained results (Table 1) it can be seen that when treatment the 3D-printed samples in chromium-sulfuric acid solution the thickness of the deposited nickel-phosphorus coatings is almost the same as the samples that are directly electroless metallized (without etching). Accordingly, with this type of treatment, the content of the included nickel and phosphorus in the coating is very small. The thickness of the metal coating on the non-etching sample is due to the fact that it has a certain porosity, wich helps to fix the metal particles in the pores.

In cases where the samples are treated with a NaOH solution, the thickness of the obtained electroless coating increases. It is observed that with increasing the concentration of the base to 200 g/L, there is almost no change in the thickness and content of the included nickel and phosphorus in the coating. At twice the base' concentration (400 g/L), the thickness of the coatings significantly decreases. This may be due to the fact that 3D-PET is resistant in highly alkaline solutions and this leads to a not well roughening surface of the samples. The adhesion of the coatings with an adhesive test with scotch tape has been determined, which established that the best adhesion of the coating to the 3D-PET samples is in the case of etching in 100 g/L NaOH.

On Table 2 are shows the data obtained from the studies performed on the effect of temperature of the etching solution containing 100 g/l NaOH at a treatment duration of 15 min.

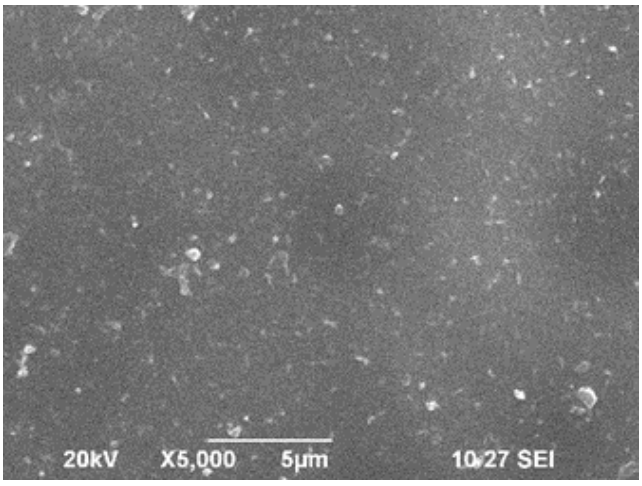

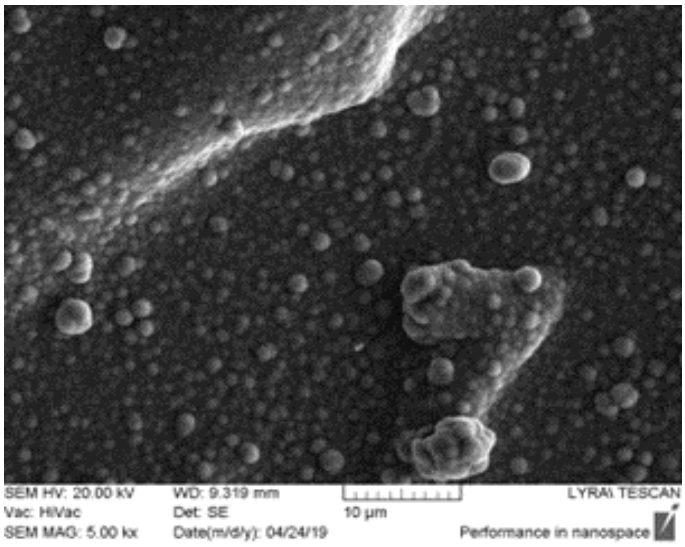

Fig.1: *SEM images of Ni-P coating deposited on 3D-PET etching in:*
a) CrO_3 u H_2SO_4; b) 100 g/l NaOH

SEM-images of the surface confirm the hypothesis that the etching in chromium-sulfuric acid solution is not appropriate for this type of 3D printed samples.

3.2. 3D printed samples of PETG (3D-PETG) with a filling density of the inner layers of 5%, 10%, 20%, 50% and 100%

The influence of NaOH concentration (Table 3) in the etching solution as well as the duration of etching (Table 4) in the obtaining of Ni-P coatings on PETG samples with a filling density of the inner layers 10 %, was investigated.

Table 3: *Dependence of the thickness and elemental composition of Ni-P coatings (deposition time 15 min) on PETG samples (with filling of the inner layers 10%) from the concentration of NaOH in the etching solution at T = 60 ^{0}C and time for etching 15 min.*

Concentration of NaOH, g/l	Thickness of Ni-P coatings, µm	EDS, %At.		
		Ni	P	Pd
Without etching	1,25	15.3	3.2	0.1
100	2,02	25.5	5.4	0.3
200	2,12	45.6	10.5	0.3
400	2,30	66.7	12.9	0.3

Table 4: *Dependence of the thickness and elemental composition of Ni-P coatings (deposition time 15 min) from the etching time in a solution containing 400 g/l NaOH at T = 60 ^{0}C.*

Etching time, min	Thickness of Ni-P coatings, µm	EDS, %At.		
		Ni	P	Pd
3	2,17	46.0	10.5	0.2
10	2,25	64.3	11.7	0.3
15	2,30	66.7	12.9	0.3
30	2,54	63.9	11.6	0.3

From the obtained data shows on Table 3 it can be seen that with an increasing concentration of NaOH in the etching solution, the thickness of the nickel-phosphorus coating increases, as does the amount of Ni deposited.
On the Table 4 presents the results for the influence of the etching duration time at concentration of the 400g/l NaOH in the etching solution.
The obtained results from Table 3 and Table 4 are also confirmed by the SEM images of nickel-phosphorus coating on PETG samples with a filling density of 10%.

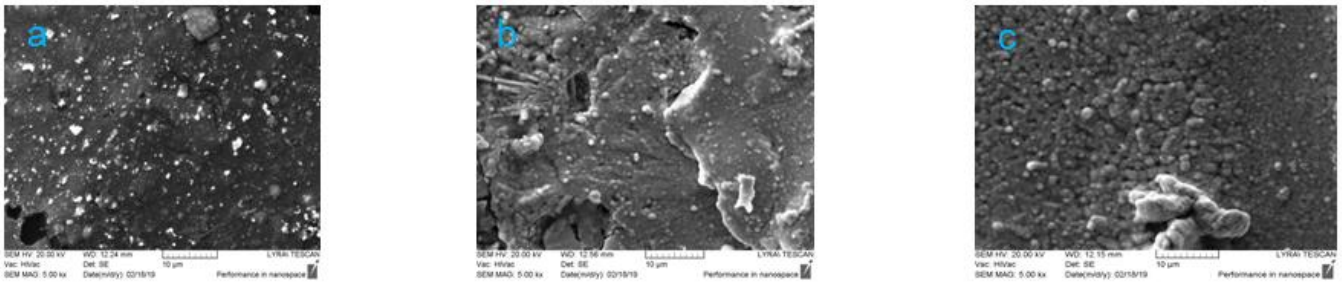

Fig. 2: *SEM-images of nickel-phosphorus coating on samples of 3D-PETG etching in: (a) 100 g/l NaOH (15 min); (b) 400 g/l NaOH (15 min); (c) 400g/l NaOH (30 min)*

On Table 5 comparing the results for the thickness and elemental composition of electroless nickel coatings obtained on 3D-printed PETG samples with different filling density of the inner layers.
The thickness data increases with the compaction of the internal layers in 3D printing. The higher content of P in the coatings also determines their amorphous character, as confirmed by the SEM-images in Fig. 3. The obtained electroless metal coatings are uniform throughout the surface with a pronounced globular structure most likely due to the higher phosphorus content.

Table 5: *Influence of the filling density of the inner layers of 3D-PETG on the thickness of the nickel coatings and the elemental composition of the coating*

Analysis		Filling density of the inner layers of 3D-PETG				
		PETG 5%	PETG 10%	PETG 20%	PETG 50%	PETG 100%
Thickness, µm	gravimetrically	1.77	2.30	2.97	3.39	3.53
	XRF	1.52	1.98	2.21	3.05	3.11
EDS, %At.	Ni	43.0	66.7	71.8	80.9	81.9
	P	9.8	12.9	16.1	15.3	15.7
	Pd	0.6	0.3	0.2	0.2	1.0

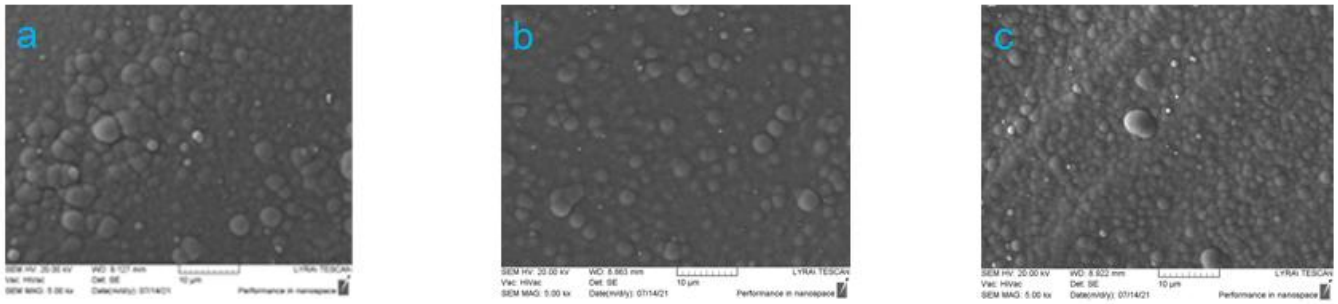

Fig. 3: *SEM images of the surface of nickel coating deposit on 3D-PETG with diferent densities of filling of the inner layers: a) 20 %; b) 50 %; c) 100 %*

4. Conclusion

Technology for electroless metalization of 3D-printed samples of PET (100%) and PETG with different densities of filling of the inner layers (5%, 10%, 20%, 50% and 100%) has been developed. The samples were treated according to the following scheme: simultaneous degreasing and etching, activation in colloidal palladium-tin solution and electroless nickel plating. Due to the harmful environmental impact of Cr^{6+} in the etching solution, other etching solutions containing different concentrations of NaOH was investigated.

The studies on the electroless nickel plating of 3D-PET samples shows that quality coatings are obtained when using the etching solution containing 100g/l NaOH.

The best quality and uniform coating are obtained on 3D-PETG samples with a 100 % filling density of the inner layers, which are etching in a solution containing 400 g/l NaOH.

The comparison of the results of samples with different filling density from 5 % to 100 % of the inner layers shows that with increasing the structural area with higher density, the deposition rate of nickel coating increases.

Acnowledgement:

This research has been carried out within the Project DN 19/1, "Metalizing of dielectric materials using innovative environmental electrolytes", funded by the National Science Found (Bulgaria).

Investigating the corrosion of bronze used for outdoor sculptures

Julieta Daniela Chelaru
Babes-Bolyai University, Romania
julieta.chelaru@ubbcluj.ro

***Abstract**: The aim of this study is to investigate the corrosion of two bronze monuments expose in the urban atmosphere. The chemical composition of the bronze and corrosion products formed on the statues's surface, were determined by SEM - EDX analysis and discussed.*

Al_2O_3 / Cu and Al_2O_3 / Ni systems as a basis for subsequent chemical deposition of metals

Christian Girginov[1], Boriana Tzaneva[2], Stephan Kozhukharov[3]
Department of Physical Chemistry, Faculty of Chemical Technologies, University of Chemical Technology and Metallurgy, Sofia, Bulgaria[1]
Department of Chemistry, Faculty of Electronic Engineering and Technologies, Technical University of Sofia, Sofia, Bulgaria[2]
LAMAR Laboratory, University of Chemical Technology and Metallurgy, Sofia, Bulgaria[3]
girginov@uctm.edu

Abstract: *It is well known that various metals can be incorporated in porous anodic oxide films on aluminum and its alloys, by means of AC-polarization from suitable electrolytes. In turn, the obtained this way systems (e.g., Al2O3 / Cu and Al2O3 / Ni) are a suitable basis for the subsequent chemical deposition of the respective metals. In this way, metal layers with good physico-mechanical and physico-chemical properties suitable for use in electronics can be formed.*

Specimens cut from the AA1050 alloy underwent preliminary surface treatment and were then anodized in a H2SO4 solution under galvanostatic conditions at constant temperature for 50 min. As a result, the obtained porous films were 20μm thick with a porosity of 0.15. Using suitable electrolytes, Cu and Ni were electrochemically incorporated by means of AC-polarization (20 V, 60 Hz, 15 min).

The obtained complex layers were characterized using modern analytical methods (optical and scanning electron microscopy, EDS, XPS, AFM). It turned out that under these conditions, highly ordered layers with reproducible composition, morphology and structure are obtained.

Acknowledgments: The authors are grateful for the financial support of this study to the Bulgarian National Science Fund (project No. КП06-Н29/1).

Out of plane MAE by dopping of novel 2D semiconductor Bi_2O_2Se

Dr. Dominik Legut
VSB - Technical University of Ostrava, Czech Republic
dominik.legut@vsb.cz

***Abstract**: For the spintronic applications like large data storages (high capacity HDD) the industry searches for ferromagnetic insulators at nanoscale size. Recently the discovery of Bi2O2 Se/Te phases that exist as 2D material and still are semiconducting attract attention. Here we investigate Bi2−nXnO2Se by transitional metal doping to introduce a magnetic spin order. We explore the electronic and magnetic properties of various ferromagnetic (e.g. Fe) or antiferromagnetic (e.g. Mn) transitional metals doped Bi2O2 Se phases within the framework of density functional theory based electronic structure calculations. We start with the magnetic order of the bulk phase in which the magnetic atoms form interlayer coupling that vary with the type and concentration of doped atoms and go towards the nanoscale dimension, i.e. 2D materials. As a result of the competitions of magnetic interactions the magnetic anisotropy energy is a crucial quantity. In combinations with Monte Carlo simulations we are able to solve the exchange interaction constants for the Heisenberg model and therefore evaluate the Curie temperature to see if these types of materials are suitable to become novel dilute magnetic semiconductors for spintronic applications at room and above temperatures.*